Cardiff School of Engineering

An Experimental Investigation into the Mixed Lubrication of Steel Surfaces

Presented for the candidature of Doctor of Philosophy

Mr. Ingram Weeks

April 2015

Declaration

This work has not previously been accepted in substance for any degree and is not concurrently submitted in candidature for any degree.

Signed …….. (candidate) Date ……..

STATEMENT 1

This thesis is being submitted in partial fulfilment of the requirements for the degree of PhD.

Signed …….. (candidate) Date ……..

STATEMENT 2

This thesis is the result of my own independent work/investigation, except where otherwise stated. Other sources are acknowledged by explicit references.

Signed …….. (candidate) Date ……..

STATEMENT 3

I hereby give consent for my thesis, if accepted, to be available for photocopying and for inter-library loan, and for the title and summary to be made available to outside organisations.

Signed …….. (candidate) Date ……..

Summary

A twin disk rig was used to perform a series of experiments investigating mixed lubrication. The disks used in the experiments were manufactured from case carburising steel, were hardened and had a surface finish ground transverse to the direction of oil entrainment in order to simulate the roughness orientation typically found on involute gear teeth.

Roughness profile measurements were taken in-situ between experiments which showed that the initial phase of operation for as-manufactured surfaces is a period of rapid plastic deformation, where asperity features on the surfaces accommodate to one another. It was found that this reduction in roughness improved the state of lubrication by reducing instances of contact between the surfaces.

Contact was assessed by measuring the electrical contact resistance between the disks during the experiments and the level of the contact voltage between the disks was used as an indicator of the state of lubrication existing between them. It was found that variations in the dimensionless film thickness strongly influenced the level of the contact voltage. The contact voltage waveform was also found to exhibit similarity between revolutions, indicating repeated contact between groups of interacting asperities.

Realigned profile traces demonstrate that prominent asperity features undergo significant plastic deformation during the running-in process. Over extended operation, it was seen that these same roughness features can be subject to a degree of fatigue at the roughness scale, which has been identified as micropitting failure in the experiments.

Modifications to an existing numerical model simulating the isothermal non-Newtonian EHL point contact to enable the use of measured 3D roughness shows that high pressures are generated in the region of interacting asperity features. Asperity contact is also seen to occur across the length of prominent ridges in agreement with images obtained from 3D profilometry which demonstrate prominent ridges experiencing fatigue.

Acknowledgements

Over the last few years I have been fortunate enough to meet some truly unique characters without whom I would have been unable to submit my thesis.

Firstly, I must acknowledge the crucial financial support provided by: The British Gear Association, X-Tribology, Goodrich and the EPSRC. Without this the research could not have taken place.

I would also like to express my gratitude and thank my three supervisors: Prof Ray Snidle, Prof Pwt Evans and Dr Alastair Clarke. Each of whom has shown dedication (and patience) in mentoring me throughout my habitation of the Tribology lab.

Thanks are also due to my good friend and teacher Dr Khayri Al-Sharif who has been most supportive in assisting me with the use of the EHL software.

Without the indispensable work and advice of the technical staff at Cardiff, we simply would not have been able to progress any experimental work and for that reason they are owed recognition for their efforts. Most notably, Steve Mead, Malcolm Seabourne, Paul Farrugia, Denley Slade and Richard Rogers.

I have also had the pleasure to share my office with a colourful group of students: Ben Wright, Anton Manoylov, Daniel Malagon, Nabeel and lastly my good friend, Ovidiu. Each of whom has been a pleasure to work alongside and interact with on a daily basis.

To some of the newer students in the department, I would also like to wish the best of luck to my friends Simon Hutt and Maasi Al-Mayali in the continuation of work in the Tribology group.

My family are also due gratitude for the love and support they have given me over the years. Without them I wouldn't be in the privileged position I am today.

Lastly, I would like to thank my girlfriend, Heather – despite living together in Wales for the last three years, she has played a crucial role in dispersing some of the clouds that have hung over me.

Table of Contents

Introduction

Tribology is the study of lubrication, friction and wear of contacting surfaces in relative motion. This thesis describes the author's role in progressing experimental work within the Tribology group at Cardiff University. Experiments were conducted using a twin disk rig to investigate the mixed lubrication regime where load between components is supported by a highly pressurised oil film as well as direct metallic contact. Due to the highly insulating nature of lubricating oil, the voltage existing between the two disks was used as an indicator of the state of lubrication at any point and this was found to vary with changes in film thickness.

A description of the twin disk rig and the author's role in implementing modifications for the purposes of investigating mixed lubrication is given in Chapter 3.

Chapter 4 describes the process of monitoring the initial period of operation a freshly manufactured surface experiences. It was clear from surface profile measurements that the surface topography underwent a significant degree of plastic deformation which has been seen as the surfaces running in. This running in that was witnessed was also found to improve the hydrodynamic performance of the surfaces allowing for greater separation between contacting bodies.

In Chapter 5, surfaces which have previously been run-in are used in speed varying experiments where changes in entrainment speed and the lubricant temperature at the inlet are both seen to have a significant impact on the level of the contact voltage. Following extended operation, disk pairs were removed and subsequently measured. It could be seen that on certain disk pairs micropitting was taking place. Surface profile measurements strongly associated the location of fatigue with the more prominent roughness features on the disks.

Modifications to existing software simulating the transient elastohydrodynamic point contact to allow the use of measured 3D surface roughness are described in Chapter 6. Time pressures restricted the author only to an initial investigation, however results were promising and

appeared consistent with experimental data with prominent roughness features experiencing greater levels of contact.

Future work will consist of further extending the results of EHL analyses to simulate the effects of plastic deformation. Profile measurements obtained showing the modification and eventual fatigue of the surfaces will also be used in the formulation of more accurate models for fatigue.

Nomenclature

h_0	Film thickness to be calculated at point of application of iterative equations (m)
h_k	Film thickness for the node (i,j) in the point solver (m)
h_u	Undeformed geometry (m)
A_0	Coefficients for unknown pressure in Reynolds equation
A_k	Pressure variable coefficients for Reynolds equation
B_0	Coefficients for unknown film thickness in Reynolds equation
B_k	Film variable coefficients for Reynolds equation
C_0	Coefficients for unknown pressure in elastic equation
C_k	Pressure variable coefficients for the elastic equation
D_0	Coefficients for unknown film thickness in elastic equation
D_k	Film variable coefficients for the elastic equation
E'	Effective elastic modulus (GPa)
$\bar{R}$	Overall reduced radius of contact (m)
R_x	Reduced radius of contact in the x direction (m)
R_{x1}	Radius of curvature in the x direction, for body one (m)
R_{x2}	Radius of curvature in the x direction for body two (m)
R_y	Reduced radius of contact in the y direction (m)
R_{y1}	Radius of curvature in the y direction for body one (m)
R_{y2}	Radius of curvature in the y direction for body two (m)
$\bar{U}$	Mean velocity component parallel to the x axis (m/s)
$\bar{V}$	Mean velocity component parallel to the y axis (m/s)
m_x	Mass flow parallel to the x axis (kg/s)
m_y	Mass flow parallel to the y axis (kg/s)

n_c	Number of neighbouring nodes used in iteration sweep for the point solver
p_0	Maximum contact pressure (Pa)
p_k	Film thickness for the node (i,j) in the point solver (Pa)
η_0	Absolute viscosity under ambient pressure conditions
σ_x	Flow factor parallel to the x axis
σ_y	Flow factor parallel to the y axis
τ_0	Eying shear stress (Pa)
a	Hertzian semi dimension on minor axis of contact (m)
b	Hertzian semi dimension on major axis of contact (m)
b	Hertzian contact semi-dimension in major axis (m)
E	Elastic modulus (GPa)
G	Dimensionless material parameter
h	Film thickness (m)
hc	Centreline film thickness (m)
hm	Minimum film thickness (m)
Hm	Dimensionless film thickness parameter
k	Coordinate system in solver
l	Coordinate system in solver
p	Pressure (Pa)
Q	Contact count rate
Ra	Roughness average parameter (m)
Rq	Root mean squared roughness parameter (m)
S	Separation of surfaces (m)
s	Coordinate used within the elastic equation
U	Dimensionless speed parameter

u	Deformed geometry (m)
V	Velocity component parallel to the y-axis (m/s)
v	Coordinate used within the elastic equation
W	Load (N)
x	Coordinate axis parallel to direction of entrainment
y	Coordinate axis transverse to direction of entrainment
z	Coordinate axis normal to the plane of contact
α	Pressure coefficient of viscosity (1/GPa)
η	Absolute viscosity (kg/ms)
Λ	Lambda ratio
ν	Poisson's ratio
ξ	Slide roll ratio
τ	Shear stress (Pa)
ρ	Density (kg/m^3)

1 Literature Review

1.1 The Study of Tribology

Tribology is defined as the study of friction, lubrication and wear of contacting surfaces and as such it is of great importance in many mechanical engineering problems. Though the term 'tribology' was not coined until the middle of the 20th century, the principles of tribology are not new and have been applied in many cases in earlier periods throughout history. There is evidence suggesting that the Ancient Egyptians may have used animal fat to lubricate the path over which building materials were hauled.

In the 21st century the study and application of tribology is at the forefront of any engineering application where contacting surfaces operate in relative motion. With the advent of more advanced materials and manufacturing methods there has been a tendency for failures in engineering systems to change from being structural to occurring at the interfaces between contacting bodies.

In more recent years emphasis has been placed on greater energy efficiency which has been prioritised in the design process across all aspects of engineering. Where the tribology of lubricated contacts is concerned this has resulted in the use of less viscous lubricants to reduce energy losses, operating in more demanding environments. Ignorance of tribological considerations can lead to inefficient operation and high friction, resulting in energy losses or the seizure and destruction of components. In any industry this is unacceptable, however, in aerospace applications where these components are often employed in safety-critical systems, such a failure can be disastrous.

The conditions to which modern day interfaces are subjected have proved both challenging for tribologists working in industry, where thinner lubricant films have put greater stress on material properties, and researchers working to produce accurate models, solving highly non-linear problems in mixed elastohydrodynamic (EHL) contacts, for example. A great challenge

also lies in producing experiments which accurately measure conditions such as surface temperature, traction and film thickness under realistic operating conditions.

1.2 Running In

When freshly manufactured components are first loaded together in operation, they tend to undergo an initial settling period which is commonly termed 'running-in'. The running-in phenomenon is specified as a series of processes during which wear rates and friction for contacting components stabilise (Hutchings, 1992). These factors are governed by changes in the surface topography due to plastic deformation and mild wear and also chemical changes that may take place in the lubricant and the formation of tribo-films on the contacting surfaces.

It has been known for over a century that proper running-in can greatly lengthen the lifespan of engineering components, though it was not fully understood at the time. Theories have now emerged that can explain why the initial period of operation is critical to a mechanism's long-term operation. These theories will be briefly discussed in the context of this thesis.

When real surfaces initially meet under a condition of no load they first contact at the tips of their roughness features, now referred to as asperities (Abbott and Firestone, 1933). This causes the real area of contact to be far less than the apparent contact area. When load is applied, high pressures will be generated in the region of these micro-contacts and the asperity features will deform until the increased bearing area is sufficient to support the applied load, this is shown schematically in Figure 1-1.

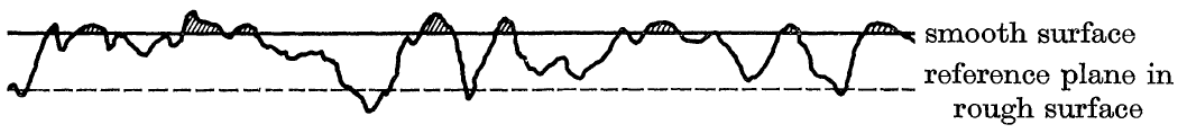

Figure 1-1 Contact of rough surfaces. Load is supported by those asperities (shaded) whose heights are greater than the separation between the reference plane (Greenwood and Williamson, 1966)

The increase in bearing area occurs as the asperity features supporting the load deform and their height decreases, bringing further roughness features into the contact to support the load.

The initial period of plastic deformation can also modify the subsurface microstructure of the contacting materials, resulting in a degree of work-hardening (Blau, 2005). However, most investigations have focussed on the geometric changes in the surface topography as this has the most immediate implications for the hydrodynamic performance of the interface.

Greenwood and Williamson, using a stylus profilometer were able to quantify the range of surface heights present on nominally flat metal surfaces (Greenwood and Williamson, 1966). Prior to this it was known that the real area of contact between two surfaces was actually far less than the apparent area of contact. In order to produce a parameter that would express the tendency for a contact to plastically deform, they modelled the surface as distribution of micro-contacts with spherical summits (Zhuravlev, 1940). From the work of Tabor concerning a ball indentation hardness test (Tabor, 1951), it was known that subsurface yielding occurred at contact pressures exceeding approximately 0.6H (where H was the hardness value). Including this in their statistical model of a surface, they were able to produce their 'plasticity index' which could be used as an indicator to predict whether a contact would be subject to yielding

The geometric change during the running-in of a surface is most frequently described by the use of the average roughness parameter. The average roughness (Ra) is used as a descriptor of the vertical departure of a roughness measurement from the mean line. Though used liberally it does not provide any information regarding the shapes of the asperities (Halling, 1975). Whitehouse and Archard set out to quantify the surface roughness using various statistical parameters that had not been previously employed as descriptors of topography. Whitehouse and Archard considered the mean radius of curvature of the asperity tips to be an important descriptor of a profile measurement (Whitehouse and Archard, 1970). It is found that when

subjected to loading, surface measurements show a rapid increase in radius of curvature of asperities as they deform (Bishop and Snidle, 1984) . When operating under EHL conditions, this change allows for more effective lubrication due to the less severe pressure spikes experienced at each 'micro-contact' due to increased conformity as the asperities become more rounded. It has become clear in this work that the shape of asperity tips is an important factor in their running-in and subsequent hydrodynamic performance.

Examples of the importance of considering running-in when commissioning new surfaces can be seen in the work of Østvik and Christensen (1968). Experiments carried out monitoring both the surface roughness and level of metallic contact were performed on a disk machine. Results showed that the load carrying capacity of an EHL contact was greatly improved by running-in and surfaces subsequently scuffed at higher loads. It was also found that as surfaces became run-in, asperity contacts became less frequent as the highest features were removed or flattened. Results from profilometry were compared which showed finer features removed as a process of wear.

Early experimental investigations into the running-in of lubricated surfaces tended to refer to the gradual reduction in roughness as a wear process and only hinted towards the plastic deformation of asperity contacts. Barber et al. (1987) conducted experiments into piston ring and cylinder materials for a range of honed surface finish qualities. It was found that under conditions of constant load, all materials reached a condition of nominally steady state wear quite rapidly – this result is displayed in Figure 1-2. Plastic deformation was not considered in this work. Initial surface finish was also investigated and found to influence scuffing load, where over a threshold of approximately 0.2µm, scuffing load was found to decrease with increasing roughness.

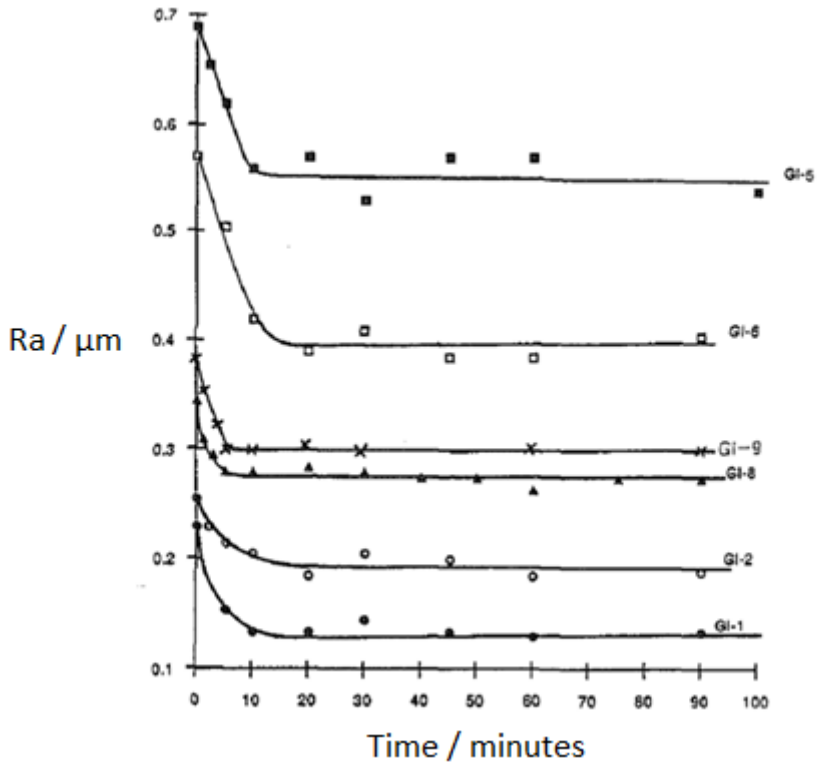

Figure 1-2 Average roughness parameter on cylinder liners versus time for a variety of different grey iron surface finishes (Barber et al., 1987)

More recently, the improvement in hydrodynamic performance has been demonstrated by the work of Lord and Larsson (2008) where using the electrical contact method on a variety of test surfaces, the run-in behaviour exhibited by all specimens showed reduced levels of metallic contact. This trend was also displayed in the earlier work of Tudor (1948), where the lubrication of journal bearings was investigated using similar methods. Tudor noticed that fewer instances of metallic contact were detected as running-in progressed. This work will be discussed further with regard to experimental technique in section 1.6.

A problem encountered in this work, was how to best compare asperity features between measurements where a degree of modification had occurred. Measurements in this work are re-plotted relative to their own mean line and accurate comparisons require an absolute reference line. Experiments into the plastic deformation of asperity features by Williamson and Hunt (1972) found asperities to persist at high loads. To further investigate the plastic deformation of asperity features whilst minimising bulk flow of material, Pullen and

Williamson conducted experiments employing their technique for relocation profilometry to ascertain the behaviour of asperity features under high load (Williamson and Hunt, 1968). Experiments were performed on a highly rough aluminium specimen (Ra = 6μm) encased in a jacket of steel to prevent sideways flow of the specimen.

It was observed that when subjected to loading, asperities on the surface of the softer aluminium specimen became flattened. Treating the mean line of a profile as an absolute reference line, valley features also appeared to rise in what was considered to be material redistributing to non-contacting areas (Pullen and Williamson, 1972), although this may be a consequence of roughness profile filtering.

Shown in Figure 1-3 are the percentiles of asperity surface heights as measured by a surface profilometer as the load applied to the rough test specimen was incrementally increased. It can be seen that as load increases, there is a pronounced decrease in the 90^{th} percentile, representing the highest peaks becoming flattened. Initially, there is a slight rise in the 80^{th} percentile, but as load increases and the tallest peaks deform, these eventually decrease with increasing load. As more regions of the surface are brought into contact with the counterface, it can be seen that the change in heights begin to level off. However, despite this levelling off that the higher percentiles experience, it can be seen that the lower, non-contacting regions of the surface experience a pronounced rise towards the mean line of the profile. This finding contrasted with existing models at the time as not all displaced material could be accommodated by residual strain (Greenwood and Tripp, 1967).

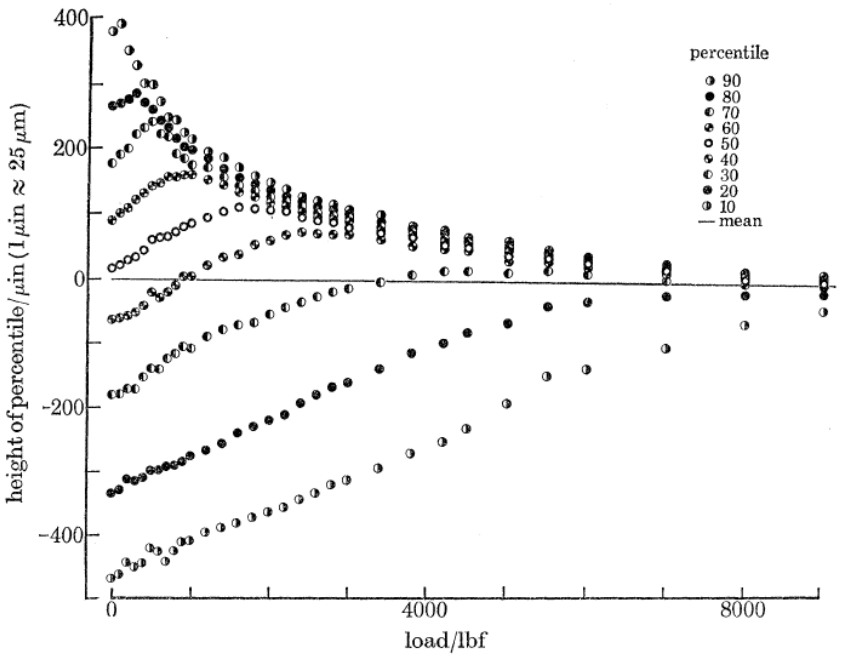

Figure 1-3 Plastic deformation of aluminium surface under high load, as shown by the changes in the deciles of its height distribution. As topmost regions of the surface move downwards, lower regions (non contacting) move upwards (Pullen and Williamson, 1972)

Whilst the smooth surface film thickness is used as an indicator of the mean gap between two surfaces, it is more helpful to apply the lambda ratio when rough surfaces are being considered. The calculation of the lambda ratio is frequently used to determine the extent to which rough surfaces will interact in a lubricated contact and it is calculated by dividing the smooth surface film thickness, h_c,by the composite surface roughness, shown in equation (1.1). Where R_{q1} and R_{q2} are the RMS roughness of each of the surfaces. Experiments in this work have found the level of contact occurring between surfaces under realistic conditions to be heavily dependent on the calculated lambda ratio. In this work, the central film thickness value h_c has been used, whereas other workers have used the minimum film thickness to calculate the lambda ratio. The central dimensionless film thickness has in this work been considered more appropriate for use with the rough mixed EHL contact. The reason for this being that the true minimum film thickness of a contact in the mixed lubrication regime is zero.

$$\Lambda = \frac{h_c}{\sqrt{{R_{q1}}^2 + {R_{q2}}^2}} \qquad \textbf{(1.1)}$$

The work of Andersson (1977) into the running-in period of gears explained the flattening of asperities as a wear process. Review of experiments conducted into running-in showed that the lambda ratio is an important parameter in determining the extent to which the asperity features on engineering surfaces are loaded.

Andersson explained that increasing the speed of the gear test rig used in experiments resulted in greater smoothing of the surface – which is now explained by decreasing inlet viscosity due to increased inlet shear heating. Scanning Electron Microscope (SEM) images produced of gear tooth flank replicas show surface asperity peaks which have been smoothed and flattened as a combined effect of surface yielding and wear while the valley features remain unchanged. Additional measurements also showed that no modification occurred in the region of the pitch point, where the lubricant film was at its thickest. It was effectively demonstrated in this work that lambda ratio is an important indicator of the normal loading experienced by asperity features, where thinner films, despite significantly reducing the applied load, can cause further modification due to higher loads experienced at the micro-contacts.

Bishop and Snidle published a number of papers describing their experimental test rig work using circumferentially ground steel disks (Bishop and Snidle, 1983, Bishop and Snidle, 1984, Bishop and Snidle, 1982). Their experiments showed that as surfaces are loaded together under EHL conditions, asperity features become rapidly flattened in response to increasing load. The mean peak radius of curvature was also seen to increase significantly as more load was applied and the valley features, which were not subject to the same high contact pressures or degree of interaction, retained their shape (Bishop and Snidle, 1984). Experiments performed to test the effect of surfaces plastically deforming and conforming to one another showed that a hard disk loaded against a soft disk would leave an imprint of its micro-geometry on the counterface (Bishop and Snidle, 1982). Axial profile measurements for the

disks used are displayed in Figure 1-4. The upper profile shows the trace for the hard disk following the application of load. It can be seen that the roughness features are very pronounced. The lower profile was taken from the softer disk in a region which interacted with the profile taken from the hard disk. It is clearly visible that an imprint of the hard surface has been left on the softer surface, where higher regions of the hard surface have created valley features in the softer surface as a result of plastic deformation and wear.

The important implications of conformity of micro-geometry could be seen much earlier in work by Tudor (1948), where putting run-in surfaces out of alignment reduced their hydrodynamic performance. These results suggest that running-in with engineering surfaces is not simply a general flattening of features but an accommodation process where the deformation of asperities is determined by the interaction with corresponding asperities on the counterface.

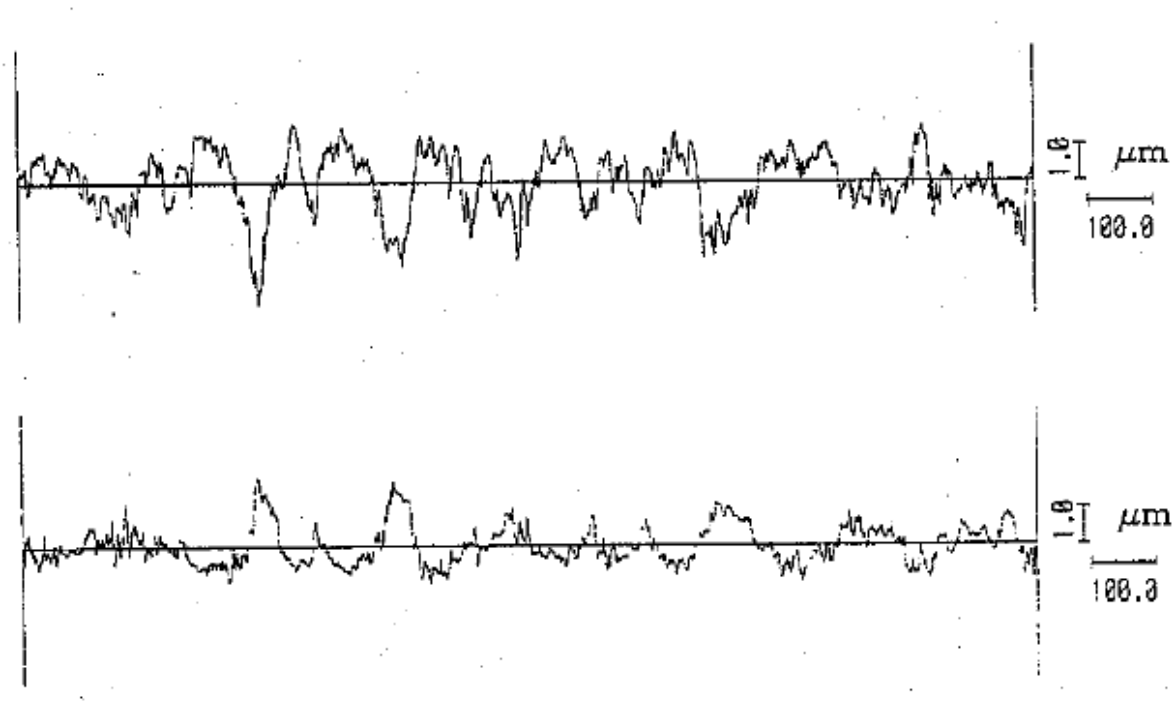

Figure 1-4 Axial profile trace of circumferentially ground test disks after running. Hard disk trace (top) and soft disk imprint (bottom) (Bishop and Snidle, 1982)

More recent interest into the process of running-in has been directed towards the long term implications of the effect that plastic deformation of asperities has on surface fatigue life.

Finite element modelling work conducted by Bryant et al.(2012) investigating the plastic deformation of rough surface line contacts draws attention to residual tensile stresses introduced by loading. Examples of these are shown in Figure 1-5 where following the removal of load, high residual stresses can be seen just below the surface aligned with the asperities. Bryant also demonstrated that the residual rough surface deformation only affects the asperity peaks and does not extend to the valley features.

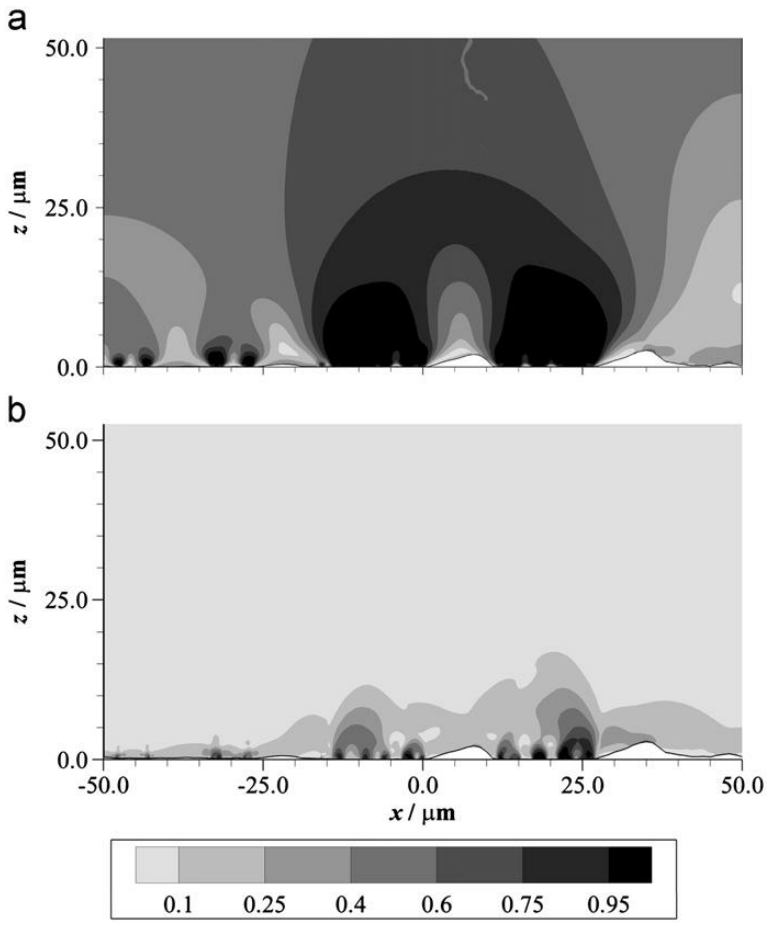

Figure 1-5 (a) Loaded and (b) residual von Mises stress contours for line rough surface line contact. Stress contours have been normalised for a yield stress of 1.62GPa (Bryant et al., 2012)

In experiments investigating the micropitting phenomena, it has also been suggested that the localised temperature rise generated by plastically deforming asperities during running-in could be associated with martensite decay, which has been found to occur with micropitting failure (Oila and Bull, 2005).

1.3 Mixed Lubrication and EHL

Disk rig experiments in this work are performed under conditions of mixed lubrication, and as such it is valuable to highlight the salient features of this area of study and its importance in an industrial sense.

Mixed lubrication is a form of elastohydrodynamic lubrication (EHL) where the film thickness is less than the composite surface roughness. In this intermediary region between boundary and full film hydrodynamic lubrication, load is shared between interacting asperities and thin lubricant films. Much attention has been directed towards mixed EHL as the majority of power transmission components operate with some degree of asperity contact. Increasing pressure on engineers to save energy leads to the use of less viscous lubricants which in turn reduces the Λ ratio causing more load to be carried by the asperities, and having implications for component lifespan. A good understanding of mixed lubrication can aid in reducing surface failure and optimising performance.

Early experimental work into lubricated contacts employed electrical contact resistance measurements from which to infer a degree of metallic contact occurring. These works revealed the existence of what is now known as mixed lubrication (Abbott and Firestone, 1933, Courtney-Pratt and Tudor, 1946, Østvik and Christensen, 1968, Furey, 1969). However, the use of electrical contact resistance as a means of providing researchers with quantitative information regarding film dimensions is considered to have fallen short of what might have been the expectation. This has paved the way for other methods of investigation, through which much has been learned, and these will now be discussed.

Optical interferometry has seen much use in the latter half of the 20th century for its ability to provide detailed images of film thickness distributions within an EHL contact. The method employs the use of interference fringes created when light is reflected back through a fluid film. The colour of the fringes will be dependent on the film thickness, from which values for

film thickness can be interpreted. One obvious drawback of using such a method is the specific material requirements of the components used. The need to use both a highly reflective and a transparent component place limitations on the comparisons that can be made directly with engineering surfaces. However, due to its ability to examine the film thickness across the contact in minute detail the method is heavily used.

Because of this valuable ability to provide researchers with quantitative data, work has often been paired with simulations and comparisons made between them. The use of interferometry has enabled researchers to observe the phenomenon of lubricant cavitation as well as the effects of micro-EHL – where roughness features are considered to behave as independent EHL contacts (Kaneta and Cameron, 1980).

Early research into interferometry in tribology stemmed from work conducted by Archard and Kirk, where upon investigating the influence on various parameters on the point contact created by crossed cylinders, an estimation of the size of the contact zone was made based upon the interference fringes created by white light passing through a perspex cylinder (Archard and Kirk, 1961). This result was also seen by Cameron and Gohar (1966)in their investigation using a steel ball on glass disk. Their work revealed the now well-known horseshoe shape seen in film thickness contours for EHL point contacts. Their work also revealed that, in contrast to line contact situations, the minimum film thickness occurs as side lobes in point contacts, as opposed to the outlet constriction. The ball on disk technique was later further refined by Cameron and Figure 1-6 was produced by Wedeven which clearly shows the restricted side lobes, reduced film thickness at the exit and cavitated wake.

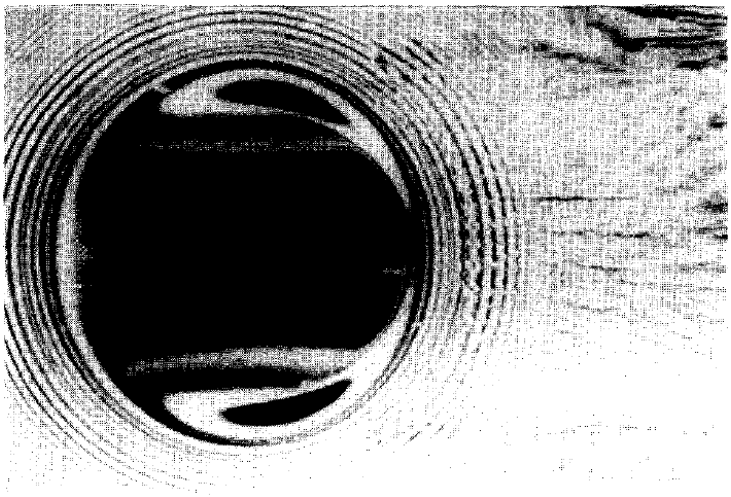

Figure 1-6 Interferogram for a ball on disk EHL point contact (Wedeven, 1970)

The interferometric method has been further developed in more recent years to allow the measurement of very thin films. This has been achieved through the use of a semi-reflective spacer-layer on the transparent surface.

In more recent years this method has been used in tandem with electrical contact resistance techniques to provide data regarding contact levels as well as film thickness (Guangteng et al., 1999).

Experimental work allows researchers to validate simulation work to some extent, but falls short in providing detailed information regarding the way in which pressure and shear stress are distributed throughout the contact. Without this information, accurate modelling of component fatigue life is impossible and predictions for surface damage are based on heuristic techniques developed from experimental observations of failure.

The early work into the simulation of EHL contacts was based upon the work of Reynolds, where the film thickness for the conformal contact of a journal bearing was calculated using the now well-known Reynolds equation. In an attempt to apply this method to contraformal contacts, Martin used an incompressible, isoviscous Newtonian lubricant to calculate the film thickness between contacting gear teeth, where the contact pressures are orders of magnitude higher than those experienced in the conformal journal bearing contact (Martin,

1916). Film thicknesses calculated were in the region of 1-10nm, far less than the average roughnesses of the surfaces considered. However, upon observation of gears that had been run for extended periods, it was identified that the original machining marks could persist on the gear tooth flanks, implying that the actual film thickness was far thicker than that Martin calculated.

Further progress in the analysis of contraformal lubricated contacts was made in the 1930s where researchers included the effect of elastic deformation at the interface (Peppler, 1936) and also the pressure dependent nature of the lubricant viscosity (Gatcombe 1945, Blok 1950). Significant progress was made when Grubin included the combined effect of local elastic deformation and the pressure dependent nature of the lubricant viscosity to produce a film thickness formula. Using the Grubin solution, the dimensions of the film thickness could be calculated by employing the following assumptions:

- The elastically deformed shape of the contacting bodies in lubricated contact is the same as that for dry contact.
- The hydrodynamic pressure at the boundary between the Hertzian region and the outlet approaches infinity.

The EHL problem was later solved numerically without the making these two assumptions. This was achieved initially by Petrusevich (1951), who presented results for three different speeds at the same conditions of load. These results showed the now well-known EHL characteristics, which included an approximately constant film thickness with an outlet constriction and an outlet pressure spike. The solutions presented by Petrusevich correctly showed the film thickness increasing with speed, however a slight increase in film thickness could also be seen with increasing load which was not understood.

Following the work of Petrusevich, Dowson and Higginson produced their important paper in which they used their newly developed “inverse method” to overcome difficulties of numerical instability and slow numerical convergence that had been associated with previous direct iterative approaches (Dowson, 1959). It was clear that the inverse approach could produce results for heavily loaded cases corresponding to real engineering practice. A formula predicting the central film thickness obtained by curve fitting a range of numerical solutions was presented by Dowson and Higginson (1961). The formula was later modified in 1965 by Dowson to the form shown in Equation 1.2 (Dowson, 1966). Where H_m is the dimensionless film thickness, R_x is the radius of curvature in the direction of entrainment and G*, U* and W* are the dimensionless material, speed and load parameters respectively.

$$H_m = {}^{h_m}/_{R_x} = 2.65G^{*0.54}U^{*0.7}W^{*(-0.13)} \quad \textbf{(1.2)}$$

Dowson and Toyoda also presented their formula for predicting the central film thickness based on numerical solutions. The formulas used to approximate the central film thickness all used the four dimensionless parameters introduced by Dowson and Higginson (1979). Later on, Chittenden *et al.* (1985) developed their expressions which allowed the accurate prediction of central and minimum film thicknesses within the EHL contact. These expressions have been used in this work in combination with knowledge of the surface roughness to produce an approximation of the lambda ratio.

As has been previously discussed, no surface is perfectly smooth. The incorporation of surface roughness into the EHL solution has proved a most challenging and active area of research. Since the 1970s, many attempts have been made at modelling the problem. Two types of solution methods have generally been applied, a stochastic approach and a deterministic

approach. Due to the large amount of computing power necessary to deal with roughness effects deterministically, early efforts generally applied a stochastic approach.

Stochastic models however are only able to produce results for general trends and approximate values. It is necessary for researchers to accurately model local variations of variables such as pressure and film thickness which can have a significant impact on the long term operation of an interface. Deterministic solutions to the rough surface EHL problem have received much more attention in the last 20 years, due to advances in computer technology.

The earliest deterministic solutions of the rough surface EHL problem modelled the effect of artificial roughness, such as sinusoidal waves and simple irregularities within the geometry, on the contact.

Early rough surface EHL models focussed upon the solution of a stationary surface with sinusoidal roughness against a smooth, moving surface under isothermal Newtonian conditions (Kweh et al., 1989). These models showed that the introduction of roughness features transverse to the direction of oil entrainment causes large pressure ripples far in excess of the maximum Hertzian contact pressure. Figure 1-7 shows results of the rough surface EHL model run by Kweh with different levels of sinusoidal surface roughness superimposed on one another. It can be clearly seen that increasing the amplitude of the sinusoidal roughness features increases the amplitude of the ripples in the pressure distribution.

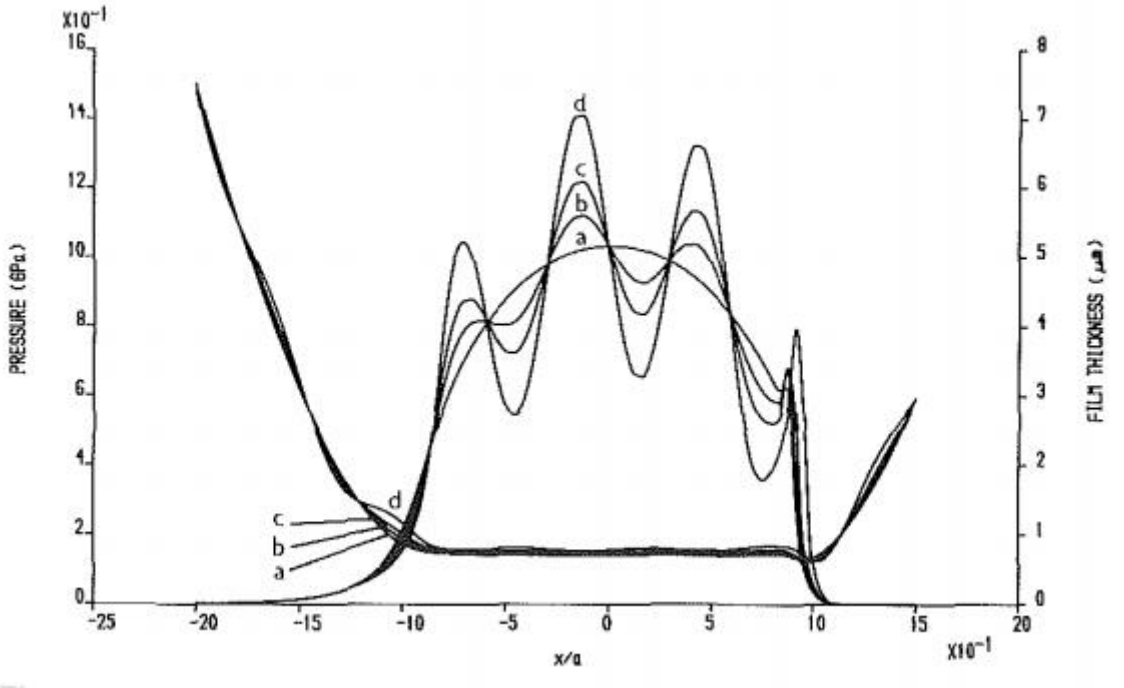

Figure 1-7 Longitudinal centreline pressure distributions and film thickness profiles at temperature of 80°C. (a) R = 0.0; (b) R = 0.0625 μm; (c) R = 0.125 μm; (d) R = 0.25 μm (Kweh et al., 1989)

The high pressures generated by the surface also caused flattening of the asperities, which had also been seen in similar work performed by (Goglia et al., 1984). Further experiments also demonstrated the effect of superimposing longitudinal sinusoidal roughness features onto the transverse roughness, generating a 3D roughness profile on the stationary surface. Results showed that transverse roughness features caused larger pressure fluctuations compared to those orientated longitudinally. It was also found that the effect of superimposing these longitudinal roughness features was to greatly reduce the film thickness levels for the cases considered. This was considered to be due to leakage into valley features. Preliminary results for a numerical solver presented in this work show a tendency for contact between surfaces to accumulate more rapidly at the edge of longitudinal scoring marks, which could also be associated with leakage.

Kweh later extended these simulations and studied the effect of incorporating real surface roughness measured by stylus profilometry into the EHL line contact model (Kweh et al., 1992). The line contact model was also run assuming isothermal Newtonian lubricant

behaviour. It was found that the introduction of transverse roughness into the line contact model causes large pressure ripples as was previously seen in the introduction of sinusoidal roughness into the EHL point contact model. Upon inspection of results it was found that large pressure maximums occurred at regions of low film thickness whereas local minimums would occur at valley features. The flattening of asperity features passing through the EHL contact was not as pronounced as that witnessed for sinusoidal roughness features under similar conditions and this was considered to be due to the higher relative frequency of the asperities on the measured rough surface.

Two dimensional roughness features were introduced by (1991). Point contact solutions to the EHL problem were obtained using 3D roughness by Xu and Sadeghi (1996) and Zhu and Ai (1997). The effect of moving roughness features on the thermal EHL problem were observed and found to be highly significant causing local pressure and temperature spikes within the contact. Modelling of the contact over a range of conditions found the effect of the roughness to be more significant when operating with thinner films. Simulations were however run under conditions of relatively thick films and did not consider mixed lubrication.

Recent investigations into mixed lubrication using measured surface profiles showed that the introduction of roughness produced large pressure spikes much greater than those seen in smooth surface solutions (Holmes et al., 2005a, Elcoate et al., 2001). In agreement with the earlier work these large pressure spikes were found to be aligned with close approach of asperities through the EHL film (Kweh et al., 1992) .

Using the coupled method to simulate the transient isothermal non-Newtonian EHL problem, Holmes et al. (2005a) developed a mixed lubrication model where direct contact of asperities was found to occur between surfaces under realistic conditions. Levels of contact were found to increase towards the transverse edges of the contact ellipse. It was suggested that this higher occurrence of contact was due to transverse leakage of lubricant occurring at the

transverse boundary of the Hertzian contact, which reduced the film thickness. Figure 1-8 shows contour plots of the cumulative contact rate for the point contact EHL problem using the coupled method (Holmes et al., 2005a). Contour plots show the results for simulations over a range of slide roll ratios, ξ, at the same mean entrainment speed. Over the length of a simulation, contact occurred occasionally between the surfaces. The contact count rate, denoted by Q, was the number of time steps a given mesh point experienced contact over the length of the simulation per unit time. It can be seen that Q is at its highest at the transverse edges of the contact.

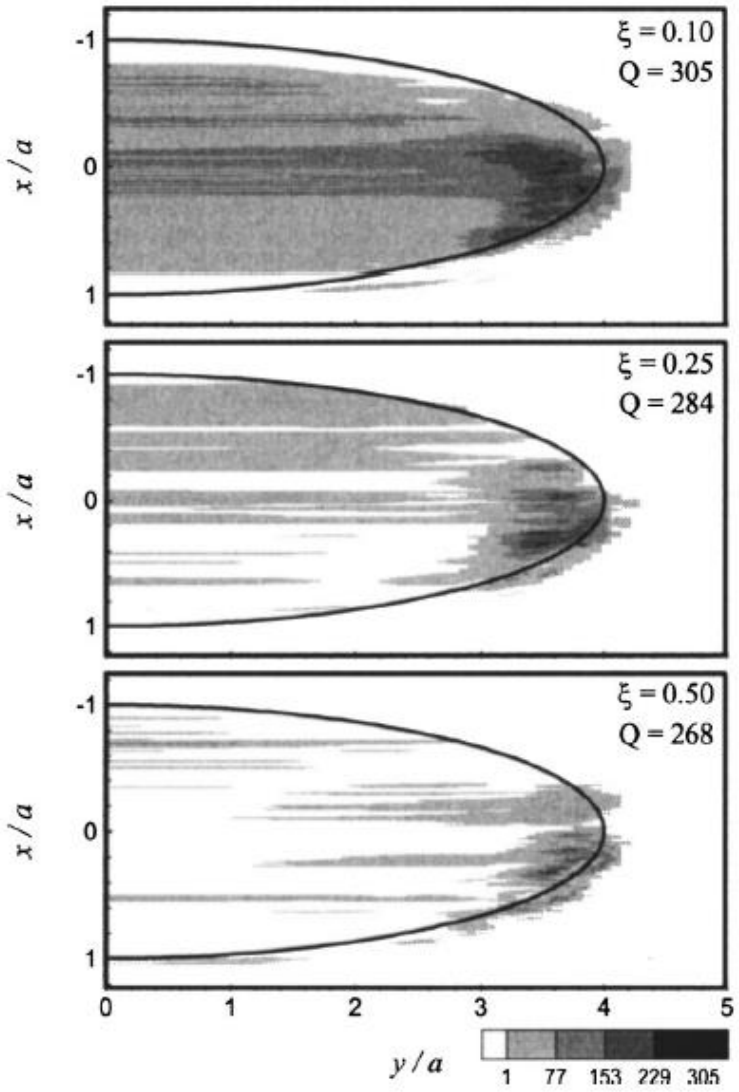

Figure 1-8 Contours of contact count rate Q/ms for the transient analysis. The heavy curve indicates a Hertzian dry contact area.

The introduction of transverse waviness into the roughness was also shown to increase the level of contact at peaks as the amplitude of the waviness was increased due to decreased film thickness as seen by Kweh et al. (1989). Results similar to those observed in EHL simulations have also been obtained experimentally by Patching et al. (1995)where scuffing tests performed on disk specimens with roughness orientated transverse to the direction of oil entrainment were found to scuff initially at the extreme edge of the running, i.e. at the transverse Hertzian contact boundaries track. Figure 1-9 shows a photograph of the surface of a test disk which has been run under load to investigate scuffing in elliptical point contacts. The transversely orientated surface finish, simulating the direction of grinding in gear teeth, is clearly visible. The contact track created by the plastic deformation of asperities under load can be seen as a dark band running normal to the direction of the grinding marks and is clearly indicated. The scuffing mark is visible as a darker band and occurs as a narrow region located towards the edge contact track. The ellipse shown superimposed on the contact track represents the size of the Hertzian region in the scuffing experiment at the load applied when scuffing occurred. It can be seen that scuffing occurred towards the edge of the ellipse in agreement with the increased contact rate seen in results of the EHL simulations shown in Figure 1-8.

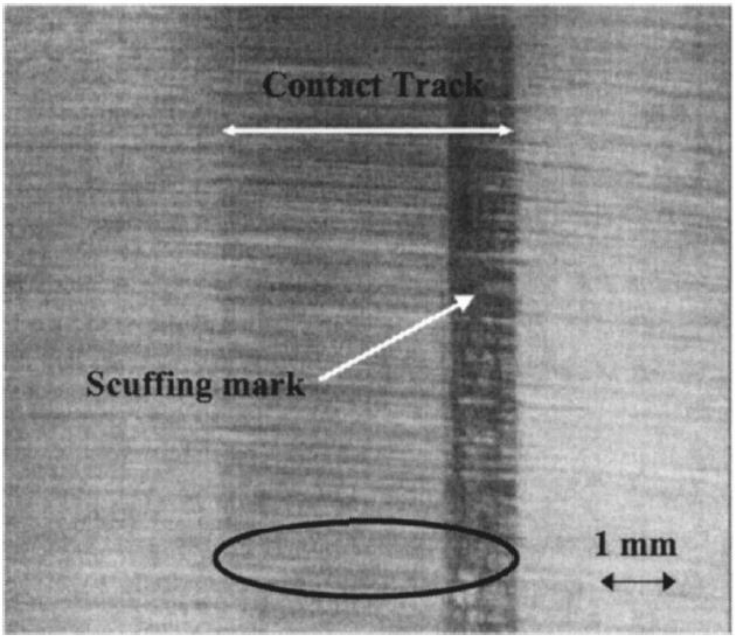

Figure 1-9 A photograph of a test disk with a finish transverse to the direction of oil entrainment where scuffing can be seen to have initiated at the edge of the contact zone (Patching et al., 1995)

The surface roughness used by Holmes et al. (2005a) was based on centre line roughness profiles taken from disks and extruded perpendicular to the rolling/sliding direction for use in the analysis. The solution method used by Holmes has been extended in Chapter 6 to include measured three-dimensional rough surfaces and calculated contact rates have also been found to be highest towards the transverse edges of the contact zone.

The coupled solution method has been most recently employed in a simulation of gear tooth contacts with measured surface profiles. It was also found that, under conditions used in gear rig tests, contact would occur intermittently and high pressures would be generated in the region of interacting asperity features. Figure 1-10 shows the solution to a time step where both surfaces are measured from gear tooth flanks used in a corresponding set of experiments. It is clear that regions of thin film correspond to particularly high hydrodynamic pressures, whereas thicker films result in lower pressures. The Hertzian pressure distribution is shown as a dashed line and it can be seen that the rough surface pressure distribution fluctuates about this.

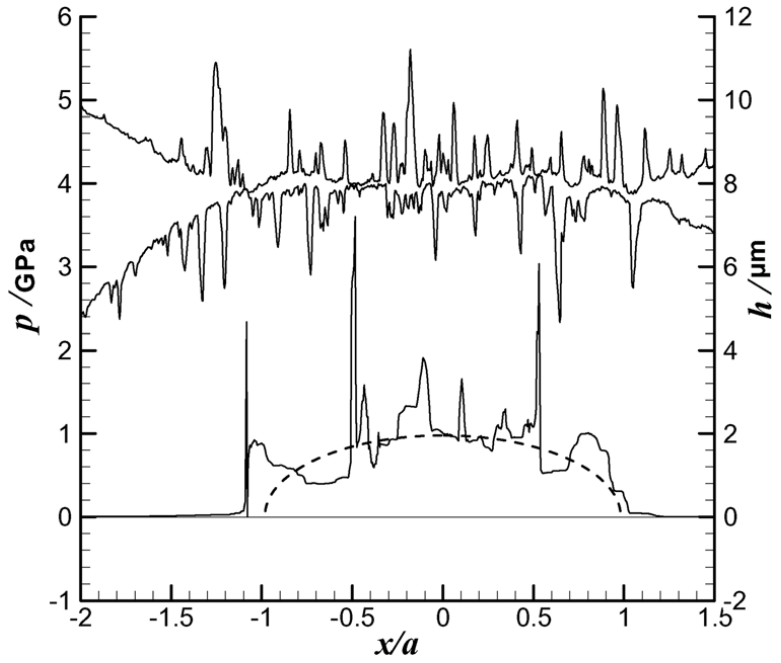

Figure 1-10 Results for rough surface EHL simulation showing pressure profile (lower curve) and deflected surfaces (upper curves) with smooth surface pressure (dashed curve) (Evans et al., 2013)

The results of these simulations have allowed fatigue calculations to be performed. These have demonstrated that the large pressures which are applied cyclically within the contact can result in subsurface damage accumulating. Figure 1-11 shows the results of a fatigue simulation with surfaces used, it can be seen that regions of higher damage shown in red, occur most frequently aligned with peaks on the surface and are highly localised. The location of damage obtained from fatigue simulations is supported by results in this work where close monitoring of the surface topography has shown micropits to form in the regions of asperity peaks.

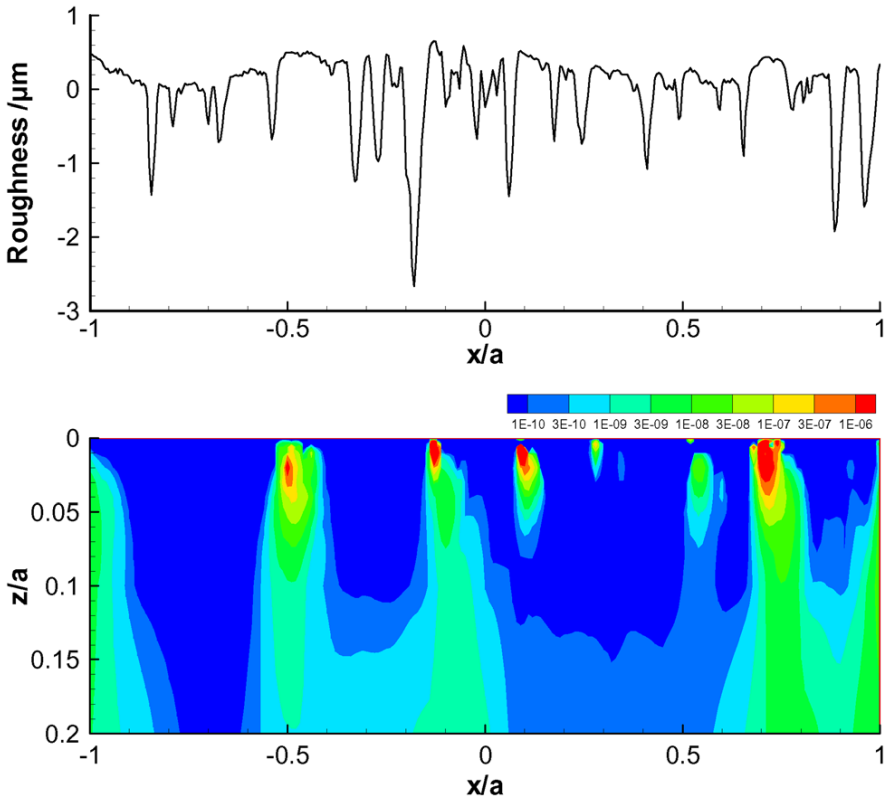

Figure 1-11 Contours of subsurface damage occurring beneath a measured rough surface taken from a gear rig experiment. The Hertzian contact dimension used is a=0.247mm (Evans et al., 2013)

Results have also shown that the rate at which damage accumulates is dependent on the level of sliding. This is related to the rate at which asperities interact as they pass through the contact (Holmes et al., 2005b, Evans et al., 2013). The level of damage is also dependent on the lambda ratio, where lower lambda ratios will result in greater asperity loading. Figure 1-12 shows the results from fatigue calculations, carried out using data generated from EHL simulations for pressure and film thickness. It can be clearly seen, that increasing the lambda ratio greatly reduces the level of damage for the surface considered (Sharif et al., 2012).

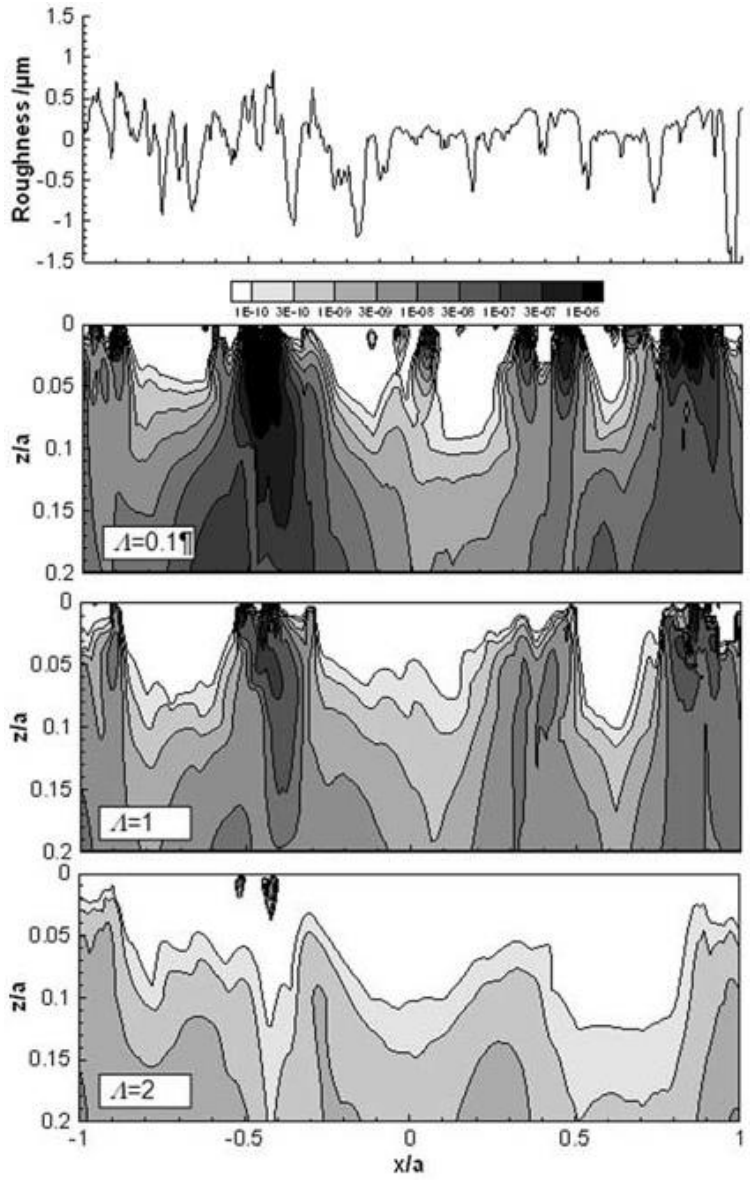

Figure 1-12 Contours of subsurface damage D for rough surface contact for varying lambda ratio (Sharif et al., 2012)

1.4 Scuffing

Scuffing of bearing surfaces operating in EHL is initiated under extremely severe conditions when the lubrication mechanism breaks down resulting in solid phase welding of components at the interface. Scuffing is characterised by rapid wear and a high coefficient of friction, in the region of 0.4-0.5 (Hutchings, 1992). This typically occurs in components operating at high sliding speeds. Scuffing is believed to arise due to a complete breakdown of the lubricant film – at high levels of sliding, frictional heating of the lubricant reduces the viscosity to such an extent that film thickness drops, decreasing the load carrying capacity of the film with

increasing speed (Hutchings, 1992). As a result of the catastrophic implication of scuffing failure resulting in the complete seizure of transmission components, much effort has been expended in reproducing scuffing experimentally in an attempt to formulate a model for failure.

Much research has been conducted investigating the effect of surface roughness on scuffing failure, comparisons made by Patching et al. (1995), using a twin disk rig, found superfinished surfaces to give superior scuffing performance over axially ground disks, where the axially ground finish was used to simulate the finish found on involute gear teeth in aerospace applications. It was later found that results from simulation work conducted at Cardiff agreed with the scuffing location on the axially ground disks, where decreasing film thickness led to a rise asperity contacts at the edge of the Hertzian zone. This was associated with side-leakage occurring due to the unsealed valley features in a transverse ground surface (Holmes et al., 2005a).

1.5 Micropitting

Micropitting is a surface fatigue phenomenon that frequently occurs on surfaces operating in the mixed lubrication regime. It has received much attention in recent years and is commonly seen to occur in case-hardened steel gears. In a similar manner to regular pitting failure, micropitting involves the cracking and breaking away of material from the surface of components, however whilst ‘macro-scale’ pits can have dimensions of the order of a few millimetres, micropits as the name suggests exist at the microscale and cannot be identified individually by eye. Seen under direct lighting, a micropitted surface gives a ‘frosted’ or matted appearance in comparison to regions without fatigue (Errichello, 2012). An example of this is shown in Figure 1-13 and similar results have been obtained in this body of work.

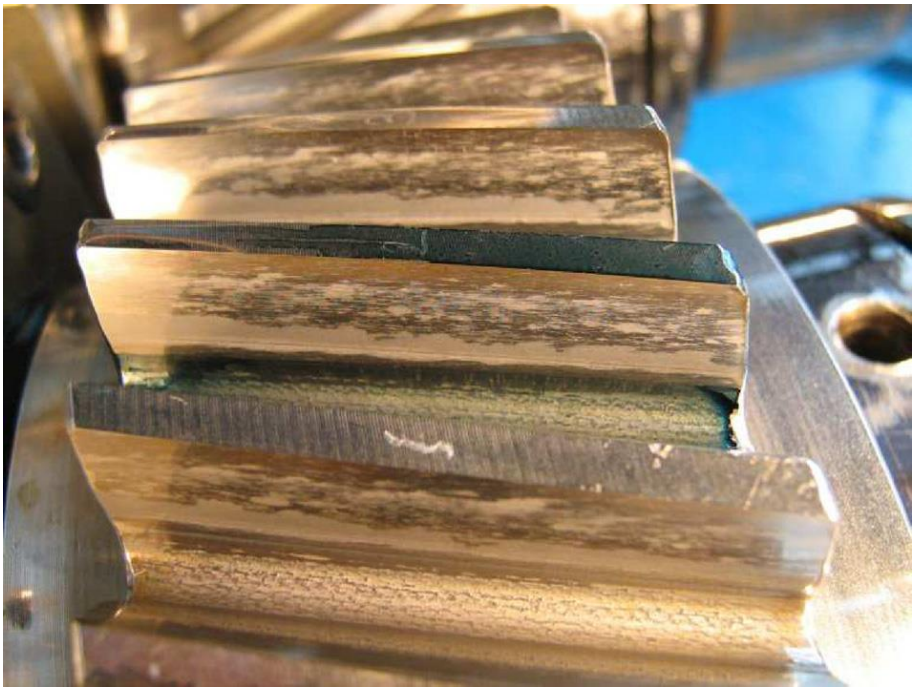

Figure 1-13 Photograph of helical gear with micropitting visible as matted region on dedendum of teeth (Evans et al., 2013)

Micropitting is now seen as a greater problem for gear designers than regular pitting failure as more advanced steel manufacturing methods produce cleaner materials with fewer inclusions making macro-pitting a less likely occurrence. As a result, micropitting is now widely considered to be the main life-limiting factor for case-hardened gears operating under moderate conditions .

Results from both experimentation and simulation have strongly associated micropitting failure with the surface topography (Evans et al., 2013) and it is believed, based on results from simulations, that failure could be related to the stress cycling experienced by individual asperity features in mixed lubrication as they pass through the contact zone and interact with features on the counterface (Sharif et al., 2012). In recent years, it has been found that additives used in more advanced lubricant formulations to reduce the likelihood of scuffing failure can sometimes accelerate the onset of micropitting fatigue (Winter, 1990, O'Connor, 2005).

As discussed in the previous section, many advances have been made in the area of simulating rough surfaces in mixed EHL contact. For a smooth surface contact, the peak subsurface shear stress is approximately one third of the maximum Hertzian pressure. This occurs at a depth which is a similar order of magnitude to the contact dimension (0.7*a* for a line contact, 0.5*a* for a circular point contact). However, the rough surface problem sees pressure spikes well in excess of the maximum Hertzian pressure. Figure 1-14 shows results obtained by Tao et al. (2003) and demonstrates the large pressure spikes obtained in rough surface EHL simulations generate subsurface stresses aligned with asperity features occurring in close proximity to the surface.

When applied cyclically, these high subsurface stresses can result in localised damage at prominent asperity features. The predicted locations of damage seen in fatigue simulations agree with experimental observations (Sharif et al., 2012). Further results in this work also confirm the asperities as being the regions of a surface most susceptible to damage. In addition to this, finite element analyses have also demonstrated the effect of the plastic deformation experienced during the initial running-in period to introduce residual tensile stresses close to the surface (Bryant et al., 2012).

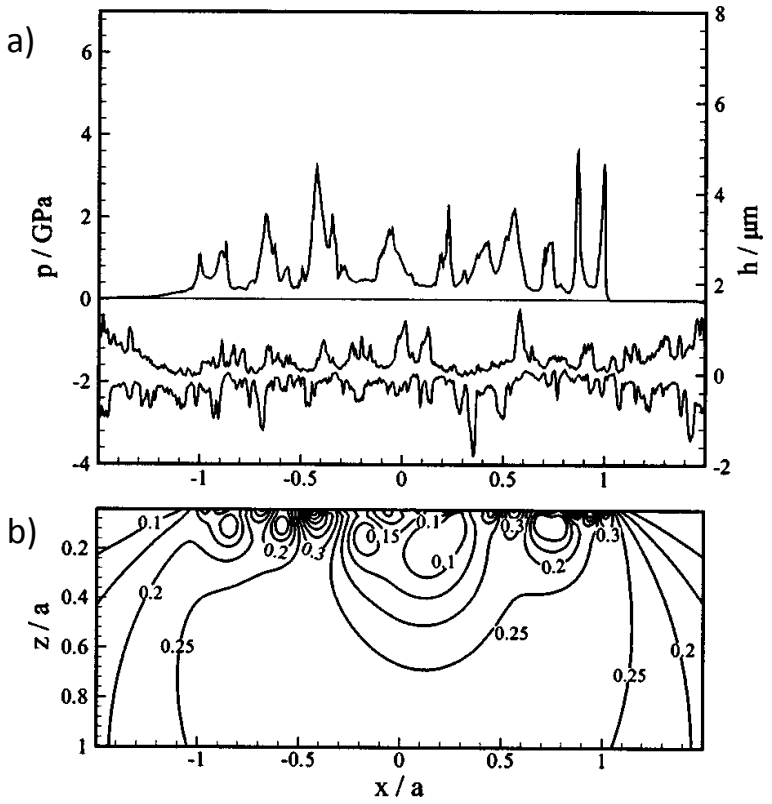

Figure 1-14 (a) Results from EHL analysis with pressure distribution as top curve and deflected surfaces as lower curves (b) corresponding subsurface shear stress distribution for lower surface in GPa (Tao et al., 2003)

Alongside the advances in simulations, experimental work into micropitting has also been conducted. Results from experimental work have shown micropitting failure to be heavily dependent on surface roughness which is considered to be the driving force behind the mechanism (Ahlroos et al., 2009). Another highly significant factor in determining micropitting performance is the level of sliding experienced at the contact, a higher level of sliding has been associated with poorer micropitting performance where the reason for this could be due to a higher rate of pressure cycling as asperities pass one another and also the shear-thinning behaviour of the lubricant (Li and Kahraman, 2013a). Examples of this can be seen in micropitted gears where fatigue has a tendency to occur towards the root of the dedendum or the tip of the addendum, where sliding is the greatest (Bull et al., 1999).

Roughness orientation has also been demonstrated to be an important factor influencing micropitting, where a transverse finish, used most frequently in ground gears, has been shown

to exhibit greater vulnerability to fatigue in comparison to surfaces where the lay of the surfaces is aligned with the sliding direction (Lainé et al., 2008).

In agreement with the hypothesis that roughness drives the failure mode, experiments conducted on polished surfaces have not shown the same propensity to fatigue failure (Ahlroos et al., 2009). The use of antiwear additives in oil has also been shown to accelerate the onset of micropitting failure which is thought to be due to the persistence of roughness features that would otherwise accommodate to one another following initial wear. Investigations into the micropitting performance of different additives have shown oils containing phosphorus or nitrogen to perform poorly in tests (Webster and Cardis, 1999).

In addition to the high subsurface stresses introduced by the roughness, it is also known that crack initiation and propagation are linked to microstructural changes occurring in regions close to the material surface (Oila and Bull, 2005). Through the use of the nanoindentation technique, experiments have identified distinct phase boundaries related to the decay of martensite along which cracks have been shown to have a tendency to propagate (Oila et al., 2005). Microstructural changes have long been associated with fatigue occurring in rolling element bearings (Voskamp, 1985), but only in more recent years have been shown to be associated with micropitting failure occurring in gears.

Following experiments conducted by Oila and Bull (2005) assessing the influence of different factors on micropitting, Oila et al. (2005) concluded that an appropriate choice of steel was the most significant factor in reducing martensite decay.. The influence of temperature was also found to be important. It was also suggested that the heat generated by plastically deforming asperities could play a role in promoting martensite decay in isolated regions. Contact pressure was also found to be influential in the initiation of micropitting, whereas sliding speed was found to be most significant in micropitting propagation (Oila and Bull, 2005).

Surface treatments have been found to influence micropitting lifespan. Experiments conducted on test disks showed that test surfaces with diamond-like carbon (DLC) coatings exhibited improved micropitting resistance compared to untreated test disks (Ahlroos et al., 2009). Carbo-nitrided components have also proved to have superior micropitting performance than case-carburised surfaces – where the inclusion of nitrogen in the alloying process is known to postpone phase transformations through enhanced tempering resistance (Ahlroos et al., 2009).

1.6 Electric Contacts

Researchers studying the state of lubrication between bearing surfaces have long been aware of the promise of electrical contact resistance methods in investigating the level of metallic contact. There is record of research being carried out in the first half of the 20th century (Bowden and Tabor, 1939, Courtney-Pratt and Tudor, 1946, Tudor, 1948). The use of electrical methods to study tribological contacts has an advantage in that it can be easily implemented and can be used to study realistic engineering components. Following the famous paper by Hertz into elastic deformation of solid bodies, many experimental investigations were carried out by researchers attempting to measure the real area of contact between loaded surfaces. Based upon the work of Hertz, it was considered that the electrical resistance between two bodies should be load dependent, due to the dependency of the real area of contact on applied load.

Shortly following the work of Hertz (1882), Bidwell (1883) carried out experiments investigating the effect of load on conductance between crossed cylinders and later Meyer (1898) performed measurements of electrical conductance between contacting steel spheres. It was later found by Binder (1912) that resistance in experiments between polished plates was greater than it would be were the observed area of the plates to be in full contact – from which he postulated that the surface only made contact over a small proportion of the observed area. Binder's theory of contact was later supported by the work of Holm (1967) who

published a series of papers stating that the resistance measured between two clean bodies in contact was in part due to a 'spreading resistance' created by current constrictions through micro-contacts between asperities.

Bowden and Tabor (1939) published their substantial work investigating the area of contact occurring between stationary and moving surfaces. The paper investigated the impact of load and sliding on electrical conductance. It was found that the real area of contact between surfaces was far less than the apparent area – conductance was found to vary positively with load, suggesting that surface asperities would deform under the application of load and the increased cross sectional area of the deformed asperities would increase the conductance, together with more asperities coming into contact. In addition to this, their work investigating conductance between sliding surfaces showed that resistance levels would fluctuate rapidly, even when apparently separated by a lubricant film, it was discovered that resistance levels were found to drop instantaneously to levels observed with unlubricated bodies.

The observations of Bowden and Tabor were further extended by Courtney-Pratt and Tudor (1946), for more practical purposes, where the state of lubrication and wear existing between the piston rings and cylinder wall of a running engine were investigated. Results demonstrated similar resistance fluctuations to those reported by Bowden and Tabor and were found to occur at locations where abrasive wear was most prevalent. The density of fluctuations recorded also showed dependency on oil viscosity and speed of surfaces, where conditions more favourable to good lubrication resulted in higher mean resistance traces. The effect of increasing speed on their measurements can be seen on oscilloscope readings shown in Figure 1-15. The figure shows four images, C1, C2, C3 and C4 taken from a cathode ray oscilloscope. Image C1 shows the scale of the contact resistance in images C2 to C4, and indicates the levels of 0Ω, 10Ω, 20Ω, 50Ω and infinite resistance. Images C2, C3 and C4 show traces taken at the indicated speeds. The figure demonstrates the effect of increased oil entrainment, where

more oil passing through the contact further separates the bodies reducing instances of metallic contact, and a low oscilloscope resistance signal is interpreted as indicative of metallic contact. The reading on the far left in Figure 1-15 demonstrates regions of both metallic contact and separation where the signal is seen to oscillate from high levels of resistance to very low values. These instances of low resistance are seen to decrease with increasing speed as the oil further separates the surfaces.

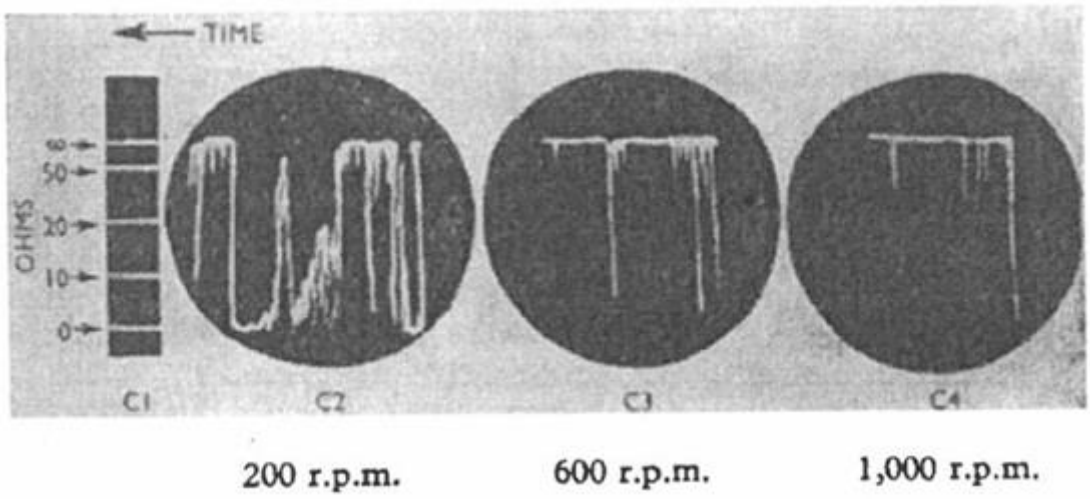

Figure 1-15 Oscilloscope traces demonstrating increasing contact resistance with speed (Courtney-Pratt and Tudor, 1946)

Tudor (1948) then went on to apply this method of investigation to the lubrication of journal bearings. Results showed that the running-in process that had previously been observed was found to also be accompanied by an overall increase in contact resistance. Over a period of running, the measured contact resistance was found to vary from predominantly zero throughout an entire revolution, indicating metallic contact, to a very high resistance after a sustained period of operation as running-in took place and the surfaces were insulated from each other by the lubricant film. It was also observed that any disturbance producing misalignment between the experimental surfaces resulted in the immediate deterioration of the lubrication (reduced contact resistance) and the surfaces would need to be further run-in. Tudor also witnessed repeatability in results which are displayed in Figure 1-16. It was found that between consecutive revolutions resistance traces were almost identical. This was

attributed to the same regions of the surface coming into contact through the high resistance lubricant film.

Tudor's results in Figure 1-16 show three resistance traces taken from a journal bearing in operation. For three consecutive revolutions. Again the scale of resistance is shown on the left as in Figure 1-15 and each frame shows a time of 0.34 seconds. It can be seen that each trace shows regions of low resistance which are considered to be due to metallic contact. Areas of high resistance are also seen where, over a portion of the trace, no contact is considered to have occurred between the surfaces. The traces appear to be fluctuating rapidly between very high and low values, indicating intermittent contact which is now known to occur in mixed lubrication. It can also be seen that the resistance traces demonstrate a very similar form. This is associated with the metallic contact occurring between the same pairs of interacting asperities over consecutive revolutions.

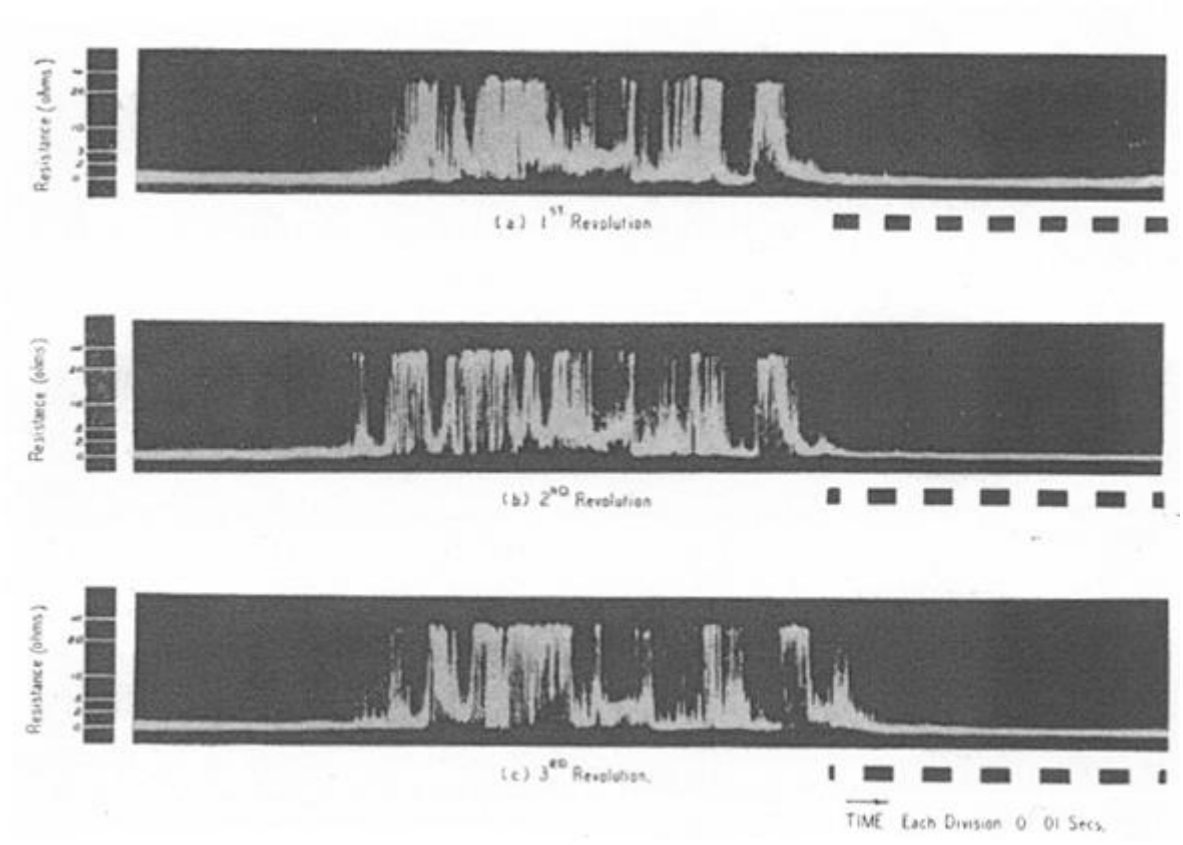

Figure 1-16 Oscilloscope traces showing repeatable contact resistance signals for consecutive revolutions (Tudor, 1948)

Further work employing the electrical resistance technique was performed by Lane and Hughes (1952) where an investigation into the various parameters affecting the state of the oil film between meshing gear teeth was conducted. It was found that resistance measurements were at their highest in the region of the pitch point and lowest in regions where high levels of sliding occurred.

Later, the work of Crook (1957)on high speed disks involved measuring the capacitance of the separating oil film and this was used as a means to obtain an approximate value for the film thickness. Crook's substantial work provided experimental results on the effects of a range of different parameters on the oil film thickness and measured friction.

An alternative approach was adopted by Cameron (1954) who used the discharge voltage to approximate the oil film thickness occurring between rotating disks. He then went on to apply this method with MacConochie to measure the range of oil film thicknesses experienced by gear teeth throughout the meshing cycle and found that the thickness at tip and root were heavily dependent on tip relief (MacConochie and Cameron, 1960). This dependence of oil film thickness on the tip relief profile has been explored recently in full transient EHL analyses of Helical gear contacts where the sensitivity of the film thickness to the form of the tip relief is clearly demonstrated (Jamali et al., 2014).

Following the early work of Cameron (1950), where experiments had been carried out using electrical resistance to interpret film thickness, El-Sisi and Shawki (1960) used additives to greatly increase the conductivity of a lubricating oil and make film thickness estimates. This work was later applied to gear teeth and found agreement with previous work judging the oil film to be at its thickest at the pitch point with tip relief greatly affecting root and tip measurements of film thickness. It was also noted that in comparisons between gear and disk experiments that the naturally relieved contact provided by a twin disk rig did not model the harsh conditions encountered in gear experiments. The additive used also provided the oil

with more predictable electrical characteristics as it has been shown that the dielectric constant of oil is dependent on both pressure and temperature (Clark, 1935).

Furey (1969) measured the instantaneous resistance between a fixed ball and rotating cylinder and, as noted by previous researchers, he found that the resistance levels occurring within a lubricated contact fluctuated between extremely high values and zero. A time average of this signal was considered to provide a fractional representation of the extent to which metallic contact was occurring. Furey went on to conclude that metallic contact was much more frequent than otherwise considered. As with earlier authors, Furey argued that the applied voltage must be kept low in order to avoid observing spurious instances of contact due to discharge across the oil film. He demonstrated that below a certain threshold voltage, the observed metallic contact remained constant. In agreement with earlier work by Tudor, he noted that increasing speed would reduce instances of contact and used a time average to measure the transition from boundary to full hydrodynamic lubrication.

In an extension of the use of fluctuating contact voltage levels, Tallian et al. (1964) considered that if interruptions in the EHL film were in fact due to asperity interactions then an approximation of film thickness could be derived using information regarding the surface microgeometry in conjunction with data obtained for frequency and duration of observed 'interactions' through the lubricant film. Based on the technique, it was found that estimates of film thickness agreed with those predicted by EHL theory. It was also found that during experiments in which there was significant interruption of the lubricant film, greater wear was found to have occurred. Tallian (1972) then extended his work to include the effect of contact pressure on surface topography.

Palacios (1983) took Tallian's work and applied it to a four ball tester where information regarding contact voltage and surface micro-geometry was used to make predictions of the

surface film thickness. Good agreement was found with theoretical values and the use of rough surfaces was produced thinner films than smooth surfaces.

More recently, Guangteng et al. (1999) employed the use the spacer layer imaging method to investigate the relationship between the real film thickness and the electrical contact resistance. Initial investigations into the electrical contact resistance using the ball on disk configuration found that increasing the rolling speed decreased instances of low resistance. It was also found that experimenting with the roughness level of the ball affected the level of contact occurring between the surfaces, where a rough ball would yield lower overall resistance levels than a ball with a smoother surface. In a similar manner to Tallian et al. (1964), Guangteng used a discriminator level to interpret contact from intermediate values of resistance. Contact interpreted from measured electrical resistance levels was shown in results to decrease upon increased rolling speed and to increase when using specimens of greater surface roughness.

Film thickness maps were obtained directly from the same system and it could be seen that increasing entrainment speed resulted in higher levels of mean film thickness. Comparisons between interpreted levels of contact and film thickness were made across a range of rolling speeds for balls of different roughnesses. Attempts to correlate levels of contact with the measured film thickness appeared largely unsuccessful and it was necessary to introduce the lambda ratio as a parameter when considering contact levels between rough surfaces.

More recently Lord and Larsson (2008) utilised a ball and disk set up, monitoring both the contact resistance and contact capacitance under conditions of running-in and subsequently lift off to give a qualitative measure of metallic contact levels and an approximation of film thickness levels. Experiments were performed on a variety of different surface finishes. Their research demonstrated that as surfaces experienced running-in, fewer contact instances were

detected and mean contact resistance levels were higher as running-in progressed, owing to the improved hydrodynamic properties of the surfaces.

1.7 Further Literature

Furustig et al. (2015) investigated the wear of a hydrualic motor, they considered the wear occurring on two scales, a global component level scale and a surface topography level scale. An isothermal mixed EHL model was used to simulate contact pressures occurring on the measured surface topography of a hydraulic motor. Results for contact pressures were then employed in simulating wear using an Archard type wear model. Results wear were compared to results from experiments running parallel. Good agreement was found between results for simulation and those obtained experimentally.

Li (2015) focussed a computational study on the effect of the directionality of surface roughness lay on micropitting severity. The study used the same technique proposed earlier to predict micropitting of a 3D surface by Li and Kahraman (2013b). The study employed a mixed lubrication model simulating a ball on plane, each with sinusoidal roughness profiles, to calculate the surface tractions generated across the contact. The calculated tractions were then employed to find the surface stress concentrations. The crack formation was then assessed using a fatigue criterion. Simulations were conducted at a range of different surface roughness orientations and found that the most favourable condition for the surface orientation in terms of micropitting severity was that where both surfaces were positioned with the roughness lay out-of-phase and parallel to the direction of rolling. In contrast to this, the configuration that was found to be most severe was that where the roughness on the ball was parallel to the rolling direction and the other was positioned normal to the rolling direction.

Zhu et al. (2015), using solutions obtained from the unified deterministic mixed lubrication model (Hu and Zhu, 1999), plotted the stribeck curves for different 3D topographies on the

point contact for a wide range of speeds. The non-Newtonian Bair and Winer model was used to calculate the friction of the lubricant film, the flash temperature was also considered in calculation of the friction. Results showed that in contrast to conformal contacts, for all surface roughness orientations considered, friction continuted to fall until very high surface speeds were attained. It was considered that this was due to the significantly higher pressures and shear strain rates experienced by the lubricant in the point contact, causing the non-Newtonian and thermal effects to become more pronounced. In addition to this, it was found that the ellipticity ratio as well as the surface roughness orientation had little effect on the observed friction. There was however some limited influence whilst the contact was operating within the mixed lubrication regime, due to the impact of surface roughness orientation on overall film thickness.

Burghardt et al. (2015) investigated the effect of running-in on the progression of wear in rolling bearings using two additive free oils. It was found that without an initial run-in procedure, the surfaces experienced severe wear. It was found that wear occurred most rapidly in the boundary lubrication regime, at lambda ratios below 0.1. In contrast to this, experiments conducted within the mixed lubrication regime demonstrated little wear occurring and the build-up of an oxide-based tribo-layer which was was the result of a run-in. After an initial run-in had allowed a tribo-layer to accumulate on the surface, it was found that wear was greatly reduced in terms of mass lost. Tribo-layers which had accumulated on the surface were identified through the implementation of nano-indentation and TEM techniques. In addition to this, it was found that the “running-in process” could be replicated (with regard to the formation of tribo-layers) through the thermal treatment of the surface, which would result in the build-up of the oxide-based tribo-layer.

Vladescu et al. (2015) conducted an experimental study into the effects of surface texture in reciprocating contacts. Their apparatus simulated the essential components of a piston ring

and liner contact employed the use of a patterned plane silca pad against a convex steel pad. Different surface textures were tested at a number of loads and sliding speeds in order to cover a range of different lambda ratios. It was found that when operating in the boundary and mixed lubrication regimes, surface textures were effective in reducing friction occurring at the contact. It was believed that this could be related to the pockets in the textures aiding the generation of an oil film. Of the surface textures investigated, it was found that grooves normal to the direction of sliding were most effective in reducing friction in the boudary and mixed lubrication regimes. However under full hydrodynamic conditions, surface textures were found to be detrimental, resulting in increased friction.

1.8 Conclusions

Researchers throughout the 20th century and in more recent years have found that when rough surfaces come into contact under load during their early period of operation they undergo a process of accommodation where high pressures generated in the region of micro-contacts cause the asperities to plastically deform. This plastic deformation has appeared in research to occur more rapidly than wear processes. Surfaces subjected to plastic deformation have been found to reach a stable condition relatively rapidly where load can be distributed over the new micro-contacts.

The reduction in roughness amplitude experienced by surfaces has been found to be beneficial in terms of reducing instances of metallic contact, which may in turn reduce levels of fatigue experienced by bearing surfaces. However, the running-in process has also been associated with introducing localised subsurface residual tensile stresses and microstructural changes which are considered to be factors aggravating the failure mechanism of micropitting.

Experiments conducted by numerous researchers investigating the electrical contact resistance between bearing surfaces have shown the existence of mixed lubrication where asperity contact takes place intermittently through a highly insulating lubricant film. Due to the

ability of electrical contact resistance to be applied effectively between realistic engineering components it will be used in this work and future works where the association between metallic contact levels, friction and surface fatigue initiation will continue to be investigated.

2 Theory and Governing Equations of Elastohydrodynamic Lubrication

This chapter introduces some of the main equations that govern the isothermal elastohydrodynamic (EHL) point contact problem. Numerical implementation of this theory is discussed in Chapter 6 where the modifications made by the author to the EHL point solver, originally developed by Holmes (2002) are presented in detail. The equations describing the area of elastic contact produced by two loaded bodies are first introduced as reference throughout experimental work in this thesis has been made to contact dimensions. The concept of elastic deformation is also vital to the EHL mechanism.

The main governing equations of elastohydrodynamic lubrication are:

- Elastic film thickness equation
- Reynolds hydrodynamic equation

The elastic equation is introduced generally with the focus on the deformation produced by the pressurised lubricant on the contacting bodies. The Reynolds hydrodynamic equation has been derived using the fluid element approach where the surface forces acting on a volume of fluid are first considered and the continuity of flow principle is applied.

2.1 Elastic bodies in Loaded Contact

When two bodies are loaded together they experience a degree of elastic deformation. The area of contact produced by the elastic deflection of the bodies is dependent on the load, contact geometry and material properties.

Elliptical contacts occur frequently between surfaces within engineering. Surfaces on components such as gears and bearings rely on elliptical contacts to transmit and distribute load.

Thus the general case for an elliptical contact, shown in Figure 2-1, has been described as it is the subject for experimental and computational work in this thesis. The approach presented here is strictly applicable to dry contact, but remains a reasonable approximation for a lubricated contact.

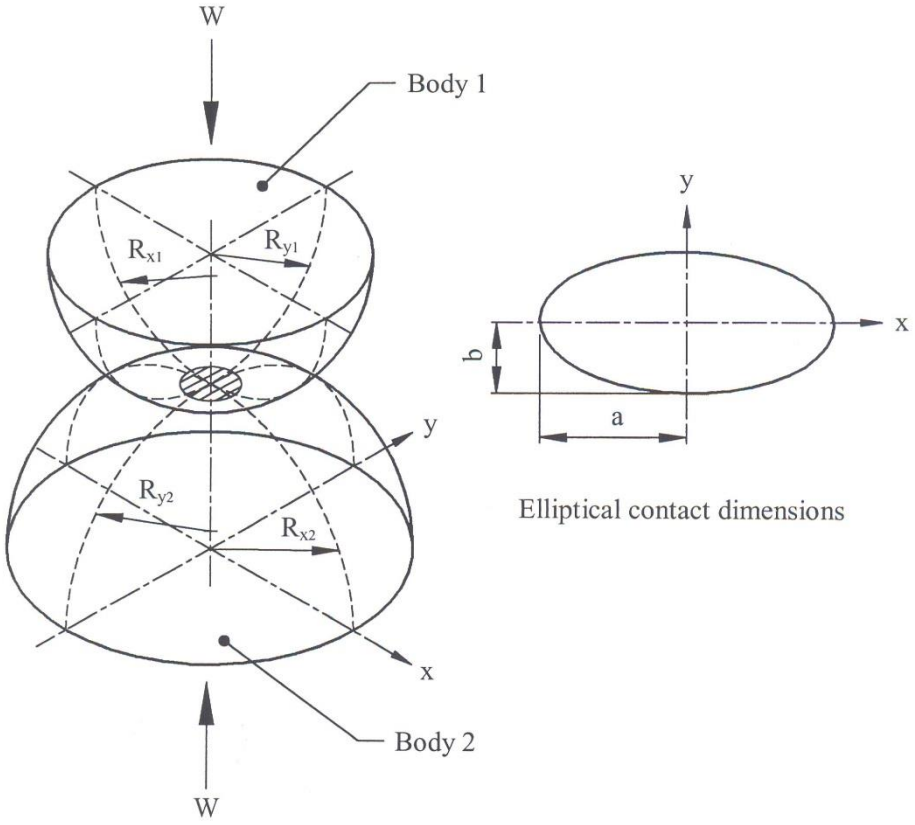

Figure 2-1 Two curved surfaces under loaded contact with contact area shown (Holmes, 2002)

A full treatment of the derivation of the contact dimensions *a* and *b* and the maximum contact pressure p_0 can be seen in Timoshenko and Goodier (1951). The equations stated below use a different notation and provide the equivalent of Timoshenko and Goodier's tabulated parameters *m* and *n* graphically in the form of parameters *k* and *F* that are functions of the ratio of the principle radii of relative curvature, as shown in Figure 2-2.

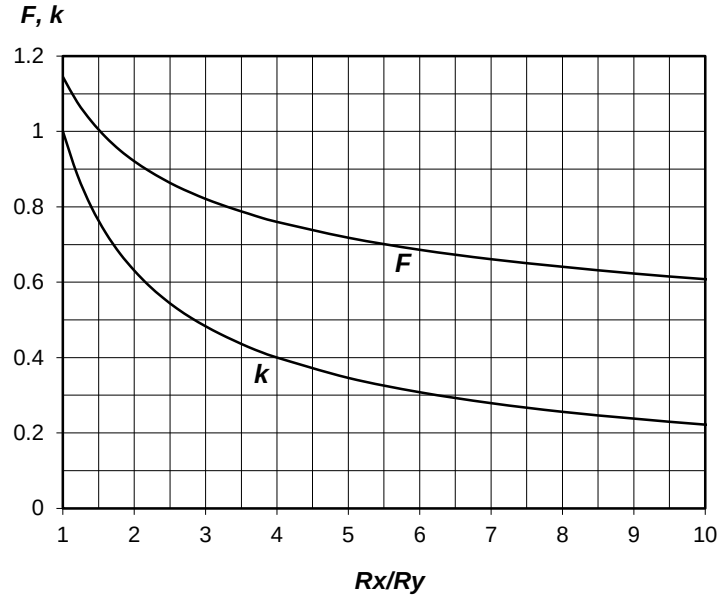

Figure 2-2 Variation of non-dimensional parameters, k and Fused in equations (2.4) and (2.5) with ratio of Rx and Ry

In order to calculate the contact dimensions, the contact geometry of both bodies are reduced to represent the contact of an ellipsoid against a plane. This is done by considering the relative radii of curvature of the two bodies; using the notation shown in Figure 2-1.

$$\frac{1}{R_x} = \frac{1}{R_{x1}} + \frac{1}{R_{x2}}$$
$$\frac{1}{R_y} = \frac{1}{R_{y1}} + \frac{1}{R_{y2}} \qquad \textbf{(2.1)}$$

Where R_x and R_y are the reduced radius of curvature in the x and y directions respectively. Thus the overall reduced radius of contact, R, is given by:

$$\frac{2}{\bar{R}} = \frac{1}{R_x} + \frac{1}{R_y} \qquad \textbf{(2.2)}$$

The material parameters (Young's Modulus, *E*, and Poisson's Ratio, *v*) of both bodies are also reduced to a single parameter, the effective elastic modulus:

$$\frac{2}{E'} = \frac{(1-\nu_1^2)}{E_1} + \frac{(1-\nu_2^2)}{E_2} \quad \textbf{(2.3)}$$

With a known load, the contact semi-dimension in the y-direction can be calculated using:

$$b = F\left(\frac{\bar{R}W}{E'}\right)^{\frac{1}{3}} \quad \textbf{(2.4)}$$

Where the parameters *F* and *k* are both constants and are functions of the reduced radii of curvature, R_x/R_y as shown in Figure 2-2.

The contact dimension in the x direction is given relative to b by:

$$a = \frac{b}{k} \quad \textbf{(2.5)}$$

The maximum contact pressure is:

$$p_0 = \frac{3W}{2\pi ab} \quad \textbf{(2.6)}$$

The pressure distribution within the contact zone is:

$$p = p_{hz}\sqrt{\frac{x^2}{a^2} + \frac{y^2}{b^2}} \quad \textbf{(2.7)}$$

The area contact pressure is given by:

$$\bar{p} = \frac{w}{\pi ab} \quad \textbf{(2.8)}$$

2.2 The Film Thickness Equation

An illustration of the variation of film thickness along the centre-line (in the direction of entrainment) for a typical elliptical contact is shown in Figure 2-3. When fluid is drawn into the contact by the moving surfaces, pressures generated within the film are sufficient to separate the bodies. The high pressure in the lubricant is also sufficient to cause elastic deformation at the interfaces. The film thickness in determined in the inlet region. EHL contact are

characterised by a near-parallel film in the central region of the contact, and the characteristic exit constriction, all of which may be seen in Figure 2-3.

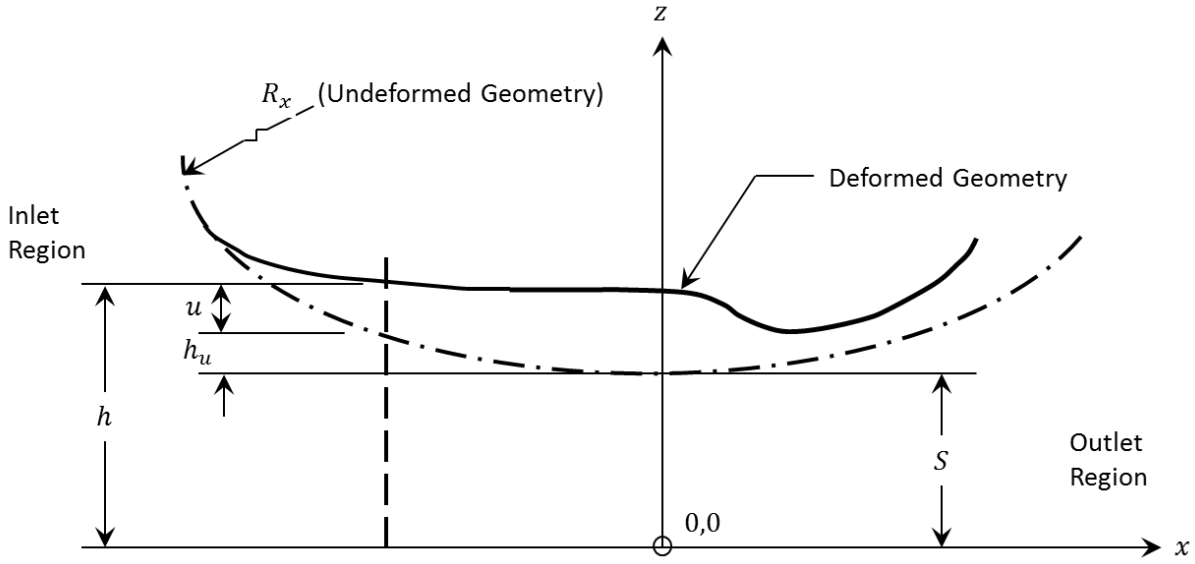

Figure 2-3 Cross section of an EHL contact at centreline

The film thickness h is thus a calculated by the sum:

$$h(x,y) = h_u(x,y) + u(x,y) + S \qquad \textbf{(2.9)}$$

The undeformed parabolic geometry, h_u, is calculated assuming the geometry is that of a paraboloid:

$$h_u = \frac{x^2}{2R_x} + \frac{y^2}{2R_y} \qquad \textbf{(2.10)}$$

The elastic deflection $u(x,y)$, due to the loading produced by the pressurised lubricant can then be calculated using the convolution integral of pressure with the appropriate weighting function given by Timoshenko and Goodier (1951). The total deformation of a node is calculated by considering the contribution to deformation of each subarea within the computing mesh, where s and t are arbitrary coordinates within the mesh. The bodies can be treated as semi-infinite, due to the relatively small size of the contact.

(2.11)

$$u(x,y) = \frac{2}{\pi E'} \iint_A \frac{p(s,t)}{\sqrt{(s-x)^2 + (t-y)^2}} dsdt$$

2.3 The Hydrodynamic Reynolds Equation

The Hydrodynamic Reynolds equation is a partial differential equation used for the calculation of pressure within thin viscous fluid films. The equation can be simplified from the more general Navier Stokes equation through the application of a number of important assumptions:

1. The fluid behaves in a Newtonian manner (although this assumption may be relaxed as discussed later)
2. The flow in the fluid is laminar
3. Inertial forces in the fluid are negligible in comparison to the viscous forces
4. No pressure gradient over the thickness of the film
5. No slip occurs at the fluid surface interface
6. Body forces on the fluid are negligible
7. Viscosity is constant through the thickness of the film

The Reynolds or hydrodynamic equation can be derived by first considering the surface forces, due to pressure and shear stress, acting on an element of fluid shown Figure 2-4. Only forces acting in the x-direction are shown for clarity.

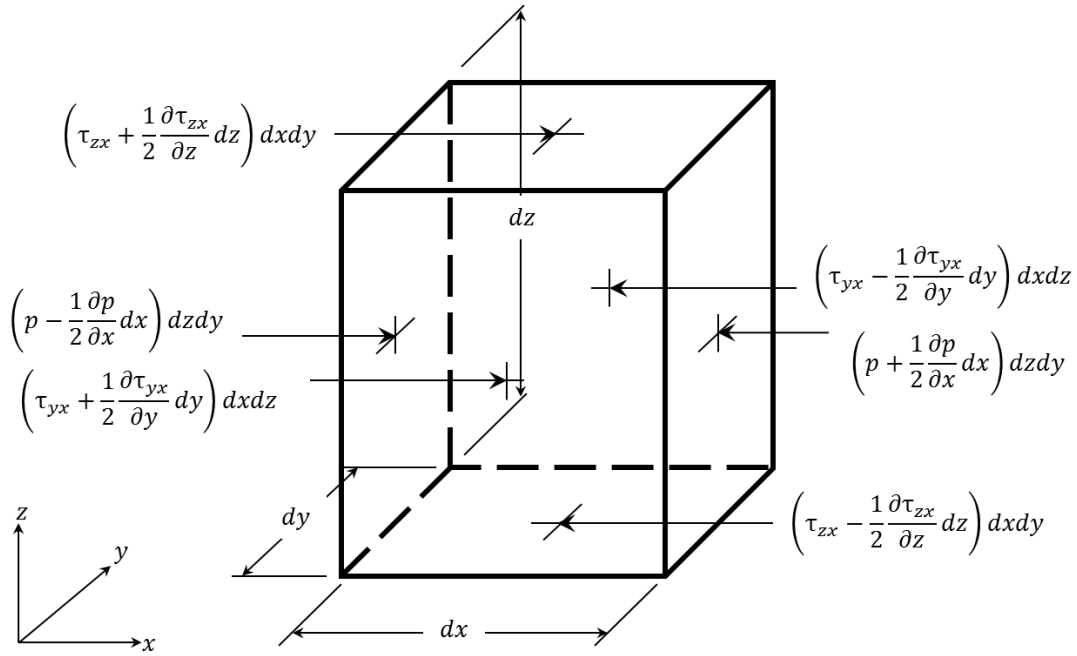

Figure 2-4 Element of fluid with surface forces acting in the x-direction shown

Summing the forces in the x-direction gives:

$$\left(p-\frac{1}{2}\frac{\partial p}{\partial x}dx\right)dydz-\left(p+\frac{1}{2}\frac{\partial p}{\partial x}dx\right)dydz-\left(\tau_{zx}-\frac{1}{2}\frac{\partial\tau_{zx}}{\partial z}dz\right)dxdy$$
$$+\left(\tau_{zx}+\frac{1}{2}\frac{\partial\tau_{zx}}{\partial z}dz\right)dxdy-\left(\tau_{yx}-\frac{1}{2}\frac{\partial\tau_{yx}}{\partial y}dy\right)dxdz$$
$$+\left(\tau_{yx}+\frac{1}{2}\frac{\partial\tau_{yx}}{\partial y}dy\right)dxdz=0$$

This simplifies to:

$$\frac{\partial\tau_{zx}}{\partial z}+\frac{\partial\tau_{yx}}{\partial y}=\frac{\partial p}{\partial x}$$

This can be further reduced as the first term on the left hand side is much larger than the second, hence:

$$\frac{\partial\tau_{zx}}{\partial z}=\frac{\partial p}{\partial x}$$

Similarly, consideration of forces in the y-direction leads to::

$$\frac{\partial\tau_{zy}}{\partial z}=\frac{\partial p}{\partial y}$$

Since the fluid is assumed to be Newtonian, the shear stresses can be considered to be proportional to the velocity gradients in the x and y direction, where *U* and *V* are component velocities, respectively:

$$\tau_{zx} = \eta \frac{\partial U}{\partial z}$$

$$\tau_{zy} = \eta \frac{\partial V}{\partial z}$$

Substituting in:

$$\frac{\partial}{\partial z}\left(\eta \frac{\partial U}{\partial z}\right) = \frac{\partial p}{\partial x}$$

$$\frac{\partial}{\partial z}\left(\eta \frac{\partial V}{\partial z}\right) = \frac{\partial p}{\partial y}$$

As it is assumed the pressure and therefore viscosity do not vary across the film thickness, integrating in the z-direction, with respect to z results in:

$$\eta U = \frac{\partial p}{\partial x}\frac{z^2}{2} + Az + B$$

$$\eta V = \frac{\partial p}{\partial y}\frac{z^2}{2} + Cz + D$$

Setting the boundary conditions in order to find constants:

$$z = h\,,\ \ U = U_1\ \ and\ \ V = V_1$$

$$z = 0\,,\ \ U = U_2\ \ and\ \ V = V_2$$

Resulting in:

$$A = \frac{\eta}{h}(U_1 - U_2) - \frac{\partial p}{\partial x}\frac{h}{2}, \qquad B = \eta U_2$$

$$C = \frac{\eta}{h}(V_1 - V_2) - \frac{\partial p}{\partial x}\frac{h}{2}, \qquad D = \eta V_2$$

The velocity profiles can then be given by:

$$\begin{aligned} U &= \frac{1}{2\eta}\frac{\partial p}{\partial x}(z^2 - zh) + \frac{z}{h}(U_1 - U_2) + U_2 \\ V &= \frac{1}{2\eta}\frac{\partial p}{\partial y}(z^2 - zh) + \frac{z}{h}(V_1 - V_2) + V_2 \end{aligned} \qquad \textbf{(2.12)}$$

A change in film thickness will yield a change in mass flow. The mass flow out of a fluid column length h between the surfaces

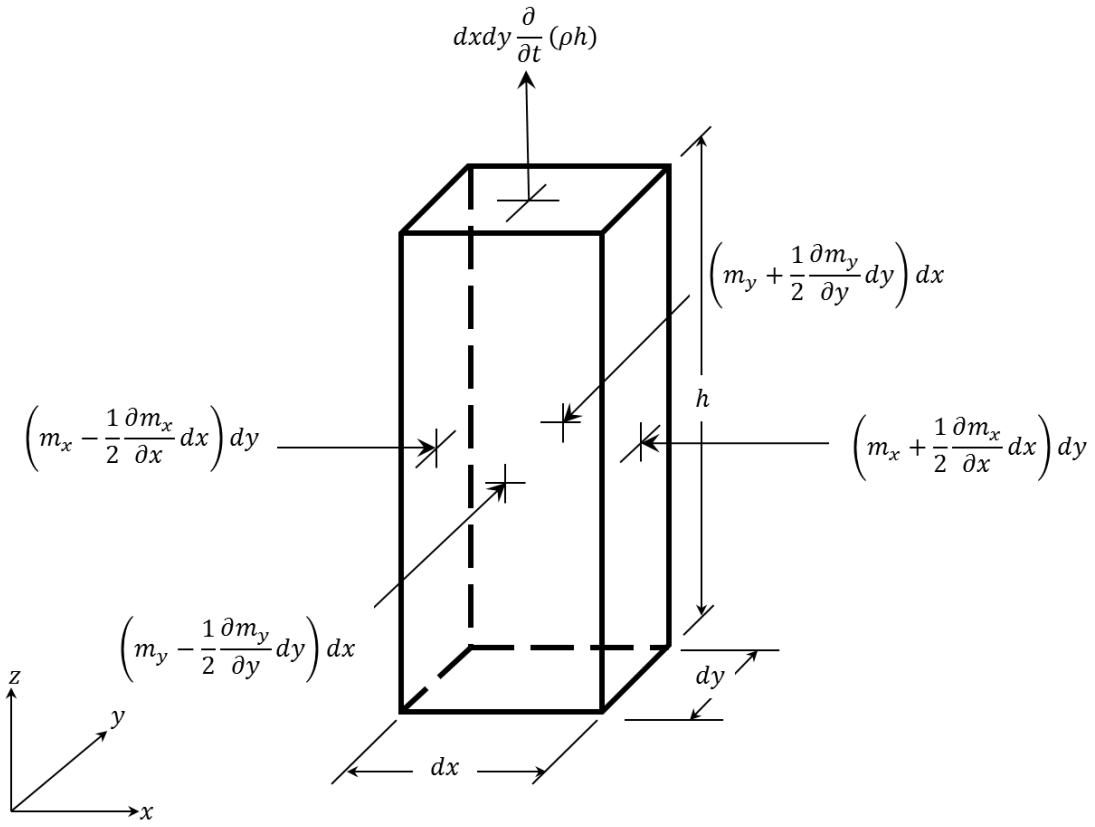

Figure 2-5 Mass flow into control volume of fluid

The mass flow in the x and y directions are therefore:

$$m_x = \rho \int_0^h U \, dz$$

$$m_y = \rho \int_0^h V \, dz \qquad \textbf{(2.13)}$$

The equation of continuity for the column of fluid is therefore:

$$\frac{\partial m_x}{\partial x} + \frac{\partial m_y}{\partial y} + \frac{\partial}{\partial t}(\rho h) = 0 \qquad \textbf{(2.14)}$$

Substituting the velocity profiles from equation (2.12) into equation (2.13) gives:

$$m_x = \rho \int_0^h \left[\frac{1}{2\eta}\frac{\partial p}{\partial x}(z^2 - zh) + \frac{z}{h}(U_1 - U_2) + U_2\right] dz$$

$$m_y = \rho \int_0^h \left[\frac{1}{2\eta}\frac{\partial p}{\partial y}(z^2 - zh) + \frac{z}{h}(V_1 - V_2) + V_2\right] dz$$

Integrating gives:

$$m_x = \frac{\rho h^3}{12\eta}\frac{\partial p}{\partial x} + \frac{\rho h}{2}(U_1 + U_2)$$

$$m_y = \frac{\rho h^3}{12\eta}\frac{\partial p}{\partial y} + \frac{\rho h}{2}(V_1 + V_2) \qquad \textbf{(2.15)}$$

Substituting equation (2.15) into equation (2.14):

$$\frac{\partial}{\partial x}\left(\frac{\rho h^3}{12\eta}\frac{\partial p}{\partial x} - (U_1 + U_2)\frac{\rho h}{2}\right) + \frac{\partial}{\partial y}\left(\frac{\rho h^3}{12\eta}\frac{\partial p}{\partial y} - (V_1 + V_2)\frac{\rho h}{2}\right) - \frac{\partial}{\partial t}(\rho h) = 0$$

Letting $\bar{U} = \frac{U_1 + U_2}{2}$ and $\bar{V} = \frac{V_1 + V_2}{2}$ and separating the pressure and the velocity term, the Reynolds equation becomes:

$$\frac{\partial}{\partial x}\left(\frac{\rho h^3}{12\eta}\frac{\partial p}{\partial x}\right) + \frac{\partial}{\partial y}\left(\frac{\rho h^3}{12\eta}\frac{\partial p}{\partial y}\right) - \frac{\partial}{\partial x}(\rho \bar{U} h) - \frac{\partial}{\partial y}(\rho \bar{V} h) - \frac{\partial}{\partial t}(\rho h) = 0$$

For convenience the flow factors are expressed as $\sigma_x = \sigma_y = \frac{\rho h^3}{12\eta}$ to generalise the Reynolds equation. The flow factors can be calculated to take account of Non-Newtonian oil behaviour and the equation becomes:

$$\frac{\partial}{\partial x}\left(\sigma_x \frac{\partial p}{\partial x}\right) + \frac{\partial}{\partial y}\left(\sigma_y \frac{\partial p}{\partial y}\right) - \frac{\partial}{\partial x}(\rho \bar{U} h) - \frac{\partial}{\partial y}(\rho \bar{V} h) - \frac{\partial}{\partial t}(\rho h) = 0 \qquad \textbf{(2.16)}$$

2.4 Viscosity

The viscosity of a lubricant is its most important property. A more viscous lubricant will separate surfaces more readily, but will generate more losses due to viscous friction. In contrast to this, a lubricant that is too thin will result in less separation which can potentially result in accelerated wear and other failure mechanisms.

It is therefore important for engineers to choose a lubricant that performs well over the range of operating conditions imposed upon the interface.

2.4.1 Pressure Dependency

The viscosity of most oils is highly pressure dependent – without this characteristic EHL could not be possible and many engineering systems would fail.

To model the pressure dependency of oil, a range of viscosity-pressure relations have been proposed in the literature such as the Roelands (1966) empirical formula which has been used in this work and is shown in Equation (2.17) where η_0 is the viscosity under ambient pressure conditions and α is the pressure coefficient of viscosity.

$$\eta = \eta(p) = \eta_0 \exp\{(\log \eta_0 + 9.67)((1 + 5.1 \times 10^{-9} p)^z - 1) \qquad \textbf{(2.17)}$$

Where:

$$Z = \frac{\alpha}{5.1 \times 10^{-9}(\log \eta_0 + 9.67)}$$

2.4.2 Non-Newtonian Behaviour

Under EHL conditions, engineering lubricants rarely behave in a Newtonian manner, where the shear stress and shear-strain rate are linear. This non-linearity is due to the complex molecular structure of many oils and greases. Shown in Figure 2-6 is a comparison of the shear response of a Newtonian and shear-thinning Non-Newtonian fluid.

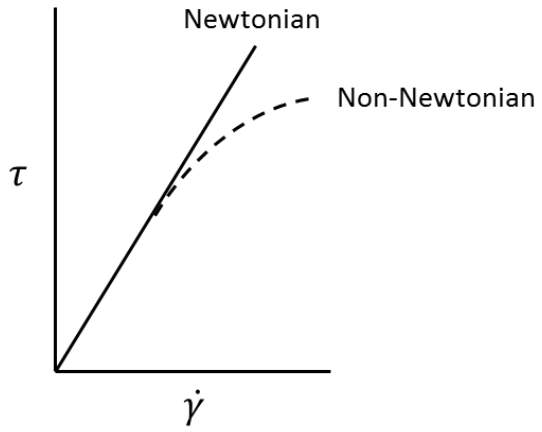

Figure 2-6 Shear-strain-rate relationship for Newtonian and Non-Newtonian fluid

In power transmission systems such as gears, lubricants tend to exhibit shear thinning behaviour. Many formulae have been proposed to simulate this. The model adopted for use in this work is the formula used by Johnson and Teevwerk (1977). Where τ_0 is adjusted to match measured traction forces.

$$F(\tau) = \frac{\tau_0}{\eta} \sinh\left(\frac{\tau}{\tau_0}\right) \qquad \textbf{(2.18)}$$

The implementation of this method has been previously discussed in detail by Sharif et al. (2001) and will not be included here.

2.5 Conclusions

The governing equations of elastohydrodynamic lubrication have been presented in this chapter. The numerical implementation of these are discussed in Chapter 6 where results for the modifications to the EHL point solver are presented and can also be found in greater detail in the thesis of Holmes (2002).

3 Development of Disk Rig for Mixed Lubrication Studies

3.1 Introduction

Disk rigs are well established in the field of experimental tribology for their ability to provide researchers investigating elastohydrodynamic lubrication with a steady state problem in terms of load and kinematics compared to gear tooth surfaces. Test specimens are relatively inexpensive and the fundamental EHL problem can be focussed upon without confounding the issue with transient kinematics for specific engineering components. The two disk rig described in this chapter was designed by Alanou (2006) based upon principles outlined by Merritt (1935) to investigate micropitting through extended running, periodical observation and measurement of the surfaces used, which were representative of aerospace gearing practice.

This chapter describes the test rig and author's role in the further development and validation of the rig for studying mixed lubrication conditions including the use of electrical contact resistance measurements. The running-in process involved in producing stable surfaces which were used to conduct the experiments was also carefully observed and documented in Chapter 4. For this work, it was necessary to record various data occurring at the contact. Data in the form of bulk disk temperatures, friction, applied load, shaft speed and contact voltage were recorded. Experiments could be controlled by changing applied load and speed (initially through controls on the inverter and subsequently remotely through computer control), and the settings on the thermostatic bath allowed the user to alter the oil feed temperature. The rig was modified by fitting a shaft encoder in order to trigger measurements starting at the same point on each surface with a high degree of accuracy. This, in combination with high-speed contact voltage sampling, provided an insight into the frequency and severity of real metallic or pseudo-metallic contact for comparison with numerical models simulating mixed lubrication. The most pertinent features of the test head are shown in Figure 3-1.

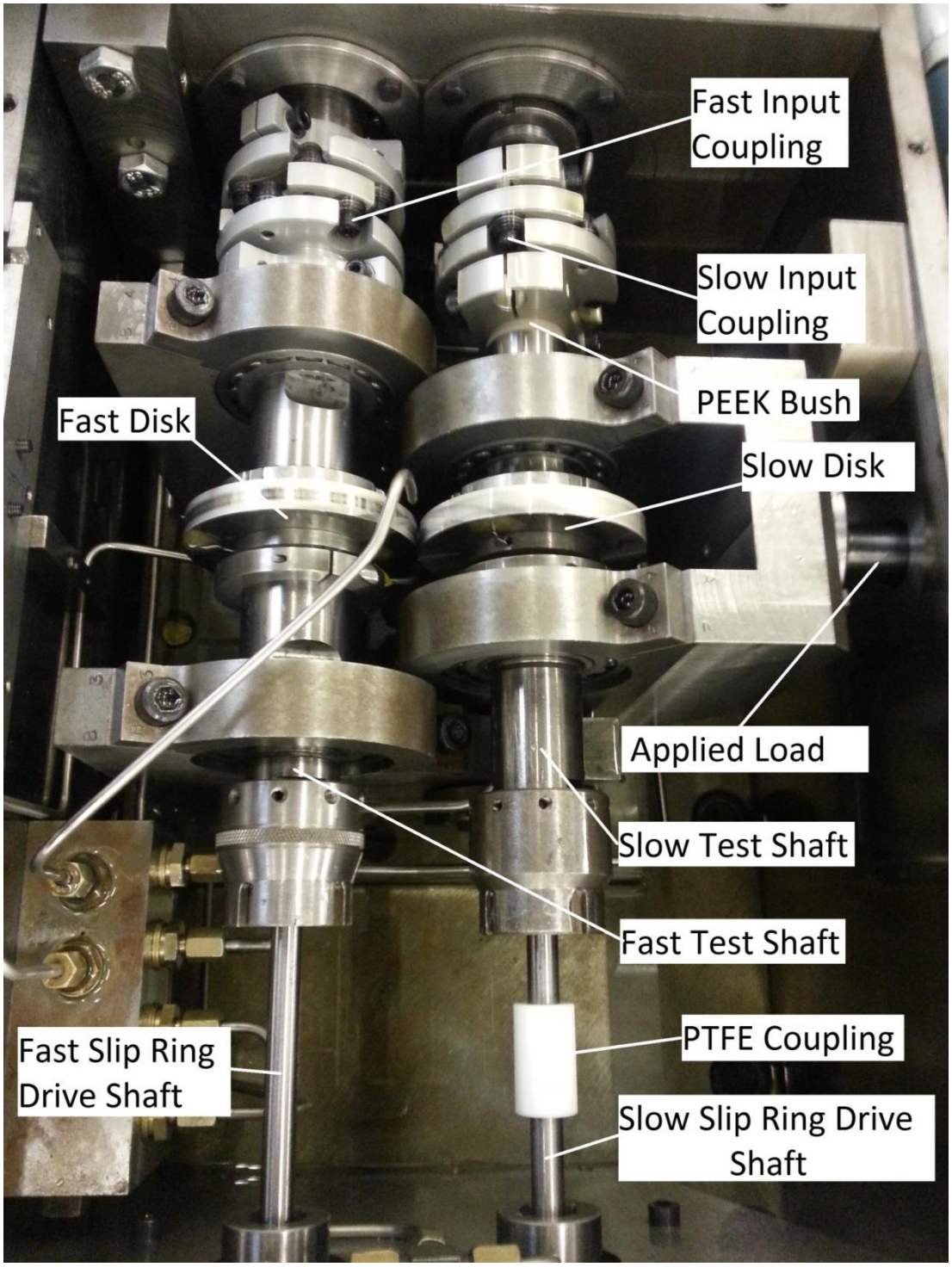

Figure 3-1 General view of the test head

3.2 Description of the Test Rig

3.2.1 Description of Load Application

The two disk test rig used for this work was developed by Alanou (Alanou, 2006) and based on the principles laid out by Merritt in his well known paper investigating the performance of worm gears (Merritt, 1935). The fundamental design has been adopted by the research community and used in other works (Williams et al., 1988, Crook, 1957). The test head consisted of two test disks which were each fitted onto hardened steel shafts using a hydraulic press. A locking washer and nut were then used on each of the shafts to ensure the disks remained in place. The test shafts were hollowed to accommodate the thermocouple and contact voltage wires which allowed measurement of the bulk disk temperatures and also the level of metallic contact occurring.

The test shafts, which were mounted on self-aligning bearings to provide equal load distribution across the contact, run parallel to one another. The bearings and shafts were firmly mounted in bolted split housings with the slow shaft bearing housing being pivoted to facilitate radial disk loading. The load was applied hydraulically to the test disks through a push-rod yoke assembly acting on the slow shaft bearing housing. This configuration provides load application up to a maximum of 8kN, corresponding to a maximum Hertz pressure of 2.1GPa for the given disk geometry (Rx = 19.8mm, Ry = 152.4mm, E'=224.6GPa) and minimises the shock loading that may occur on manually applying load through a weighted lever assembly that has been employed by authors in the past (Merritt, 1935, Williams et al., 1988). A 3D CAD model showing a section view of the loading mechanism is displayed in Figure 3-2.

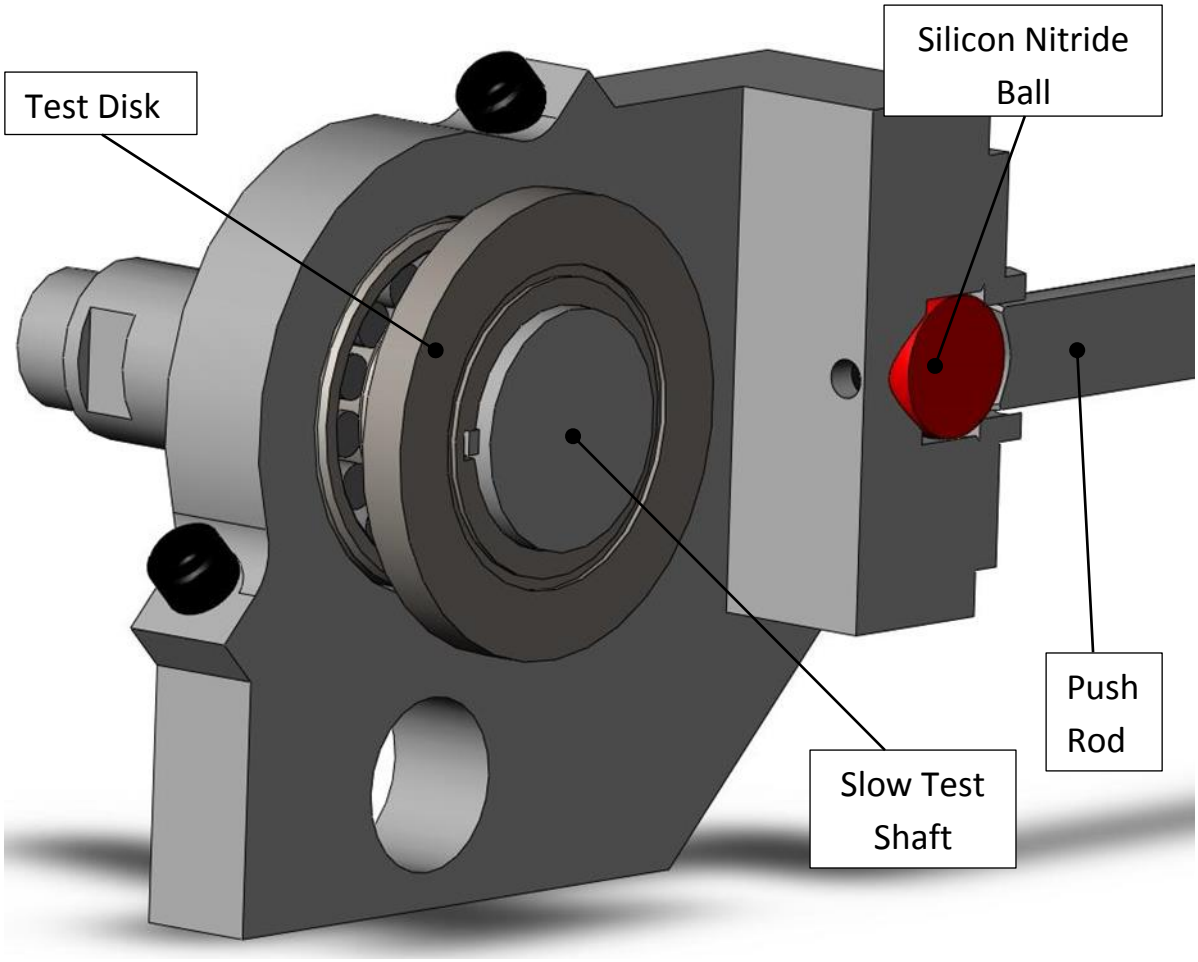

Figure 3-2 3D CAD model showing a section view of the push-rod and yoke mechanism

3.2.2 Description of Drive to Test Rig

Originally the test rig had been driven by an inverter powered two-pole motor allowing high speeds to be produced. In contrast to the work carried out by Davies (2005), for this research it was required to run experiments at lower speeds to investigate mixed lubrication and encourage asperity interaction. The two-pole motor was found to be inadequate as it struggled to maintain stability at the low entrainment speeds required. As a result, the original motor was replaced with a Marathon Electric 5.5kW three-phase asynchronous six-pole motor, providing the steady lower speeds required when investigating mixed lubrication conditions. With the new motor, the minimum and maximum fast shaft speeds were 200rpm and 2000rpm, which correspond to slow shaft speeds of 155.6rpm and 1555.6rpm at the slide to roll ratio of 0.25 which was used for the majority of this work. In order to avoid scuffing in the experiments carried out in this research, the slide roll ratios adopted were 0.25 and 0.5. The

load was limited in each case to give a maximum Hertzian pressure of 1.7GPa. Experience gained from the extensive scuffing tests carried out by Patching (Patching, 1994) suggested that these conditions were below the limit at which scuffing might occur. In the initial experiments while the rig and experimental procedure was being developed. The slide-roll ratio was restricted to 0.25 to minimise the possibility of a scuffing failure with consequent delay in remanufacturing and instrumenting the test disks. The aforementioned slide-roll was a chosen in order to minimise the risk of scuffing the disk surfaces.

In order to successfully mount the motor, spacer plates were manufactured as the supports on the six-pole motor were too narrow for the existing configuration. It was also necessary to manufacture an additional coupling adapter to attach the motor output shaft to the test rig.

The drive from the motor was transferred to the fast drive shaft through a fixed 2:1 reduction gearbox which is shown in Figure 3-3. To enable a degree of sliding between the test disk surfaces, the test shafts were geared together. The spur gears that had been used previously by Davies (2005) were replaced with helical gears in order to minimise backlash and reduce misalignment between the disks. Four pairs of gears were obtained for use which gave slide roll ratios of 0.25, 0.5, 0.75 and 1.

In the interest of acquiring contact voltage data from the same interacting asperity features, it was desirable to reduce torsional compliance. To that end, the slow and fast test shafts, upon which their test disks were mounted, were clamped to their drive shafts using single and double stage HUCO membrane couplings, respectively – which provided a high degree of torsional rigidity.

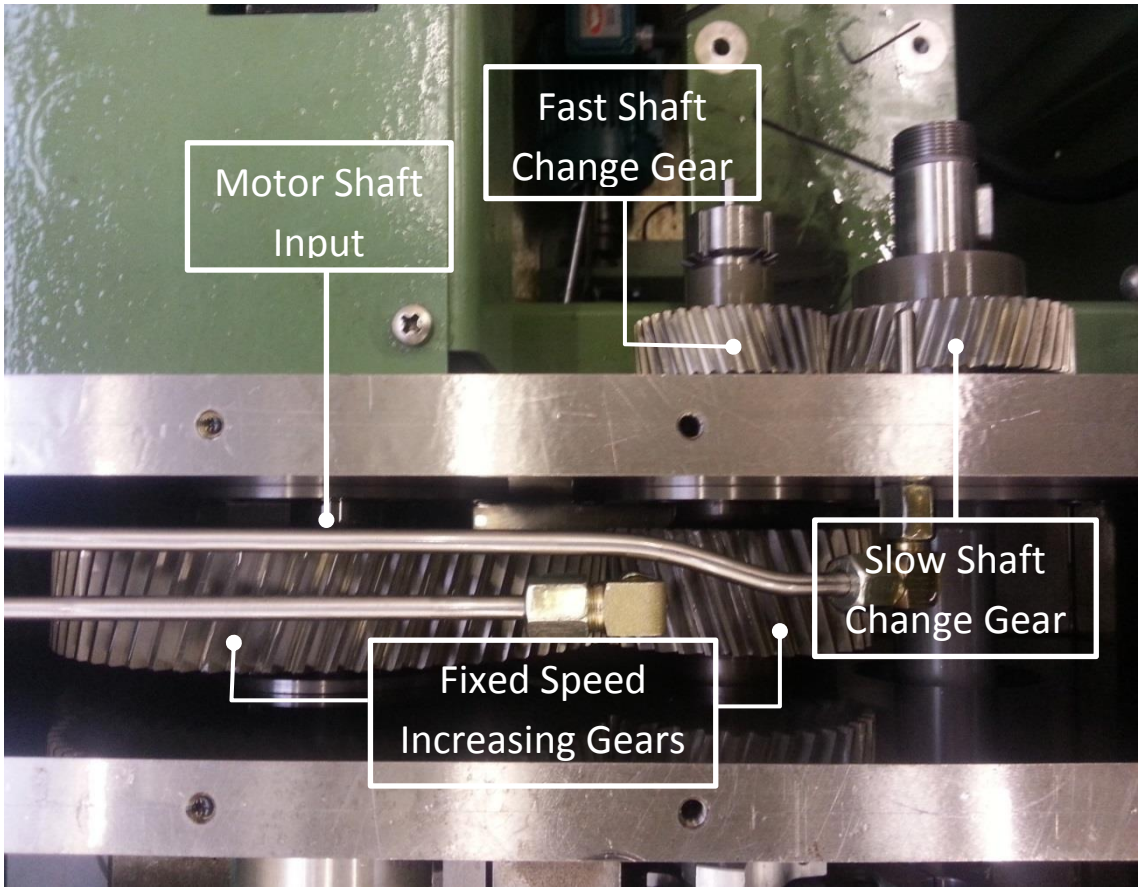

Figure 3-3 Photograph of fixed speed gearbox and the change gears between test shafts

3.2.3 Description of Electrical Isolation

In order to monitor the contact voltage the test disks were isolated electrically from each other, reducing the conduction path to that which occurred via the contact between the disks. To achieve this, several features were included in the design of the test rig.

The slow shaft was chosen for electrical isolation as the modifications could be more easily implemented. The yoke upon which the test shaft was mounted was isolated from the test rig through the inclusion of insulative silicon nitride rolling element bearings. Silicon nitride was also used in the manufacture of the ball upon which the push-rod actuated and provided a further necessary insulative barrier. This arrangement can be seen in Figure 3-2. The slow test shaft was isolated from the slow drive shaft through the manufacture of an insulative bushing composed of PEEK. This addition required the double-stage membrane coupling to have its

bore increased. At the opposing end of the slow test shaft, a PTFE coupling was used to provide the final insulative barrier. These modifications are illustrated in Figure 3-1.

3.2.4 Description of Torque Transducer

The rig required the use of a torque transducer through which to measure the friction occurring at the contact. The friction between the test disks was calculated by using the measured value for the torque and dividing by the test disk radius. A description of the torque transducer used in this work is now given.

In previous work, the friction occurring at the contact had been measured through the use of a torque transducer coupled between the motor drive shaft and the input shaft to the test rig. This provided an approximate value as a portion of the torque was required to overcome the inertia of the rig. The original arrangement was also outside the torque loop of the rig compared to the more direct friction measurement now introduced. To improve upon this, a modification was required. A new torque transducer in the form of a quill shaft was manufactured - a CAD model demonstrating the modification is shown in Figure 3-4.

The shaft was fitted with a full 45° strain-gauge bridge, the resistive elements were mounted upon a reduced diameter section in order to increase the measurement sensitivity. The strain gauges were bonded to the shaft using the services of a specialist supplier, Procter and Chester Measurements Ltd. and the arrangement was self-compensating for temperature. The quill shaft was fitted following modifications to the slow drive shaft. The drive shaft was bored through to accommodate the transducer. The quill shaft was designed to be fed through the modified gear shaft and coupled at the motor end, to increase the torsional deflection for a given friction force, providing a more accurate reading.

During the first set of running in experiments, conducted with a maximum Hertzian contact pressure of 1.7GPa, it was observed that there was a degree of torsional oscillation exhibited by the quill shaft which subsided when the load was decreased. This oscillation was not

observed during the speed varying experiments after the surfaces had stabilised, during which a maximum Hertzian contact pressure of 1.4GPa was used. The oscillation occurred at speeds of 750rpm and 1500rpm suggesting a torsional oscillation in the shaft.

To prevent torsional oscillation in further running-in experiments, a replacement for the quill shaft was manufactured where the reduced section had a greater diameter which was then fitted with strain gauges by the same company. Following this modification a second set of running-in experiments was conducted and no further oscillation was observed.

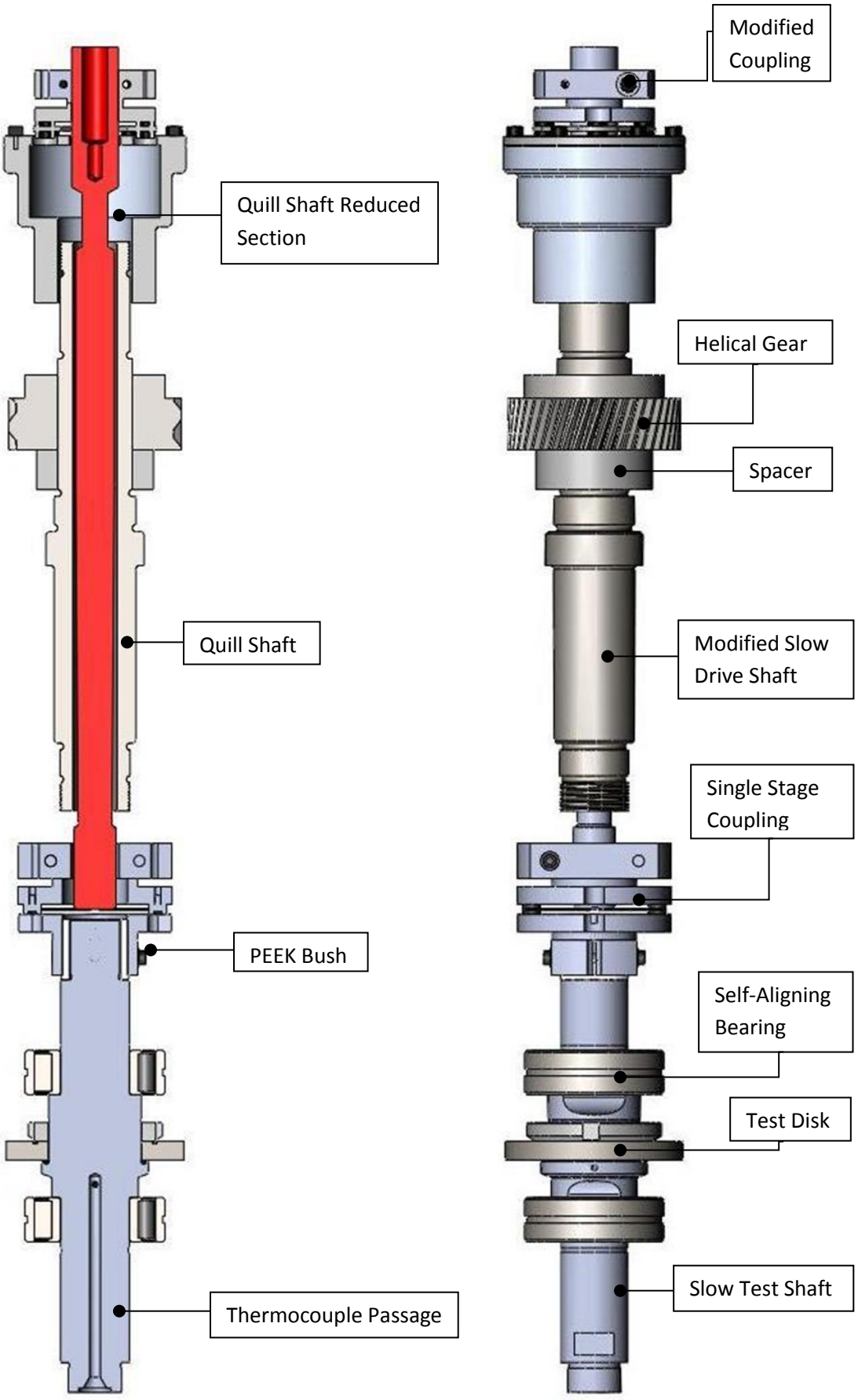

Figure 3-4 3D CAD model showing slow shaft assembly (right) and section view (left)

3.2.5 In-Situ Profile Measurement

To generate meaningful data for comparison with numerical models, it was necessary to use surfaces on which no significant plastic deformation was occurring, to that end – it was a requirement that surfaces go through a preliminary running-in process in order to stabilise them sufficiently, these experiments are described in Chapter 4. In order to monitor the change in the surface topography, the rig had been designed with a stage on which to locate a Taylor Hobson Form Talysurf surface profilometer. This enabled the collection of linear profile data in the circumferential direction, allowing for rapid in-situ assessment of the change in surface roughness between experiments. The stage could be manually traversed in the *y* direction (shaft axis direction), allowing circumferential profiles to be acquired at different axial positions. A dial gauge was used to accurately position the stage to within 10μm. To measure changes in both the slow and fast disk, the stage was designed with recesses for three point mounting as shown in Figure 3-6 that allow the unit to be located in either a forward or backward position.

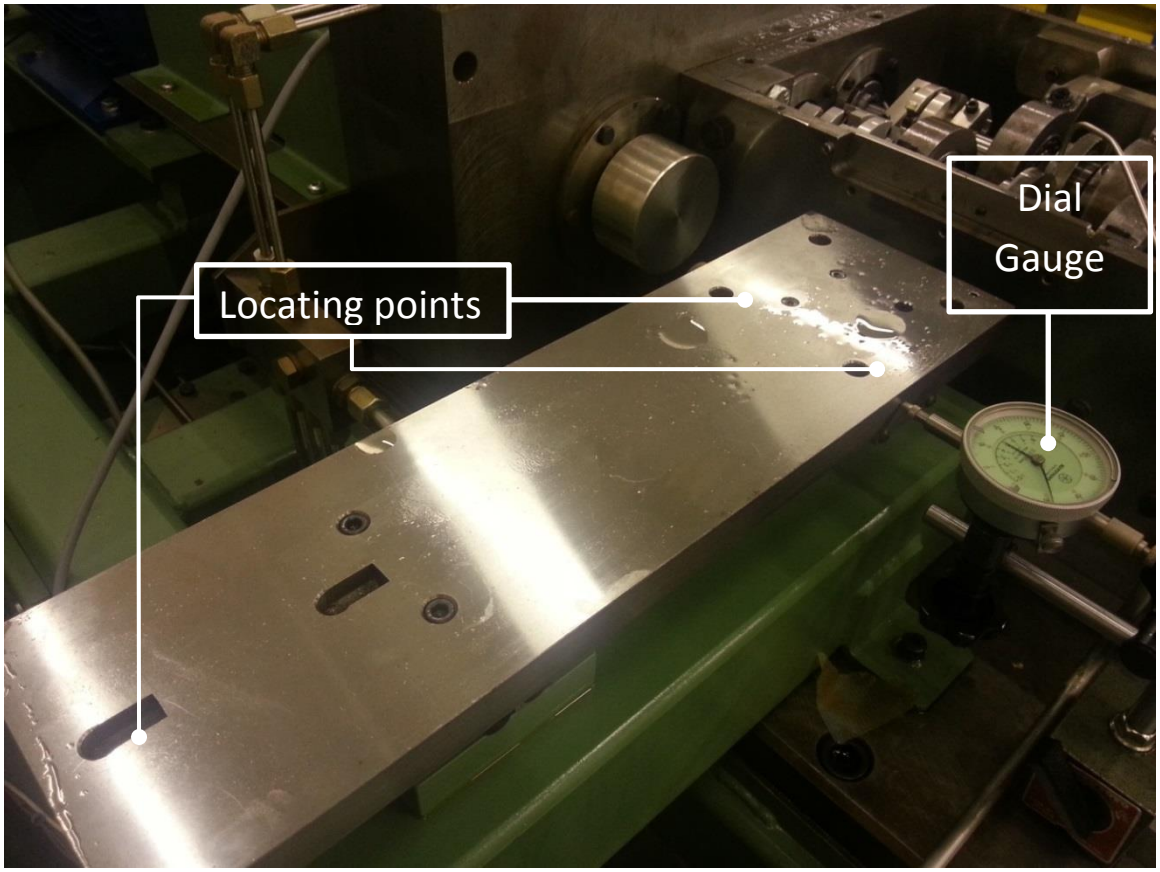

Figure 3-5 Talysurf stage and dial gauge setup

Figure 3-6 shows a photograph of the Talysurf positioned in the backward position to take in-situ circumferential profile measurements from the fast disk surface. The coordinate system of the Talysurf has been superimposed on the figure in order to aid description of profile measurements.

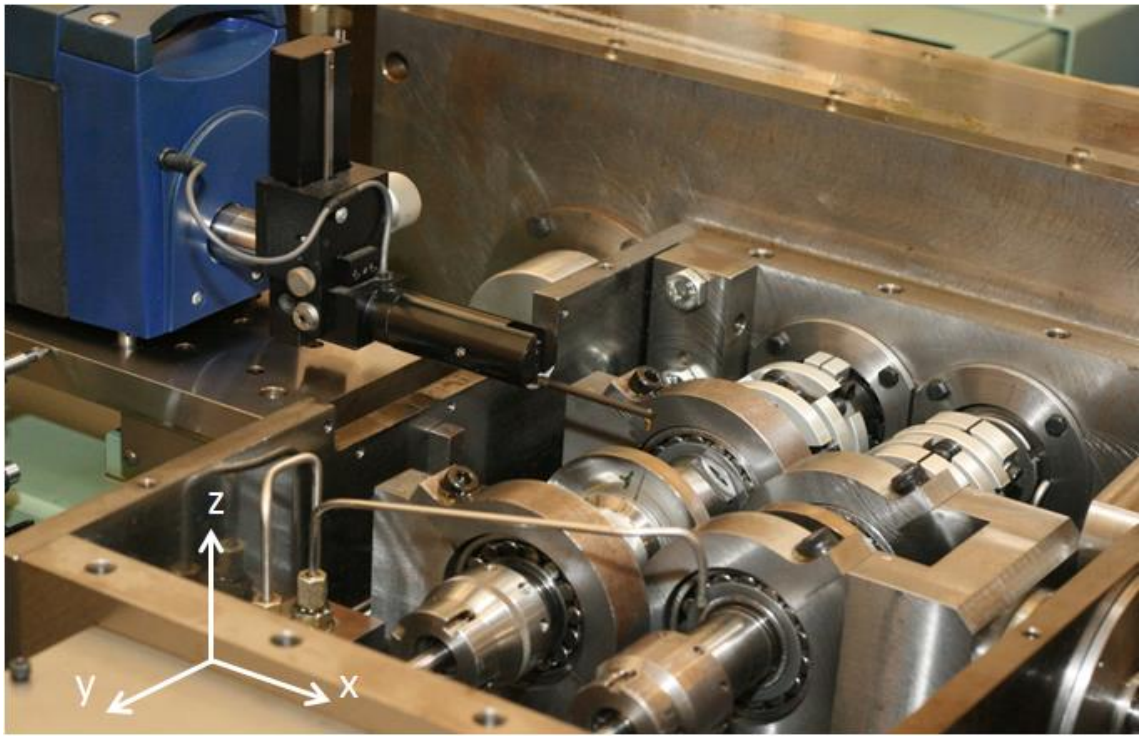

Figure 3-6 Talysurf setup on stage in 'back' position for in-situ profile measurements of the fast disk

The ability to attain in-situ measurements was necessitated by the requirement that the disks remain in the same relative position to one another. Preventing relative movement maintained the alignment of surface features on opposing disks. This was of great importance as new surface features coming into contact could generate high pressures and further plastic deformation, providing misleading results in the investigation.

Disk profiles were acquired prior to and following each load stage during the running-in process to monitor the evolution of the surface topography. For each measurement twelve profiles were taken from each disk. The measurements were taken at four marked circumferential positions per disk and at each circumferential location three profiles were taken, at the disk centreline and offset axially by ±0.2mm. The reasoning behind this was that

occasionally profile measurements could contain error caused by vibration from external sources or residual debris producing misleading peaks. As a result of the prominent and approximately axial grinding marks, profiles that had been offset by 0.2mm in the finishing direction would contain the same major asperity features whilst avoiding potential sources of error in previous measurements. The visual similarity between axially offset profile traces is demonstrated in Figure 3-7 where profile measurements taken at the same circumferential location are shown. It is clear that a large amount of agreement between the prominent asperity features exists which is due to the highly directional lay of the surface finish. Note that the grinding process leading to the crowned disk profiles involves a conical grinding wheel and the lay of the surface is not entirely axial as can be seen in the photograph given in Figure 5-31. Consequently it is inevitable that there will be differences in the profiles obtained with different axial offsets.

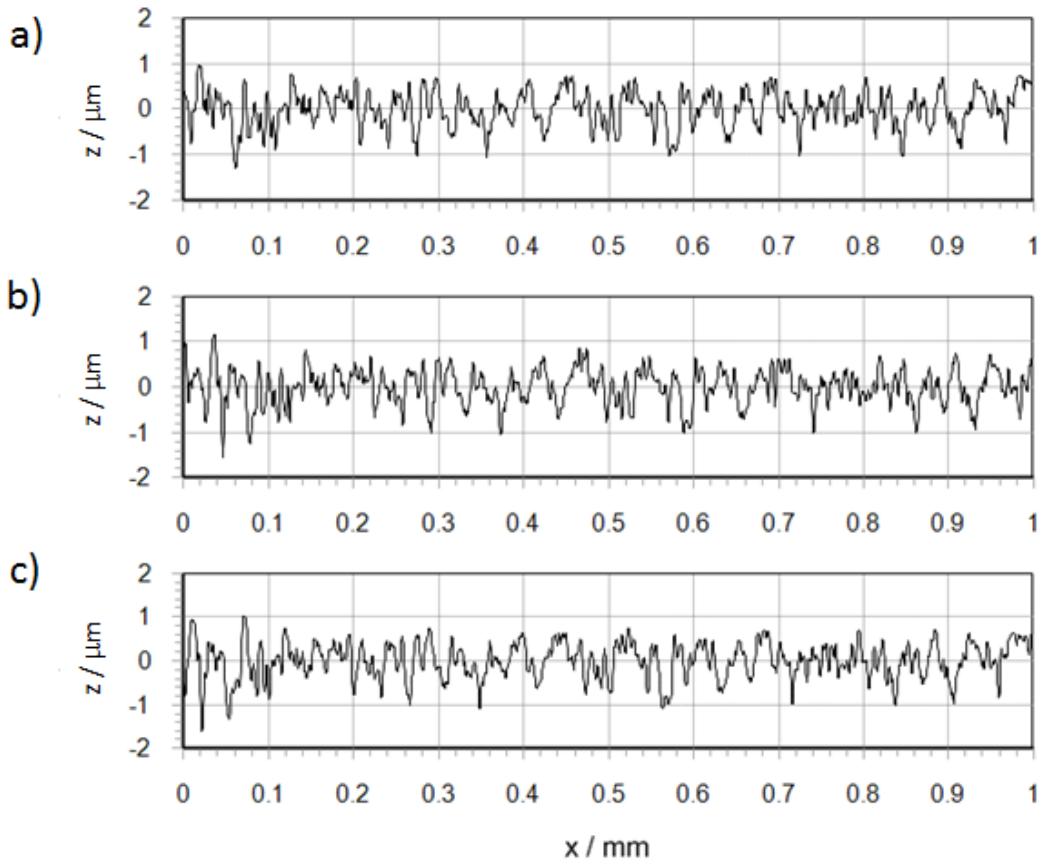

Figure 3-7 Filtered roughness profile traces taken at a) centreline position b) 0.2mm axial offset parallel to the y axis (towards the fixed gears) c) 0.2mm axial offset parallel to the y axis positive (towards the slip rings). Profiles show conformity between major asperities

The method established for initiating a set of profile measurements is shown in Table 3-1. Steps 1 to 4 were conducted every time the Talysurf unit was moved to initiate a new set of disk measurements and steps 6 to 11 were conducted for each new circumferential position on a disk.

Table 3-1 Procedure used to relocate on test disks and take profile measurements

1.	Position the dial gauge perpendicular to the mounting stage.
2.	Approximately locate the crown of the disk and lower the stylus into contact.
3.	Move the stage carefully in the negative y-direction until the Talysurf z reading experiences a sudden drop of 25µm.
4.	Set the dial gauge to zero at this position.
5.	Move stage 4.8mm in the y-direction.
6.	Perform Autocrest function in software to locate disk crown.
7.	Move stylus out of contact with the surface.
8.	Manually rotate disk to align stylus with circumferential marking.
9.	Lower stylus into contact.
10.	Traverse stylus in negative x-direction 4.3mm.
11.	Acquire profile, run-up length 0.3mm, data length 8mm, spacing 0.5µm, measurement speed 0.25mm/s.

3.2.6 Contact Voltage Measurement

A description of the electrical isolation used within the test head to enable the implementation of electrical methods to investigate the state of lubrication occurring at the contact has been described in section 3.2.3. Many different electrical methods have been used in the past by researchers (Crook, 1957, Furey, 1969, Tallian et al., 1964, Courtney-Pratt and Tudor, 1946, Williams et al., 1988, Lane and Hughes, 1952) as a means of qualitatively assessing metallic contact levels occurring between tribological components. Whilst these methods are not new, they are indeed useful indicators and should be used in conjunction with the friction coefficient to provide information as to the lubrication regime experienced by the contact. A similar technique was used in the current research to that employed by Furey (Furey, 1969). In his well-known work on the investigation of metallic contact in lubricated contacts, where the application of low voltage across a lubricated contact was used to assess the level of

interaction occurring between the surfaces. A simple diagram for the electrical circuit used in the author's work is shown in Figure 3-8. It can be seen in the diagram that the voltage across the disks was obtained through the division of the 4.02 V supply across a high resistance bridge circuit. The purpose of this was to minimise both the voltage and current to reduce the extent to which discharge could occur across the lubricant film. A voltage of 43mV was applied to the disks through the slip rings. When no conduction path existed between the disks a voltage of 43mV could be measured, when contact occurred between the surfaces the resistance would decrease, yielding lower voltage levels. The work of Davies (2005), used a voltage of 15mV. It was shown by Furey that an applied contact voltage as great as 1.5V could be used in the study of observed metallic contact without influencing results (Furey, 1969). Higher voltages were found to increase the level of contact detected and this was argued to be due to electrical discharge between asperities. The circuit used by the current author was developed to increase the voltage used by Davies by a factor of three in order to increase the signal to noise ratio and stay well away from possible discharge effects. This was increased by the current author commencing work to increase the signal to noise ratio.

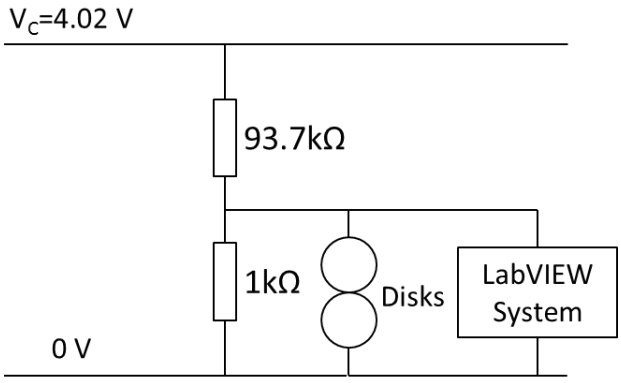

Figure 3-8 Circuit diagram for the electrical system providing contact voltage

Originally the objective had been to use the existing shaft encoder to produce triggered contact voltage readings, but it was established early on that the encoder itself was generating a large amount of noise which was interfering with the measurement of other channels. The initial set of experiments which did not employ the use of triggering are not contained in this

thesis as they were also subject to the previously mentioned oscillation of the torque transducer.

A Taylor Dynamics TEH75I Incremental Hollow Shaft Encoder was purchased to replace the old encoder. Following this, it became possible to monitor both the speed of the rig and use a digital pulse produced from the encoder to trigger the acquisition of the contact voltage at the same location during subsequent rotations of the fast disk. This gave the capability to sample the contact voltage channel at high speed, where fluctuating, repeatable measurements indicated repeated asperity interactions. Figure 3-9 shows a photograph taken at the driven end of the test rig where the shaft encoder is clearly shown mounted on the encoder drive shaft. The encoder drive shaft is coupled to the fast drive shaft hence speed measurements in this work are described with reference to the speed of the fast shaft.

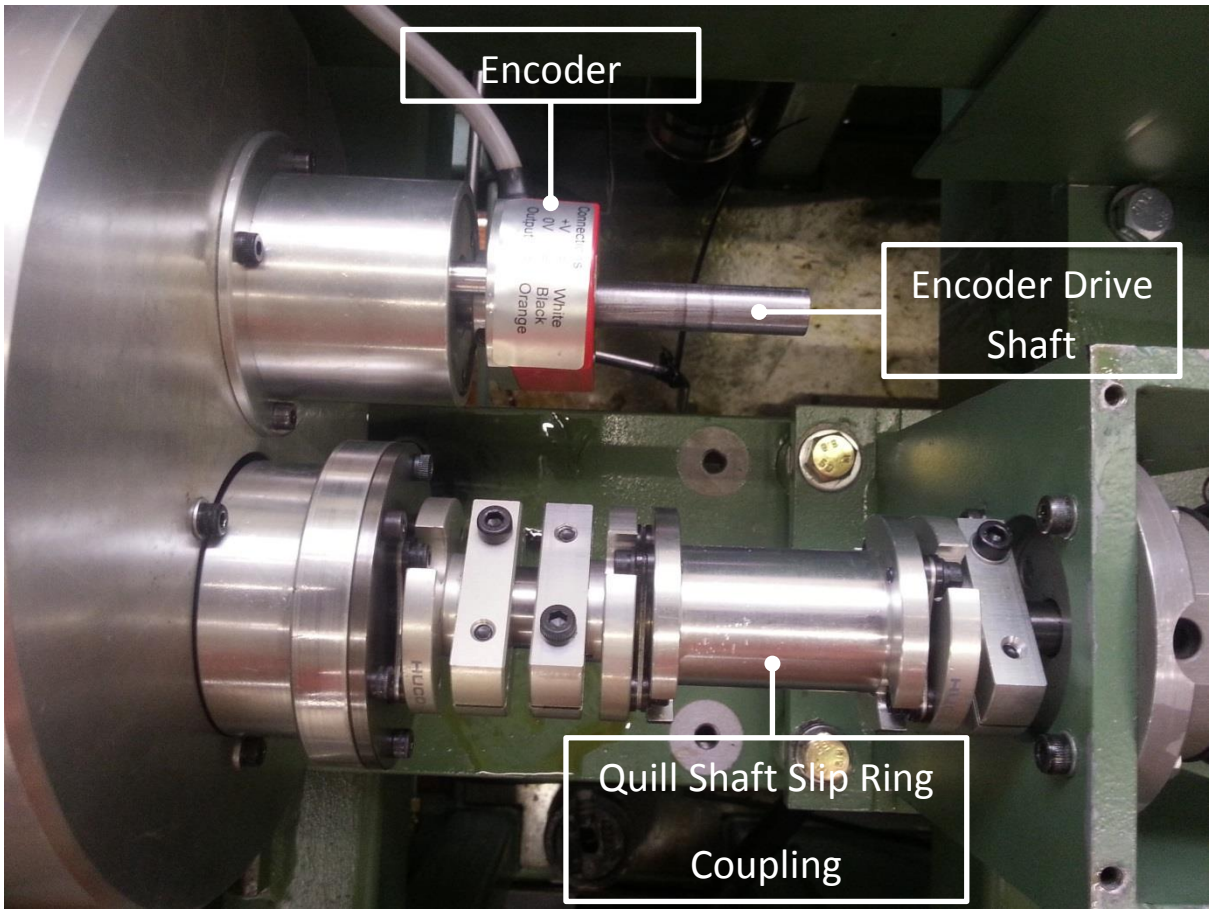

Figure 3-9 Photograph of the driven end of the test rig showing the shaft encoder mounted on the fast shaft and slip ring

It was found when testing the encoder that the data acquisition system would receive many spurious pulses, which would cause unacceptable error in measurement of the contact voltage signal. To overcome this difficulty, an inverse pulse channel on the encoder was used, this significantly reduced the likelihood that noise would be the cause of spurious trigger as the channel from the encoder would remain high throughout the entirety of the revolution and only drop during the trigger pulse.

When sampled at high speed, a high degree of electrical noise was apparent in the measurements. This noise was associated with the inverter and found to have a mean value of zero, and therefore did not invalidate contact voltage readings taken previously. In order to reduce the interference from the inverter, the contact voltage signal wires were shielded which greatly reduced the amplitude. However to attain acceptable levels, it was decided to employ digital filtering in the data acquisition software. The selection process for the filter characteristics is described in section 3.5.3.

3.2.7 Calibration of Torque Transducer

In order to calibrate the torque transducer accurately, the change gears connecting the two shafts were removed and a lever was manufactured and attached to the diaphragm coupling used to house the connecting wire to the transducer as shown in Figure 3-10. The calibration process involved the incremental addition of masses to the lever to apply a known torque to the transducer. Prior to the calibration, weight was also added to counterbalance the lever, whilst ensuring that the tool remained horizontal, until equilibrium was achieved. Following this, the test shaft was clamped inside the test head to prevent any movement of the quill shaft. A bipolar calibration was performed through the incremental addition of load in the clockwise and counter-clockwise directions.

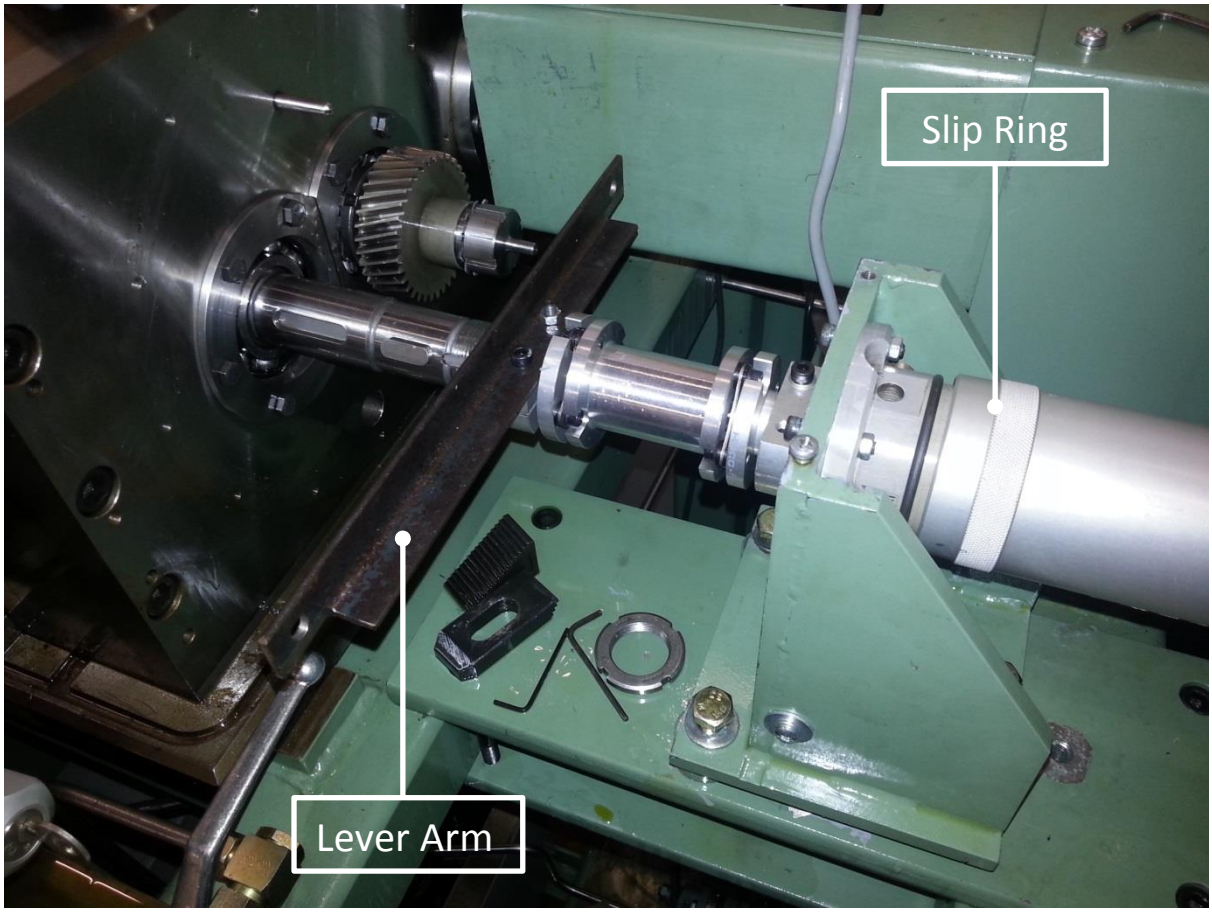

Figure 3-10 Torque transducer calibration setup with lever attachment for diaphragm coupling

The results for the clockwise and counter-clockwise calibration procedure are displayed in Table 3-2 and Table 3-3 respectively. The maximum load used in clockwise and counter-clockwise direction was 10kg and 12kg, giving applied torques of -14.7Nm and 11.8Nm, respectively. In each case, after ensuring that the values on the indicator display and the analogue output read on the computer had settled, the set point was saved. The masses were then removed and load was reapplied incrementally. Following each load increment the analogue output reading was carefully noted and recorded.

Table 3-2 Clockwise calibration of quill shaft torque transducer

Load / kg	Force / N	Theoretical Torque at Quill Shaft CW / Nm	Analog Output Voltage / V	Torque Reading / Nm	Error / %
0	0.00	0.00	-0.01	-0.13	-
2	19.62	1.96	0.18	1.81	-7.75
5	49.05	4.91	0.47	4.74	-3.36
7	68.67	6.87	0.67	6.69	-2.58
10	98.10	9.81	0.96	9.59	-2.24
12	117.72	11.77	1.16	11.57	-1.72

Table 3-3 Counter-clockwise calibration of quill shaft torque transducer

Load / kg	Force / N	Theoretical Torque at Quill Shaft CW / Nm	Analog Output Voltage / V	Torque Reading / Nm	Error / %
0	0	0.00	0.00	0.00	-
2	19.62	-2.94	-0.29	-2.93	-0.44
5	49.05	-7.36	-0.74	-7.36	0.03
7	68.67	-10.30	-1.03	-10.29	-0.10
10	98.1	-14.72	-1.48	-14.75	0.24

The response of the quill shaft torque transducer over the range of applied torque is illustrated in Figure 3-11. It is apparent that the indicator readings for measured torque align very closely with those for theoretical torque over the range of load applied. The calibration yielded an average error over the range tested of 1.87%.

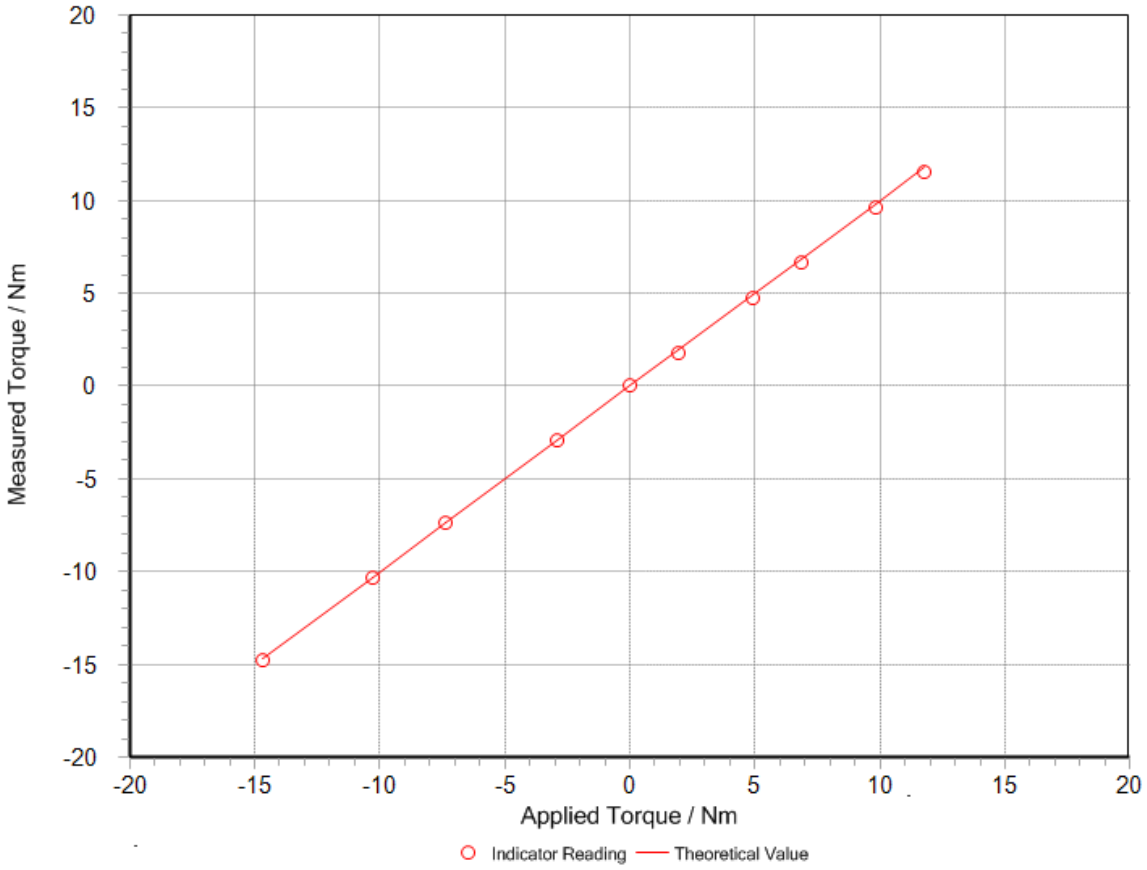

Figure 3-11 Scatter plot showing the results for calibration performed on the quill shaft

3.2.8 Measurement of Bearing Friction

It was necessary to establish the impact the friction generated in the bearings of the test shafts had on the overall friction measured at the contact. This was achieved by disconnecting the fast test shaft from the fast input coupling. When the load was applied to the test disks, the fast shaft was driven by the slow shaft in a condition of pure rolling. In this condition of rolling, the torque measured was the torque required to drive the bearings on both the fast and slow test shafts. The bearing support of both shafts was identical so this value could then be halved to establish the level of friction arising from one set of bearings.The value calculated would represent that which should be subtracted from the measured torque to provide a more accurate estimate of the traction.

Figure 3-12 shows the bearing friction calculated for one set of bearings for the range of speeds and loads considered. It is apparent that an increase in load and speed both yield increases in measured friction. It can be seen that an inconsistency exists for all loads considered at a fast shaft speeds of 300rpm or 400rpm where a reduction in friction is visible. The source of this was not established but it is suspected to be associated with a resonance in the quill shaft as the level of noise apparent in the friction measurement at 300rpm is much higher than at the neighbouring speeds. This may be seen in Figures 5-15 and 5-16, for example. However the levels of bearing friction at 300rpm are low in comparison to the friction measured during experimentation.

The friction is recorded from the bearings is highest at a speed of 2000rpm across all loads. At this speed, the bearing friction amounts to 19% of the total measure friction at a contact load of 1.0GPa. The proportion of the total measurement that can be attributed to bearing friction is greatest in these circumstances and the bearing friction calibration allows this effect to be removed in any subsequent calculations.

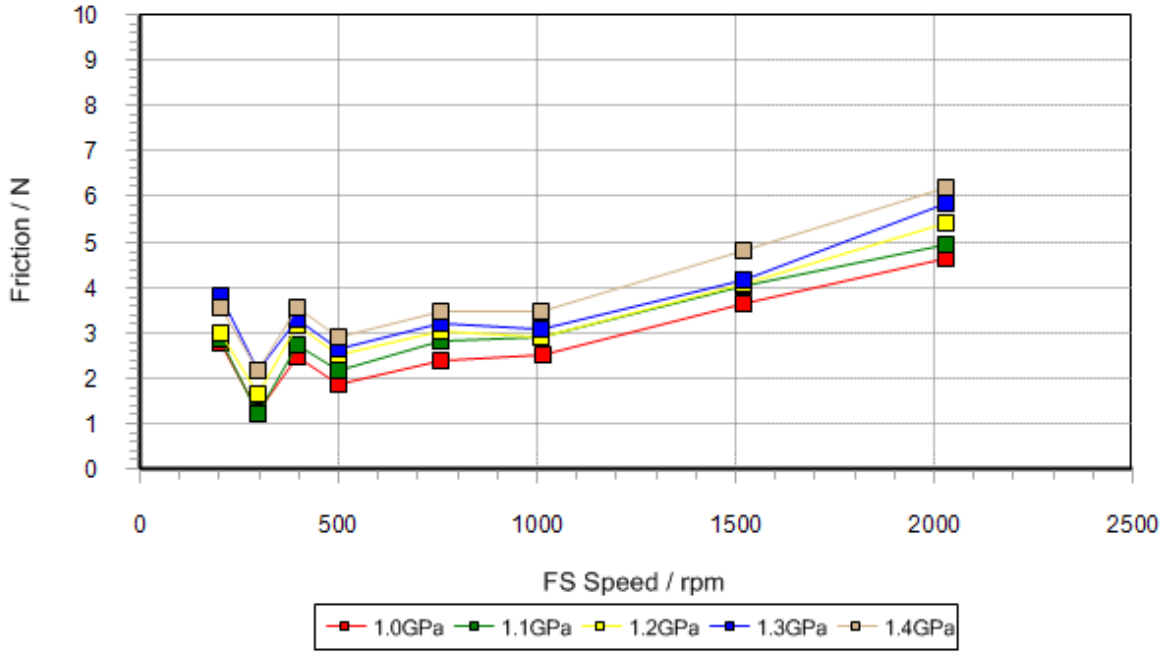

Figure 3-12 Results of bearing friction measurement as function of contact pressure and speed

3.2.9 Load Cell Calibration

In order to accurately measure normal force applied to the test disks, a button load cell was mounted on the end of the hydraulic ram used to apply pressure to the yoke assembly. The signal from this transducer was displayed on an RDP E725 digital indicator, the analogue output from which was sampled by the data acquisition software.

It was possible to detach the unit from its mounting point and using the ample length in the signal wire, relocate it to a nearby test rig substituting it in for the local load cell. Figure 3-13 shows the setup used to calibrate the button load cell used in all experiments throughout this work. Positioned as shown in a nearby test rig, calibration could be performed through the use of a specially designed lever arm, on which high load could be applied incrementally, employing the mechanical advantage provided by the design.

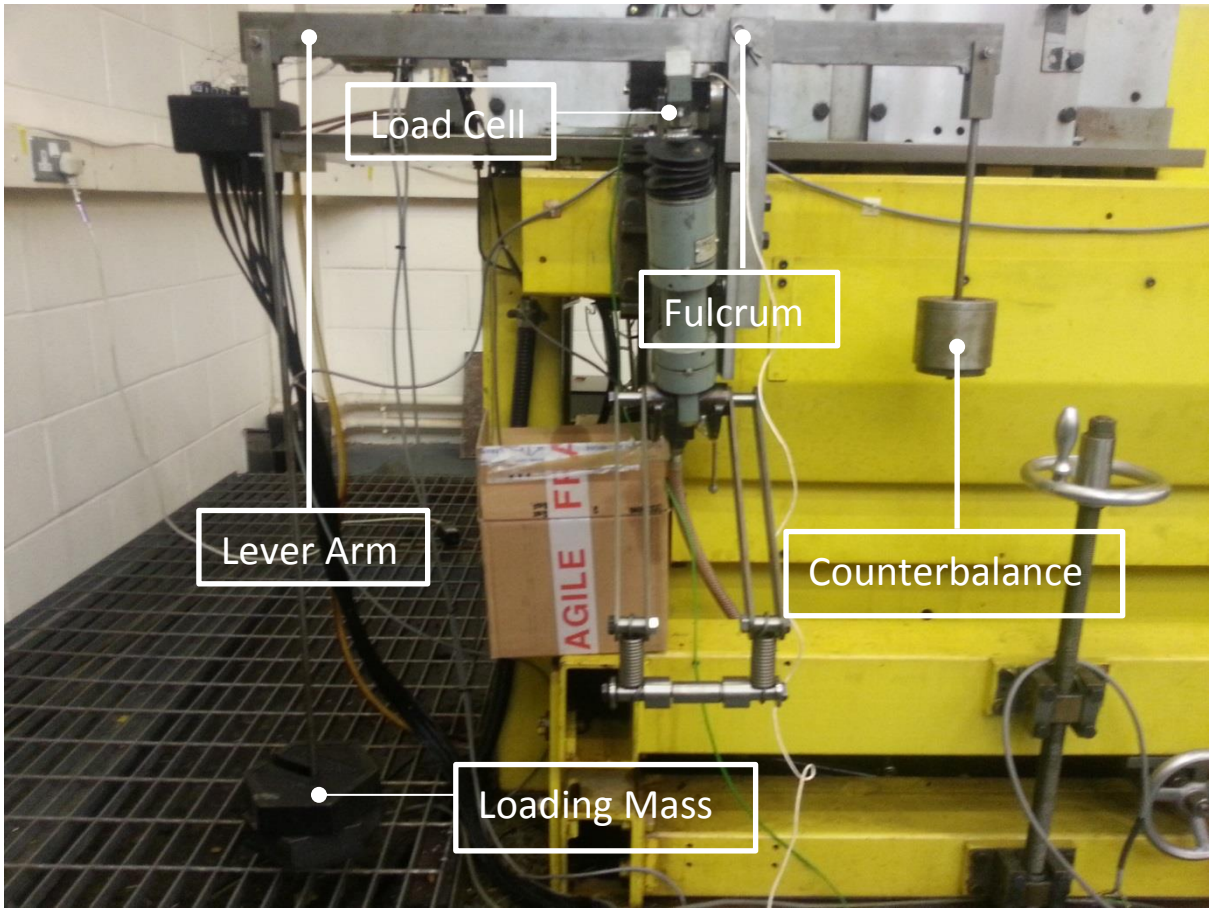

Figure 3-13 Load cell calibration setup with lever arm attachment

To begin the calibration process, the lever arm was counterbalanced through the addition of small masses. Once a state of equilibrium was achieved, the load indicator and analogue output of the indicator were zeroed. The transducer was calibrated to a maximum applied load of 5740N, which equated to a mass of 55kg suspended from the lever arm. Once the load had been applied and the indicator reading had settled, this value was used as the high set point for the calibration process. To verify the calibration, the load was removed and reapplied in 5kg increments. The load and indicator reading were recorded in each instance having ensured that the display had settled. Load was added in this fashion until the set point of 55kg was reached, at this point the same procedure was followed whilst the load was removed incrementally. The results of the new calibration used in this work show much greater accuracy than the values used by previous workers. Over the range of load applied an average error of 1.65% was found. A comparison between the previous and most the recent load calibration is shown in Figure 3-14. The values recorded at each of the load increments are recorded in Table 3-4.

Table 3-4 Results of the load cell calibration

Applied Load (kg)	Force (N)	Theoretical Force at Load Cell (N)	Loading (N)	Error (%)	Unloading (N)	AO Error (%)
0	0.0	0.0	-4		-5	
5	49.1	521.8	487	6.67	509	2.45
10	98.1	1043.6	1045	0.13	1053	0.90
15	147.2	1565.4	1598	2.08	1595	1.89
20	196.2	2087.2	2150	3.01	2133	2.19
25	245.3	2609.0	2682	2.80	2657	1.84
30	294.3	3130.9	3198	2.14	3183	1.67
35	343.4	3652.7	3716	1.73	3692	1.08
40	392.4	4174.5	4222	1.14	4210	0.85
45	441.5	4696.3	4734	0.80	4723	0.57
50	490.5	5218.1	5242	0.46	5237	0.36
55	539.6	5739.9	5751	0.19		
			Mean	1.92	**Mean**	1.38
			Max	6.67	**Max**	2.45
			Min	0.13	**Min**	0.36

Figure 3-14 shows a comparison of the results for the new load cell calibration with the previously used calibration. It is visible that there is very close alignment between the applied load which is displayed as a solid red line and the most recent calibration, shown in blue. In contrast to this, the previously used calibration drifts quite significantly from theoretical value at higher loads where at an applied load of 5740N a measured value of 6214N is received, equating to an error of approximately 8.3%

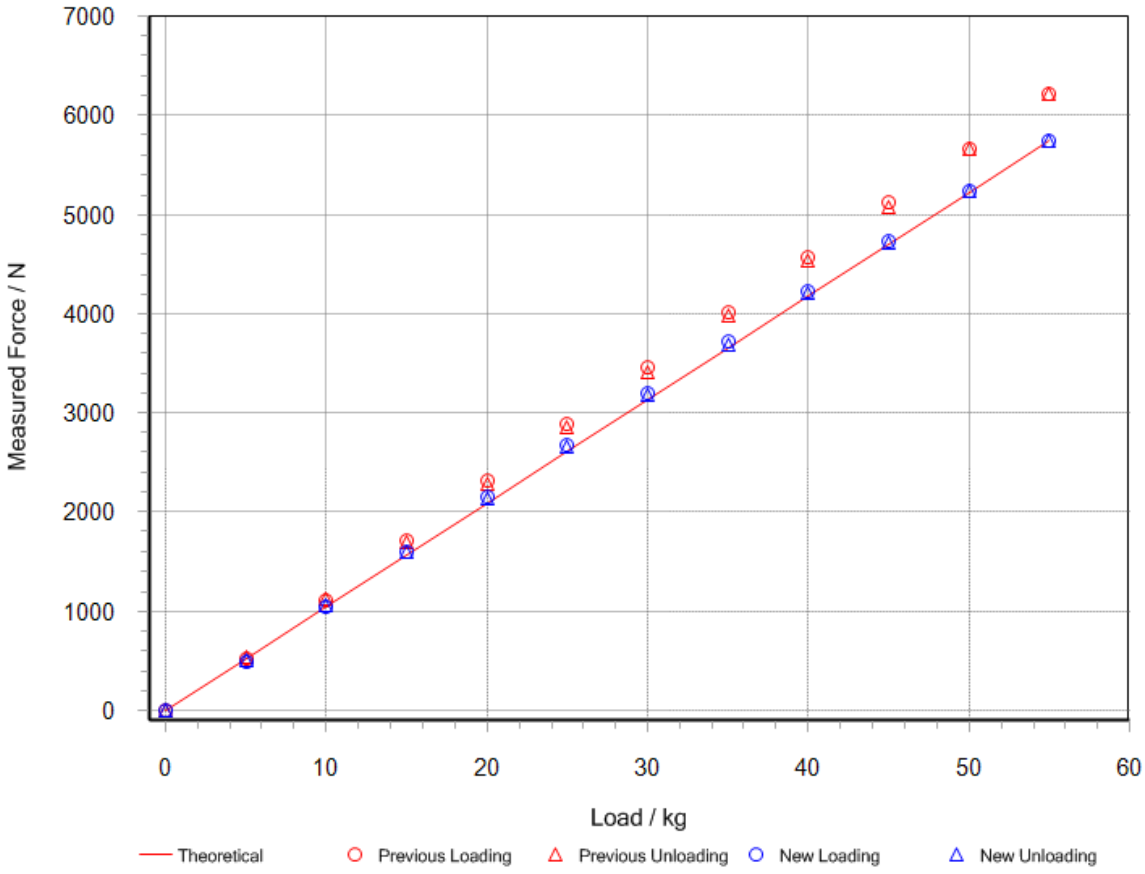

Figure 3-14 Plot of previous and new load cell calibration

3.3 Description of Disk Geometry

The test specimens used in this work, described in Figure 3-15, were 76.2 mm (3”) diameter disks which had a thickness of 9.53mm (3/8”) upon which a crown radius of 304.8 mm (12“) was imparted through the use of an internal conical abrasive wheel which produced an approximately axial finish. Also shown in the figure is a 2.2mm diameter blind hole that allows the thermocouple to be positioned 3.17mm below the centre of the running track. This grinding process resulted in the lay of the roughness being orientated transverse to the direction of entrainment, simulating finish found on typical involute gear teeth in aerospace applications. The elliptical contact produced by the crowned geometry of the disks removed the potential for unexpected edge effects that could arise in a line contact situation and also made the contact self-aligning. The orientation of the roughness has been shown through numerical simulation by Zhu and Wang (2013) to have a significant effect on performance. In elliptical contacts where the aspect ratio is less than 1, a longitudinal roughness orientation was in fact shown to be of benefit in providing effective lubrication. In this work, the aspect ratio of the contact produced by applied load to the test specimens is approximately 4:1, where a transverse roughness orientation has been shown to be an advantage as side leakage no longer dominates the flow of lubricant in the contact (Zhu and Wang, 2013).

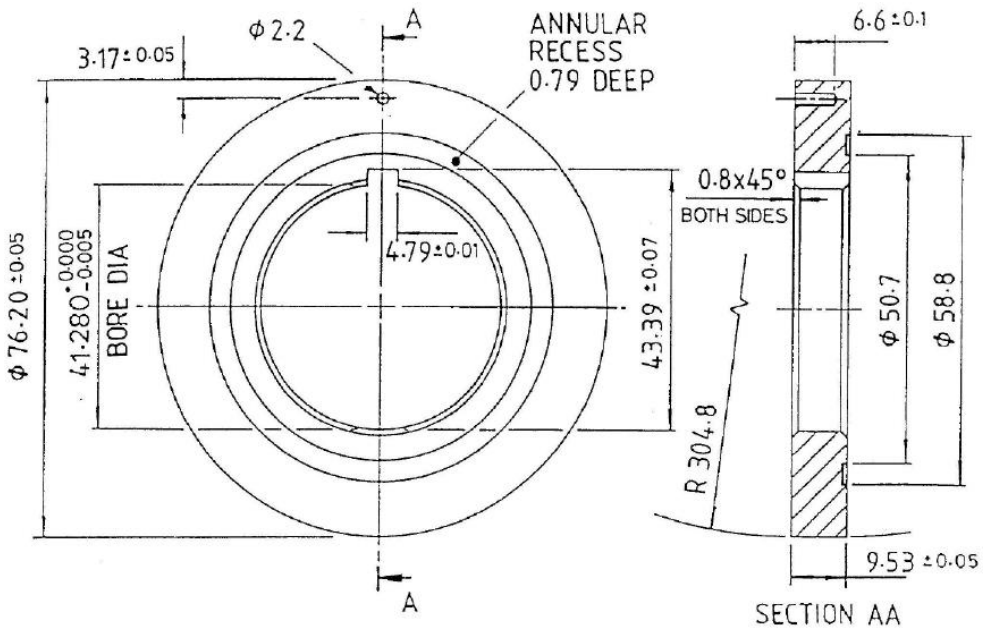

Figure 3-15 Drawing of a test disk used for experiments discussed in this work (all dimensions in mm)

3.4 Description of the Disk Material

The test disks were manufactured in two batches from nickel-chromium steel previously supplied by Rolls Royce to their steel specification 6010, with a composition typical of that found in aerospace gearing. The test specimens described have been employed and described in other publications by the research group at Cardiff University (Patching et al., 1995). The material specification is shown below in Table 3-5.

Table 3-5 Showing Elemental Composition of the RR6010 Steel by % Mass

Element	C	Si	Mn	P	S	Ni	Cr	Mo
Max	0.18	0.35	0.55	0.015	0.012	4.30	1.40	0.30
Min	0.14	0.10	0.25	0.0	0.0	3.80	1.00	0.20

The test disks used in this work were manufactured from the same bar of steel and heat treated separately by a specialist firm following the same procedure, which is described in Table 3-6 and is a typical case-carburising specification used in aerospace gearing.

Table 3-6 Treatment procedure for RR6010 steel disks used tests

• Normalise @ 930°C ± 10°C for 3 hours ± 15 minutes
• Harden @ 850°C ± 10°C for 3 hours ± 15 minutes
• Temper @ 530°C ± 10°C for 3 hours ± 15 minutes
• Carburise @ 927°C ± 10°C to yield a carburised case depth (Rc 50) of 0.036" to 0.042", with a surface carbon (second 0.002" cut) of 0.65% to 0.95% carbon
• Cool to room temperature after carburising
• Stress relieve @ 566°C to 621°C for 4 hours ± 15 minutes, then air cool
• Harden @ 788°C to 829°C for 30 minutes, then oil quench (24°C to 60°C)
• Sub-zero treat, within 60 minutes of quenching, for 3 hours minimum at -79°C or lower
• Temper @ 160°C ±5°C for 3 hours ± 15 minutes
• Final carburised surface hardness to be HRC 60 to 63
• Case depth (HRC 50) to be 0.036" to 0.042"
• HRC 60 depth to be 45% of 0.036" (0.016" of case)
• Core hardness to be HRC 36 to 41

Indentation hardness readings were taken at three positions on each disk using a Vickers indenter at 30 kgf. Indents were made on the side of the disk so as not to risk modifying the topography of the running track. Hardness measurements were also taken on the running track of disks that had been previously run and results were not found to differ between the two locations.

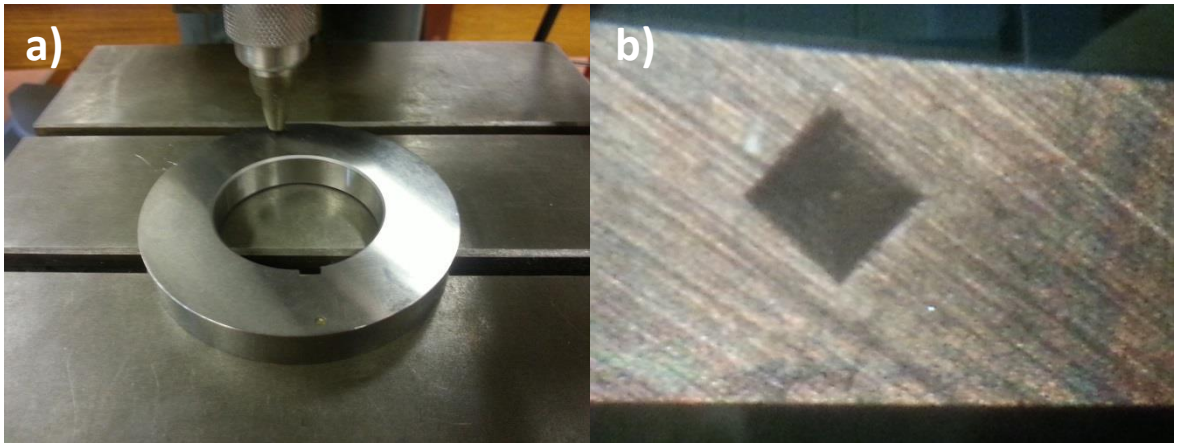

Figure 3-16 (a) Vickers indentation hardness testing of a test disk (b) magnified residual Vickers indentation

Upon inspection it was discovered that the hardness values from the first batch of disks were approximately HV 650 whereas the second batch of disks were found to have different hardness values of HV 810. In the work reported here the origin of each disk is made clear given the batch to batch variation in surface hardness as shown in Table 3-7 to Table 3-12.

Table 3-7 Hardness measurement for RR6010B – 38

Location	Dimension / mm	Vickers Hardness / kgf / mm^2	Yield Strength / GPa
1	252	836	2.73
	267		
2	255	849	2.78
	257		
3	258	842	2.75
	255		
Average	257	842	2.75

Table 3-8 Hardness measurement for RR6010B - 31

Location	Dimension / mm	Vickers Hardness / kgf / mm^2	Yield Strength / GPa
1	251	856	2.80
	258		
2	257	849	2.78
	255		
3	264	798	2.61
	263		
Average	258	834	2.73

Table 3-9 Hardness measurement for RR6010B - 14

Location	Dimension / mm	Vickers Hardness / kgf / mm^2	Yield Strength / GPa
1	260	823	2.69
	260		
2	265	804	2.63
	261		
3	258	829	2.71
	260		
Average	261	819	2.68

Table 3-10 Hardness measurement for RR6010B - 2

Location	Dimension / mm	Vickers Hardness / kgf / mm^2	Yield Strength / GPa
1	261	823	2.69
	259		
2	260	810	2.65
	264		
3	264	792	2.59
	265		
Average	262	808	2.64

Table 3-11 Hardness measurement for RR6010A - 44

Location	Dimension / mm	Vickers Hardness / kgf / mm^2	Yield Strength / GPa
1	292	652	2.13
	292		
2	293	650	2.13
	293		
3	292	652	2.13
	292		
Average	292	651	2.13

Table 3-12 Hardness measurement for RR6010B - 32

Location	Dimension / mm	Vickers Hardness / kgf / mm^2	Yield Strength / GPa
1	260	810	2.65
	264		
2	263	786	2.57
	269		
3	269	807	2.64
	257		
Average	264	801	2.62

3.5 Description of Data Acquisition System

3.5.1 Description of Hardware

The computer used for the running of the data acquisition software, was a PC using an Intel Core 2 5420 CPU at 2.1GHz with 1.97GB of RAM. Data was acquired using two different

National Instruments data acquisition cards which fitted into two available PCI slots. The cards used were an M-Series PCI-6250 for the higher speed acquisition of the contact voltage data and a slower, PCI-6220 for recording the bulk disk temperatures, friction, speed and load. The faster PCI-6250 had a maximum sampling rate of 1.25MHz whereas the PCI-6220 had a more modest sampling rate of 250kHz.

The thermocouples used for the acquisition of the bulk disk temperatures were both PTFE coated type J. To provide amplification and cold junction compensation, AD594 thermocouple amplifier chips with integrated cold junction compensation that had previously been installed were used with the system. These gave a voltage output of 10mV/°C. These were connected to the PCI-6220 (slow) card through one of two CB-68LP I/O connector blocks, using an SHC 68-68LPM cable which were both manufactured by National Instruments.

The shielded wires used for the acquisition of the contact voltage were run from silver-graphic slip rings into an analogue input on the PCI 6250 card. The connector blocks were mounted in an enclosure in an effort to reduce the overall noise to which the system was exposed.

3.5.2 Description of Software

For the purpose of acquiring experimental data, programs were written by the author. The proprietary language used to interface with the hardware was National Instruments LabVIEW. National Instruments LabVIEW is a graphical programming language designed to function with National Instruments hardware. The language utilises a flowchart style code to allow users with little experience to build and implement test and control software quickly and simply. The development of a LabVIEW program or 'Virtual Instrument' (VI) is performed in two separate GUI windows. The code is built in a block diagram window where function blocks are connected with a series of 'wires' enabling the user to intuitively visualise dataflow. The plotting and 'display' of live data is performed through the front panel window where the

programmer can choose to fix various controls and indicators. The front panel display for the rig software is shown in Figure 3-17.

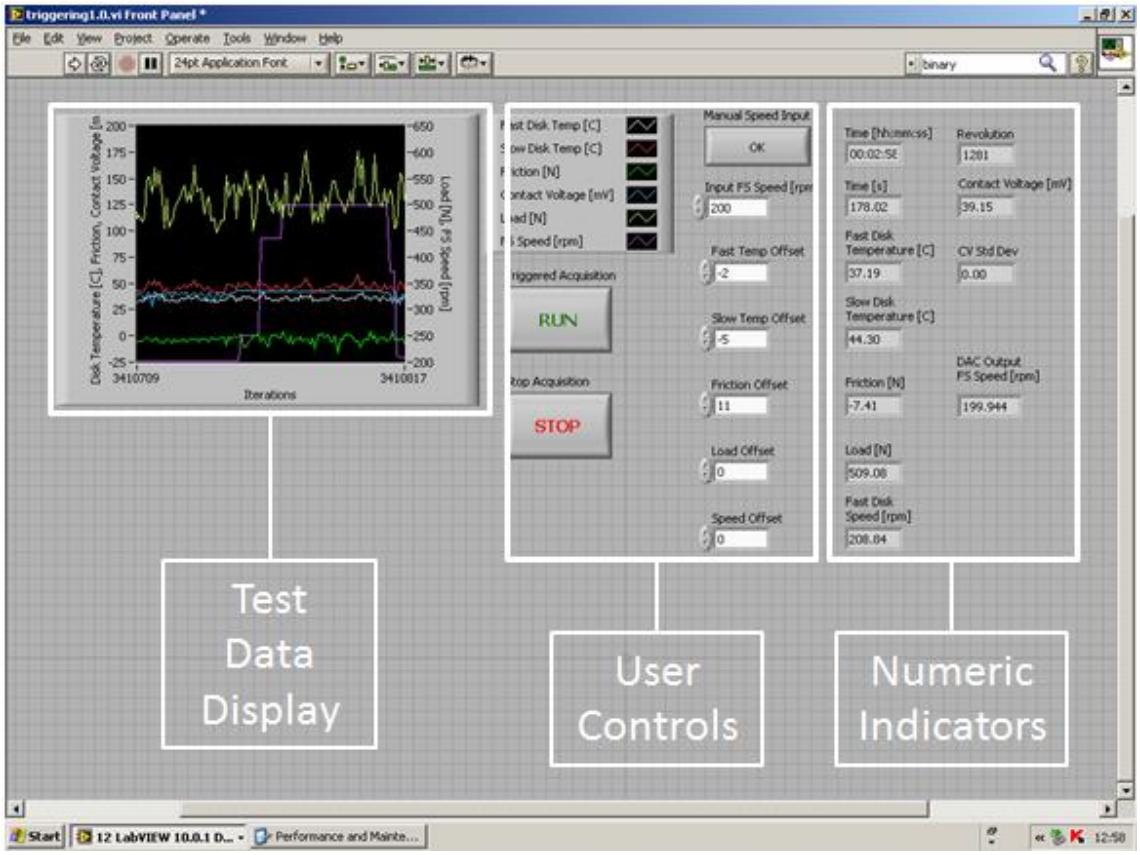

Figure 3-17 Screenshot of LabVIEW front panel for rig data acquisition software

Over the span of the project experimental data was acquired using a number of different LabVIEW VIs. This was driven by greater familiarity with the software, changing experimental focus and the introduction of new hardware into the system. Despite the constant updates and overhauls the software experienced, the purpose remained unchanged and the general procedure for acquisition remained similar. Due to the high amount of noise present in the laboratory environment and the large oscillation present in the thermocouple and strain gauge signals, it was necessary to average the data over enough samples and an appropriate time period so that the value reflected the bulk trends experienced by the system. This required the time period to be long enough to avoid detecting effects induced by minor load fluctuations and small enough to provide the sensitivity desired to show responsiveness under transient

conditions. A description will now be given of the most recent iteration of the rig software with which the results presented in Chapter 4 and 5 were produced.

3.5.2.1 LabVIEW VI

In order to reliably proceed with an investigation into relocatable contact voltage traces, it was necessary to consistently trigger data acquisition at specific locations. To do this, a once per revolution pulse on the rotary encoder was employed and the VI was designed around this purpose. The VI used several subroutines (sub-VIs) to make debugging the program less challenging. It was realised that sampling and saving large amounts of data every revolution would be challenging in terms of processing speed. As a result of this it was decided to use a producer-consumer architecture for the program, where priority would be given to data acquisition taking place in the producer loop. The saving and processing of data did not require the same strict timekeeping and was performed in the separate consumer loop which did not interfere with acquisition.

The contact voltage was sampled at the highest possible frequency of 1.25MHz on the PCI-6250 with the number of samples taken dependent on the speed of rotation. The purpose of this was to capture the maximum possible contact voltage samples whilst avoiding missing trigger pulses. In order to do this it was important to reserve a period of time for the producer loop to finish acquiring and queuing the data. The thermocouples, load cell, encoder and torque transducer were sampled on the PCI-6220 at a rate of 50kHz per channel. This allowed a maximum number of 100 samples per channel to prevent trigger pulses being missed at the highest speed. The basic function of each loop used in the acquisition of test data is shown in Figure 3-18. It can be seen in the flowchart describing the consumer loop that saving the contact voltage data requires the loop iteration I_n, which corresponds to the revolution number, to be a multiple of N_t. This provides the program with the ability to save only the revolutions that correspond to the same interacting areas of the disks. Where N_t is dependent on the ratio of the change gears.

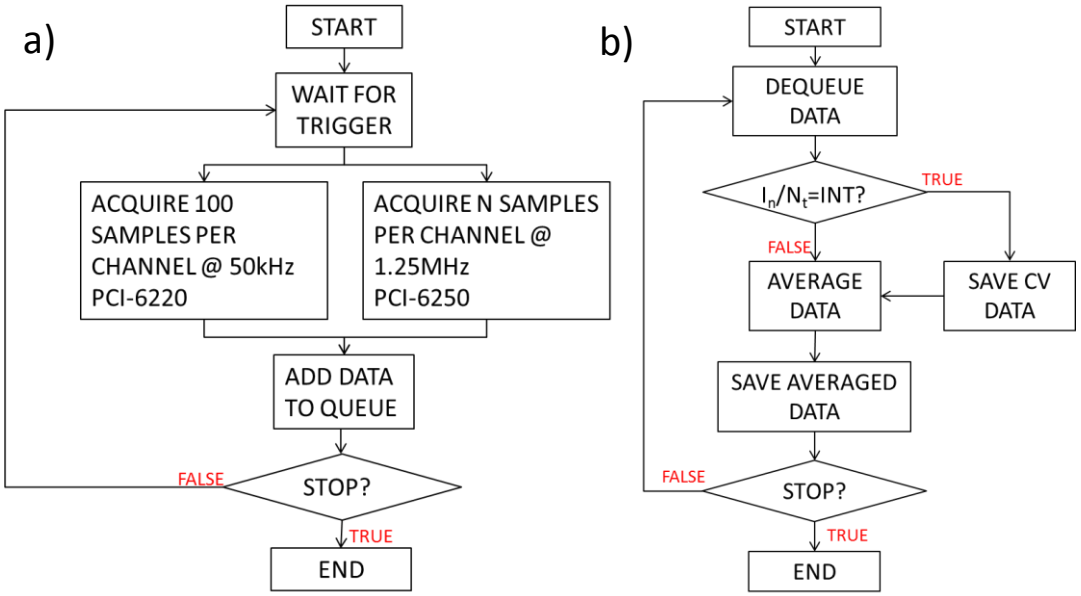

Figure 3-18 Flow charts describing operation of a) producer loop b) consumer loop

3.5.2.2 LabVIEW SubVI Motor Controller

A design feature of the LabVIEW VI was the integration of a motor controller sub-VI, this enabled the rig operator to program, or manually alter the speed once the rig was in operation. The speed of the motor was controlled by the inverter using a speed set point derived from 0 to 10V analogue input. For safety reasons, the maximum speed setting on the inverter was limited to the highest operating condition – which equated to a fast shaft speed 2000rpm - this would prevent over speed in the event of the user mistyping the commands. The minimum speed setting was a programmed as the lowest used in the experiments, which resulted in a fast shaft speed of 200rpm.

The LabVIEW code utilised the 12 digital IO ports available on the PCI-6220, these served as the input to a 12-bit digital to analogue converter, manufactured within the university for use with the rig. To protect the data acquisition system in case of a power surge, the D to A converter was fitted with opto-isolators.

With the maximum and minimum settings in place, the linear speed-voltage relationship is shown in equation (3.1) where the V_{Target} is the required voltage output from the D to A

converter to reach the desired speed, ω_{rpm}. The accuracy of this equation was checked using the shaft encoder signal.

$$V_{Target} = ((\omega_{rpm}/40)-4.8113)/4.5127 \quad (3.1)$$

In manual and pre-programmed mode, the VI would respond to a given speed demand by indexing through an array of values each equating to an input on the D to A converter and summing them to meet the closest value that would not exceed V_{Target}. With the automatic setting enabled, the user could pre-set a series of speeds and the times at which the VI would request them from the inverter.

3.5.3 Contact Voltage Signal Filtering

Initial investigations into high speed contact voltage measurements were conducted using superfinished disks that had been previously run. The purpose of this was to avoid using a new pair of ground disks which were required for future experiments. A test was performed at a fast shaft speed of 500rpm with the disks loaded to give a maximum contact pressure of 1.4GPa and the voltage between the disks was sampled at a rate of 1.25MHz. Figure 3-19 shows the resulting waveform obtained from the contact voltage channel. It is clear that a large amount of noise is present in the signal, the magnitude of which can be seen to greatly exceed the applied 43mV. Within this noise, however, it is also visible that a lower frequency waveform exists which can be seen to oscillate between 43mV and 0mV. The rapid fluctuation between the open circuit voltage and 0mV is in agreement with the results of earlier research where it was theorised that the behaviour of the signal was related to interaction between bodies (Courtney-Pratt and Tudor, 1946).

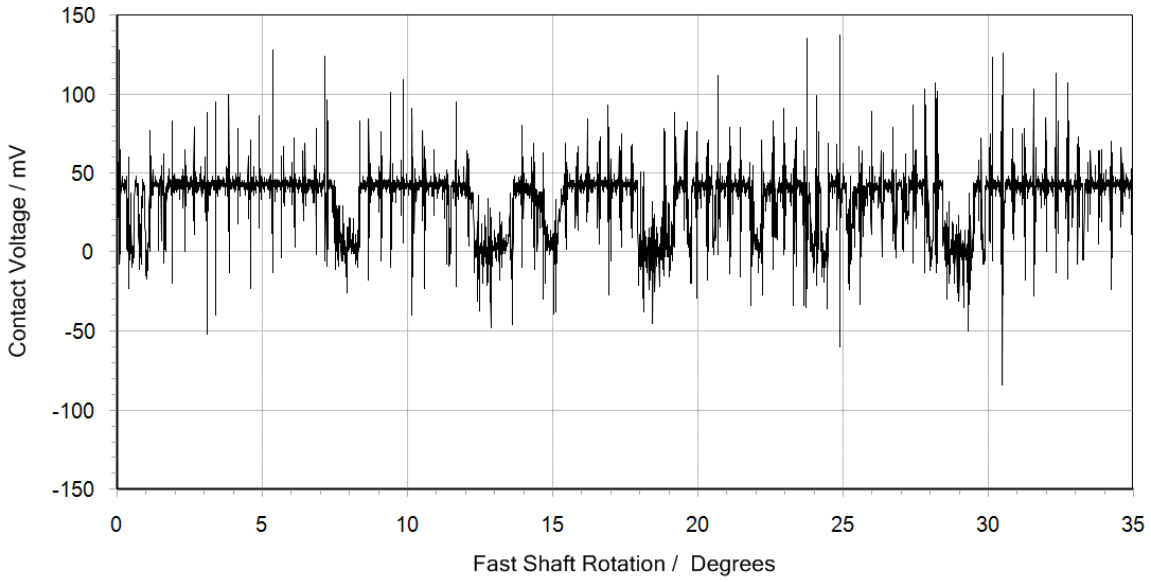

Figure 3-19 Inverter noise visible on contact voltage signal

After investigation, it was found that the inverter used to power the motor was the source of the electrical noise shown in Figure 3-19. After making every effort to reduce the level of noise by shielding the contact voltage signal wires it was decided to use a standard low pass filter function in LabVIEW to remove the interference in post-processing. The filter selected was a 3rd order Butterworth filter, which was used because it had zero ripple in the passband. A test was conducted employing a range of different cut-off frequencies to establish which could remove the noise without appreciably attenuating the fluctuations attributed to asperity interactions. Figure 3-20 shows the effect of experimenting with the cut-off frequency of the low pass filter used to filter the contact voltage waveform. Waveforms are offset from one another by 50mV for clarity. The test shows the same extract of the contact voltage channel sampled at 1.25MHz shown in Figure 3-19. Where a cut-off frequency of 150kHz was used, it can be seen that there is far less noise present on the waveform in comparison to the unfiltered signal shown in Figure 3-19. There is however still evidence of the periodic noise signal superimposed on the contact voltage waveform. As the cut-off frequency is further decreased it is apparent that the periodic electrical noise on the signal is greatly reduced and the larger fluctuations attributed to intermittent asperity interaction are left undisturbed. At a

cut-off of 30kHz, there is almost complete attenuation of the noise signal, however it can also be seen that some of the finer fluctuations have also been affected. This can be seen at approximately 1.8 degrees and also 33.3 degrees of fast shaft rotation on the 30kHz waveform shown in Figure 3-20. A compromise was decided where in order to preserve some of the finer detail in the waveform, a higher cut-off frequency of 50kHz was selected.

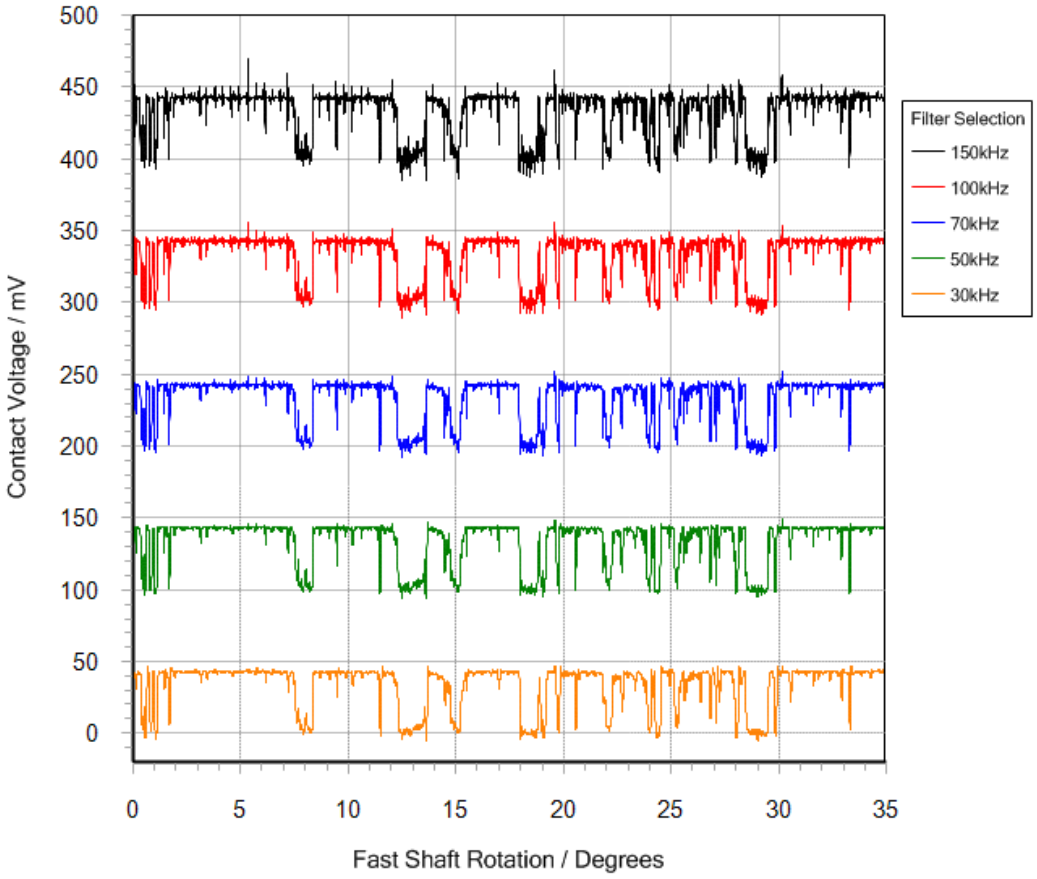

Figure 3-20 Different filter cut-offs offset for clarity, shown from top to bottom: 150kHz, 100kHz, 70kHz, 50kHz, 30kHz

After observing the effect of different cut-off frequencies on the contact voltage waveform, spectral analyses of the pre and post-filtering signals were undertaken and are shown in

Figure 3-21. It can be seen in the prefiltered frequency analysis shown in

Figure 3-21a that there is a significant amount of between 100kHz and 400kHz centred on 250kHz. Electrical noise at this frequency is produced by power inverters. There is also a lower

frequency region that is associated with the lower frequency behaviour of asperity interactions.

Figure 3-21b shows the results of the frequency analysis following the application of a 50kHz filter. It can be seen that the amplitude of the signal in the 250kHz region has been reduced significantly whilst leaving the lower frequency region of the waveform undisturbed. It can also be seen in Figure 3-20 that the 50kHz cut-off is the highest cut-off frequency removes the spurious voltages exceeding 43mV that can only be attributed to electrical noise present.

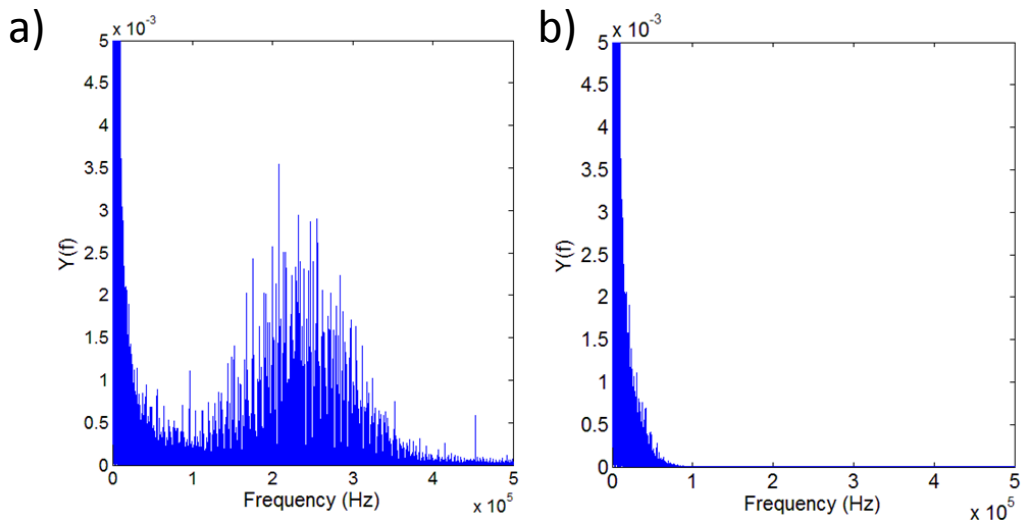

Figure 3-21 Spectral analysis of contact voltage signal a) before filtering b) after use of 50kHz filter

The acquisition of the fluctuating signal obtained from an EHL contact has been in the past associated with asperities interacting in the Hertzian region. It has been shown by Tudor where the electrical contact resistance of a journal bearing was acquired that these fluctuations show repeatability between consecutive revolutions, as discussed in Chapter 2 (Tudor, 1948).

However, to obtain repeatable measurements between running test disks, it was important to ensure that the encoder was employed so as to sample the contact during instances when the same regions of the surfaces interacted. This was dependent on the gear ratio used between

the test shafts. Where repeatable measurements have been presented in this work a gear ratio of 9:7 has been used with the power recirculating gears having 45 and 35 teeth producing a slide-roll ratio of 0.25 at the disk contact. At this gear ratio when the fast disk has completed exactly 9 revolutions the slow disk has completed exactly 7 revolutions. In order to sample trigger data acquisition at the same relative location on the disks, it was necessary to sample every 9^{th} fast disk rotation.

Repeatability experiments were conducted with disks that had been run in and achieved asperity shape stability as described in Chapter 4. It was found that when sampling the contact every 9^{th} revolution that repeatability could be seen between acquired signals. **Error! Reference source not found.** shows three traces of the contact voltage signal between running test disks taken 9 revolutions apart for 90 degrees of a fast disk rotation. Each trace displayed in **Error! Reference source not found.** shows the contact voltage signal fluctuating rapidly between high values of nominally 43mV and 0mV. The nature of these rapid fluctuations has been attributed to the highly dissimilar conductivity of the mineral oil relative to the metallic junctions made intermittently by asperity features between the surfaces (Furey, 1969). It is apparent that a large degree of similarity exists between the three traces where regions of high and low voltages can be seen to remain consistent between similar values of fast disk rotation. Examples of this can be seen from 36° to 61° where a region of relatively low voltage exists. Finer details can also be correlated between traces where regions of high and low voltage appear at the same positions between rotations.

There are however some inconsistencies, these are attributed to minor fluctuations in operating conditions such as applied load and speed variations introduced by vibrations occurring within the test rig.

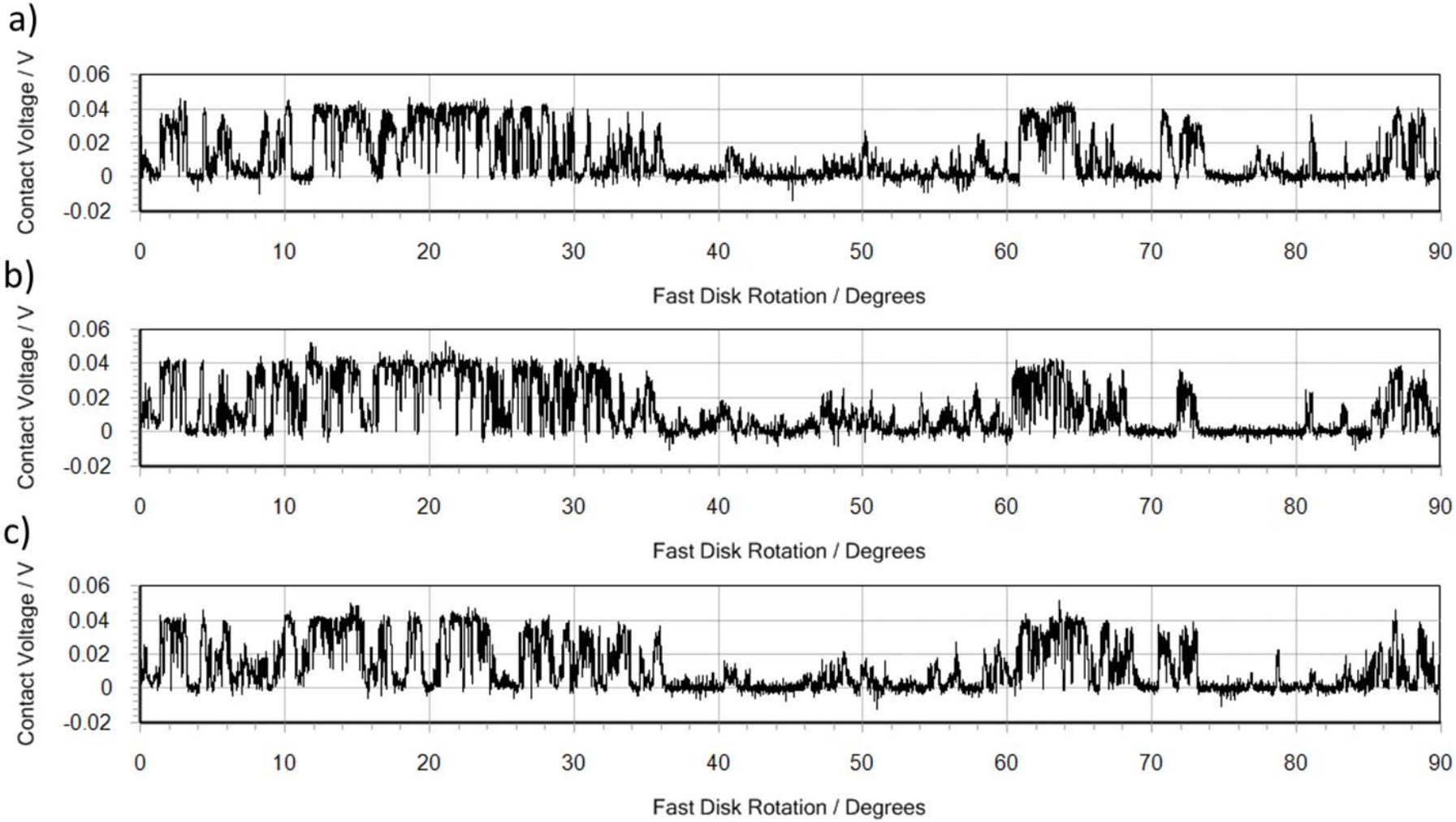

Figure 3-22 Contact voltage traces for a) 9th revolution b) 18th revolution c) 27th revolution. The test rig was run for a period prior to acquisition of displayed traces in order for temperatures to become nominally stable.

The ability to trigger data acquisition at an exact location on the fast disk allowed the observation of repeatable asperity contact events. When traces were sampled over an extended duration, these could be combined to create contour plots over which clear bands of different voltages across the traces could be identified; illustrating repeatability over a family of consecutive measurements. An example of a contour plot is shown in Figure 3-23. Consecutive traces are plotted adjacent to one another in the time axis and each trace extends in the y-direction. It can be seen that there are prominent bands spanning the plot in the x direction, indicating similar voltage values occurring at nominally the same relative position between traces acquired every 9 fast disk rotations.

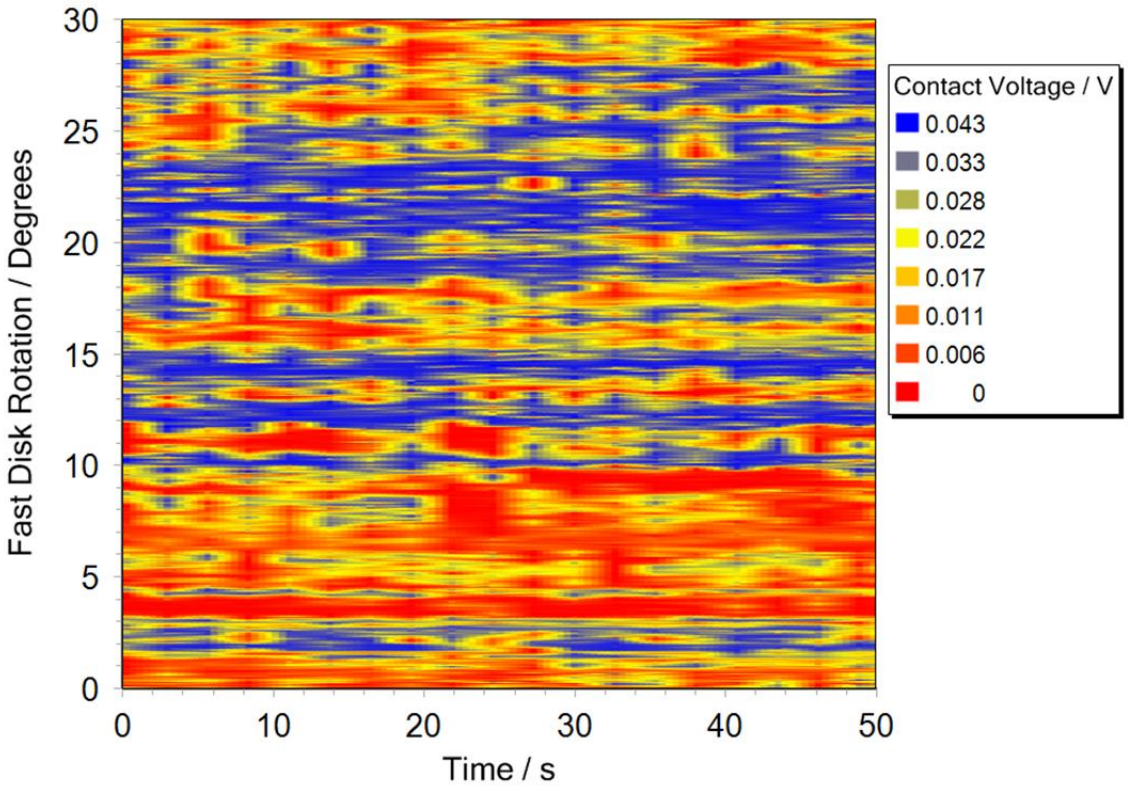

Figure 3-23 2D contour plot of superfinished disks running at 200rpm at 1.4GPa with data acquisition triggered every 9 revolutions

Figure 3-24 shows a 2D contour plot taken under the same conditions with the same pair of disks, however in this case sampling of the contact voltage channel occurred every 10 revolutions. In a similar manner to Figure 3-23, Figure 3-24 shows the contact voltage traces

rapidly fluctuating between high and low values. However, it is clear that where Figure 3-23 saw distinct banding in the x-direction, this is no longer apparent. This lack of conformity between adjacent traces is due to the triggering occurring at an interval inconsistent with the interval required to capture the same groups of asperities interacting. Figure 3-24 does however show some similar values occurring at the same angle of fast disk rotation periodically as time progresses. These periodic similarities are attributed to relatively aggressive asperity features on the fast disk entering the contact zone and interacting with the opposing surface.

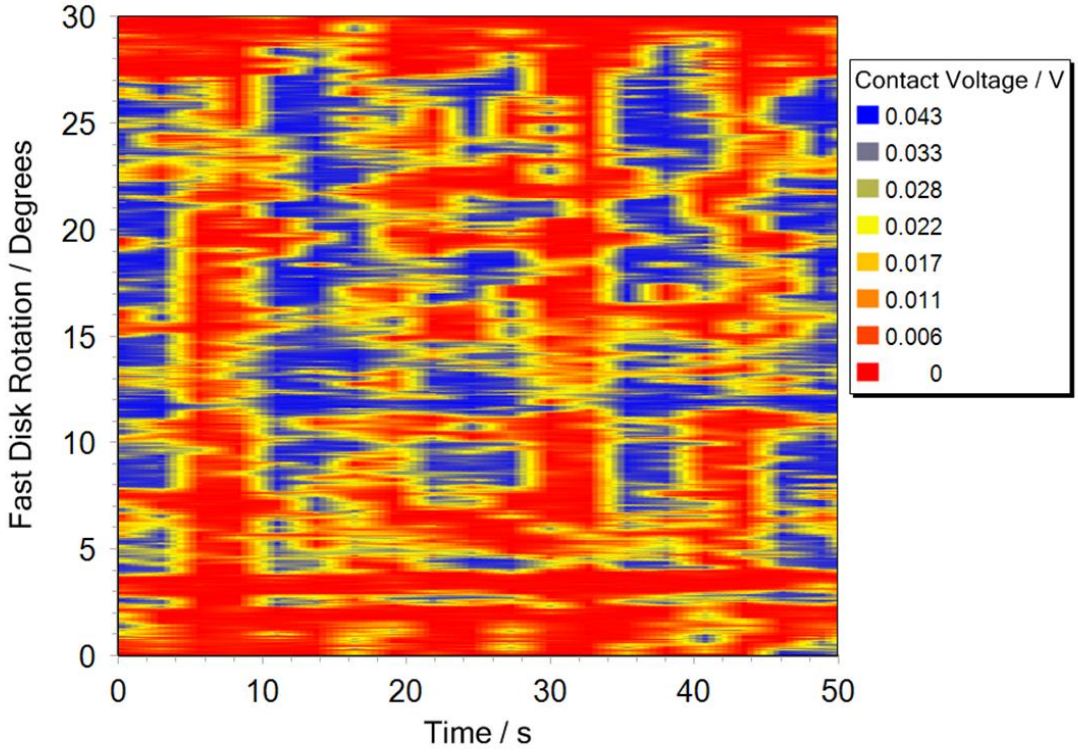

Figure 3-24 2D contour plot of superfinished disks running at 200rpm at 1.4GPa with data acquisition triggered every 10 revolutions

3.6 Discussion

The combination of a two disk test rig and purpose built data acquisition software allow the user to observe the fundamental conditions affecting and brought about by the EHL contact. Inclusion of the encoder provides the ability to observe repeatable fluctuations in contact voltage during the times in which the same sections of the rough surfaces enter and re-enter the contact zone together. In future work, comparisons of greater detail between contact voltage traces could be provided by access to more powerful computing tools. The user would then have the ability to draw contrast between traces run at different speeds with a proportional sampling speed, providing the same resolution at higher speeds.

Attaining in-situ profile measurement provides the user with running-in data, valuable for work into investigating plastic deformation within the research group. To provide more meaningful data for both finite element analysis and the numerical modelling work, a means of accurately measuring the corresponding surface so as to determine the alignment of individual interacting features would be beneficial. Early experiments by Tudor (1948) found that misalignment between interacting surfaces would result in increased metallic contact, the reason for this was later confirmed experimentally to be the tendency for asperities conform to their counterface as shown by Bishop and Snidle (1982). This tendency causes any relative movement between surfaces resulting in misalignment to affect levels of metallic contact. In the case of producing accurate simulations of real surfaces, these will therefore tend to overestimate contact levels unless surfaces have been previously run together at the same relative rotational positions to each other. Accurately relocating on the disks for profile measurement could perhaps be facilitated by the use of a Vickers indenter mark placed on the running track, creating a visible etch at various positions on the counterface. The use of existing instrumentation might also hold promise, using the shaft encoder – it could be possible to accurately track the relative position of the counterface and measure at an appropriate location.

The use of a strain gauged quill shaft as a torque transducer enables users to measure friction occurring due to shear stress at the contact more accurately. The measured friction coefficient can be used in conjunction with contact voltage measurements to build an accurate impression of the lubrication regime. Whilst other authors such as Guangteng and Spikes (1997) have combined these methods with spacer layer imaging experiments, giving quantitative values for film thicknesses across rough components, it should be said that the use of steel components is a more representative simulation of power transmission components. That being so, it could be useful to apply a similar method in attempting to validate and draw more accurate comparisons with film thickness values calculated from numerical models. The space layer imaging method could also be applied in parallel with the twin disk rig to give contact voltage values greater context.

3.7 Conclusions

The twin disk rig is a reliable tool that can allow for the simulation of a range of different EHL conditions on realistic engineering surfaces, the full expanse of which have not been covered in this work. Following the work of Davies (2005), further development of the contact voltage acquisition has allowed the author to introduce the technique well documented by Furey and others (Crook, 1957, Furey, 1969, Tallian et al., 1964, Courtney-Pratt and Tudor, 1946, Williams et al., 1988, Lane and Hughes, 1952) to add confidence to friction measurements.

Throughout this work, the test rig has been used primarily as a platform to generate large amounts of data for comparisons with numerical models being developed. The continuous improvement of the test rig in future research will prove an invaluable aid in both the continuing refinement of simulation work and furthering understanding of engineering tribology and mixed lubrication.

4 An Investigation into the Running In Process for Test Disks

4.1 Introduction

This chapter describes the process of running in for the test disks subjected to a maximum smooth surface Hertzian contact pressure of 1.7GPa in order to produce a stable unchanging surface topography with which to continue experimentation under variable speed and load. This helps furthering modelling work where the surfaces were subsequently measured for simulation purposes in the EHL point solver, as described in Chapter 6.

It was necessary to run the disks in thoroughly as the mixed EHL model used in this work does not yet include the effects of plastic deformation and hence will produce un-realistic results if "as manufactured" surface topography is used. As a useful by-product of this process, surface profile data was acquired at various stages of the running in process for future use by researchers investigating plastic deformation within the research group.

Profile data from the running in process was acquired from three pairs of test disks. Subsequently, it was discovered that the stylus used to attain the initial set of measurements was damaged – therefore profile data taken during the initial experiments were considered unreliable and these measurements have not been used by the author. All profiles reported within this work were acquired using an undamaged stylus.

The running in processes documented in this chapter are those for disk pairs of equal hardness where significant plastic deformation can be observed in both surfaces. In disk pairs where one of the surfaces is significantly harder than the other, the plastic deformation can be seen to take place almost entirely in the surface that has the lower hardness.

Results show that for disks of both equal and different surface hardness, plastic deformation of the most prominent asperities took place very rapidly, with the surface quickly attaining a stable and nominally unchanging topography.

For both sets of disks, it was found that there was tendency during the running-in process for asperities to become flattened into load bearing areas (referred to as “lands”), whilst leaving valleys relatively unchanged – a feature well documented in the literature (Bishop and Snidle, 1983, Østvik and Christensen, 1968). Measurements taken in this work appear to portray a slight tendency for valley features to rise. This feature of the results was considered to be primarily due to the filtering, where the proprietary software used would output results relative to a mean line which was recalculated for each surface. Other factors which may have influenced this could be a combination of material conservation where plastically deformed material is being redistributed to areas not in intimate contact as seen by Pullen and Williamson (1972), and a result of the relative dimensions between the stylus and valley features to some extent.

Profiles taken from experiments at a slide to roll ratio of 0.5 showed the formation of new valley features on both surfaces after a relatively low number of load cycles of the order 500,000 on the slower surface. These new valley features appeared to occur at the locations of previously observed asperities. Results for a cross correlation between the original surface and that which was measured following apparent fatigue damage implied greater change of these new features to occur in the slow surface.

4.2 Test Procedure

Test disks that were selected from an existing stock were engraved on their plane faces at four circumferential locations to aid relocation of the profile measurements. The specimens then had type J thermocouples fitted in the purpose drilled holes 3.17mm (1/8”) beneath the running tracks, as shown in Figure 3-15 Chapter 3. This was considered to be a location that would measure the bulk temperature of the disk without significantly influencing the bulk elastic properties of the surfaces. The thermocouples were then secured with two-part epoxy resin and the disks were pressed onto their respective shafts – giving a tight interference fit

and ensuring the disk was mounted concentrically onto the shaft. Care was taken to note the unique batch and serial number on each of the disks to avoid future confusion. To provide additional security, disks were then fastened to the shafts using a lock washer and lock nut. This configuration gave confidence that no significant axial movement would occur under test conditions. The shafts and disks were then cleaned by submerging them in solvent in an ultrasonic bath for 5 minutes to reduce the possibility of measurements being contaminated by residual debris.

After being cleaned, the test shafts were placed in their split bearing housings and the test disks aligned axially using a straight edge. Once the test shafts were fitted in the rig, care was taken to clamp them securely and ensure that all couplings were tightened. This was important in reducing any misalignment in results, which could lead to additional running-in (Tudor, 1948).

Tests were carried out with an oil meeting the OEP-80 performance specification (defence specification 91-74) pumped from the thermostatic bath at a feed temperature of 50°C. The general characteristics of the oil are shown in Table 4-1. The variation of absolute viscosity and pressure viscosity coefficient with temperature is shown in Figure 4-1.

Table 4-1 General characteristics of OEP-80 (defence specification 91-74)

Minimum viscosity at 100°C	8.0 cSt
Viscosity at 40°C	61.2 - 74.8 cSt

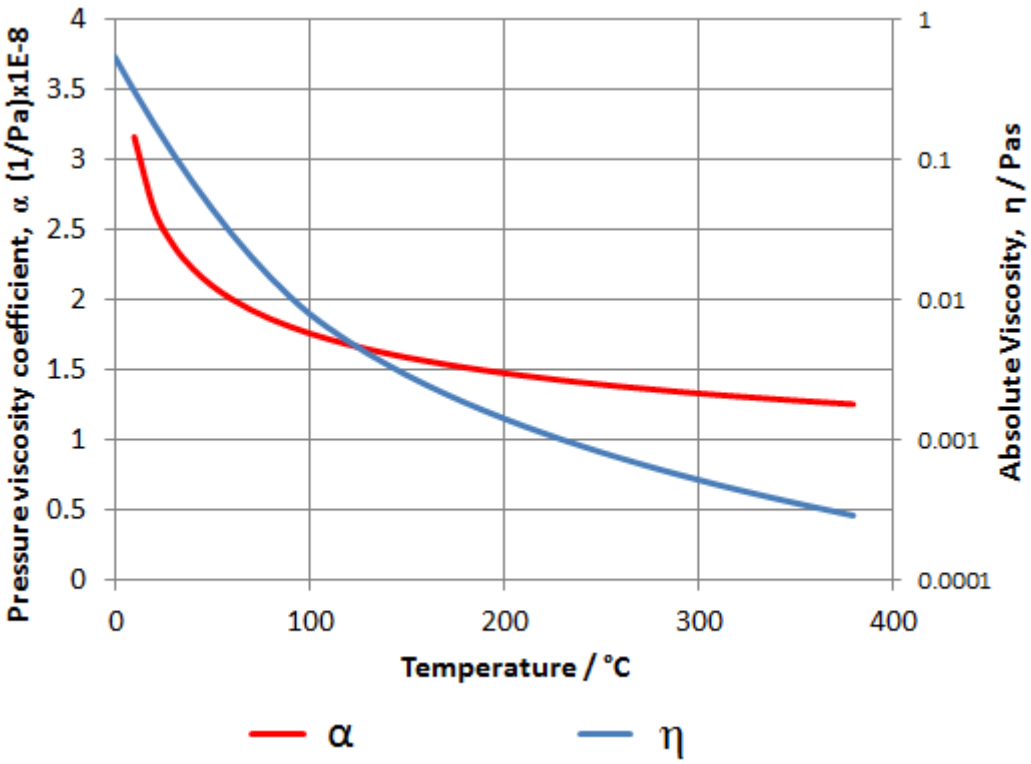

Figure 4-1 A graph of the variation of absolute visocity, η , and the pressure viscosity coefficient, α, with temperature for OEP-80

The oil was allowed to circulate through the test rig for 2 hours prior to experimentation with the rig running with no load applied to enable the temperature to stabilise and allow inspection of transducer signals. When the disks had reached the desired temperature, the load was set using the process described in Chapter 3.

The rig was run up to a fast shaft speed of 1500rpm and a load of 4150N, giving a maximum Hertzian contact pressure of 1.7GPa, was applied for approximately 27 seconds in all experiments with the exception of the first experiment using disk set B, where load was applied for 10 seconds. Once the test duration had elapsed, the load was removed manually, the rig was stopped and the data for the experiment was saved. The guard over the test head was unfastened and removed to allow air to circulate, cooling the disks.

When the temperature of the test specimens had returned to ambient values, profile data could then be collected for the load stage. The portable profilometer was set up and located on the stage. Residual oil was removed from the disks using degreaser and profiles were taken

according to the method described in Chapter 3. Both unfiltered and filtered profile data were saved for each surface in order to provide data for researchers investigating the effects of removing form and waviness on surface roughness measurements. For this work, the author used the Gaussian filter included with the proprietary software to remove form and waviness set with a cut-off of 0.25mm which is of the order of the Hertzian contact semi dimension in the rolling/sliding direction for the loads applied in the experiments.

4.3 Results for surfaces of equal hardness

Experiments were conducted on axially ground disks of similar hardness at a slide to roll ratio of 0.5. Three loading stages at 1.7GPa were conducted at a fast shaft speed of 1500rpm. Load was applied for a duration of 27 seconds in each of the cases, these data are described in Table 4-2. A significant increase in bulk disk temperature occurred as a result of the brief loading. Disk profiles of the unrun surface as well as intermediate data taken at the end of each loading stage were recorded throughout the process. The intermediate data allowed the gradual running in of the surfaces to be examined.

Table 4-2 Test data for running in load stages for hard-hard disk configuration

Load Stage	Load / N	FS Speed / rpm	Oil Temperature / °C	Duration / s	Fast Ra / µm	Slow Ra / µm
Unrun	-	-	-	-	0.318	0.365
1	4150	1500	50	27	0.261	0.274
2	4150	1500	50	27	0.262	0.272
3	4150	1500	50	27	0.264	0.275
18	-	-	-	-	0.234	0.236

4.3.1 Test data for disks of equal hardness

4.3.1.1 *Load Stage 1*

The test data for load stage 1, shown in Figure 4-2, shows the measurements of bulk disk temperatures, friction, rotational speed of the fast shaft and contact voltage. The load was applied at $t = 0$ and it can be seen that there is a transient response in the measurements of all but the speed curve which remains constant. The signals shown in the test data have been averaged over several revolutions to reduce the effect of noise.

Following the application of load there is a rapid increase in bulk disk temperature and friction over the length of the loading duration. It can be seen that the bulk disk temperatures rise steadily from the oil feed temperature of 50°C at $t = 0$, where the load is applied to approximately 90°C when the load is removed at $t = 27$s. The value of the fast disk

temperature can be seen to exceed that of the slow disk temperature by around 5°C at the end of the experiment. Over the 27 second duration, the measured friction also rises from a mean value of around 170N to a maximum of 215N at the end of the experiment. The contact voltage signal falls from a value of approximately 23mV to 17mV over the 27 seconds. This fall can be mainly attributed to an increase in disc bulk temperature reducing lubricant viscosity at the inlet and hence reducing film thickness, leading to more metallic interaction between the surfaces. Prior to the application of load at $t = 0$, it is apparent that the contact voltage signal, which is averaged over several revolutions maintains a high value of around 43mV. Before load is applied, no conduction path exists between the disks themselves and the signal is not indicative of the state of lubrication at the contact.

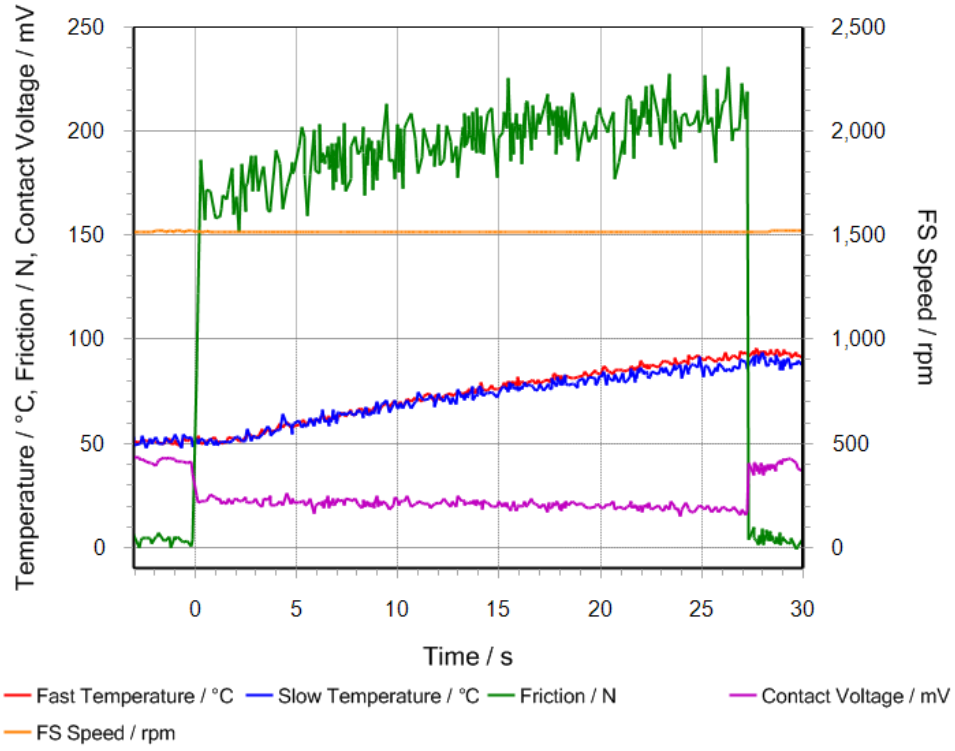

Figure 4-2 Test data for Load Stage 1 for rough disks of equal hardness at 1.7GPa at a SRR of 0.5

4.3.1.2 *Load Stage 2*

Examination of Figure 4-3 where the test data for load stage 2 is shown again demonstrates that the disks experience a similarly rapid increase in bulk temperature. The friction values are also seen to increase over the 27 seconds. The bulk disk temperatures rise from a feed temperature of 50°C to around 90°C at the end of the experiment in a similar way to Figure 4-2. There does however appear to be a smaller difference between the recorded disk temperatures at the end of the experiment in comparison to load stage 1. The friction occurring over the experiment in load stage 2 is generally lower than that of load stage 1. When load is applied at t = 0, it can be seen that Figure 4-3 has a mean friction value of approximately 150N, where Figure 4-2 has a value of 170N. Immediately before the load is removed, load stage 2 attains a maximum value of friction of 205N where it can be seen in Figure 4-2 that a maximum of 215N was attained. The contact voltage is seen to fall steadily over the length of the experiment, and lower values are achieved in comparison to Figure 4-2.

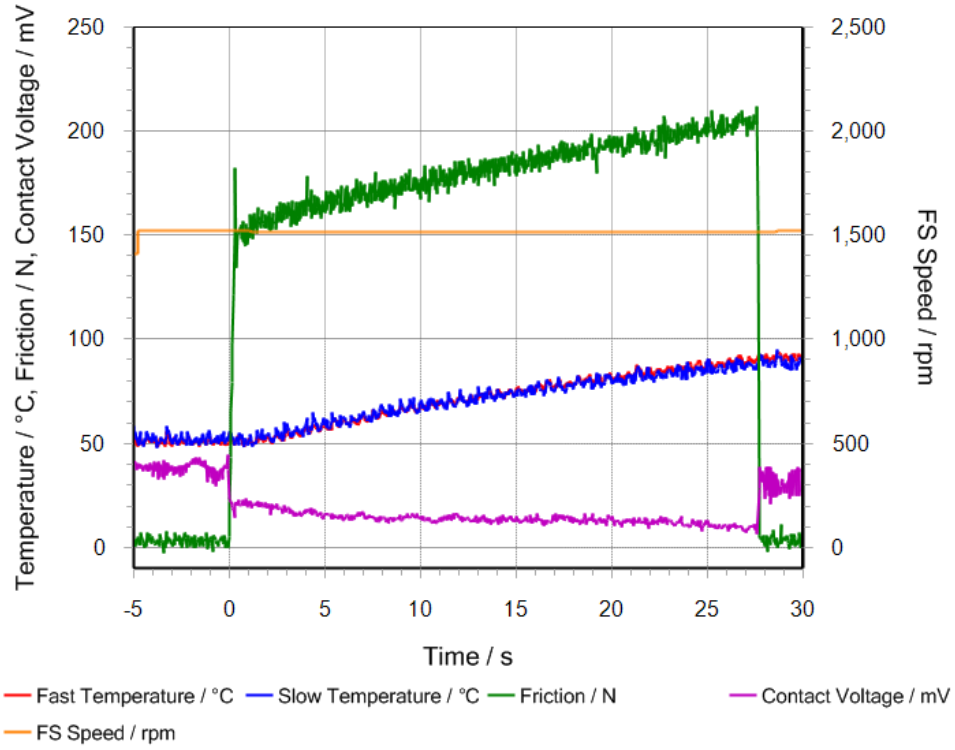

Figure 4-3 Test data for Load Stage 2 for rough disks of equal hardness at 1.7GPa at a SRR of 0.5

4.3.1.3 *Load Stage 3*

Load stage 3, plotted in Figure 4-4, exhibits a similar behaviour to load stage 2, with friction values increasing from 150N and attaining a maximum of approximately 200N at the end of the load stage. Bulk disk temperatures appear to attain a slightly lower maximum value of approximately 87°C in comparison to earlier load stages. The contact voltage appears to fall throughout the load stage to a minimum of 17mV. The first two seconds of the load stage appear to show relatively steady thermal response and also a steady contact voltage reading. The lag in thermal response reflects the fact that the thermocouples are positioned 3.17mm below the surface and is a feature of all the temperature measurements.

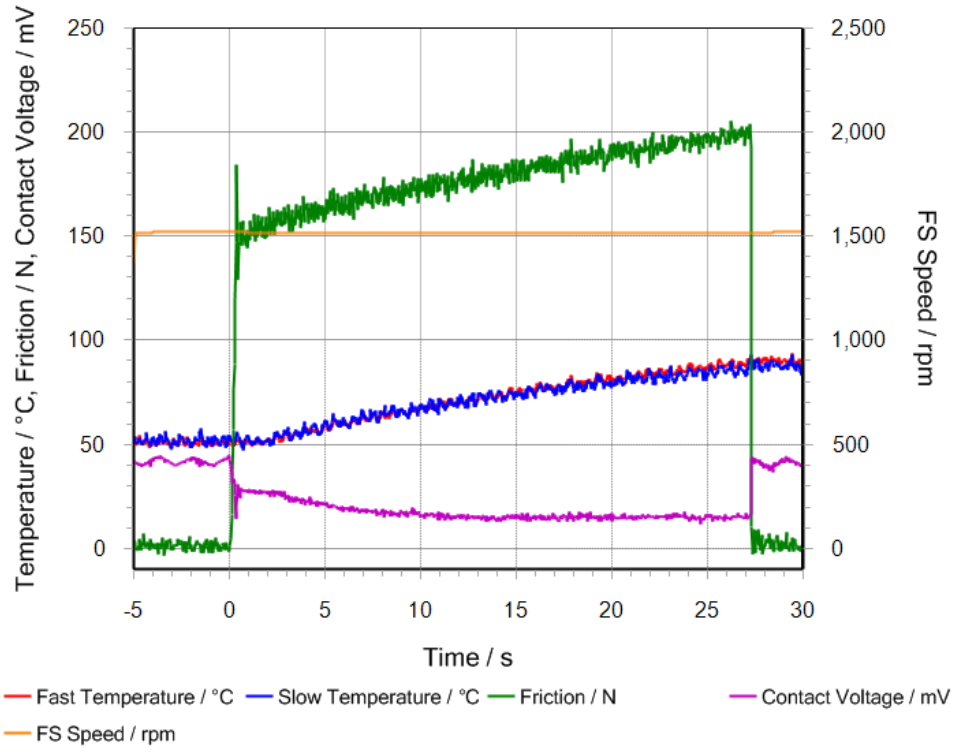

Figure 4-4 Test data for Load Stage 3 for rough disks of equal hardness at 1.7GPa at a SRR of 0.5

4.3.2 Profile data for disks of equal hardness

Profile data acquired from transversely ground disks of equal hardness showed the asperities on both surfaces becoming plastically deformed and reaching a nominally steady state with the valley features remaining relatively unaffected. Profile data showing the progressive modification of the surface topography for the fast disk is shown in Figure 4-5 and the slow disk is shown in Figure 4-6.

These disks were then used in the speed varying experiments discussed in Chapter 5, following which they were again measured and it was found that after a relatively modest number of load cycles a degree of fatigue had initiated. Profiles were taken at each of the four circumferential locations on each of the disks and traces shown are typical of results taken at each loading stage. Realigned profile data is compared in this section and its significance in relation to results from fatigue modelling are discussed.

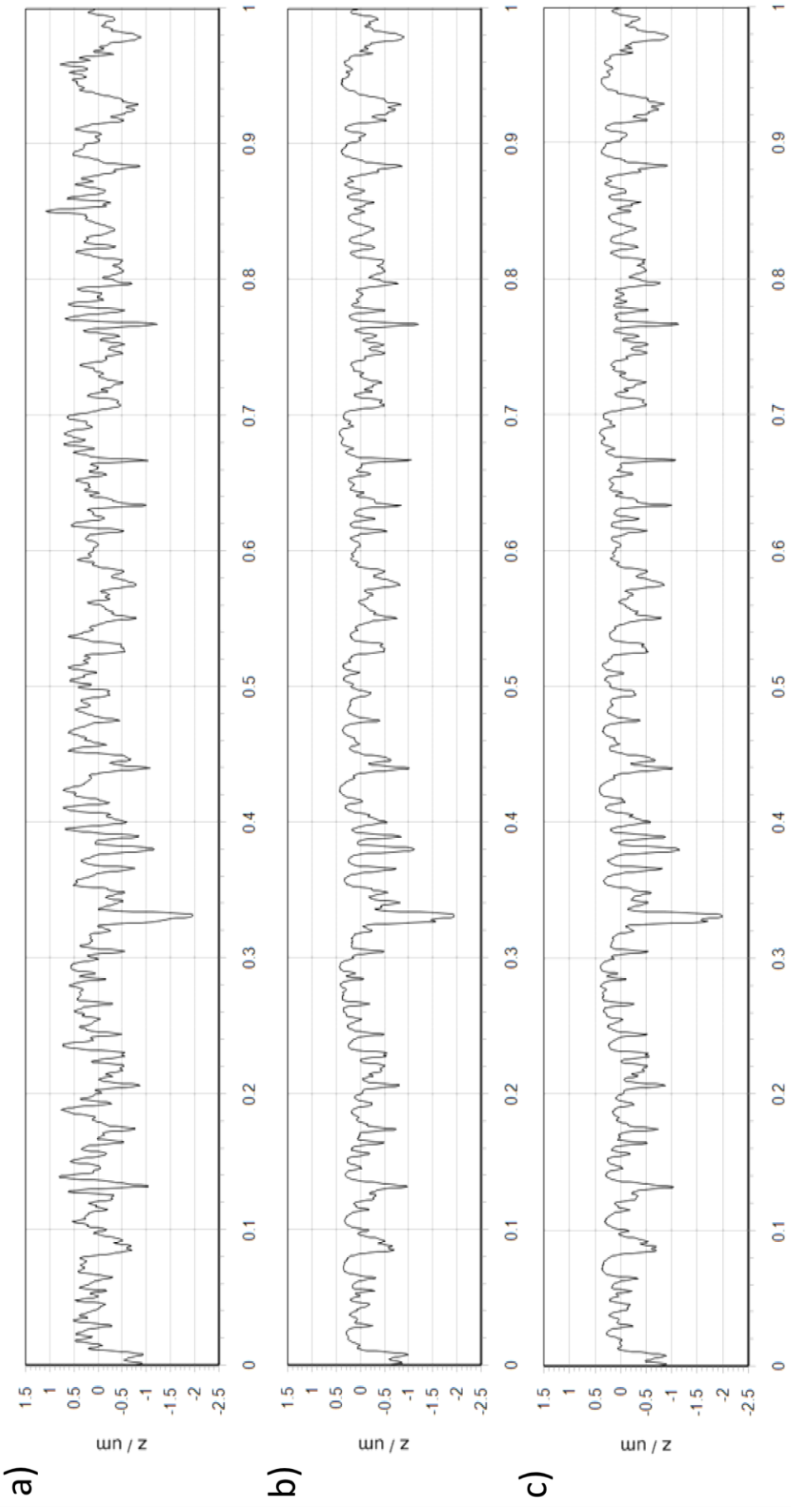

Figure 4-5 Profiles taken from 1mm section of fast disk for a) unrun surface b) load stage 1 c) load stage 3

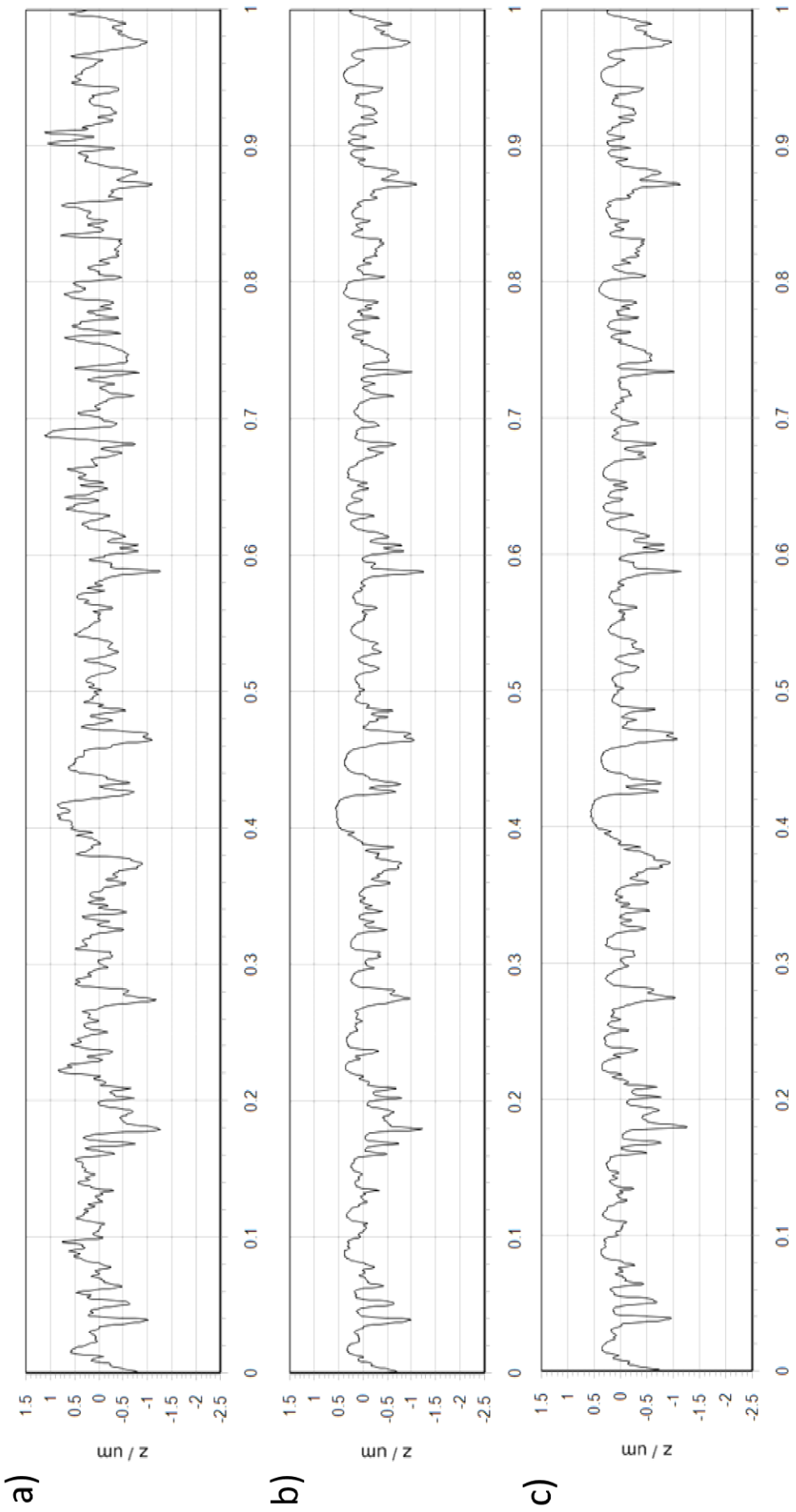

Figure 4-6 Profiles taken from 1mm section of slow disk for a) unrun surface b) load stage 1 c) load stage 3

4.3.2.1 *Load Stage 1*

Profile data from both the slow and fast disk are shown in Figure 4-5 and Figure 4-6 - it can be seen that a significant amount of plastic deformation occurs during the first load stage of both disks. The asperity features become almost uniformly flattened leaving rounded lands. The valley features however are shown to remain relatively unchanged as high localised loads occur predominantly between interacting asperities (Holmes et al., 2005b).

Figure 4-7 shows a more detailed comparison between the unrun surface topography, shown in black, and measurements taken following load stage 1, which are shown in red. The surfaces for presentation were realigned by adjusting the surface heights by subtracting a constant value from all measured surface heights on the modified profile. This would cause the whole profile to shift downwards so that the prominent valley features were nominally aligned vertically. This intervention was performed to counteract the fact that the filtering software calculates the mean line for each profile and these can differ. It is clear from comparisons of measurements where a gross amount of plastic deformation has occurred that adjusting the profiles to nominally realign valley features in the z direction provides a satisfactory result for presentation purposes. Realignment has been performed in this manner for all comparisons between profiles shown in this work.

On inspection of Figure 4-7, it can be seen that a large amount of modification occurs during load stage 1. The greatest changes occur at prominent asperity features. In particular, Figure 4-7a shows a large and isolated asperity at x = 0.125mm (A). Taking the valley features of the previous measurements as an acceptable datum point, this prominent feature experiences a change of height of approximately 0.8µm. Another prominent feature at x = 0.42mm (B) has a greater width than the feature occurring at x=0.125mm and does not experience the same level of modification, reducing in height by some 0.3µm. Similar features on the slow disk shown in Figure 4-7b are reduced in height, this can be seen where a peak aligned with x=0.225mm (C) is reduced in height by approximately 0.45µm. In general, asperity features on

both surfaces appear to experience a large reduction in height whereas valley regions do not appear to show any significant modification.

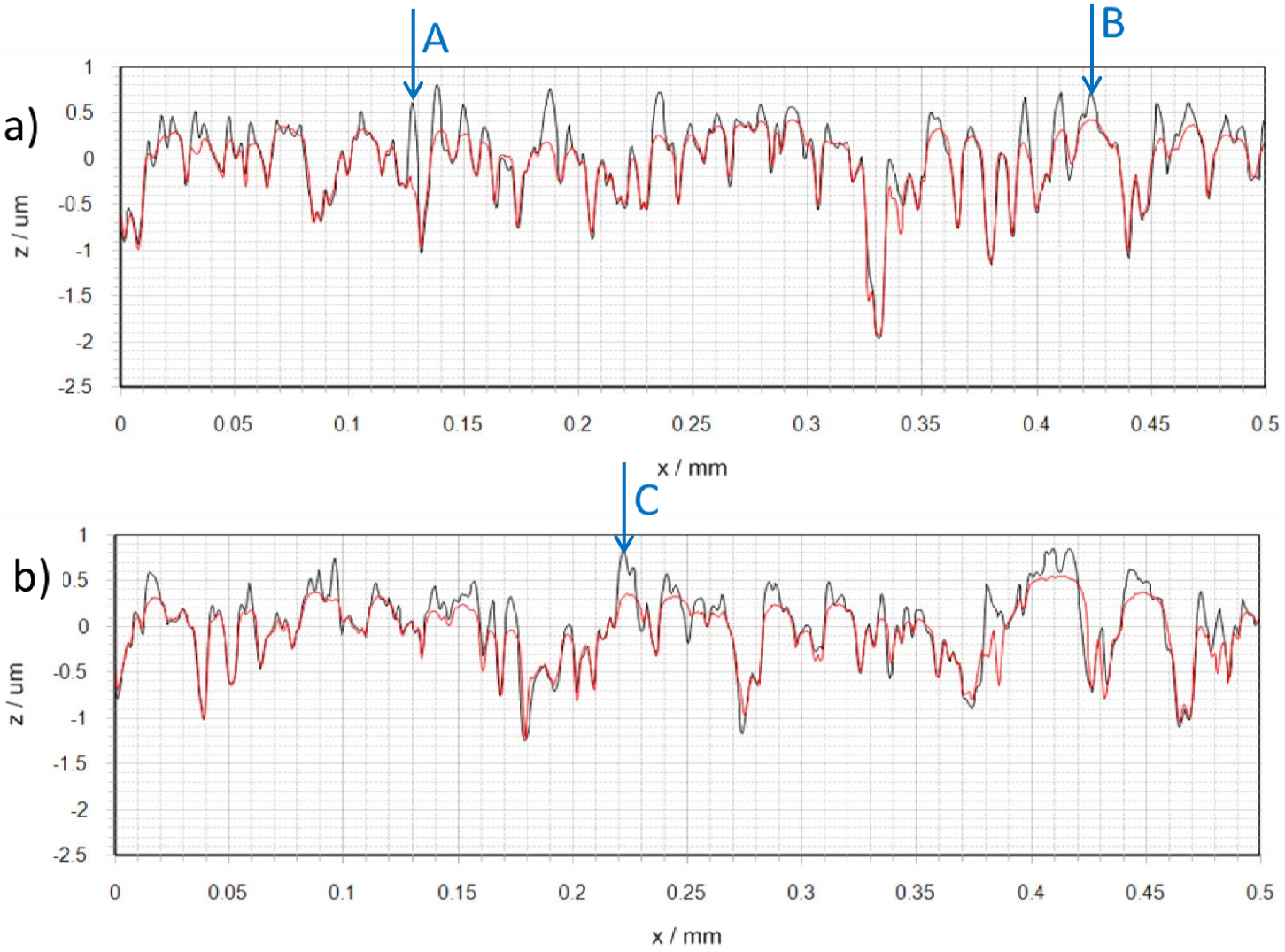

Figure 4-7 Load stage 1 shown in red superimposed on unrun profile for a) fast disk b) slow disk

4.3.2.2 *Load Stage 2 and 3*

Following a further 27 seconds of loading of the two surfaces, the asperities show comparatively little change. Running at a speed of 1500rpm, the surfaces have already experienced every possible loading combination at the gear ratio used and come into contact with the same portion of the counterface multiple times. The major asperities remain very closely aligned between measurements, and this demonstrates that plastic deformation occurs in the initial load cycles of the running-in process.

Similarly little plastic deformation appears to have occurred between load stage 2 and load stage 3. This can be judged by the close alignment between profiles taken following each load stage.

Comparisons between profiles taken following load stage 1 and load stage 3 have been made in Figure 4-8 where very close correspondence can be seen between the profile taken from load stage 3, shown in red and the load stage 1 profile, shown in black.

There are some instances where profile features appear not to align. These can be seen in Figure 4-8a at x=0.02mm (A) and x=0.336mm (B). Figure 4-8b also shows similar anomalies at x=0.38mm (C) and x=0.48mm (D). Reasons for inconsistency between measurements could be due to axial misalignment when using the profilometer between experiments. Alignment can still be made between the most prominent asperity features, but as the surface profiles are not perfectly axially extruded there is inevitably some variation in the axial direction.

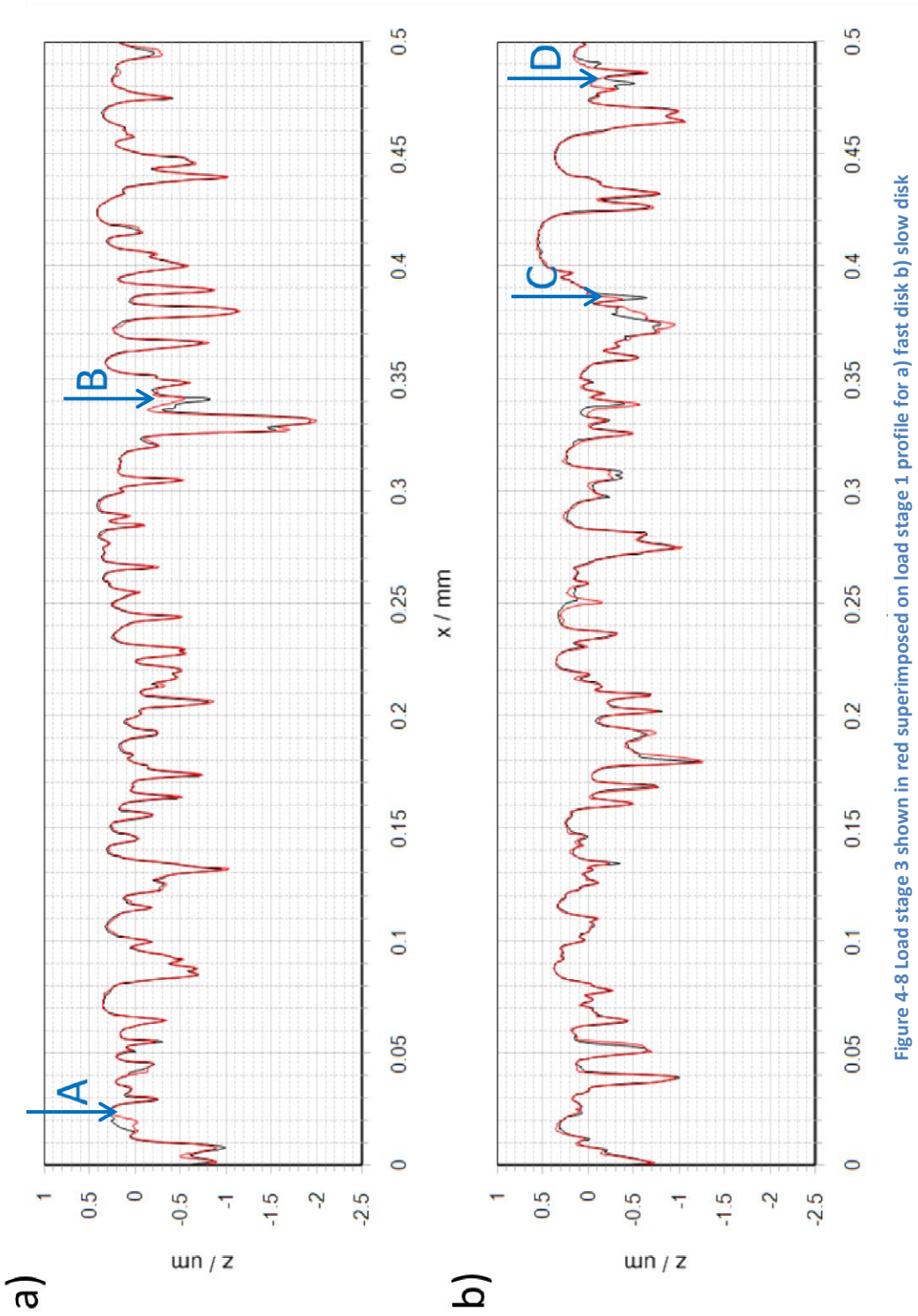

Figure 4-8 Load stage 3 shown in red superimposed on load stage 1 profile for a) fast disk b) slow disk

4.3.2.3 *Load Stage 18*

Surface profiles are now presented which were measured from the same pair of disks following the experiments described in Chapter 5.

The profiles measured following what was termed as load stage 18 appear to show a large amount of modification. It was believed that the profiles had attained a nominally stable condition following load stage 3 evidence of which can be seen in Figure 4-8. It is therefore considered that the change occurred during the new conditions experienced in the speed varying experiments. Unfortunately, due to time constraints profile measurements were not taken between experiments described in Chapter 5. Despite the change that appears to have occurred between profiles, it was still possible to align using valley features that did not experience the same level of modification.

The realigned profiles for load stage 3 and load stage 18 are presented in Figure 4-9. The surface topography can be seen to have altered quite substantially. Asperity features can be seen to have experienced further rounding and flattening, for example in Figure 4-9a at x=0.356mm (A) a small feature can be seen to have reduced in height by around 0.1µm and also at x=0.425mm (B) where a change of 0.12µm can be seen to have occurred. These changes have also taken place on the slow disk where in Figure 4-9b at x=0.295mm (C) a feature has undergone a change of 0.18µm.

Although examples of asperities becoming rounded following load stage 18 can be identified from the profiles shown in Figure 4-9, it is also clear that regions of the profile bear little resemblance to their load stage 3 counterpart. These features can be identified in Figure 4-9a at x=0.075mm (D) and x=0.275mm.(E) Similar features can be seen over the length of the profile shown in Figure 4-9b and are most apparent at x=0.005mm (F) and x=0.245mm (G). All stated examples share a common feature in that where prominent asperity features are shown in black, over prolonged running a prominent valley feature appears to have been created. The

measurement of new valley features did not occur in the earlier load stages where the predominant action appeared to be a uniform flattening and rounding taking place.

Inspection of valley features measured in Figure 4-9a at x=0.075mm (A) and x=0.275mm (B) show that the edges are closely aligned with those of previous valley features, with the maximum depth nominally aligned with the asperity peaks. This is also the case in Figure 4-9b where new valley features show close alignment with previous asperities.

The rounding of asperity peaks shown in Figure 4-9 is consistent with the running-in process, where a gradual flattening of peaks will occur. However, due to the large change occurring between some features shown in Figure 4-9, running-in cannot be considered the mechanism for this alteration as changes in measured surface height of over 1.0μm are seen. Due to these large isolated changes it is believed that surface fatigue is the mechanism causing these observed modifications, which are the result of the removal of material. In comparison to results of observed wear from disks of different hardness, it can be seen that finer features on asperities remain visible. It is also clear on inspection of the fatigued topography as measured by 3D profilometry, presented in Chapter 5, that the surface appears to have a 'pitted' appearance. In comparison to this, results for wear, also shown in Figure 5-32 in Chapter 5, do not have a pitted appearance. As such, the profile taken following load stage 18 will be referred to as the 'fatigued profile.'

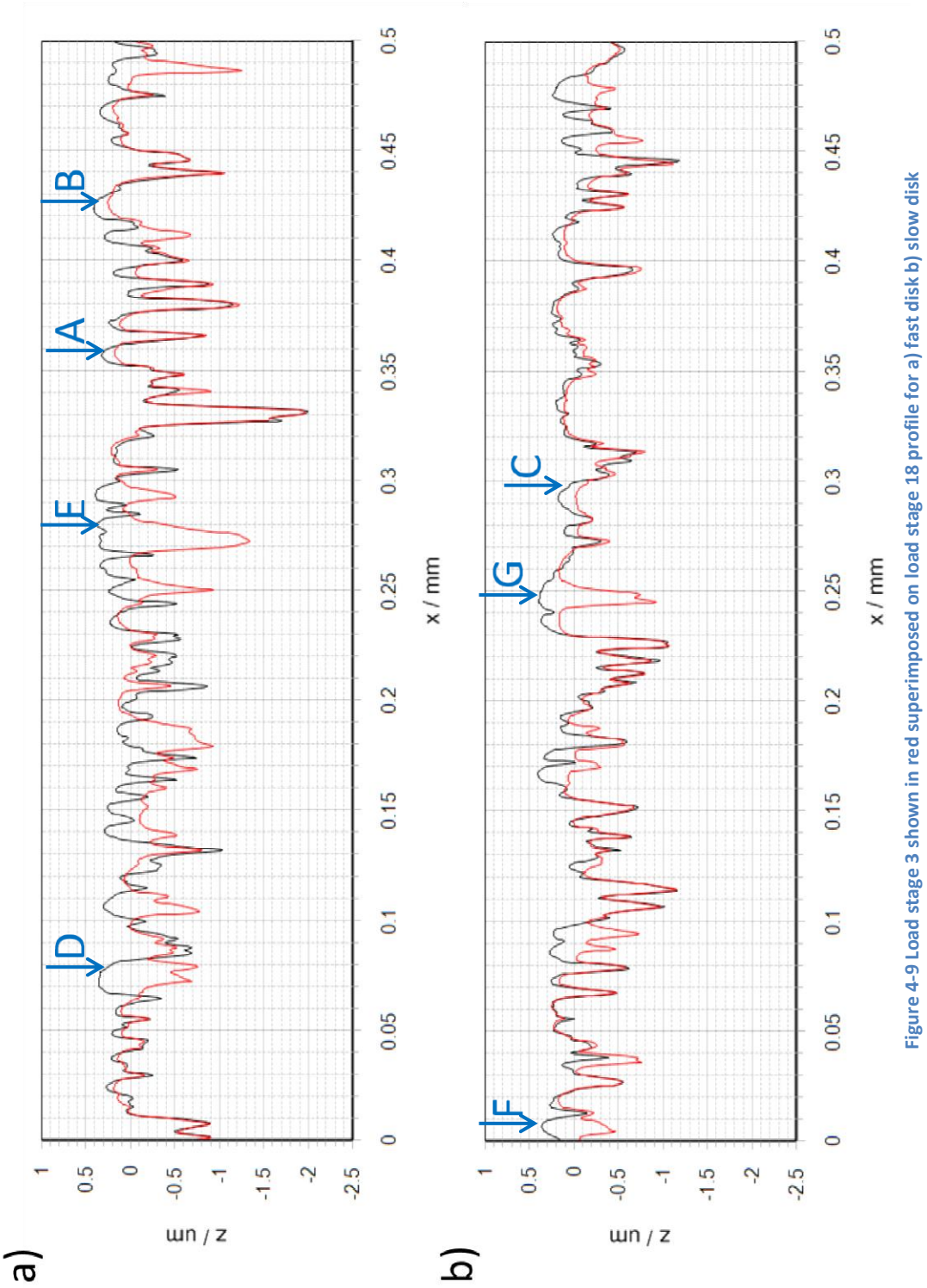

Figure 4-9 Load stage 3 shown in red superimposed on load stage 18 profile for a) fast disk b) slow disk

Figure 4-10 shows a smaller portion of fatigued profile realigned and superimposed against previous measurements taken from the unrun and the stable profile attained after the experiments described in this chapter. Note that where new valley features appear the surfaces cannot be realigned locally. However, these traces have been realigned considering the whole length of the profiles.

When realigned with the unrun surface, it appears that asperity features which undergo large initial plastic deformation are at risk of failure. Examples of this can be seen in Figure 4-10a where at x=0.187mm (A) the un-run profile, shown as dotted black, is flattened substantially by 0.55µm and after sustained running gives way to a valley at a position of z=-0.93µm. Another demonstration of this can be seen on Figure 4-10b where at x=0.243mm (B) a very prominent asperity feature on the un-run profile is flattened by approximately 0.7µm. Sustained running of the profile resulted in the creation of a valley at a depth of z=-0.91µm.

Figure 4-11 presents longer sections of the same superimposed profiles. Close inspection of the new valley features appear to show a degree of offset between newly formed valley features and run in asperity peaks. To highlight this, blue arrows have been drawn with the arrowheads of the dashed shafts carefully aligned with the valley features of the fatigued profile and the solid arrows aligned with the peaks on the stable profile. In Figure 4-11a these can be most clearly identified at x=0.17mm (A) and x=0.275mm (B). Figure 4-11b also clearly shows an offset at x=0.257mm (C). The direction of offset of new valleys from former asperity features appears to be dependent upon the surface, suggesting an association with traction or the sliding direction.

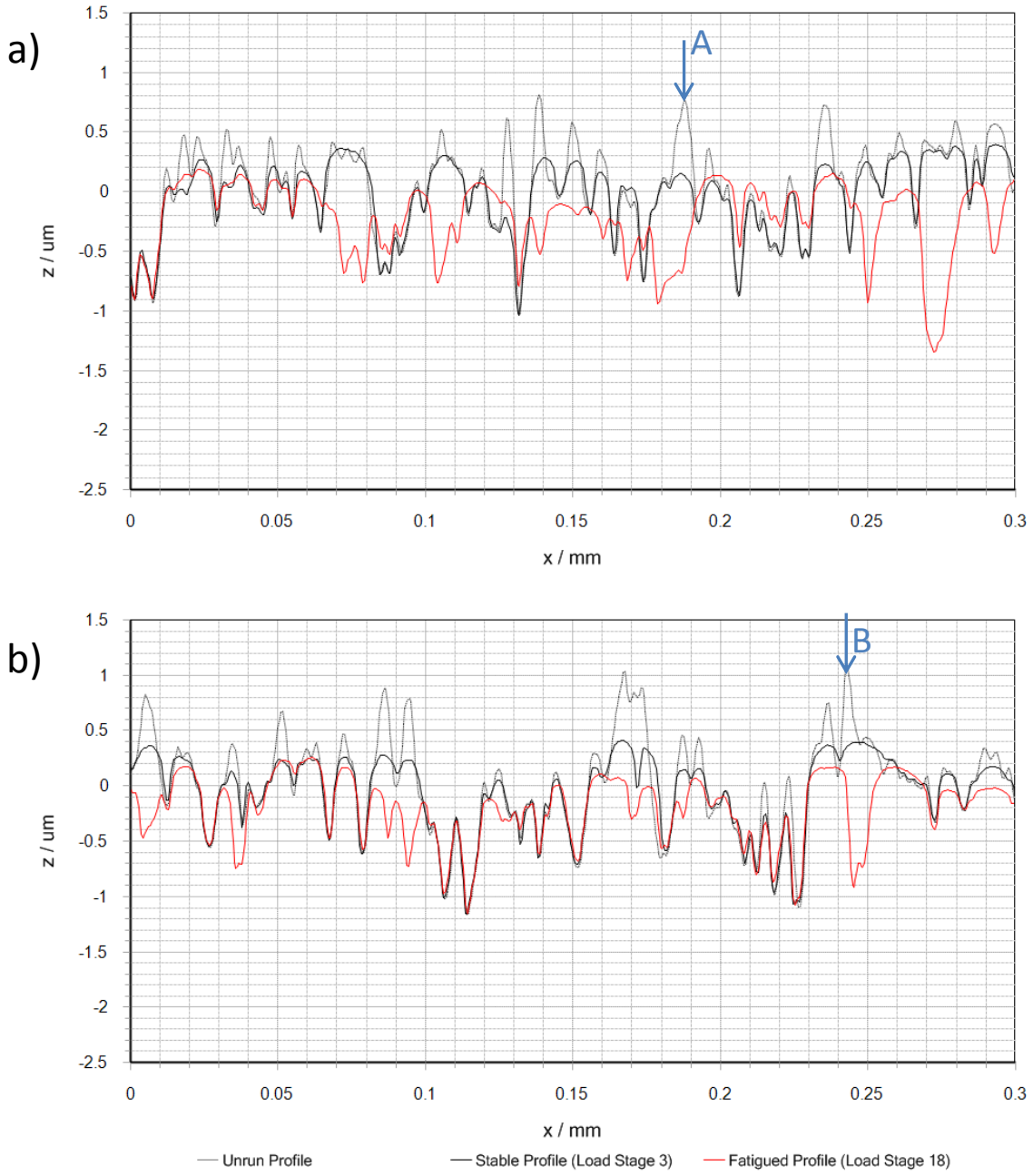

Figure 4-10 Realigned profiles superimposed demonstrating relation of new valley features in relation to former asperities a) fast disk b) slow disk

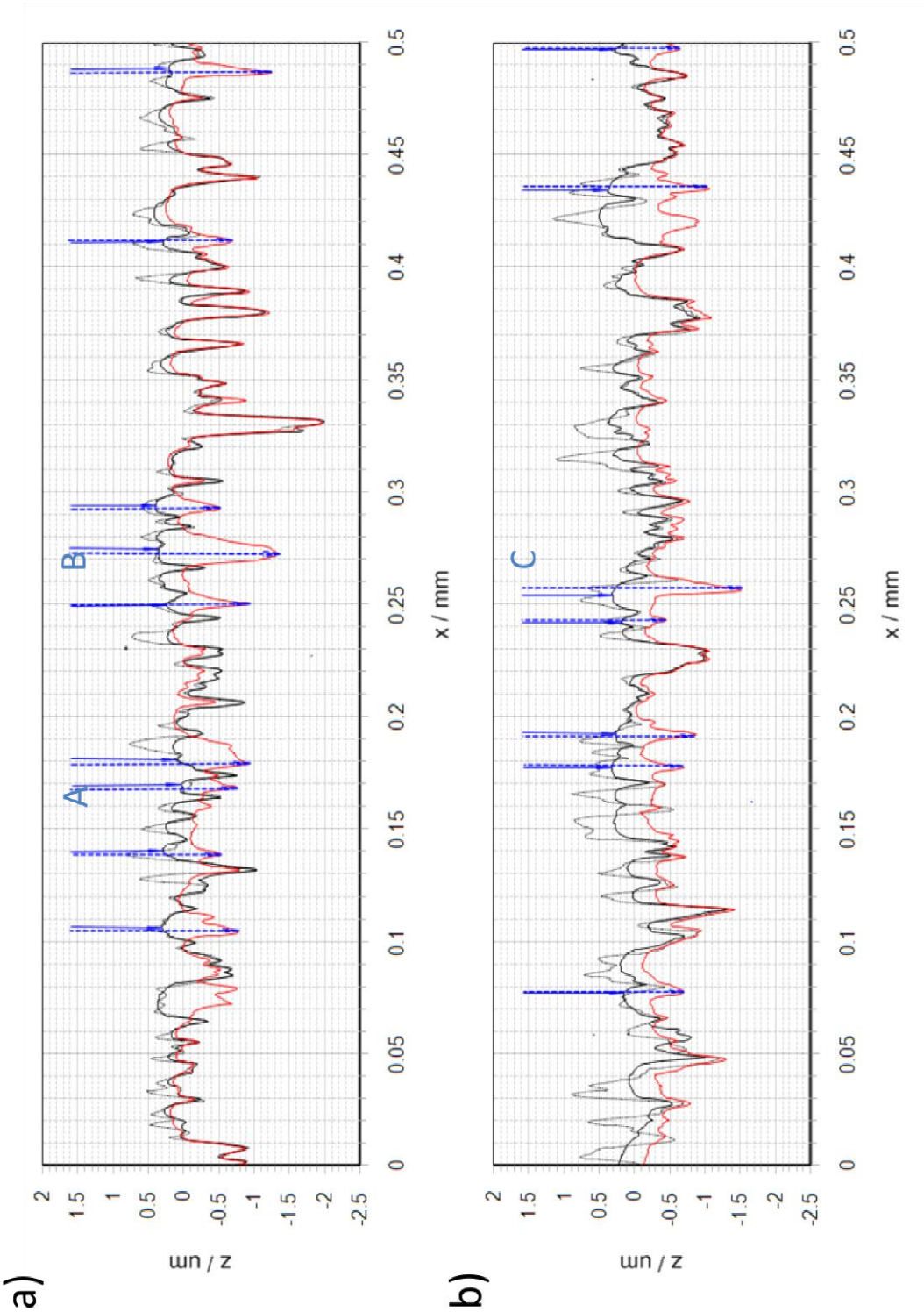

Figure 4-11 Superimposed profiles showing fatigued profile (red) stable profile (black solid) unrun (dotted) with arrows to indicate offset of damage from former asperities a) fast disk b) slow disk

4.3.2.4 *Cross Correlation Values*

Values for cross correlation between profile measurements have been calculated in an attempt to quantify the level of fatigue present on the surfaces. The values for the fast disk are presented in Table 4-3 and values for the slow disks are shown in Table 4-4. These show the level of correlation between the un-run surface and profiles taken at nominally the same location at different stages of running realigned by maximising the cross correlation value. The values for cross correlation describe the modification in surface topography between load stages. Calculated values for cross correlation did not appear to vary significantly between locations and therefore the presented values can be considered to be representative of the entire surfaces. An averaged value for cross correlation is calculated for each load stage from the three profiles taken at each of the four circumferential locations. A description of the profile measurement positions has been given in Chapter 3.

Table 4-3 shows values for the maximum cross correlation for surface profiles with the measurements taken before running. The table shows values taken for different circumferential positions, indicated by M1 through to M4. Indexes 1 to 3 indicate different axial offsets. It can be seen that for the first three load stages shown in Table 4-3, little modification occurs, with the correlation maintaining an average value of approximately 0.9. Following additional running and the initiation of fatigue it can also be seen that the correlation with the original surface drops to an average value of 0.57.

Table 4-3 Values for maximum cross correlation between un-run profiles and profiles taken at each load stage for different circumferential and axial locations on the fast disk

	Index 1				Index 2				Index 3				
	M1	**M2**	**M3**	**M4**	**M1**	**M2**	**M3**	**M4**	**M1**	**M2**	**M3**	**M4**	**Average**
Load Stage 1	0.877	0.900	0.917	0.920	0.872	0.860	0.919	0.921	0.832	0.887	0.893	0.926	**0.894**
Load Stage 2	0.872	0.870	0.930	0.894	0.867	0.850	0.916	0.897	0.835	0.875	0.915	0.902	**0.885**
Load Stage 3	0.874	0.910	0.943	0.916	0.883	0.894	0.925	0.911	0.895	0.914	0.900	0.921	**0.907**
Load Stage 18	0.481	0.642	0.662	0.532	0.509	0.590	0.685	0.434	0.503	0.573	0.636	0.529	**0.565**

Table 4-4 shows the cross correlation values for the slow disk. It can be seen that like the fast surface, the topography remains relatively stable from load stage 1 to load stage 3 with the cross correlation having a nominal value of 0.83, a lower value in comparison to that of the fast surface. After fatigue was seen to initiate on the surface, the correlation value drops below that of the fast surface to 0.45, indicating a significant change in the measured profiles due to fatigue.

Table 4-4 Values for maximum cross correlation between un-run profiles and profiles taken at each load stage for different circumferential and axial locations on the slow disk

	Index 1				Index 2				Index 3				
	M1	M2	M3	M4	M1	M2	M3	M4	M1	M2	M3	M4	Average
Load Stage 1	0.830	0.867	0.796	0.810	0.856	0.854	0.792	0.833	0.852	0.840	0.809	0.801	**0.828**
Load Stage 2	0.828	0.856	0.792	0.820	0.852	0.838	0.815	0.847	0.839	0.828	0.807	0.808	**0.828**
Load Stage 3	0.844	0.863	0.790	0.823	0.860	0.834	0.809	0.851	0.853	0.839	0.824	0.815	**0.834**
Load Stage 18	0.486	0.515	0.382	0.463	0.434	0.515	0.434	0.398	0.467	0.441	0.364	0.438	**0.445**

Shown in Table 4-5 are cross correlation values calculated between the stable profile and the fatigued surface. The purpose of this was an attempt at isolating the impact of fatigue on the correlation by reducing the influence of the plastic deformation. However, it can be seen from profile measurements that a degree of plastic deformation did occur along with the fatigue seen after load stage 18. Values for cross correlation again show a lower average value for the slower surface than that of the faster surface, suggesting more modification. This is an interesting result as the faster surface undergoes 66% more load cycles.

Table 4-5 Values for maximum cross correlation between profiles taken after load stage 3 and fatigued profiles for different circumferential and axial locations on the both disks

	Index 1				Index 2				Index 3				
	M1	M2	M3	M4	M1	M2	M3	M4	M1	M2	M3	M4	Average
Fast Disk	0.590	0.728	0.711	0.603	0.580	0.691	0.739	0.506	0.606	0.650	0.718	0.587	**0.642**
Slow Disk	0.604	0.604	0.519	0.601	0.558	0.624	0.580	0.519	0.580	0.558	0.522	0.564	**0.569**

4.3.3 Height distributions for surfaces of equal hardness

Using the measurements gathered from the Talysurf profilometer, histograms representing the distribution of surface heights were produced to summarise the data for each load stage. Surface heights were calculated in terms of standard deviations. This was achieved by dividing the surface heights by the standard deviation of the all measured heights for each load stage. Values were then organised into equally sized bins with the distribution normalised and superimposed on a Gaussian distribution curve having the same mean and standard deviation for comparison.

For the distributions calculated, the data are shown in Table 4-6, where it can be seen that over the course of running, the distribution of surface heights is seen to decrease as asperities become flattened and data becomes more clustered about the mean. The values of skewness and kurtosis are also included in the table. Skewness is a measure of the asymmetry in the height distribution. Distributions also become increasingly skewed as a result of the flattening.

Table 4-6 Roughness distribution data for test disks of similar hardness

Load Stage	Disk Position	Standard Deviation / µm	Skew
Unrun	Fast	0.404	-0.502
	Slow	0.480	-0.135
1	Fast	0.335	-1.066
	Slow	0.357	-1.321
2	Fast	0.335	-1.062
	Slow	0.354	-1.254
3	Fast	0.338	-1.078
	Slow	0.360	-1.325
18	Fast	0.308	-1.332
	Slow	0.322	-1.735

Frequency histograms, f(h) were plotted for the un-run surface and are shown in Figure 4-12 and Figure 4-13 for the as manufactured surfaces. These demonstrate distributions approximately similar to the superimposed Gaussian curve. Subsequent load stages whose histograms are shown in Figures 4-13 to 4-18 do not have the same impact on the form of the distribution, for that reason load stage 2 has been omitted from the figures presented.

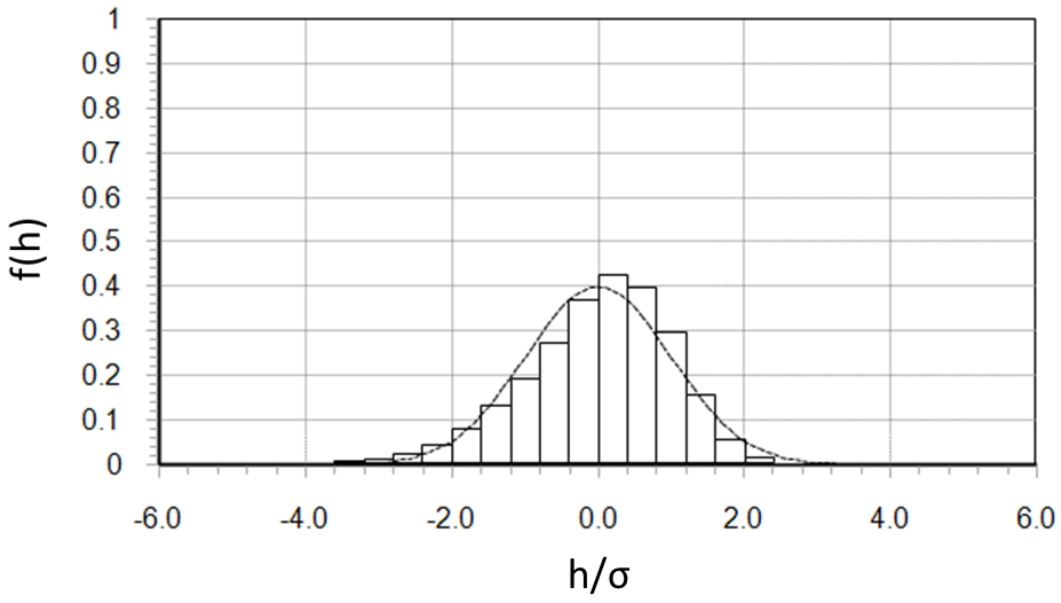

Figure 4-12 Histogram of surface heights for un-run fast disk with Gaussian distribution curve (dashed)

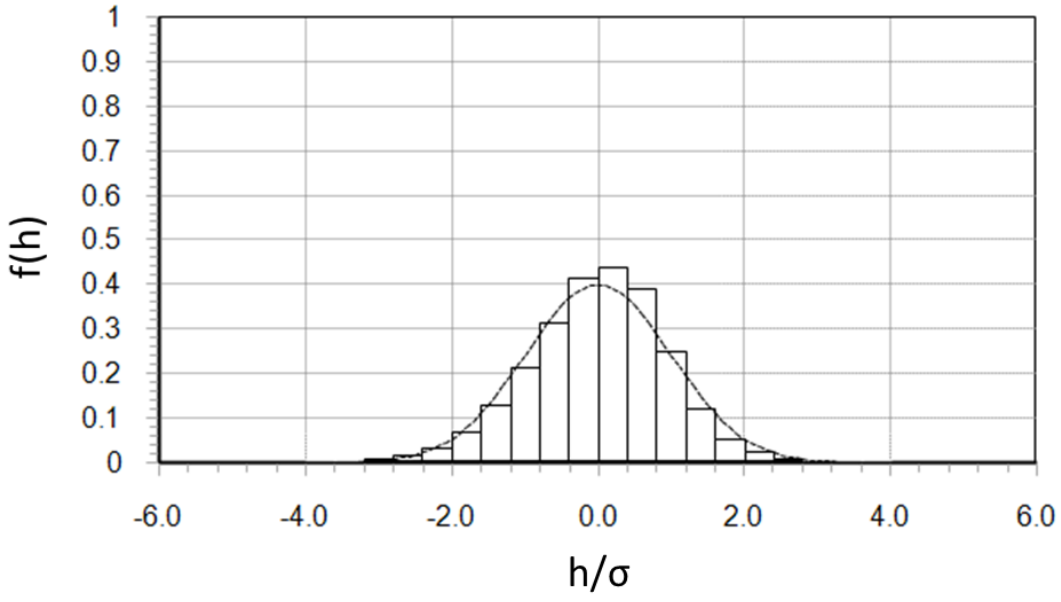

Figure 4-13 Histogram of surface heights for un-run slow disk with Gaussian distribution curve (dashed)

The histograms for the initial load stage are shown for the fast and slow surface in Figure 4-14 and Figure 4-15, respectively. The initial load stage can be seen to heavily skew the surfaces with asperity peaks becoming deformed on both surfaces and the positive tail of the distribution experiencing a reduction. It can be seen that the negative tail does not change significantly as the surface modification occurs primarily at the asperity tips.

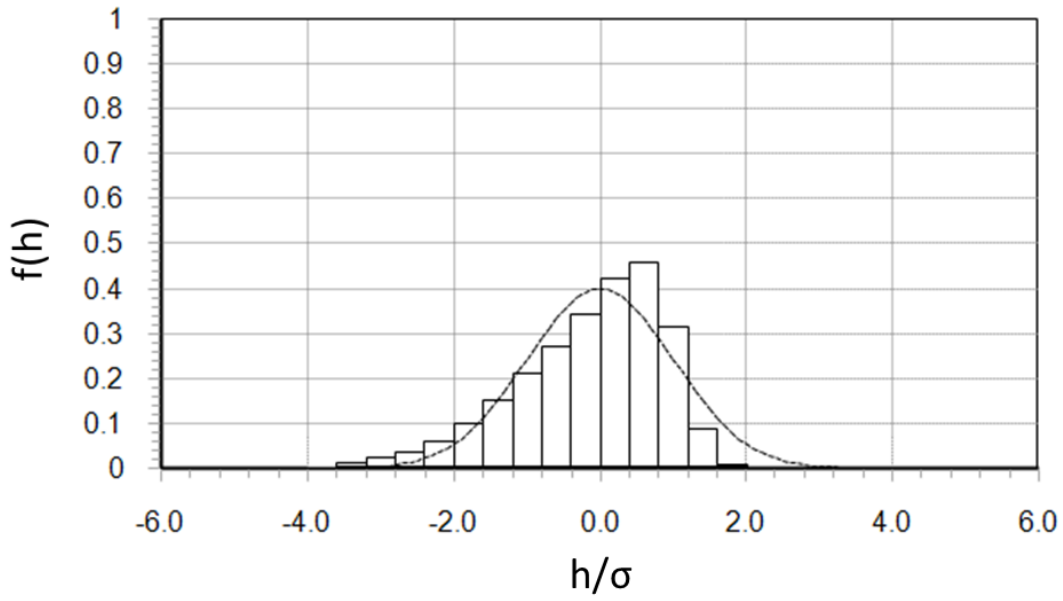

Figure 4-14 Histogram of surface heights for load stage 1 fast disk with Gaussian distribution curve (dashed)

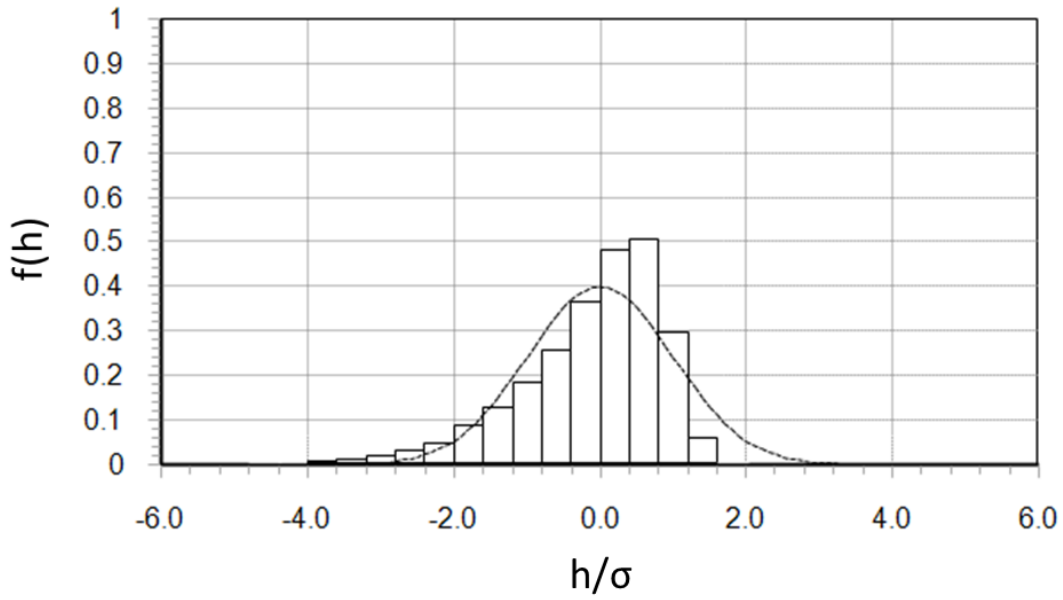

Figure 4-15 Histogram of surface heights for load stage 1 slow disk with Gaussian distribution curve (dashed)

Distributions for load stage 3 are shown in Figure 4-16 and Figure 4-17. These demonstrate little sign of modification in comparison to load stage 1 as can be expected given the similarity of the profiles between the load stages. Load stage 3 was the final load stage of the running in process as it was considered that the surface had attained a nominally steady topography.

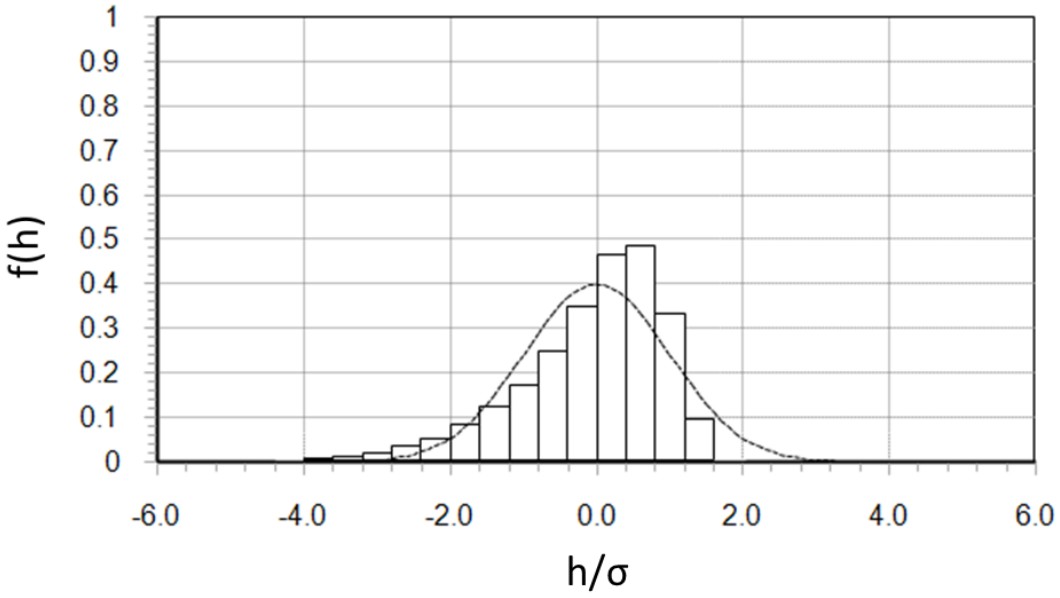

Figure 4-16 Histogram of surface heights for load stage 3 fast disk with Gaussian distribution curve (dashed)

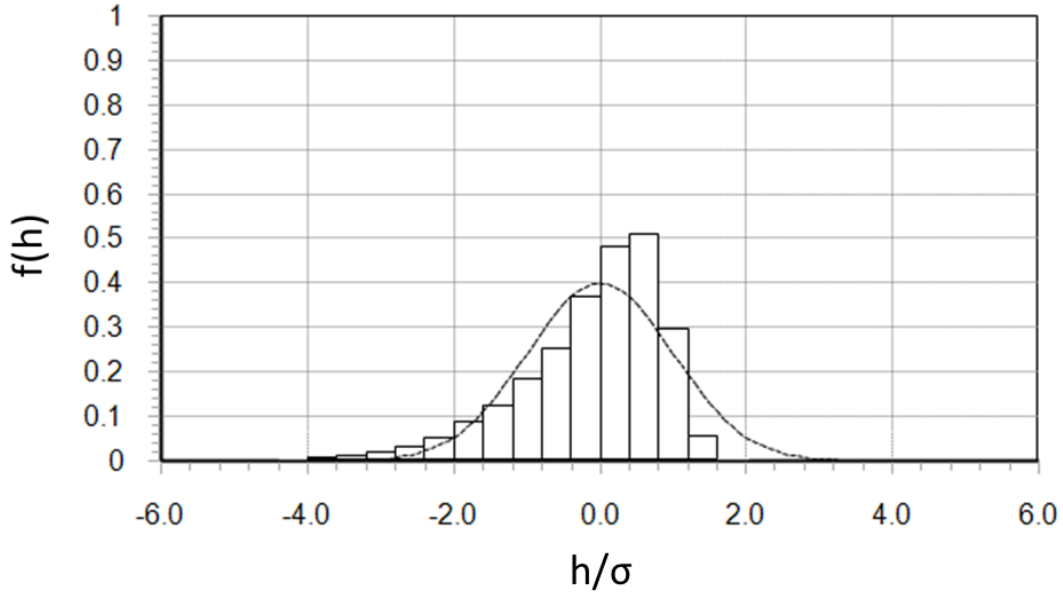

Figure 4-17 Histogram of surface heights for load stage 3 slow disk with Gaussian distribution curve (dashed)

Distributions plotted for the fatigued surfaces are shown in Figure 4-18 and Figure 4-19. These show the impact of further running in where the heights become more skewed and the tallest asperity features are flattened. Also visible is the impact of new valley features appearing where an increase in features registering below the mean can be seen.

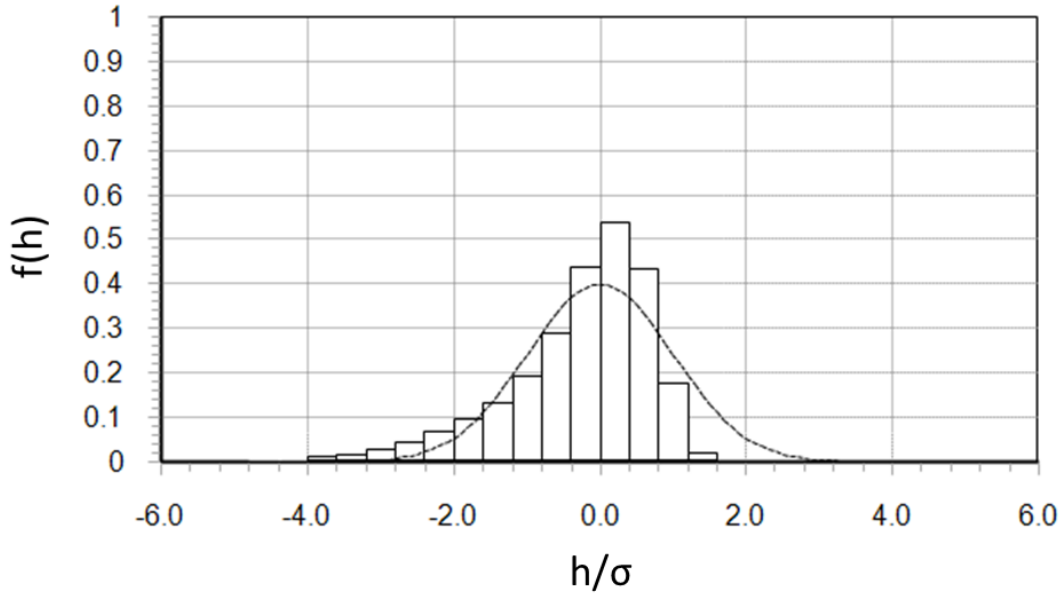

Figure 4-18 Histogram of surface heights for load stage 18 fast disk with Gaussian distribution curve (dashed)

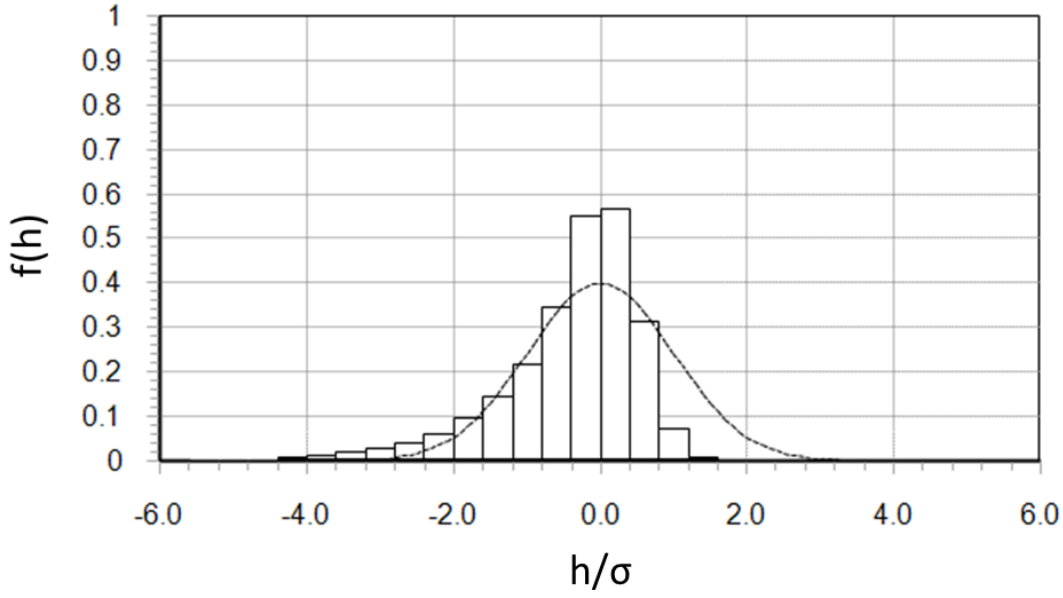

Figure 4-19 Histogram of surface heights for load stage 18 slow disk with Gaussian distribution curve (dashed)

4.4 Results for surfaces of different hardness

To provide insight into the effect surface hardness has during the running-in process and work into mixed lubrication, two axially ground disks of significantly different hardness values were selected from the available stock. A fast disk with a hardness of 652 Hv and a slow disk with hardness of 801 Hv were used.

It was found from the results of the initial load stages that far more plastic deformation was apparent in the low hardness surface, with relatively little observed in the harder surface. This smoothing effect on the softer surface with the use of oils containing extreme pressure additives was described by Rowe in his investigation into the running-in process on plain bearings (Rowe et al., 1975).

For the first experiment, load was applied for a short time of approximately 10 seconds in order to assess the rapidity at which asperity shapes were modified. The purpose of this initial short test interval was an attempt to quantify the level of plastic deformation that would occur after a brief loading period. Since the load was applied manually it was not feasible to adopt shorter initiali loading stages in a consistent way. The next set of experiments had load applied for approximately 25 seconds under the same test conditions. In comparison with tests run with disks of similar hardness, many more load stages were run in order to better observe the wear processes taking place alongside the rapid plastic deformation. The experimental programme and calculated Ra values of the surface are shown in Table 4-7.

Two sets of running-in experiments were conducted. Initial experiments were conducted from load stage 1 to load stage 5 at a maximum contact pressure of 1.7GPa and a fast shaft speed of 1500rpm. The second set of experiments was conducted from load stage 17 to load stage 29 at a lower contact pressure and lower speed of 200rpm. Between these running in tests, a set of experiments were conducted at lower loads at a speed of 1500rpm. These tests investigated instances of repeatable asperity interaction between the surfaces using triggered contact

voltage measurements. Because the tests were conducted at a lower load, and therefore thicker films – it was not necessary to measure the surfaces between every load stage as little modification would occur. This was verified at load stage 16 where no significant change was observed.

Table 4-7 Test data for running in load stages for hard-soft disk configuration

Load Stage	Load / N	FS Speed / rpm	Oil Feed Temperature / °C	Duration / s	Soft Disk Ra / µm	Hard Disk Ra / µm
Unrun	-	-	-	-	0.240	0.369
1	4150	1500	50	10	0.185	0.346
2	4150	1500	50	25	0.174	0.353
3	4150	1500	50	25	0.173	0.348
4	4150	1500	50	25	0.172	0.352
5	4150	1500	50	25	0.169	0.349
6	2320	1500	50	25	-	-
7	850	1500	50	25	-	-
8	2320	1500	50	25	-	-
9	2320	1500	50	25	-	-
10	2320	1500	50	25	-	-
11	2320	1500	50	25	-	-
12	1260	1500	50	25	-	-
13	2320	1500	50	25	-	-
14	2320	1500	50	25	-	-
15	2320	1500	50	25	-	-
16	2320	1500	50	25	0.169	0.349
17	2320	200	65	25	0.113	0.340
18	2320	200	65	25	0.107	0.340
19	2320	200	65	25	0.104	0.342
20	2320	200	65	25	0.100	0.338
21	2320	200	65	25	0.099	0.341
22	2320	200	50	25	0.100	0.341
23	2320	200	65	25	0.099	0.337
24	2320	200	65	25	0.099	0.341
25	2320	200	65	25	0.098	0.334
26	2320	200	65	25	0.097	0.336
27	1850	200	65	25	0.096	0.334
28	1850	200	65	25	0.096	0.334
29	1850	200	65	25	0.094	0.334

4.4.1 Test data for disks of different hardness - 1.7GPa 1500rpm

4.4.1.1 *Load Stage 1*

It can be seen from the test data for load stage 1, shown in Figure 4-20, that following load application there is a rapid rise in the friction signal to a value of 200N. The initial friction spike is related to the load spike which is a characteristic of the loading mechanism. There is also present very noticeable interference on the thermocouple channel which was later associated with the analogue output from the load indicator, this interference resulted in a step increase in measured signal. Following attempts to prevent this issue, it was decided to remove the signal altogether as the on-line measurement of load was not essential to the results.

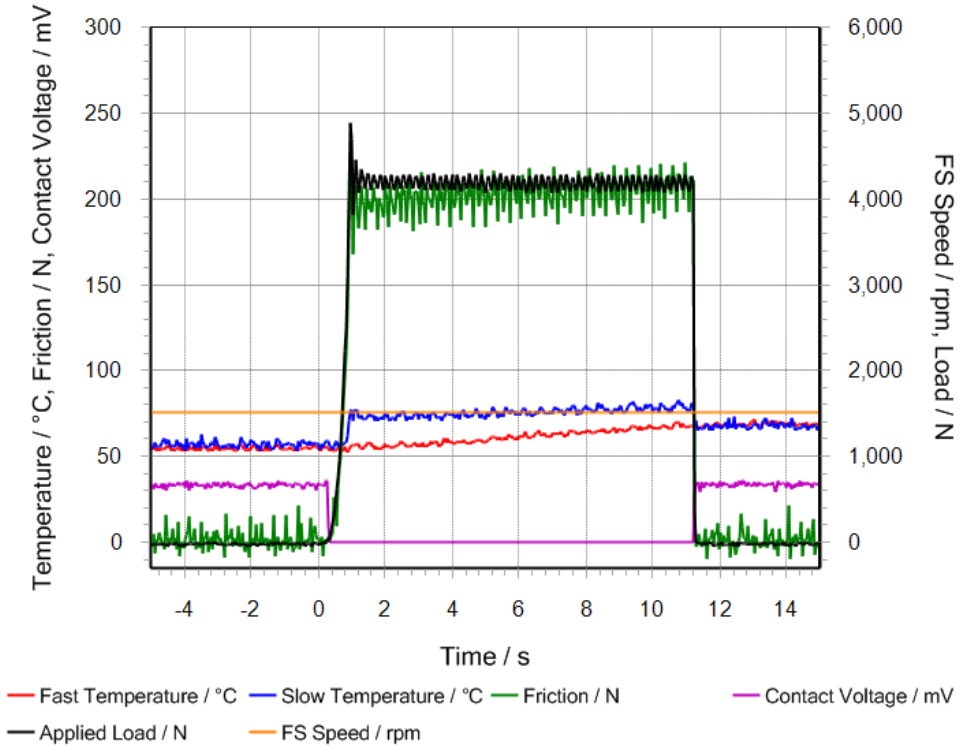

Figure 4-20 Test data for Load Stage 1 for disks of different hardness at 1.7GPa at a SRR of 0.25

Friction rises from an initial value at t = 0 of 195N to a final value of approximately 207N. Bulk disk temperatures can also be seen to rise over the load stage, from a value of around 55°C to a final value of 70°C. It can also be seen that the contact voltage drops to a value of 0mV throughout the test, suggesting continual metallic contact.

4.4.1.2 *Load Stage 2*

Load Stage 2 had a duration of 22 seconds and hence a greater rise in bulk disk temperature can be seen in Figure 4-21. The faster of the two surfaces also shows a greater temperature increase over the period, attaining a value of 75°C, which exceeds the 72°C of the slow disk. The bulk disk temperatures continue to rise following removal of the load as a result of the thermal lag introduced by fixing the thermocouples beneath the running track. Over the length of the experiment, the contact voltage signal remains at 0mV, indicating continuous contact metallic is taking place. The friction signal from the torque transducer also shows a gradual increase over the length of the experiment rising from an initial average value of 183N at t = 0, a lower value than that of load stage 1, to a final value of 207N immediately before removal of the load.

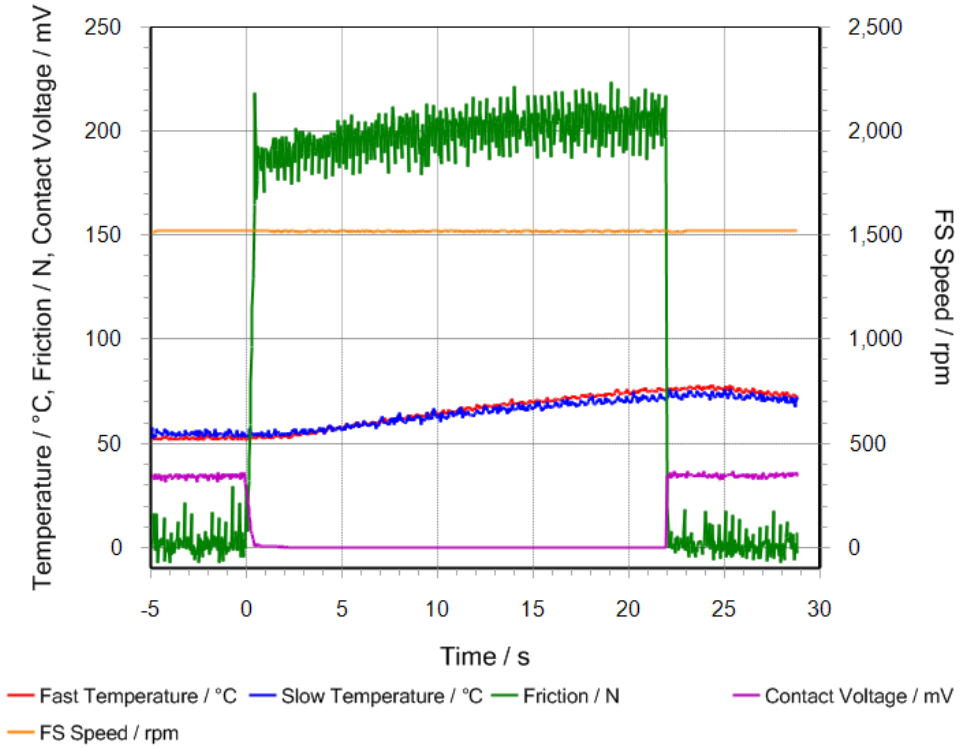

Figure 4-21 Test data for Load Stage 2 for disks of different hardness at 1.7GPa at a SRR of 0.25

4.4.1.3 *Load Stage 3*

In Figure 4-22, load stage 3 is shown. Load is applied for 25 seconds over which time the bulk disk temperatures can be seen to rise from a mean value of 52°C to a mean value of nominally 74°C. At t = 0 the contact voltage can be seen to drop to zero and quickly rise to attain an intermediate value of 13mV, indicating discontinuous film formation. This intermediate value then diminishes to zero after 8 seconds. The friction rises over the 25 seconds from an initial value of approximately 180N to a 210N, the final value exceeding that of the previous load stage.

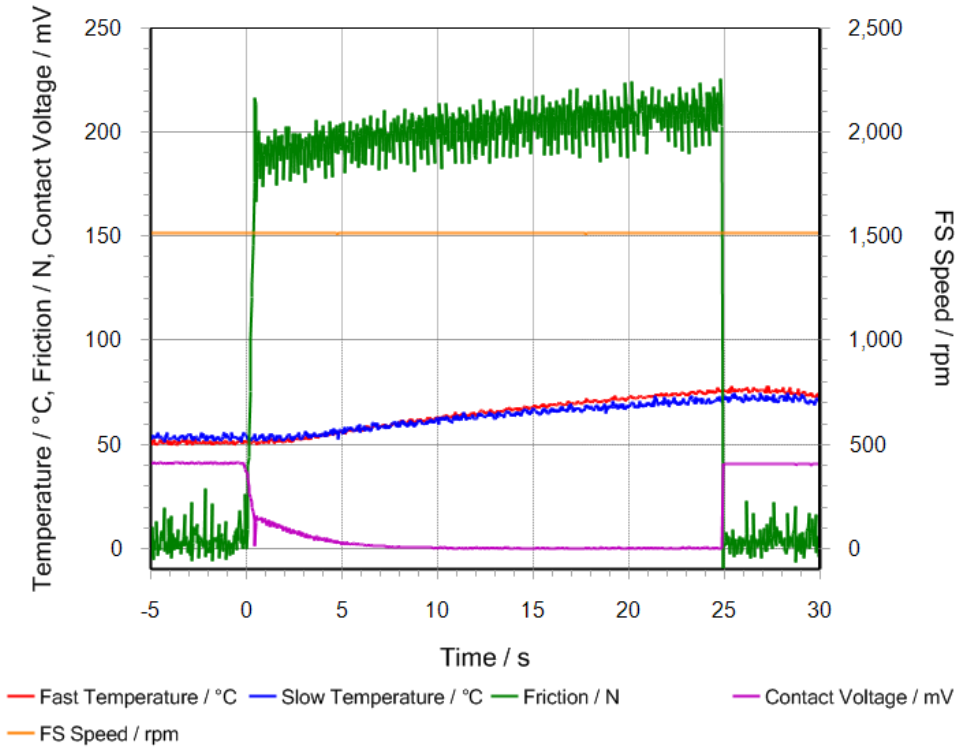

Figure 4-22 Test data for Load Stage 3 for disks of different hardness at 1.7GPa at a SRR of 0.25

4.4.1.4 *Load Stage 4*

Load was applied for approximately 26 seconds in load stage 4 which is shown in Figure 4-23. During this time, mean bulk disk temperatures rise from an initial value of 50°C at t = 0 to a final value of 74°C. The friction behaves in a similar way to that shown in load stage 3. Compared to load stage 3, shown in Figure 4-22, the contact voltage can be seen to attain a higher initial value of 25mV at t = 0, reducing to 0mV at t=15s as bulk disk temperatures rise.

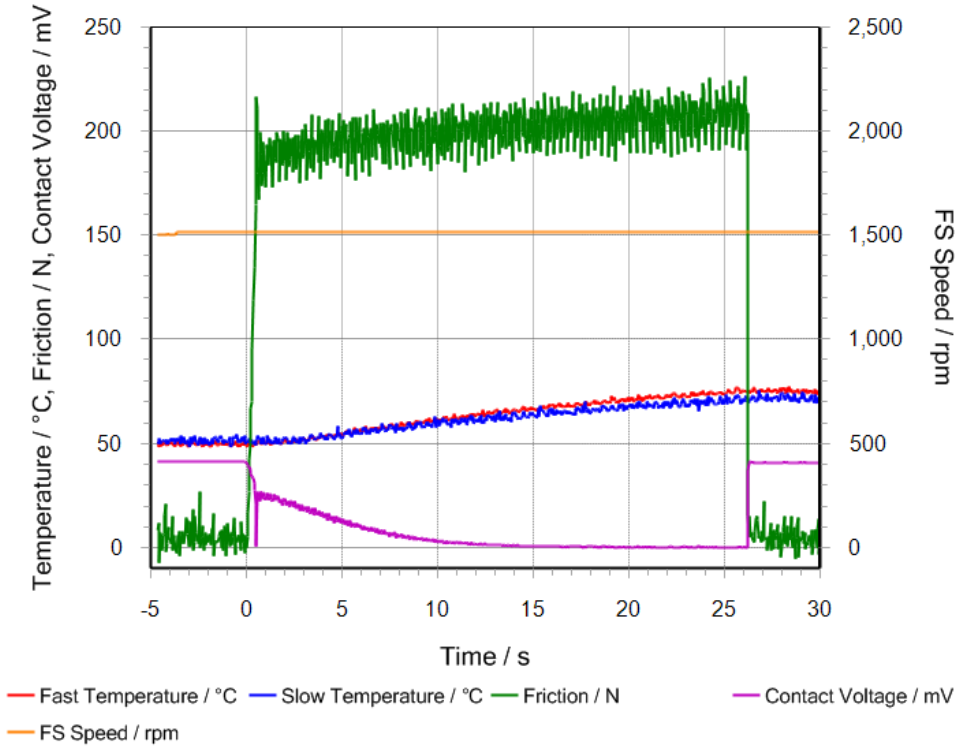

Figure 4-23 Test data for Load Stage 4 for disks of different hardness at 1.7GPa at a SRR of 0.25

4.4.1.5 *Load Stage 5*

Similar values for friction and bulk disk temperature to those observed in load stage 4 are recorded during load stage 5. Contact voltage in Figure 4-24 can be seen to attain a value of approximately 25mV at t=0s, diminishing to 0mV at approximately 19 seconds.

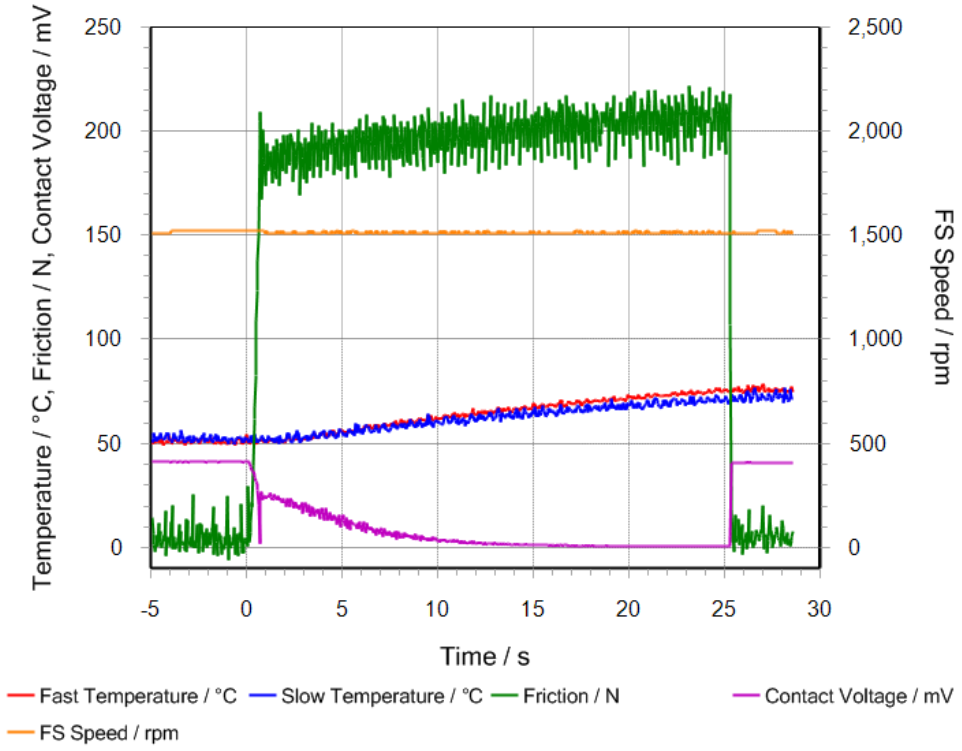

Figure 4-24 Test data for Load Stage 5 for disks of different hardness at 1.7GPa at a SRR of 0.25

4.4.2 Profile data for disks of different hardness - 1.7GPa 1500rpm

Inspection of profile traces taken between experiments demonstrate that where two rough surfaces of significantly differing hardness are loaded together in mixed lubrication conditions, plastic deformation occurs almost entirely in the asperities of the lower hardness surface. The plastic deformation of the low hardness surface is clearly shown in Figure 4-25a-d where profiles from initial loading stages have been realigned to show the progressive modification.

Prominent asperity peaks on the low hardness surface show significant rounding off as they come into contact with portions of the opposing body with smaller scale roughness features also appearing to diminish. This can be seen at x=0.34mm where a peak is flattened from 0.62μm to 0.38μm after the first load stage with the finer features covering the asperity becoming less visible after subsequent load stages.

Despite this severe deformation occurring on the peaks of the surface, it is clear that the valley features remain undisturbed throughout the loading process, as experiments reported in section 4.3 with two hard surfaces have shown. It is clear that the most significant change in profile occurs following the initial loading process, subsequent load stages do not demonstrate the same level of modification, with load stage 2 only showing slight change.

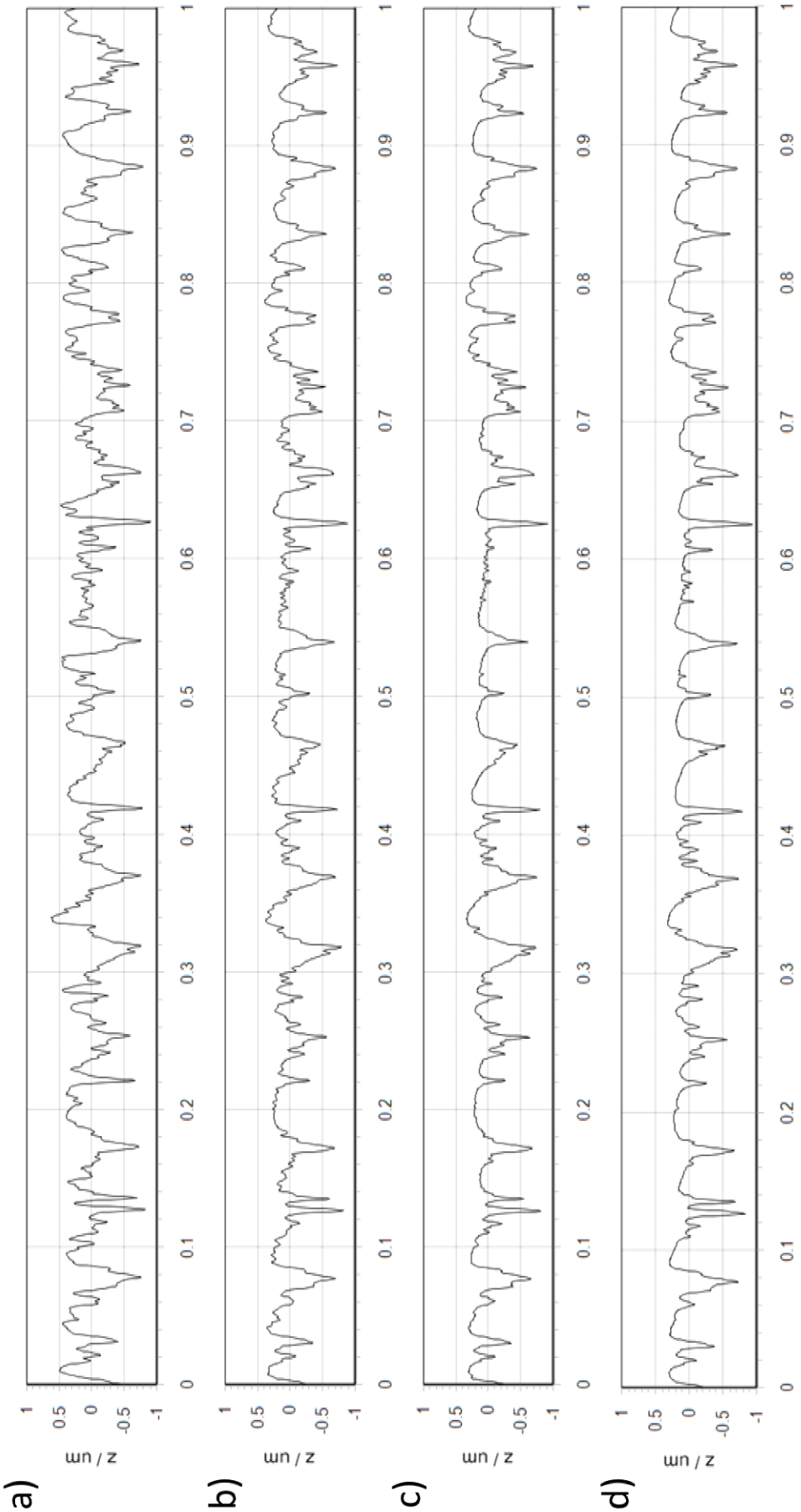

Figure 4-25 Profile traces from the lower hardness disk for (a) Unrun Surface (b) Load Stage 1 (c) Load Stage 2 (d) Load Stage 5

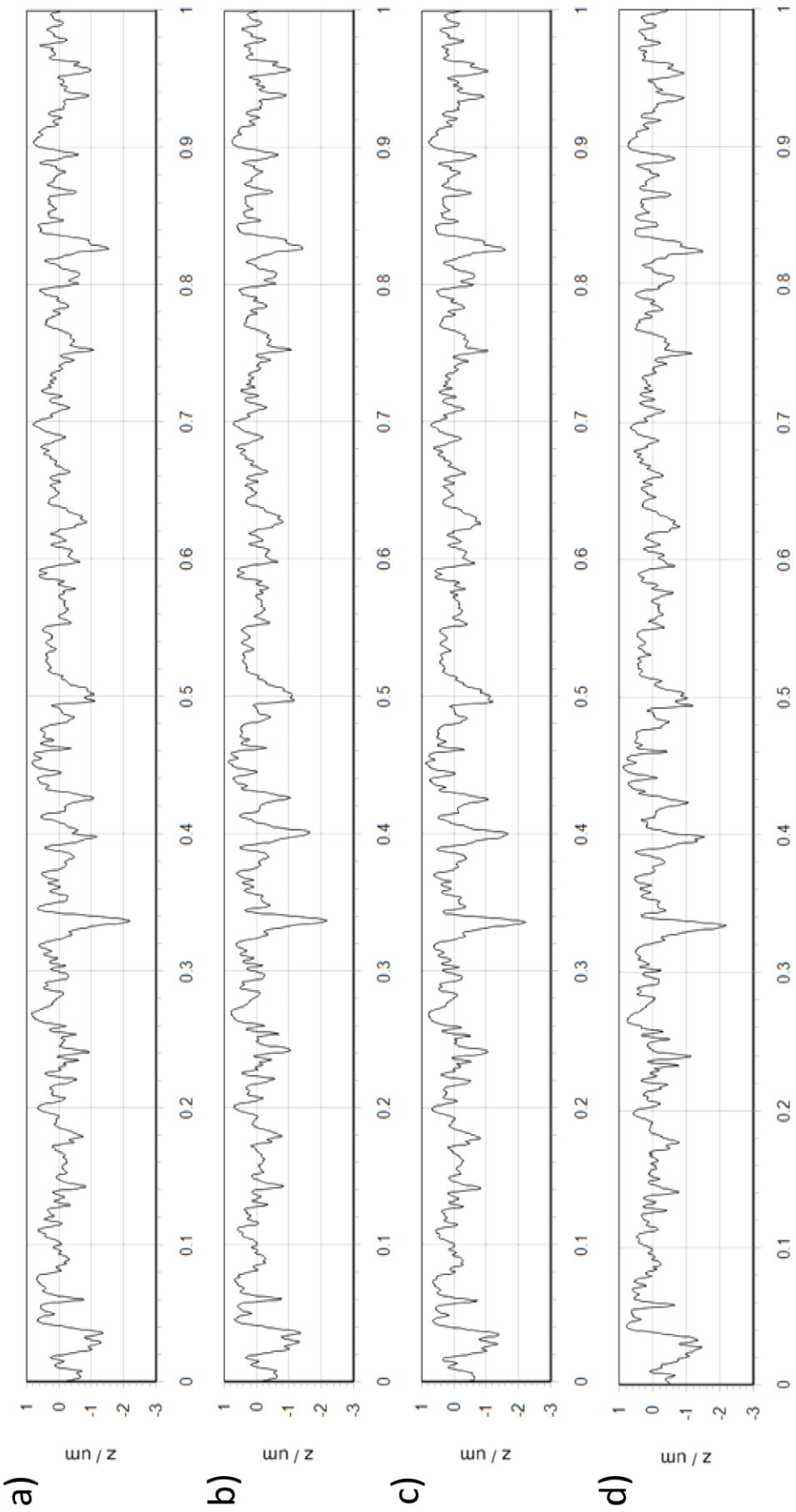

Figure 4-26 Profile traces from the higher hardness disk for (a) Unrun Surface (b) Load Stage 1 (c) Load Stage 2 (d) Load Stage 5

In stark contrast to the results seen for the low hardness surface, the slower and harder surface undergoes almost no modification whatsoever – this persistence is clearly visible in Figure 4-26 where, at the scale shown, prominent peaks endure the harsh loading process. Realigned with their original profiles in Figure 4-27, it is clear that only the very tips of the hard surface experience any plastic deformation. The running-in of both surfaces can be seen by the decreasing Ra value shown in Table 4-7.

Further highlighting the great disparity in levels of modification, Figure 4-27a and 4-26b show a shorter section of profiles taken following the initial load stage superimposed and realigned with their as-manufactured counterparts. A large amount of deformation can be seen to occur at the asperity tips of the low hardness surface as they encounter the asperities on the harder surface which maintain their geometry as they traverse the EHL contact.

Figure 4-27a shows finer asperity features at x=0.288mm (A) and x=0.34mm (B) which experience a reduction in surface height of approximately 0.3µm and also features with larger tip radii that do not experience the same reduction in height; an example of this is seen at x=0.43mm (C) where a feature deforms by around 0.1µm. In comparison to this very little deformation can be seen to occur on the harder surface. It is possible to identify some very slight changes in Figure 4-27b, at x=0.389mm (D) and x=0.473mm (E) for example where very fine asperity tips experience a change in height of approximately 0.2µm each following load stage 1. However, some differences may arise from axial misalignment as has previously been discussed, an example of this can be seen at x=0.45mm (F) where the profile representing load stage 1 is briefly seen to exceed that of the un-run measurement.

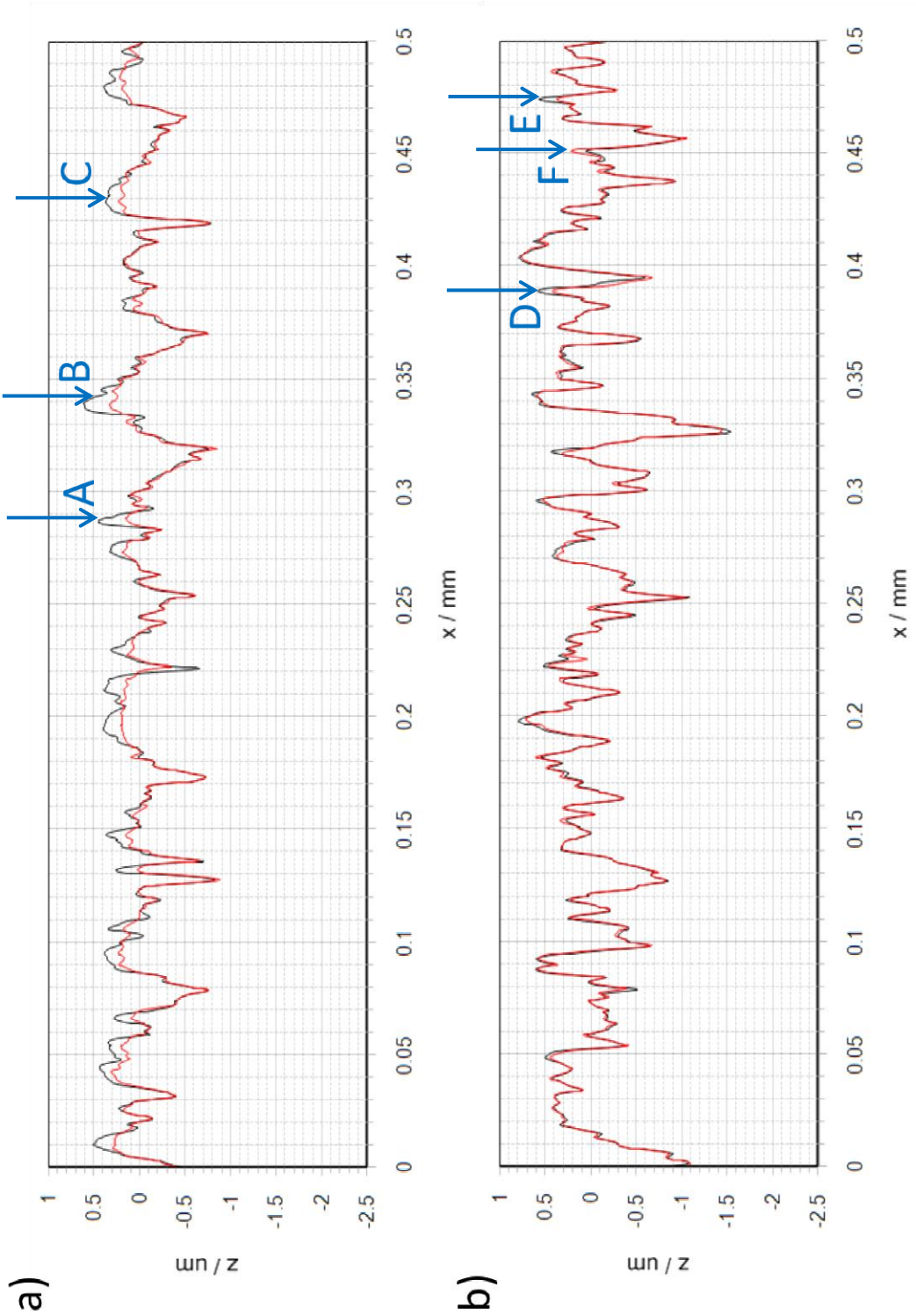

Figure 4-27 Load stage 1 shown in red superimposed on un-run profile for a) low hardness disk b) high hardness disk

Figure 4-28 shows overlays of profiles taken after load stage 4 and load stage 5 of the experiments. These show that both surfaces have attained a nominally steady state with very close agreement between both sets of measurements.

Profile traces from the low hardness disk also show a tendency for large asperity features to adopt a pronounced slanted shape at the scale shown, where due to the traction force from the opposing surface, their tips are distorted in the direction of traction. This phenomenon is most visible in Figure 4-28a in the range $0.02 \leq x \leq 0.09$ (A) and again towards the end of the trace between $0.45 \leq x \leq 0.5$ (B). Data acquired from the harder disk do not demonstrate this effect at the scale shown as very little modification occurs throughout the first set of experiments.

Also apparent, are the appearance of circumferential markings on the soft disk where the hard asperities of the surface have deformed regions of the soft disk – these are visible in the 3D measurements shown in Chapter 5 taken following the removal of the disks from the rig in Figure 5-32. These markings reduce conformity between profiles in the lay of the major asperities and place greater importance on accurately relocating axially. The harder of the two surfaces does not show the same scoring in the circumferential direction.

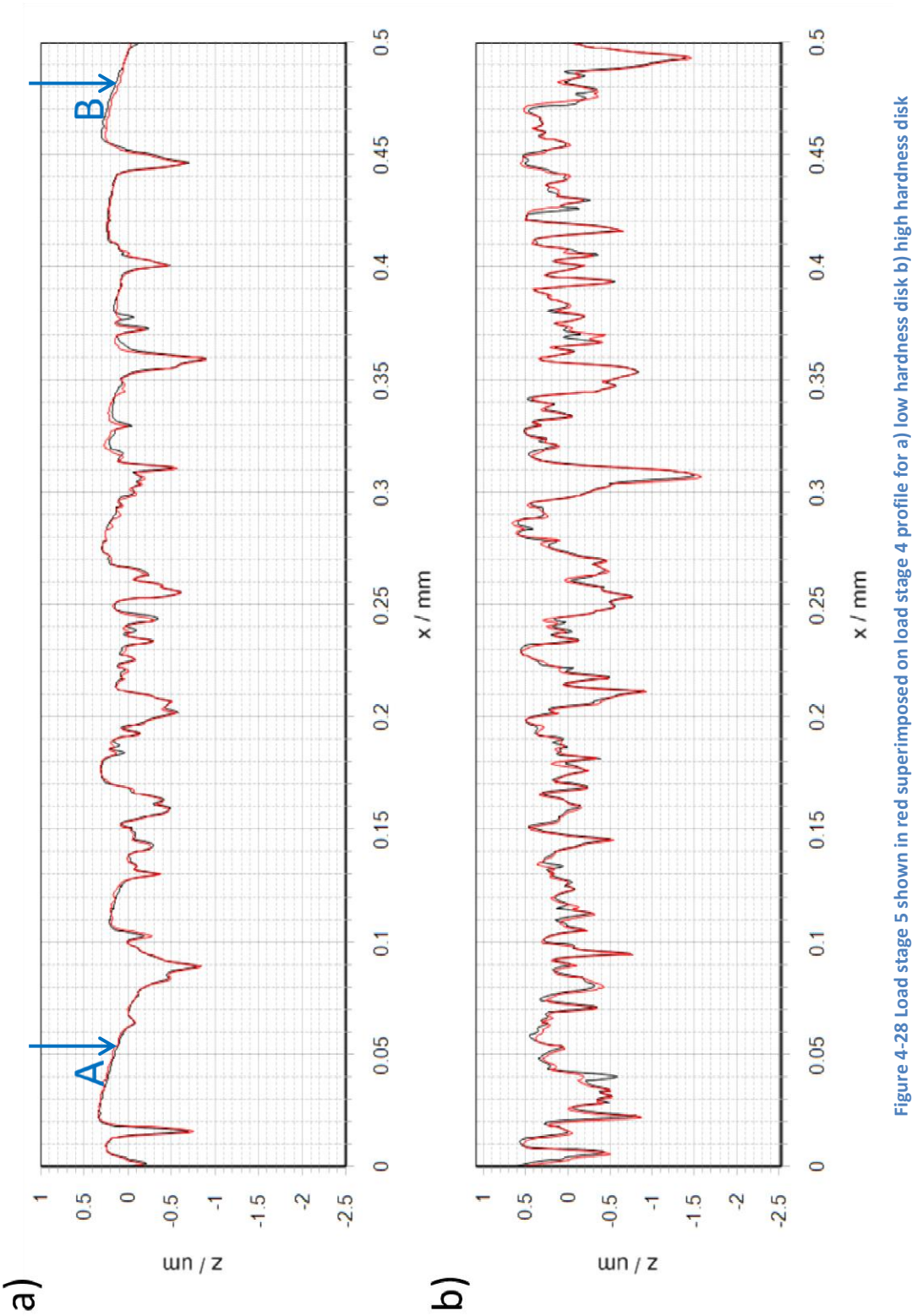

Figure 4-28 Load stage 5 shown in red superimposed on load stage 4 profile for a) low hardness disk b) high hardness disk

Following the measurements of load stage 5 and the indication from the contact voltage signal that the surfaces had stabilised, it was decided to continue with a series of experiments into triggered contact voltage readings employing the use of the encoder. A number of experiments were conducted at lower loads, maintaining the same speed – the purpose of this was to avoid further modification during experimentation, the results of these tests are presented and discussed in Chapter 5.

To assess the impact of these experiments further measurements were taken and the profiles realigned. Realigned profiles for load stage 5 and load stage 16 are shown in Figure 4-29. It is apparent that no significant modification had occurred between these two load stages. Some minor changes can be seen to have occurred on the hard disk where tips of prominent asperity features are no longer present, this can be seen most clearly at x = 0.9mm (A) and is attributed to fatigue. However, it can be seen that with the exception of some minor differences, there is very close alignment between the profiles taken after load stage 5 and load stage 16. This is also demonstrated in the Ra values shown in Table 4-2.

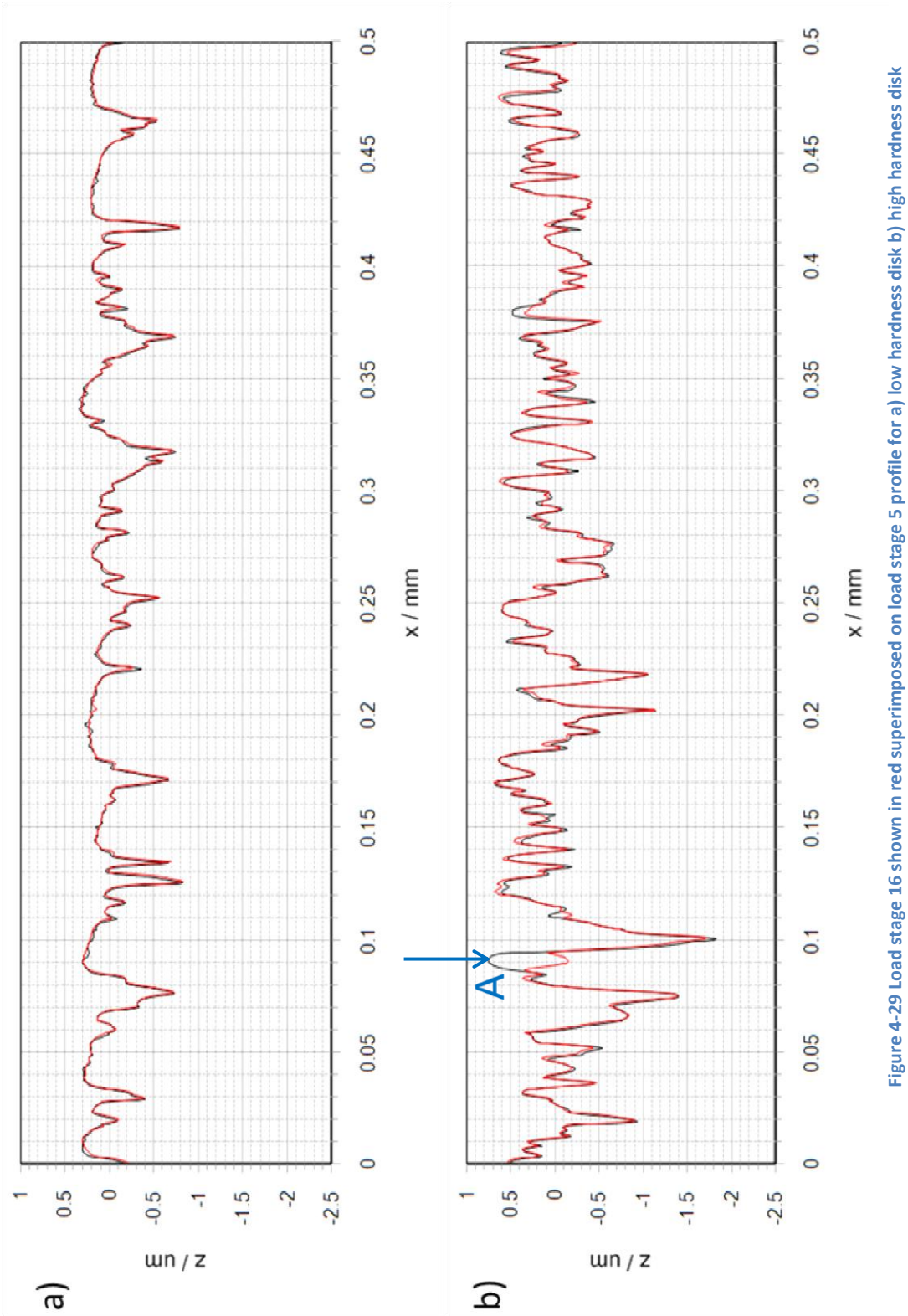

Figure 4-29 Load stage 16 shown in red superimposed on load stage 5 profile for a) low hardness disk b) high hardness disk

4.4.3 Test data for disks of different hardness - 1.4GPa 200rpm

In a bid to further run in the surface it was decided to reduce the film thickness as it was expected that this would increase asperity loading. Conditions selected were based on predictions for the lowest lambda ratios during speed varying experiments, it was decided to run the test disks at a lower load whilst elevating the oil feed temperature, raising the bulk disk temperature and lowering the entrainment speed. Experiments were interspersed with surface profile measurements and it was decided after extensive running to lower the maximum contact pressure to 1.3GPa in order to reduce the wear processes observed to be occurring on the low hardness surface.

4.4.3.1 *Load Stage 17*

Figure 4-30 shows the test data for the first experiment run at lower speed. The graph can be seen to contain fewer data points due to reduced fast shaft speed and hence lower triggering frequency, as explained in Chapter 3. The experiment demonstrates very low contact voltage levels throughout, suggesting continuous metallic contact. The contact voltage signal can be seen to take a value of approximately -2mV in this and other experiments - the cause of this slight offset was attributed to electrical noise within the laboratory area, as this was not seen in other experiments.

Due to the significantly lower load and sliding speed, there is little heat generated at the contact. It can be seen that the bulk disk temperature rises from approximately 65°C at t = 0 to around 68°C at the end of experiment. The measured friction can also be seen to be stable over the length of the experiment with a value of approximately 190N. This equates to a friction coefficient of approximately 0.08. The speed can also be seen to be affected by the load application where there is a slight drop whilst the traction remains high.

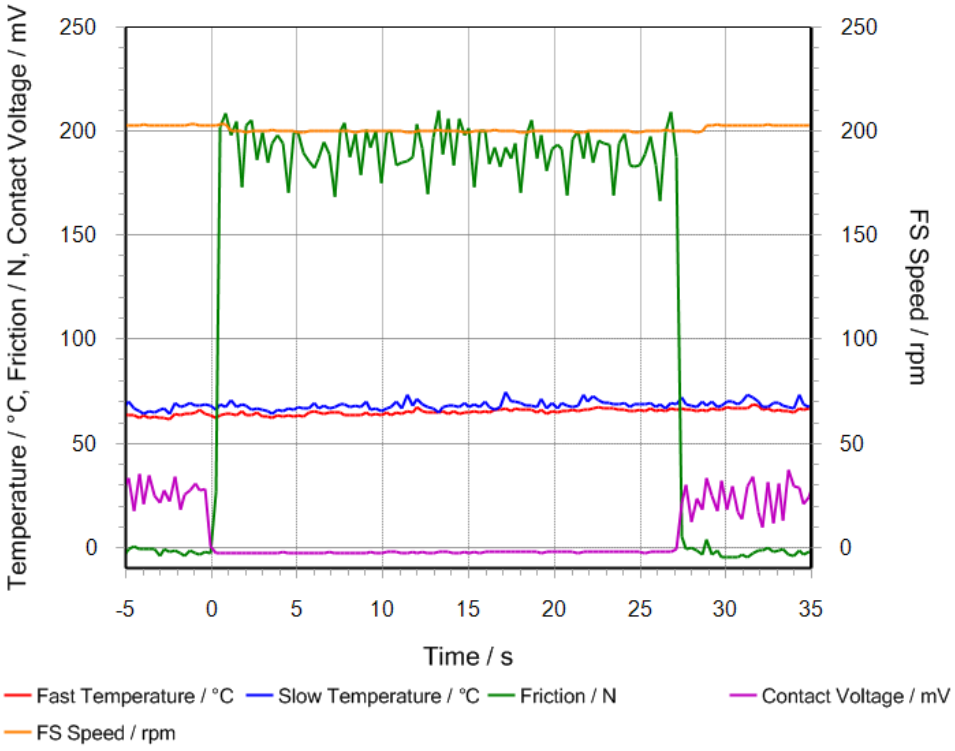

Figure 4-30 Test data for Load Stage 17 for disks of different hardness at 1.4GPa at a SRR of 0.25

4.4.3.2 *Load Stage 18*

A large degree of asperity interaction can be inferred from the low contact voltage signal for load stage 18 presented in Figure 4-31, which maintains a value of -1mV over the loading duration. A very small rise in bulk disk temperature can be observed as in the previous load stage where in load stage 18 the mean bulk disk temperature can be seen to rise from approximately 64°C at t = 0 to around 67°C. Close inspection of the friction signal displays a slightly lower mean value of nominally 185N which remains steady over the experiment.

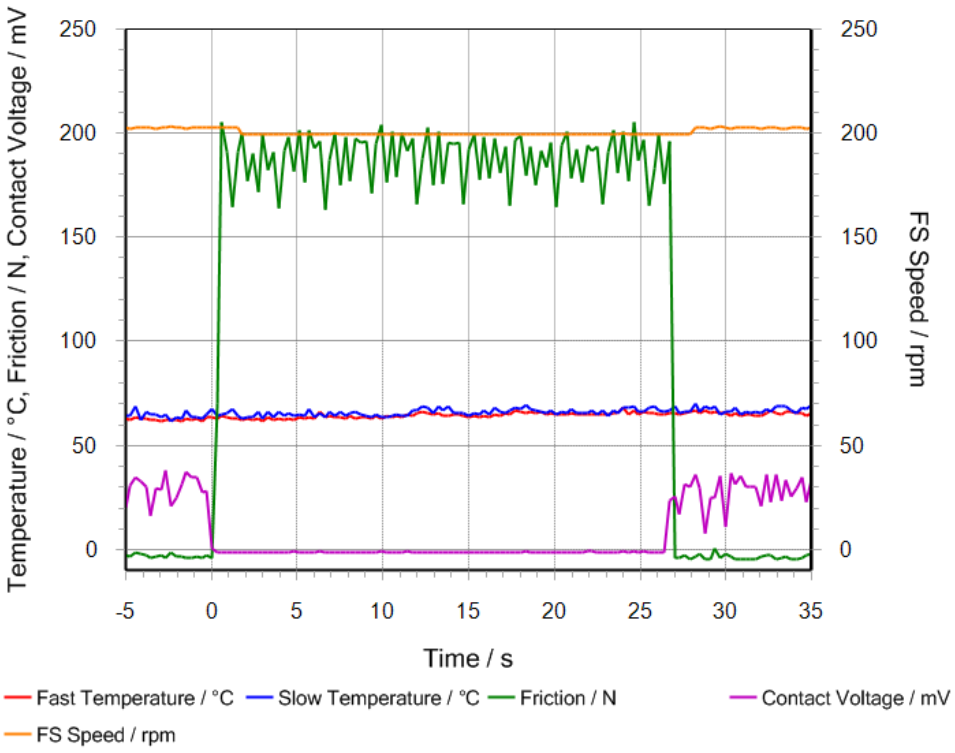

Figure 4-31 Test data for Load Stage 18 for disks of different hardness at 1.4GPa at a SRR of 0.25

4.4.3.3 *Load Stage 19 to 26*

Load stages 19 to 26 display very similar transducer responses to previous experiments at similar conditions. In comparison to load stages 1-5, the contact voltage signal under the lower speed conditions cannot be seen to develop higher levels. Profile data taken between experiments demonstrated what appeared to be some modification occurring, though alignment at this late stage of running where the axial conformity of the roughness lay had decreased was more difficult to obtain. Average roughness values displayed in Table 4-7 compiled from the 12 profiles taken from each disk show a gradual decrease in value as experiments progress, illustrating the action of wear processes.

Figure 4-32 shows the test data for load stage 20 which is representative of experiments conducted between load stages 19 to 26. It can be seen that the behaviour of the friction, temperature and contact voltage are all very similar to previous experiments. The bulk disk temperatures do not experience a large change and the friction maintains a value of nominally 185N over the length of the experiment. The contact voltage signal remains low from t = 0 until load is removed 27 seconds into the experiment.

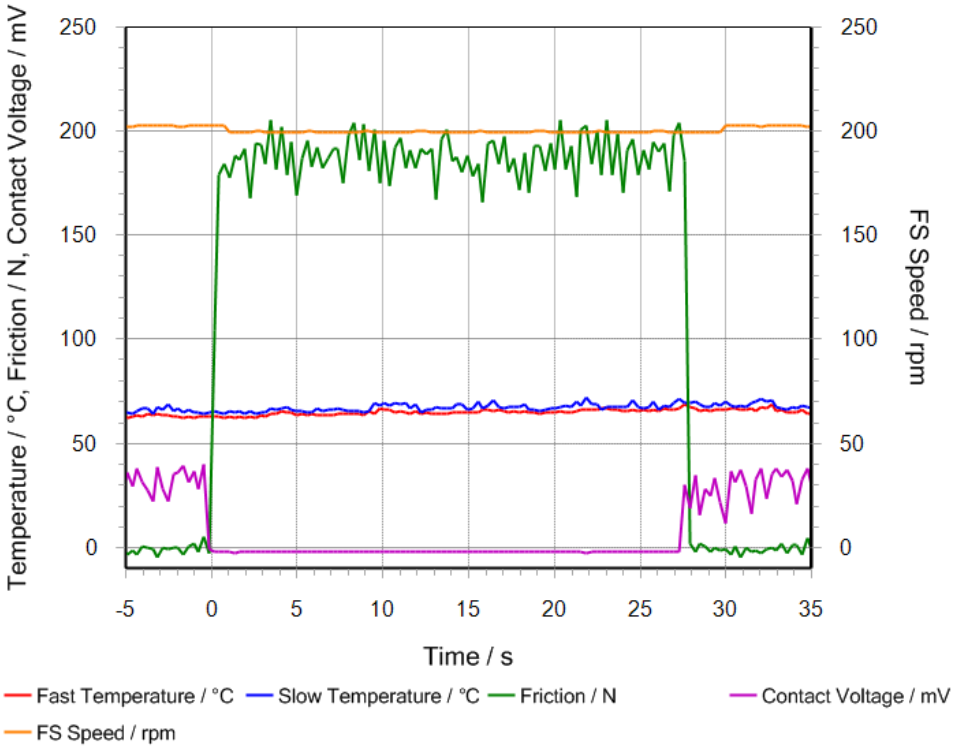

Figure 4-32 Test data for Load Stage 20 for disks of different hardness at 1.4GPa at a SRR of 0.25

4.4.3.4 *Load Stage 27*

Upon observation of profile data described in the proceeding section of this chapter, it was decided to reduce the maximum Hertzian contact pressure from 1.4GPa to 1.3GPa in order to reduce the rate at which the lower hardness hard disk experienced wear. Three of these experiments at a lower load were run and interspersed by profile measurements to observe any modification occurring on the surface.

Figure 4-33 shows the test data for the first experiment run under the lower load conditions. It can be seen that there is still frequent metallic contact occurring. This observation was true for all experiments run under lower load conditions. The bulk disk temperatures can be seen to rise slightly from nominally 62°C to 64°C over the length of the experiment. The measured friction force, understandably, is lower under the conditions of reduced load with a mean value of 145N whilst load is applied. A friction coefficient of 0.078 along with the contact voltage level suggests a high level of interaction between the surfaces. It can be seen in Table 4-7 that the Ra value for the surfaces did not experience a significant change due to the lower normal loading experienced by the surface. The experimental data for each of the three experiments was very similar and is not shown here.

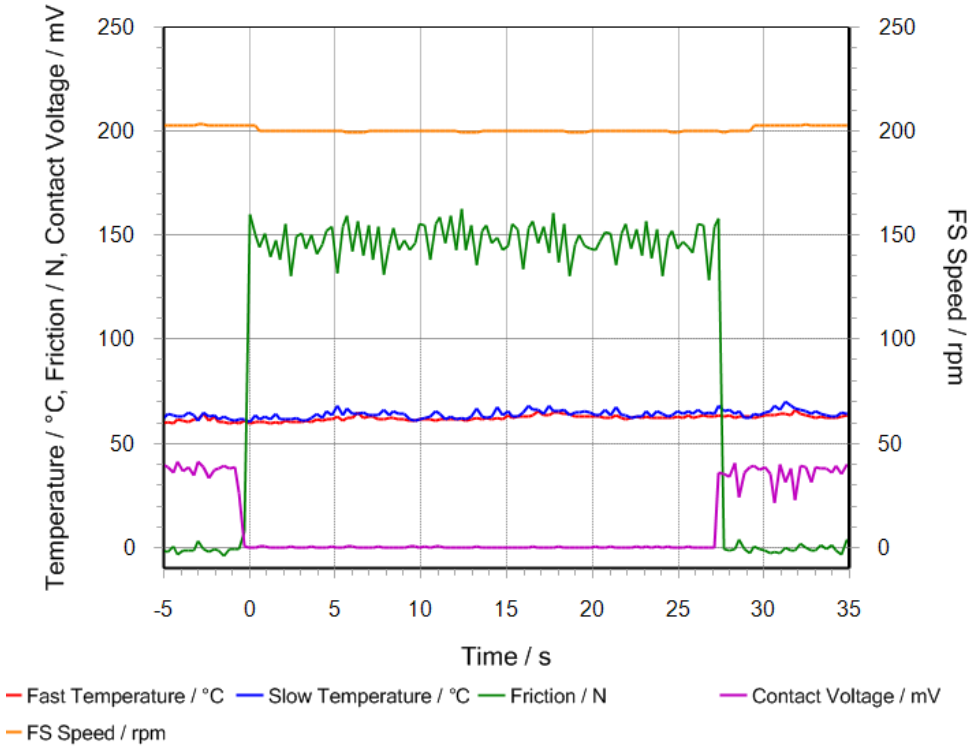

Figure 4-33 Test data for Load Stage 27 for disks of different hardness at 1.3GPa at a SRR of 0.25

4.4.4 Profile Data 1.4GPa 200rpm 65°C

Figure 4-34 shows an example of the progressive modification of a 1mm section of a profile trace taken from the fast disk. It can be seen that a large amount of plastic deformation takes place between load stage 16 and 17 where many smaller features appear to become merged due to their growth in the normal direction. This is accompanied by a degree of material removal, where after load stage 18 many of the finer features on the surface can no longer be identified and where portions of the profile portray the appearance of being 'excavated.' This can be identified between $0.26 \leq x \leq 0.32$ (A) where many finer features can be seen to experience an initial reduction in height and subsequently appear to become more smooth. The entire profile demonstrates this behaviour where finer features appear to gradually diminish.

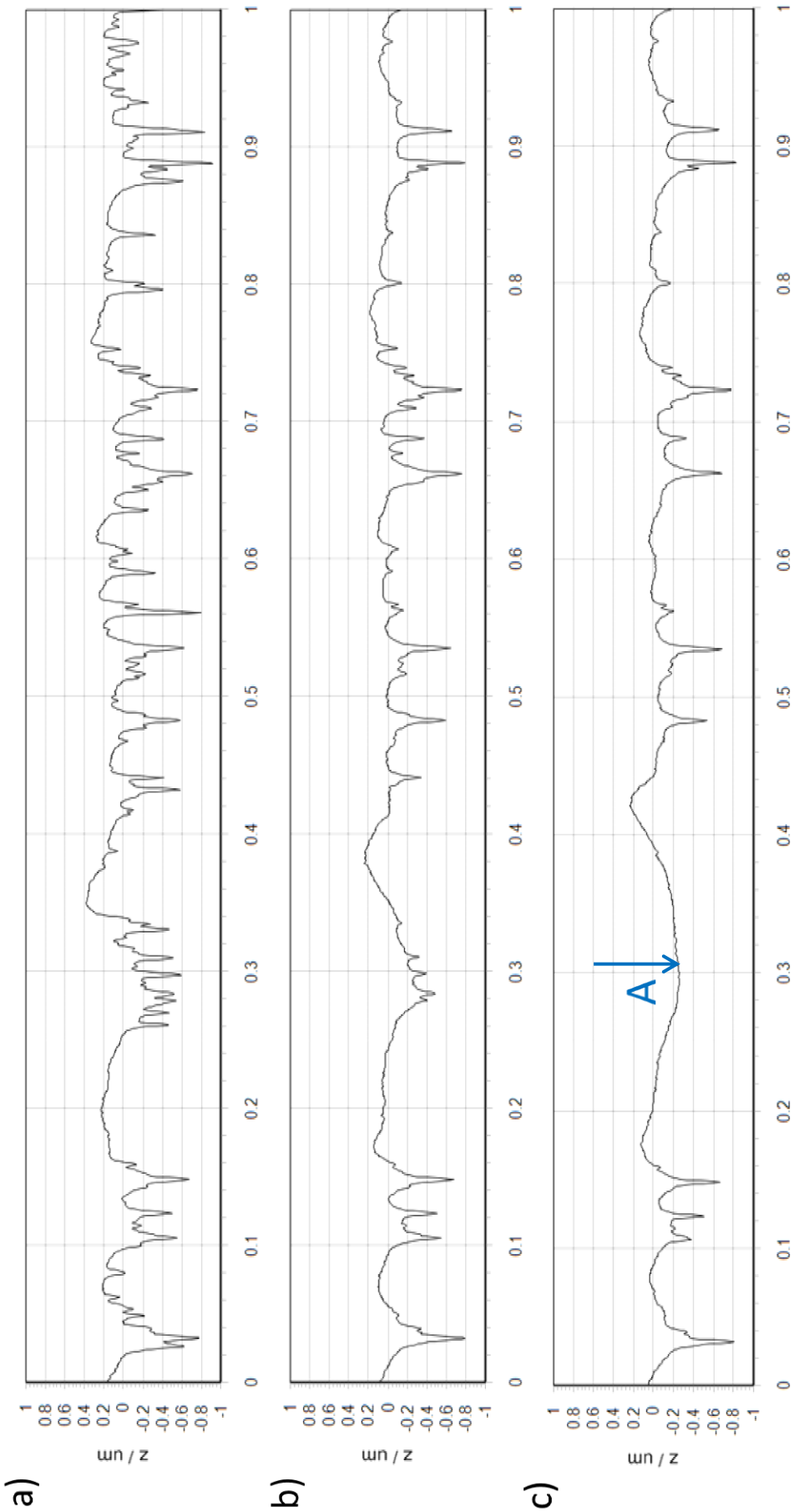

Figure 4-34 Profile traces from the lower hardness disk for (a) Load Stage 16 (b) Load Stage 17 (c) Load Stage 18

4.4.4.1 *Load Stage 17*

Profile measurements following the first experiment run under the new conditions, plotted in Figure 4-35, show a large degree of modification of the low hardness surface and visually, the surface takes on a polished appearance. The large amount of the normal loading applied to the asperities and consequently the deformation taking place shows the valley features 'closing up' in response to this resulting in asperities appearing to become merged. This can be seen in Figure 4-35a at x=0.113mm (A) and also at x=0.154mm (B).

The hard surface shows little change in Figure 4-35b with only the most aggressive peaks becoming more rounded; this is reflected in the nominally unchanging Ra value shown in Table 4-7. The most prominent peaks between x=0.35mm (C) and x=0.40mm (D) can all be seen to experience a reduction in height. Other sections of the profile measured from the slower and harder disk appear to show some discrepancies that are attributed to axial misalignment between measurements.

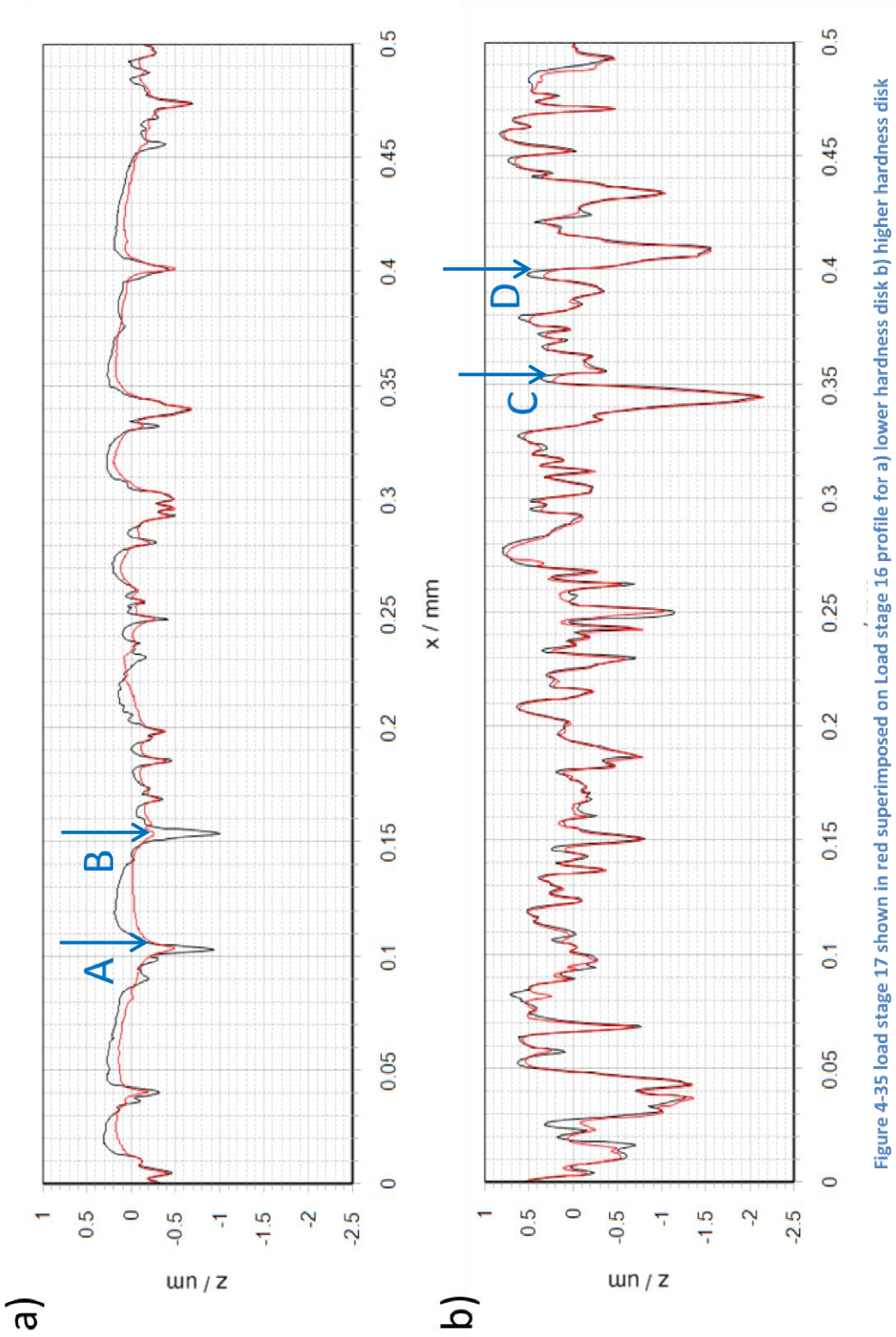

Figure 4-35 load stage 17 shown in red superimposed on Load stage 16 profile for a) lower hardness disk b) higher hardness disk

4.4.4.2 *Load Stage 18*

Profile measurements shown in Figure 4-36 taken following load stage 18 appear to show further modification occurring on the lower hardness surface. Realignment in the axial direction from load stage 18 onwards poses some difficulty due to the wear occurring in the circumferential direction, reducing conformity. Valleys on the soft surface can be seen to close up further, which is visible at x=0.113mm (A) and x=0.4mm (B). The soft surface does not experience the same reduction in height as was seen following load stage 17, shown in Figure 4-35a. The hard surface can be seen to experience very little modification, with close alignment between prominent peaks and valleys.

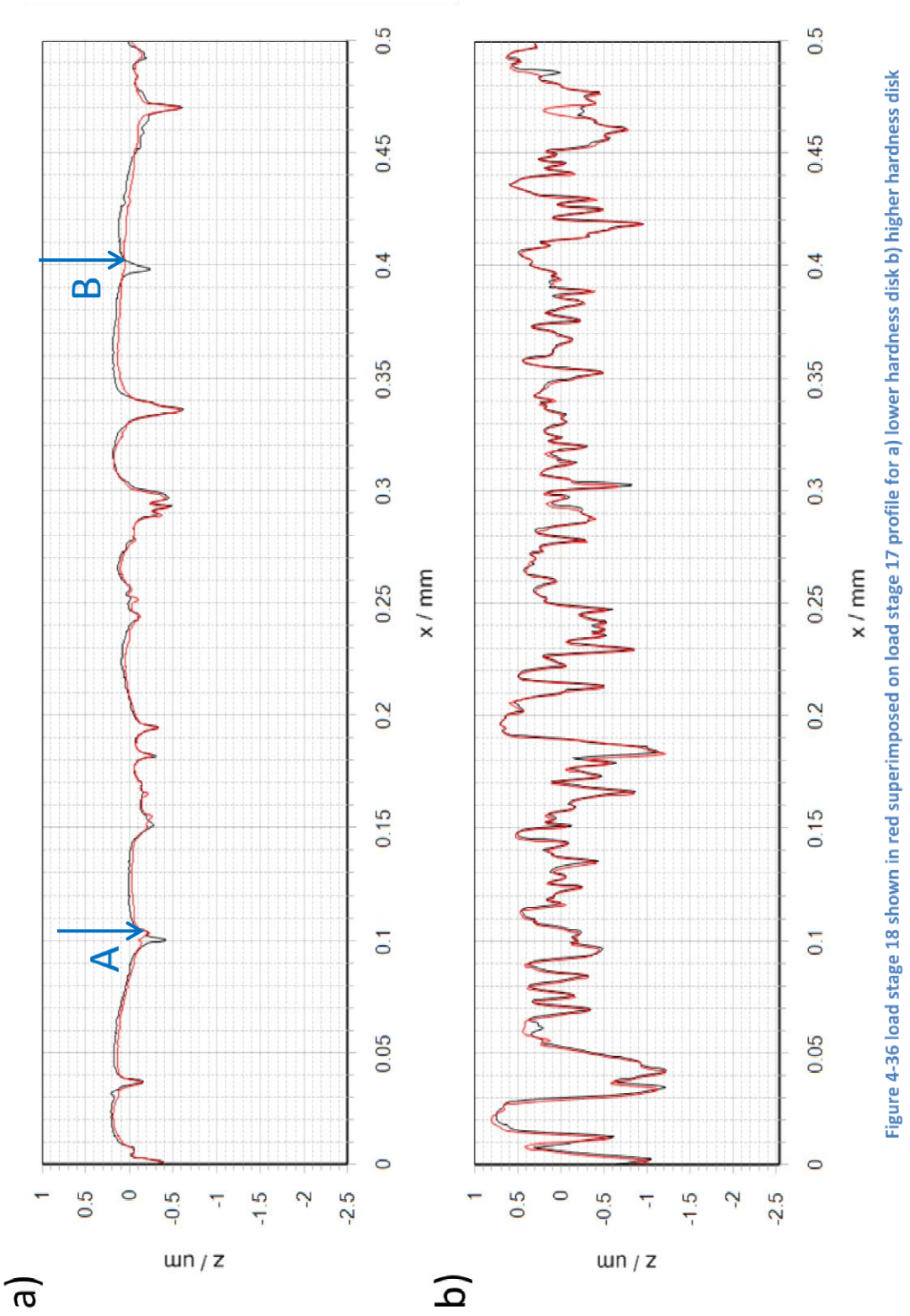

Figure 4-36 load stage 18 shown in red superimposed on load stage 17 profile for a) lower hardness disk b) higher hardness disk

4.4.4.3 *Load Stage 26*

Figure 4-37 shows two 1mm long superimposed relocated profiles taken from the faster, low hardness disk following load stages 17, 18 and 26. The figure demonstrates the progression of modification where it can be seen that asperity features in general become less prominent over time. This is consistent with Ra values shown in Table 4-7 which are seen to decrease with running. The figures shown have also been presented as they appear to include the aforementioned removal of material. This is visible between 0.6≥x≥0.7 (A) on Figure 4-37a and more clearly between 0.15≤x0.45 (B) on Figure 4-37b where concave features appear. The shapes of these features are not consistent with the rest of the profile where a run in ground surface tends to appear as a series of convex asperity features interspersed by valleys. Where material appears to have been removed in Figure 4-37b, it can be seen that the edges of the concave region, in relation to the rest of the profile are quite jagged and exposed.

In Figure 4-37b a large spike can also be occurring at x=0.3mm (C). Similar features have been found throughout measurements taken on the low hardness disk at later load stages. Where similar features have been identified during the measurement process, the surfaces have been cleaned and remeasured. It was found that spikes similar to that seen in Figure 4-37b have tended to persist despite repeated cleaning with solvent spray and wiping, suggesting that the feature is debris contaminating the profile trace and could potentially be the result of wear particles embedded in the softer surface.

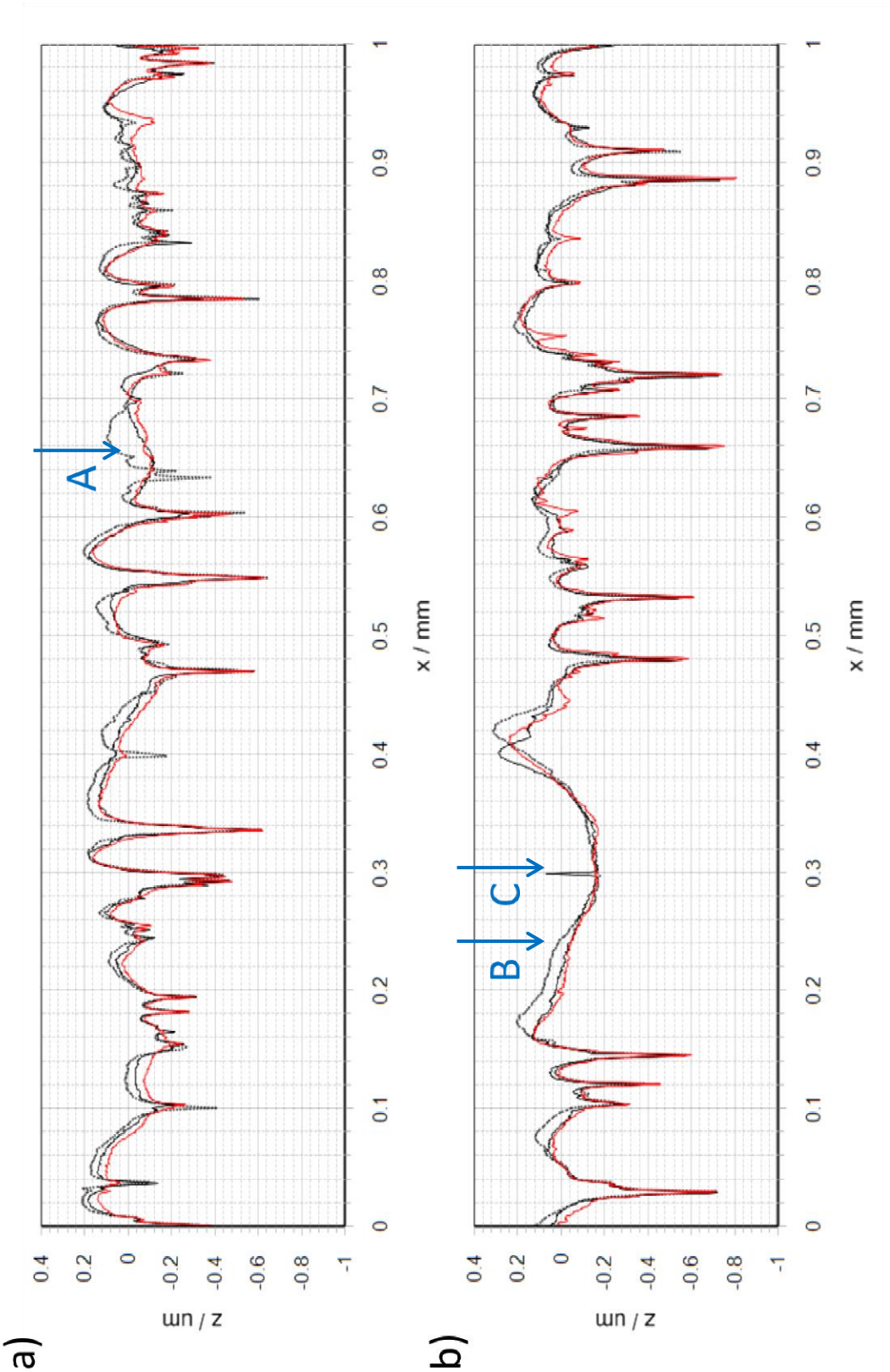

Figure 4-37 Load stage 17 (black dotted) load stage 18 (black solid) load stage 26 (red) superimposed for the fast, low hardness disk

4.4.5 Height distributions for surfaces of different hardness

In a similar manner to values plotted for two hard disks, profiles were relocated manually in the z direction by seeking the best possible alignment of the valley features. The histograms have been created which describe the change in surface topography of the disks of different hardness. Histograms are presented in terms of standard deviations and normalised in sections 4.4.5.1 and 4.4.5.2. The results demonstrate how the roughness on the low hardness disk quickly becomes skewed with the positive roughness features becoming flattened, leaving the valleys relatively undisturbed. Results for the hard disk show very little modification, as seen in profile traces and the calculated average roughness parameters shown in Table 4-7. With little modification occurring, only the height distributions for the initial profile and the last set of measurements are presented. Data for a range of measurements however is shown in

Table 4-8. Shown in each of the figures are the asperity heights in standard deviations with a normal distribution curve superimposed for comparison.

Table 4-8 Roughness distribution data for test disks of different hardness

Load Stage	Disk Position	Standard Deviation / µm	Skew	Kurtosis
Unrun	Fast	0.295	-0.291	2.732
	Slow	0.479	-0.734	4.661
1	Fast	0.231	-0.829	3.416
	Slow	0.448	-1.028	4.988
2	Fast	0.220	-0.964	3.839
	Slow	0.458	-1.068	5.092
3	Fast	0.220	-0.985	3.921
	Slow	0.450	-1.038	4.925
4	Fast	0.219	-1.044	4.018
	Slow	0.454	-1.014	4.854
5	Fast	0.215	-1.050	4.054
	Slow	0.451	-1.034	4.904
16	Fast	0.215	-1.055	4.061
	Slow	0.451	-1.026	4.906
17	Fast	0.154	-1.432	6.426
	Slow	0.441	-1.089	5.067
20	Fast	0.139	-1.508	7.125
	Slow	0.438	-1.106	5.105
23	Fast	0.138	-1.701	9.714
	Slow	0.437	-1.114	5.150
27	Fast	0.133	-1.646	8.173
	Slow	0.431	-1.081	4.931

4.4.5.1 *Soft disk roughness modification*

Figure 4-38 shows the histogram of initial measurements from the faster, low hardness disk which can be seen to align very closely with the superimposed normal distribution curve, with the majority of measurements falling within two standard deviations of the mean value.

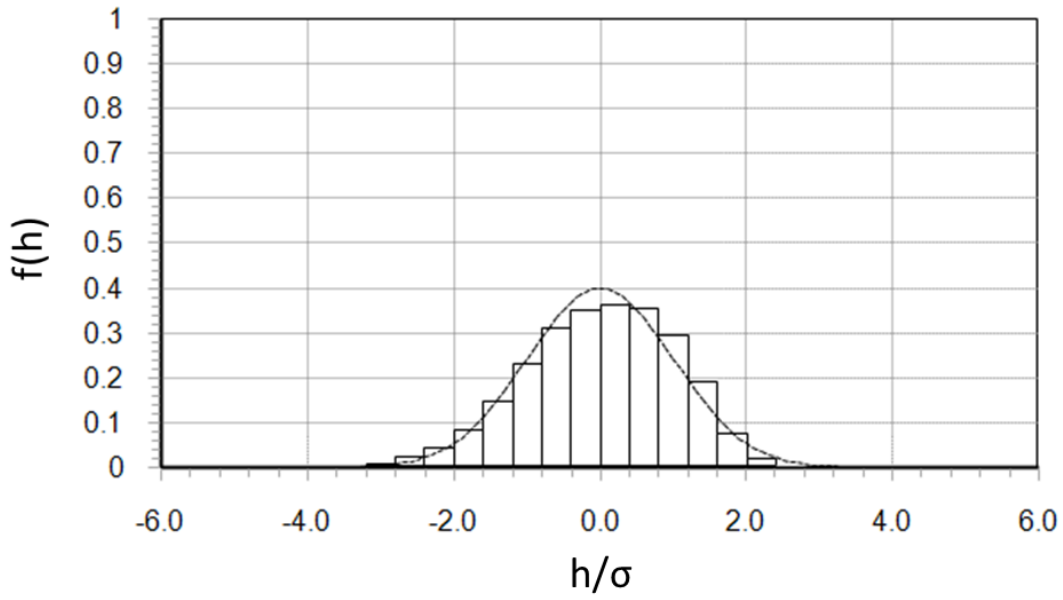

Figure 4-38 Histogram of surface heights from the un-run lower hardness disk with Gaussian distribution curve (dashed)

Following the first load stage the histogram in Figure 4-39 shows that a large amount of modification has occurred. This can be seen by the cropping in the positive tail of histogram. As a result of this, positive measurements become less widely distributed so that the high points of the profile are much closer to the mean. The negative tail of the histogram however has not experienced much change.

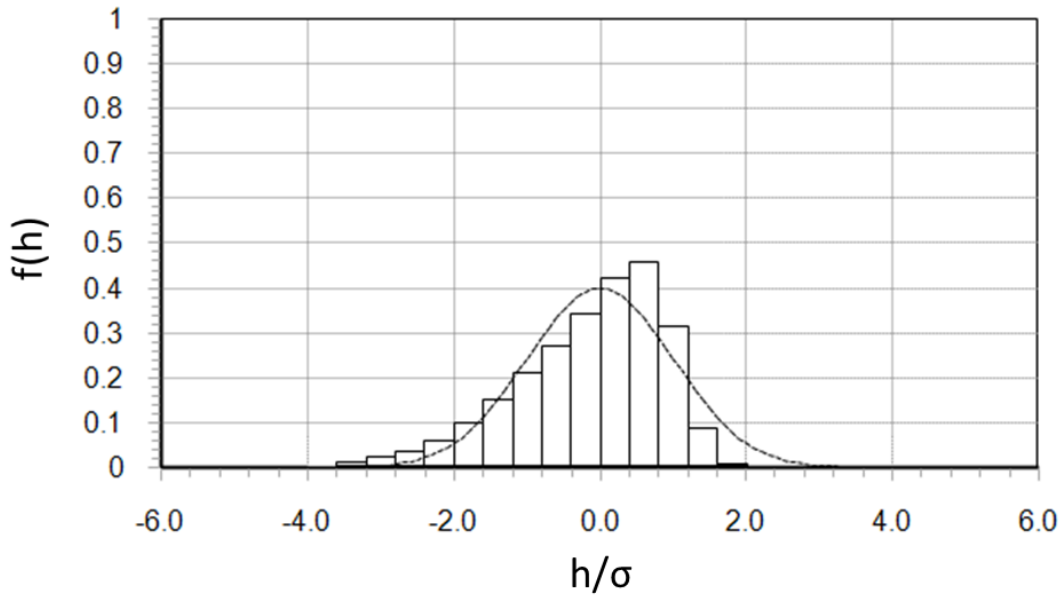

Figure 4-39 Histogram of surface heights taken following load stage 1 for the lower hardness disk with Gaussian distribution curve (dashed)

The histogram for heights after load Stage 2, shown in Figure 4-40, demonstrates that far less change has occurred during this load stage than during the initial load stage. As shown in realigned profile measurements, the tips of the asperities are seen to become more rounded due to the lower lambda ratios experienced. These subtle changes can be seen in the frequency histogram, where there is an increase in count of features lying close to the original mean line where asperity features are deformed by the running process.

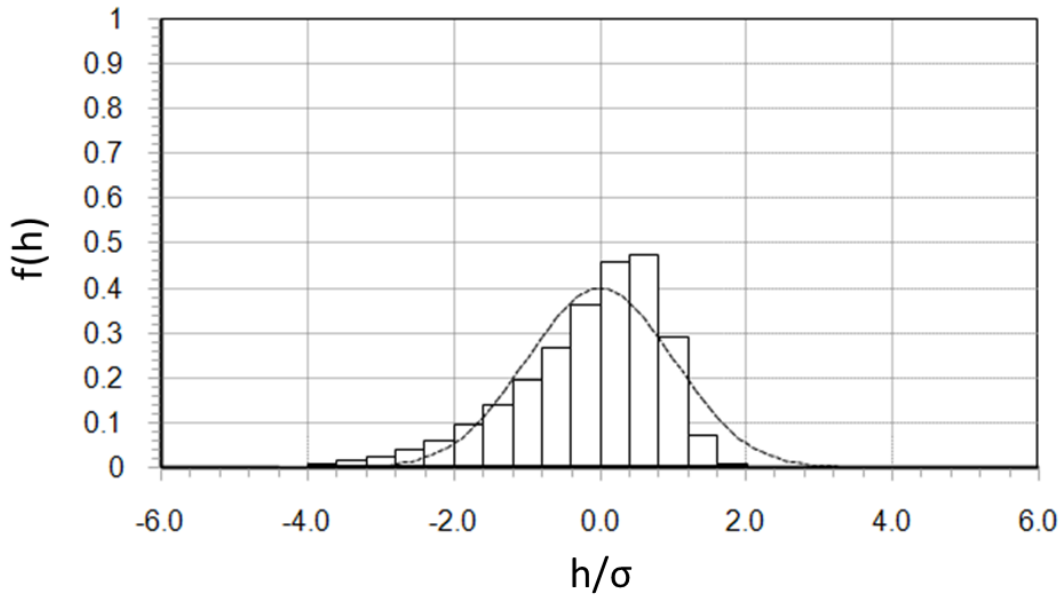

Figure 4-40 Histogram of surface heights taken following load stage 2 for the lower hardness disk with Gaussian distribution curve (dashed)

Further histogram plots demonstrate very subtle changes occurring due to the wear processes and are broadly similar. In Figure 4-41 these differences can be seen for Load Stage 16 where positive features have become more rounded. Despite these changes occurring to the asperity tips, the negative tail of the distribution curve remains relatively stable and unchanging between experiments. This demonstrates that the wear and plastic deformation processes occur at the tips of the asperity features. Average roughness values show some change due to wear between experiments, but the overall shape of the distribution which has been generated by the initial plastic deformation processes has remained consistent.

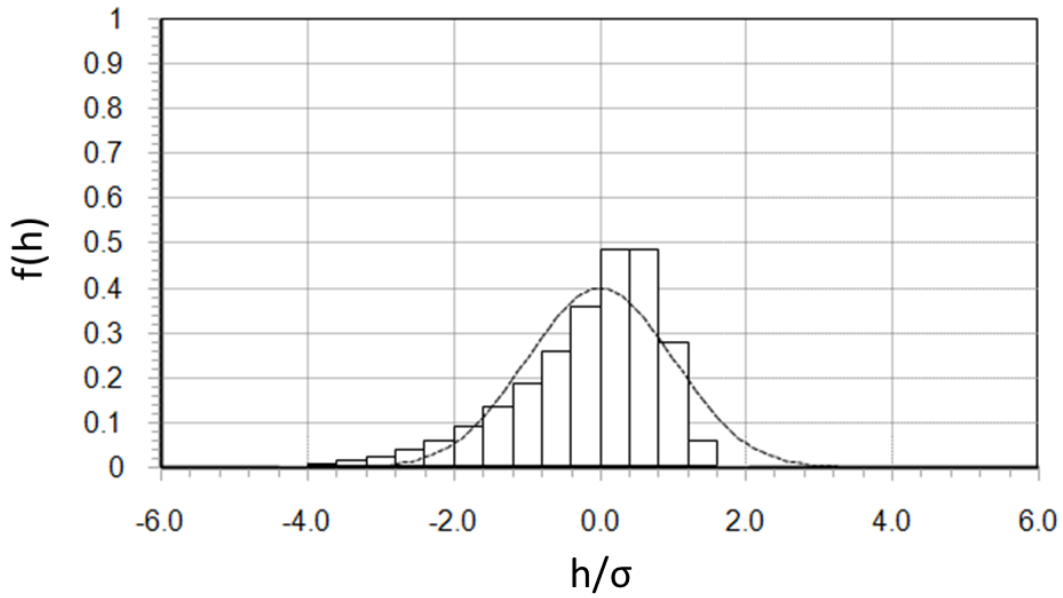

Figure 4-41 Histogram of surface heights taken following load stage 16 for the lower hardness disk with Gaussian distribution curve (dashed)

For distributions plotted using measurements taken at reduced lambda ratios, the modification of roughness features is plainly visible. It can be seen in Figure 4-42 that an increase in measurements that register below the original mean line is apparent – this is due to many of the asperity features becoming run in to a similar level as the original mean line, which is apparent on observation of relocated profile measurements.

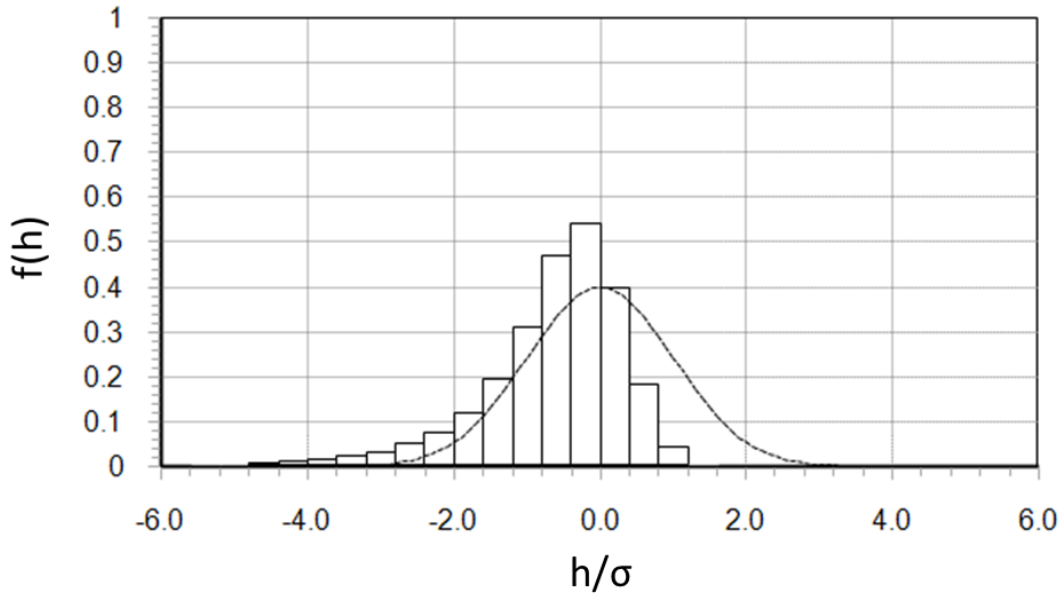

Figure 4-42 Histogram of surface heights taken following load stage 17 for the lower hardness disk with Gaussian distribution curve (dashed)

Further wear processes at work for load stages 19 and onwards show growth in frequency of more negative profilometer readings with the peak of the distribution becoming more rounded as the remaining prominent features become worn. This characteristic is demonstrated in Figure 4-43 where the height distribution following load stage 27 is shown.

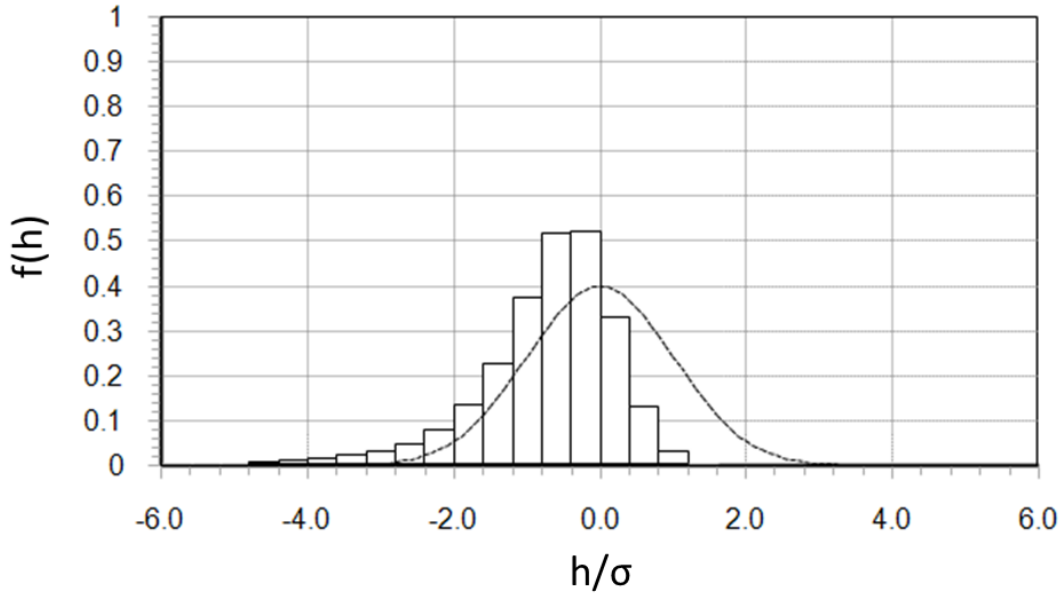

Figure 4-43 Histogram of surface heights taken following load stage 27 for the lower hardness disk with Gaussian distribution curve (dashed)

4.4.5.2 *Hard disk roughness modification*

Observing realigned profile measurement throughout the running process, it is clear that little change had occurred on the harder surface. This is also reflected in the similar final average roughness value of the surface in Table 4-7. The height distributions of the surface show little variation, with only the most extreme features becoming more rounded and the shape maintaining a nominally Gaussian appearance. Shown in Figure 4-44, the nominally Gaussian distribution of the un-run hard surface can be clearly seen.

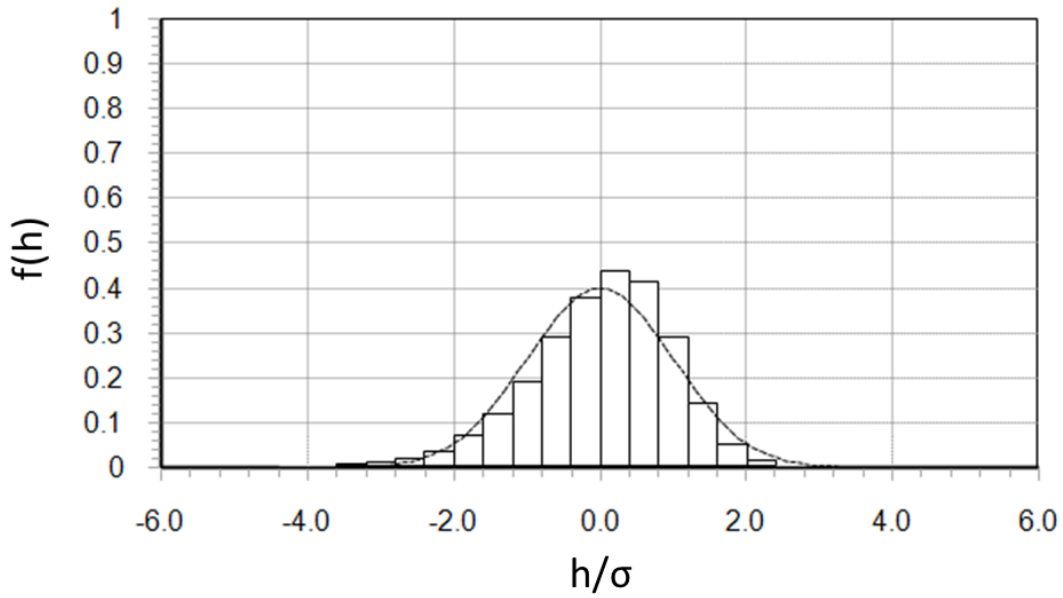

Figure 4-44 Histogram of surface heights taken from the un-run harder surface with Gaussian distribution curve (dashed)

Following the initial loading phase, plastic deformation could only be seen to occur in the finest asperity features. This is further emphasised in Figure 4-45, where the height distribution for load stage 1 attained by amassing all 12 profiles from the surface shows very little modification with only the most extreme heights curtailed.

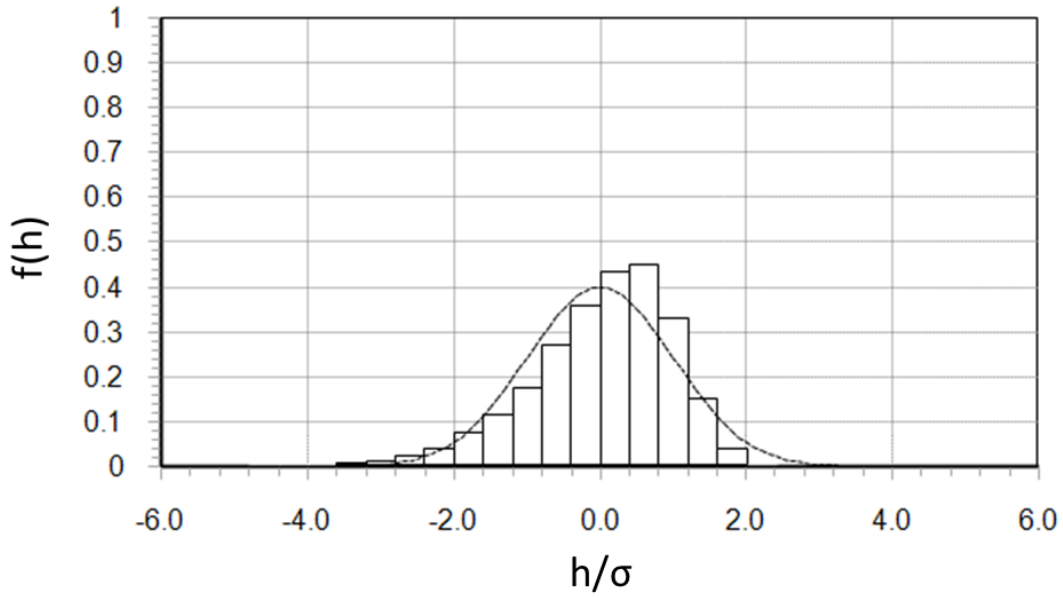

Figure 4-45 Histogram of surface heights taken from the harder surface following load stage 1 with Gaussian distribution curve (dashed)

There was very little modification to the harder surface following the initial loading experiment and the histograms for load stages 2 – 16 have not been presented. Figure 4-45 shows the histogram for load stage 17 where the lambda ratio has been reduced by elevating the temperature and reducing the entrainment speed. Additional modification can be seen to affect the most extreme asperities in Figure 4-45 whilst the bulk of the distribution remains relatively unchanged.

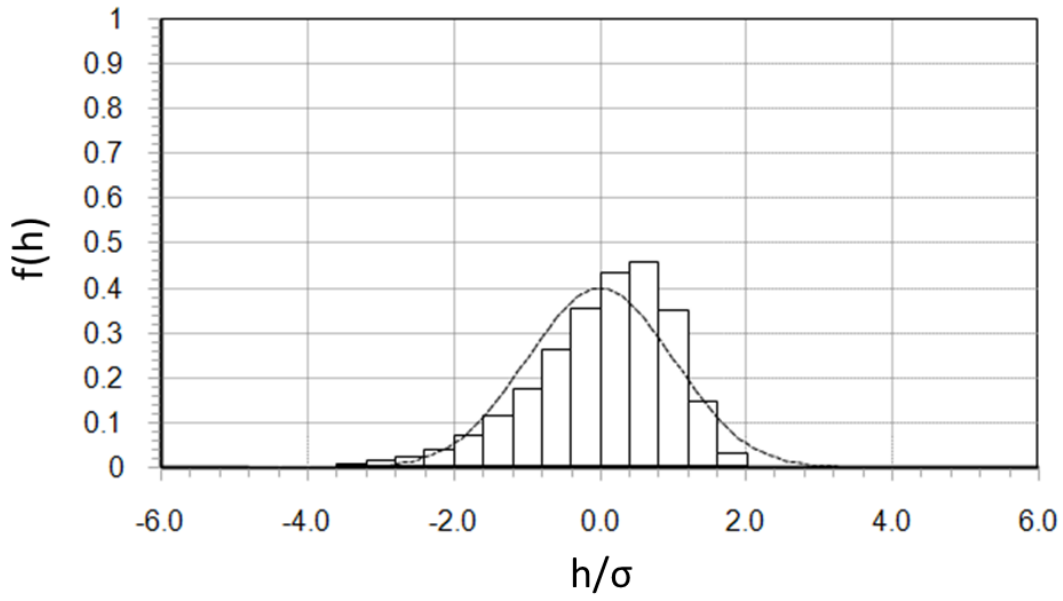

Figure 4-46 Histogram of surface heights taken from hard surface following load stage 17 with Gaussian distribution curve (dashed)

All subsequent 10 load stages can be seen to have little impact on the height distribution of the harder surface and the general shape of the histogram can be seen to remain very similar, as shown in Figure 4-47.

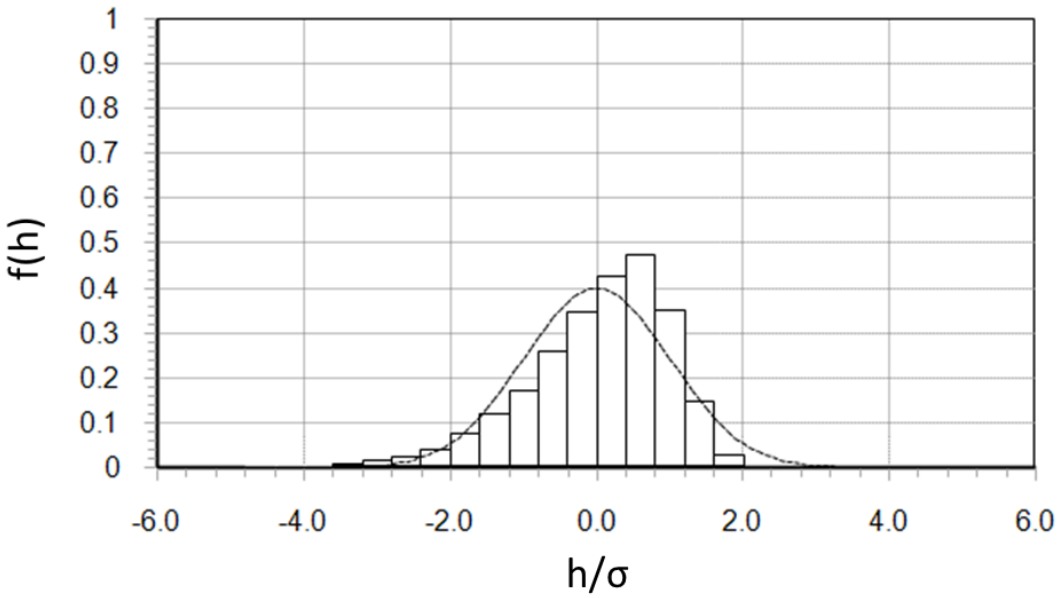

Figure 4-47 Histogram of surface heights taken from the harder surface following load stage 27 with Gaussian distribution curve (dashed)

4.5 Discussion

Results for both sets of disks used in experimentation have shown that the plastic deformation, occurs rapidly. Similar results have been shown by Barber et al. (1987), where a range of surface finishes were all found to reach a nominally steady Ra value in a similarly rapid manner upon the application of load. The experimental results obtained using the surface profilometer have shown distinct differences in the running-in behaviour of contacts between surfaces of equal hardness and contacts between surfaces of different hardness. In the situation where a hard surface comes into contact with a lower hardness surface under moderate loads, a degree of abrasive wear is observed at the tips of the asperity features. This is accompanied by a large proportion of the plastic deformation occurring in the lower hardness surface, whereas the harder surface tends to experience deformation only at the most aggressive protrusions.

Based on experiments conducted with disks of different hardness it is clear that the shear force at the surface can also have an impact on the plastic deformation experienced by

asperity features. This can be seen most clearly in Figure 4-28 where asperities on the lower hardness surface appear to become tilted under the influence of traction.

It has also been seen that when considering plastic deformation of surfaces, it is important to take into account not only the normal load applied but also the lambda ratio. Reducing lambda ratios increases the local contact pressures experienced at asperities. This is a result of a lower proportion of the load being supported by an oil film and a greater proportion therefore being transferred due to direct surface contact. Results from rough surface numerical simulations presented in Chapter 6 have also shown this, where thin films and metallic contact result in high pressures at asperities as they traverse the contact zone.

It can be seen on inspection of profile traces that where plastic deformation tends to occur, it makes the largest changes to finer asperities which experience higher contact pressures. It can also be seen that the reduction in height experienced by asperity features is related to their overall prominence in relation to other neighbouring features. A prominent asperity feature on one surface will be relatively isolated when brought into contact with another and must experience a certain amount of deformation before other features can be brought into contact, increasing the bearing area and supporting the load (Abbott and Firestone, 1933). Evidence of this can be seen in histograms produced from profile data, where plastic deformation causes surface heights to become increasingly negatively skewed and less distributed about the mean.

Surfaces of a similar hardness exhibit far less wear, maintaining finer features as they run in. However, under moderate conditions after sustained loading, the mechanism of deterioration appears to be much more akin to micropitting with the plastically deformed asperity peaks, which have been associated with regions of high residual tensile stress as seen by Bryant et al. (2012), giving way to new valley features. This failure mechanism has in the past been associated with the roughness features of the surface as seen by Tao et al. (2003). It has also

been found that lubricant additives may in some cases accelerate failure (Winter, 1990, O'Connor, 2005).

Relocated profiles from the surfaces very clearly demonstrate the strong relationship between the location of surface fatigue with prominent asperity features. Furthermore – realigning fatigued profiles with the un-run surface appears to demonstrate a relationship between the most severely plastically deformed regions during running and subsequent locations of surface fatigue, though this will also be influenced by their retained prominence in the contact. An initial observation of the offset of valley features from locations of previous asperity features appears to show results that are consistent with modelling work performed by Sharif et al. (2012), where it was postulated that the direction of sliding was of influence to damage location due to the micro-EHL outlet pressure spikes. It has also been verified that where micropitting is seen to occur, a greater amount of modification will be present on the slower surface, despite undergoing fewer load cycles. The reason for this is considered to be related to the load cycling encountered by asperity features as they traverse the contact zone (Sharif et al., 2012).

As with the work of Østvik and Christensen (1968) and more recently Lord and Larsson (2008) the test data has shown that the effect of running-in improves the hydrodynamic performance of the surface. This has been inferred from the behaviour of the contact voltage signal, where progressive running under moderate conditions has been found in some cases to yield higher initial contact voltage values, indicating reduced metallic contact. It has also been shown that the initial reduction in roughness experienced under a given loading regime will result in a decrease in measured friction.

In order to produce experiments that offer a better comparison with modelling work, it would be useful to run a harder, highly superfinished surface against a ground surface. As in current work asperity features experience pressures dependent on their asperities interacting as they

slide through the contact. In the situation where a highly polished surface runs against a rough surface, contact points would be more isolated due to the dependence of interaction heavily weighted on the rough surface, and a stronger association between fatigue location and asperity features would be possible. This could also prove valuable for work into the simulation of contacts as the difficulty in aligning rough surfaces may result in simulations including the effects of asperity interactions which, if they occurred in practice, would modify the geometry of the interacting asperities.

4.6 Conclusion

Where plastic deformation occurs in lubricated contacts, it is a rapid process and is influenced not only by the smooth surface contact pressure but also by the lambda ratio. It is postulated that the level of running-in experienced by a rough surface contact will be a function of both the maximum applied load and minimum lambda ratio experienced at the contact.

The running-in process will negatively skew the surface topography as plastic deformation is seen to occur most significantly at the asperity peaks which support the load under conditions of mixed lubrication.

In cases where surface fatigue is seen to occur, it can be associated with the prominent asperity features present on rough surfaces.

Where two surfaces of greatly varying hardness are loaded against one another, plastic deformation occurs almost exclusively in the softer surface.

5 Thermal Investigation into Mixed Lubrication of Steel Surfaces

5.1 Introduction

In this chapter, experiments conducted using the twin disk rig with surfaces that had previously been run in are reported. A description of the test rig is given in Chapter 3 and the running in process of the test disks is described in Chapter 4. The purpose of these tests was to observe the behaviour of friction, temperature and contact voltage at constant load under variable degrees of entrainment and sliding speed in rough surface contacts – simulating realistic conditions encountered in power transmission components and providing reliable data for comparison with computational models. In order to conduct these tests, the original two-pole motor driving the test rig was substituted for a six-pole drive, providing greater stability at lower speeds and enabling a broad study of lubrication over a range of lambda ratios extending well into the mixed lubrication regime.

Pairs of disks of both similar and varying hardness were selected for these experiments allowing the effect of differing composite surface roughness to be investigated. In order to observe the instantaneous contact voltage fluctuations described in the work of Furey (1969), it was decided to use software that would acquire and record these fluctuations at high frequency to further understand the contact voltage signal in an effort to correlate these variations with film thickness.

Experiments conducted at different slide roll ratios are distinct from one another at higher loads in terms of the level of heat generated. These variations demonstrate the relationship between surface temperature and film thickness and the influence of this on the friction coefficient and metallic contact levels under the same sequence of constant speed and load conditions.

The hard on soft disk configuration used for one of the sets of experiments demonstrates different behaviour in comparison to tests using disks of similar hardness, partially due to differences in surface topography.

For each test condition an approximate value for the lambda ratio was calculated using surface roughness measurements taken at the centre of the running track and values of bulk disk temperatures obtained from the disk thermocouples. The values obtained for lambda ratios generally lay within the range in which mixed lubrication has been found to occur (Guangteng and Spikes, 1997). It was seen that under conditions of moderate sliding, both the contact voltage and the friction coefficient varied systematically with the lambda value showing very similar behaviour for both the hard-hard and the hard-soft configuration. This similarity was reduced at the higher slide-roll ratio considered where the resulting high temperatures caused much decreased lambda values at higher loads in excess of 1.2GPa. Results from the speed varying experiments at loads of 1.4GPa also showed a tendency for the highest speeds to yield lower contact voltage values – an indication of increasing asperity contact and the decline of the lubrication mechanism's effectiveness.

5.2 Test Procedure

Experiments were conducted on disks which had previously been run in, this allowed the author to investigate the influence of a range of parameters on the mixed EHL contact without being required to consider the impact of changing topography.

Tests were performed at constant load with the speed varied at predetermined intervals throughout. The results were recorded using the data acquisition software described in Chapter 3. Oil from the thermostatic temperature controlled bath was supplied using separate jets to both the inlet and outlet of the contact. Prior to carrying out a test, the rig was run for 2 hours under zero load with oil circulating at 50°C to stabilise temperatures. Tests would then commence with the rig running at the lowest entrainment speed, which corresponded to a fast

disk speed of 200rpm and a peripheral velocity of 0.797m/s. The speed was then increased every 300 seconds to the next value in the selected speed sequence until the maximum value of 2000rpm was attained after some 35 minutes, corresponding to a fast disk peripheral velocity of 7.97m/s. Once the rig had attained the highest speed for the test the speed was incrementally decreased through the same range of speed values, with the experiment concluding at the original speed. The overall rise in temperature of the test rig due to the heat dissipated at the contact meant that a further range of temperatures was attained in the descending region of the test, increasing the number of individual lambda values seen in these experiments. Slide-roll ratios of 0.25 and 0.5 were used in the set of experiments described.

A set of experiments was commenced at the highest load to be applied to the disks. It was observed that despite efforts to achieve complete running in of the disks prior to conducting the tests, measurements of the surfaces and the behaviour of the contact voltage signal implied a small degree of modification was taking place. This was due to the fact that although the running in tests were carried out at higher load they were also carried out at a higher speed than the lower values used in the speed varying tests. Further running in was thus found to occur at the lowest speeds in the tests. To achieve a stable surface roughness for the full tests the highest load test was conducted repeatedly until the results became repeatable. This meant that the surface roughness changes due to plastic deformation of the asperities were complete and no further changes would occur during the tests run at lower loads. This allowed the aim of performing a full set of experiments at all speeds and loads with a nominally unchanging topography to be achieved. Repeat experiments were run at each load to ensure consistent data. The range of loads used and their resultant contact pressure and contact dimensions are shown in Table 5-1.

Table 5-1 Nominal loads applied to disks and resulting maximum Hertzian pressures and dimensions

Load / N	Max Hertzian Pressure / GPa	a / mm	b / mm
850	1.0	0.324	1.190
1120	1.1	0.357	1.309
1460	1.2	0.389	1.428
1850	1.3	0.422	1.550
2320	1.4	0.454	1.667

5.3 Results

Constant load, speed varying experiments were conducted on three pairs of transversely ground disks. Two experiments were conducted on disk pairs of similar hardness and roughness at different slide to roll ratios and a further set of experiments was conducted on a pair of disks of differing hardness and roughness. The initial and final Ra values of the surfaces used are shown in Table 5-2. The load was varied between experiments from the lowest value of 850N resulting in a maximum Hertzian contact pressure of 1.0GPa to the highest of 2320N giving a maximum pressure of 1.4GPa. A maximum load of 1.4GPa was chosen in order to avoid conditions that might initiate scuffing failure - as it was of importance in this work for the author to preserve the test specimens for subsequent measurement.

Table 5-2 Initial and final Ra values for disks used in speed varying experiments

Disk Set Designation	Shaft Mounting	SRR	Steel Type	Disk Serial Number	Initial Ra / µm	Final Ra / µm	Vickers Hardness
A	Fast	0.25	RR6010-B	38	0.377	0.267	842
	Slow		RR6010-B	31	0.347	0.233	834
B	Fast	0.25	RR6010-A	44	0.227	0.084	652
	Slow		RR6010-B	32	0.343	0.323	801
C	Fast	0.5	RR6010-B	2	0.318	0.231	808
	Slow		RR6010-B	14	0.365	0.232	819

5.3.1 Experiments at Slide Roll Ratio = 0.25

A moderate level of sliding was selected for the first set of experiments to reduce the likelihood of scuffing failure. The set of gears used to connect the shafts had 35 teeth on the pinion and 45 teeth on the wheel, resulting in a gear ratio of 7:9 and a slide roll ratio of 0.25 at the contact. The resultant disk speeds at each of the stages is shown in Table 5-3. Experiments were conducted on disk set A and disk set B.

Table 5-3 Data for disk kinematics when geared to a slide-roll ratio of 0.25

Time / s	Fast Shaft Speed / rpm	Fast Surface Peripheral Velocity / ms^{-1}	Slow Surface Peripheral Velocity / ms^{-1}	Entrainment Speed / ms^{-1}	Sliding Speed / ms^{-1}
0	200	0.798	0.621	0.709	0.177
300	300	1.197	0.931	1.064	0.266
600	400	1.596	1.241	1.419	0.355
900	500	1.995	1.552	1.773	0.443
1200	750	2.992	2.327	2.660	0.665
1500	1000	3.990	3.103	3.547	0.887
1800	1500	5.985	4.655	5.320	1.330
2100	2000	7.980	6.206	7.093	1.773
2400	1500	5.985	4.655	5.320	1.330
2700	1000	3.990	3.103	3.547	0.887
3000	750	2.992	2.327	2.660	0.665
3300	500	1.995	1.552	1.773	0.443
3600	400	1.596	1.241	1.419	0.355
3900	300	1.197	0.931	1.064	0.266
4200	200	0.798	0.621	0.709	0.177

5.3.1.1 Disk Set A– Test Data

Results from experiments conducted at a slide to roll ratio of 0.25 for disk set A are presented in figures 5-1 to 5-5. Figure 5-1 gives the results obtained at the lowest load where the maximum Hertzian pressure for corresponding smooth surfaces is 1.0GPa. The figure shows the five quantities measured during the experiment plotted against time. During this test the contact voltage measurement was close to the maximum value of 43 mV for most of the test and only showed lower levels during the first and last stages where the shaft speeds were at their lowest values. The measured friction value can be seen to be almost constant over each fixed speed section and has lower values in each fixed speed stage as the speeds increase, and vice versa.

The highest values obtained are about 60 N and the lowest is 28 N. The temperatures measured by thermocouples embedded beneath the disk surface start at around 56 °C at the start of the test and rise slowly from speed stage to speed stage, reaching peak values of

around 64 °C when the highest speed is reached. The slow disk thermocouple signal experiences a shift of about 4 °C at that speed stage. This feature was investigated and is believed to be due to a speed related electrical interference. The variation of disk temperature in this test is low in comparison to those carried out at increased loads.

The variation in contact voltage observed at the lowest speeds in Figure 5-1 becomes more distinct in figure 5-2 which presents the results for a maximum Hertzian pressure of 1.1 GPa. The high value of 43 mV is seen to occur for a shaft speed of 400 rpm or above, but the value at the lowest speed stages shows a transient variation over the speed stage. During the first speed stage the initial value is close to 43 mV but this falls, rapidly initially, to reach a near steady value of 30 mV at the end of the stage. During the last speed stage the value falls abruptly from 43 mV to about 18 mV as the speed change occurs and then climbs, rapidly initially, and then less rapidly to reach a value of 30 mV at the end of the speed stage. This behaviour is attributed to the temperature changes occurring during the speed stage. In the first speed stage heat starts to be dissipated at the contact and the disk temperatures rise during the speed stage, with a resulting fall in the viscosity of the lubricant film separating the surfaces. This falling viscosity is reflected in a reducing film thickness and an increase in metallic contact as indicated by the contact voltage measurement. Conversely, at the beginning of the last speed stage there is an immediate loss of entrainment velocity leading to increased metallic contact and reduced contact voltage. The disk temperatures correspond to the previous load stage but then start to fall in response to the reduction in heat generation at the contact. The falling disk temperature over the speed stage leads to increasing viscosity and film thickness. It is interesting to note that the final contact voltage in the speed stage is about 30 mV which is also the value at the end of the first speed stage. This pattern of approach to the final contact voltage value from above during the speed increasing phase of the experiment and from below during the speed decreasing phase is characteristic of all the experiments carried out. The friction values measured in this experiment are higher than in the

1 GPa test and vary from 83 N at the slowest speed to 38N at the highest speed. This increased friction leads to a greater increase in measured disk temperatures during the test.

The pattern of measurements described is seen to a greater extent in the remaining tests in this sequence. Figure 5-3 presents the results for the 1.2 GPa load case. The measured contact friction values vary between 112 N at the lowest speed and 55N at the highest speed. The measured temperatures now climb higher reaching 72 °C for the fast disk which reaches a higher temperature than the slow disk. This is a characteristic of disk tests with appreciable energy dissipation at the contact (Patching, 1994). The contact voltage measurement pattern is largely unchanged by the increased load but the values at the end of the first and last speed stages are no longer the same which is in accordance with the observation that the measured disk temperatures are now different at these times.

The trends discussed for Figure 5-2 continue in Figure 5.4 where the friction measurement range is from 72 N to 140 N and a highest disk temperature of 79 °C is observed. The change in contact voltage in the last speed stage has an initial reduction to 8 mV with subsequent recovery to 25 mV. This pattern of contact voltage change can also be seen to occur to a lesser extent in the penultimate speed stage.

Figure 5-5 shows the results for a load of 1.4 GPa with friction forces varying between 94 N and 176 N and a maximum measured fast disk temperature of 86 °C. The fall in contact voltage at the start of a load stage and subsequent recovery is apparent in the last three speed stages with a lowest value of 6 mV attained at the beginning of the slowest speed stage.

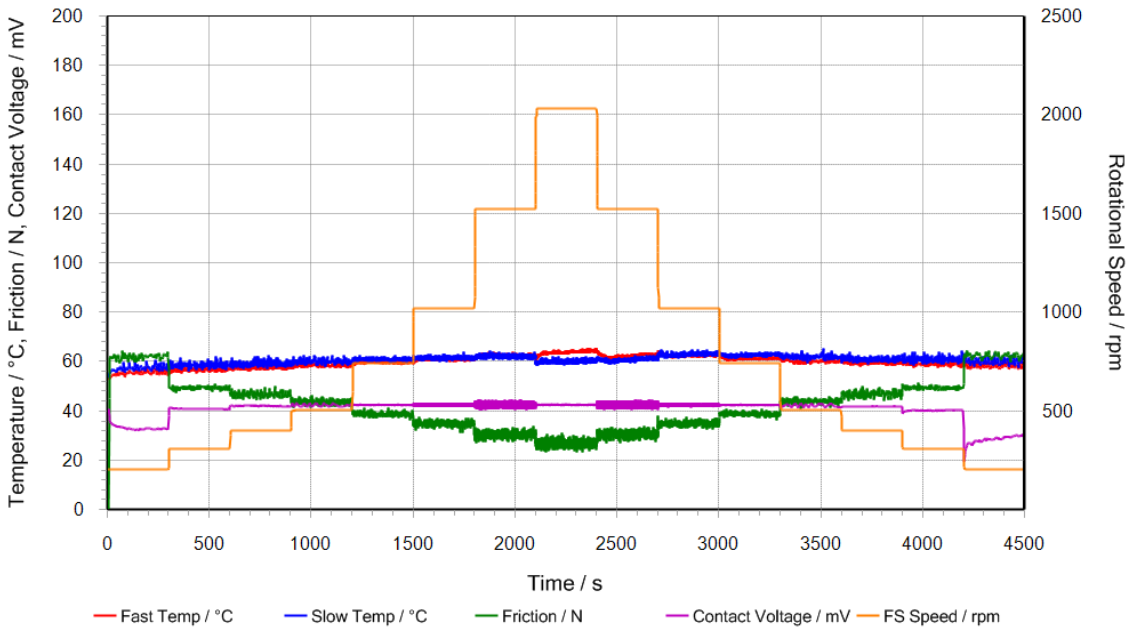

Figure 5-1 Speed varying experiment for maximum pressure of 1.0GPa at a SRR of 0.25 on disk set A

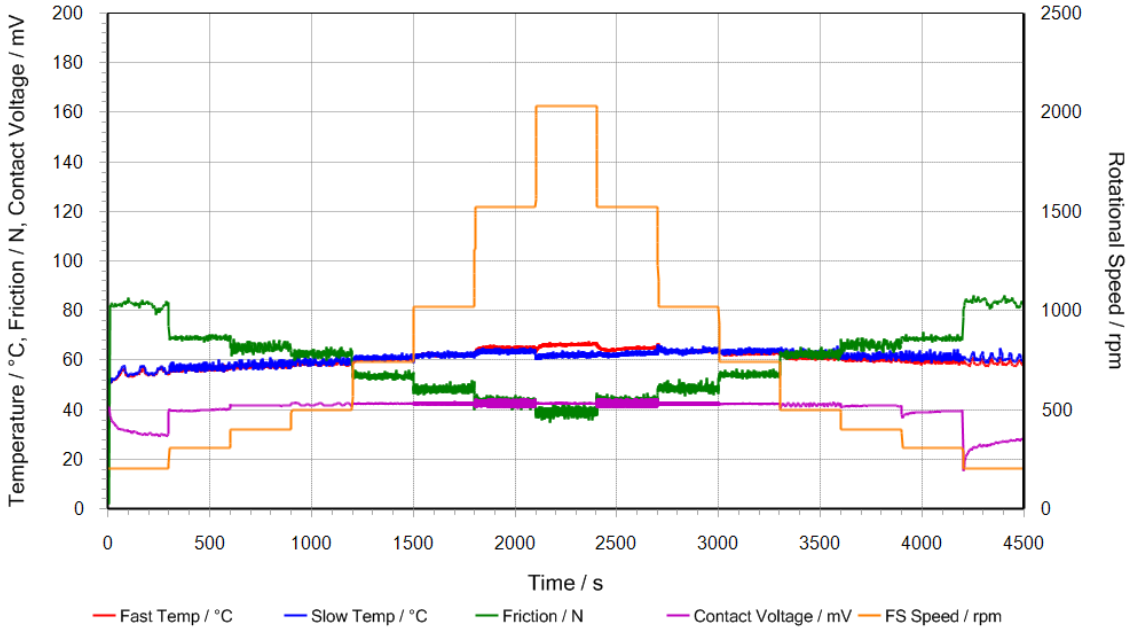

Figure 5-2 Speed varying experiment for maximum pressure of 1.1GPa at a SRR of 0.25 on disk set A

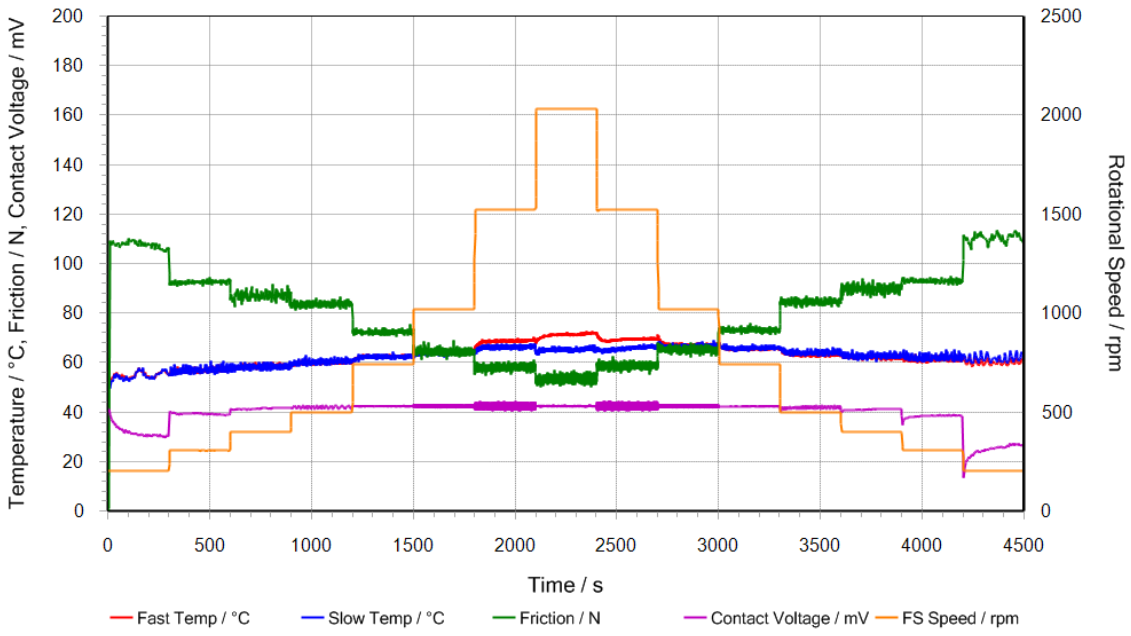

Figure 5-3 Speed varying experiment for maximum pressure of 1.2GPa at a SRR of 0.25 on disk set A

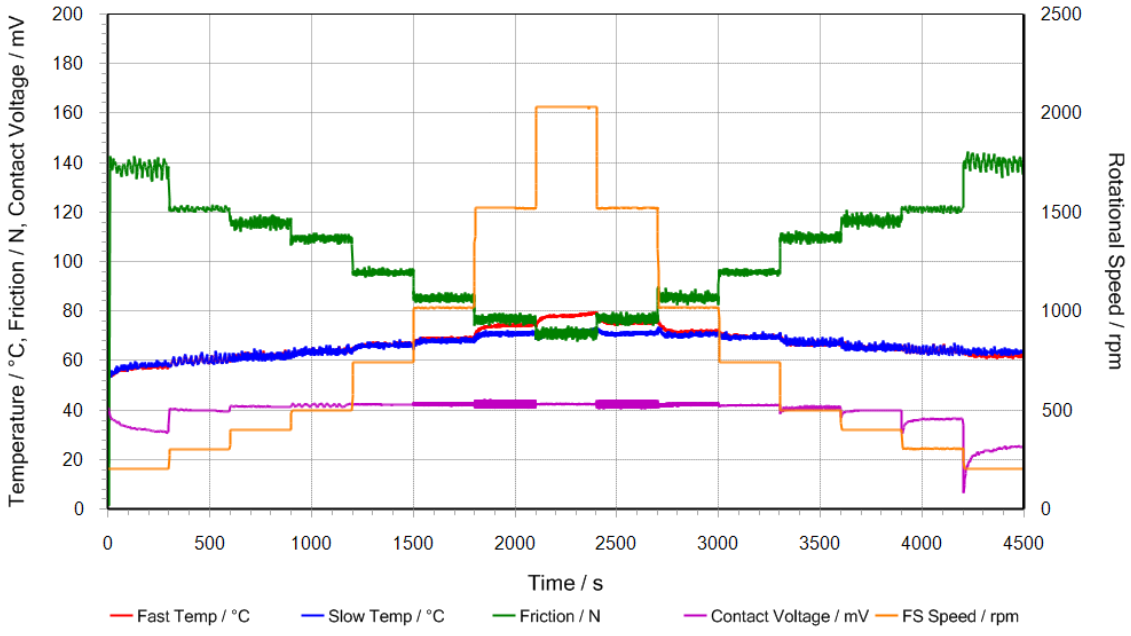

Figure 5-4 Speed varying experiment for maximum pressure of 1.3GPa at a SRR of 0.25 on disk set A

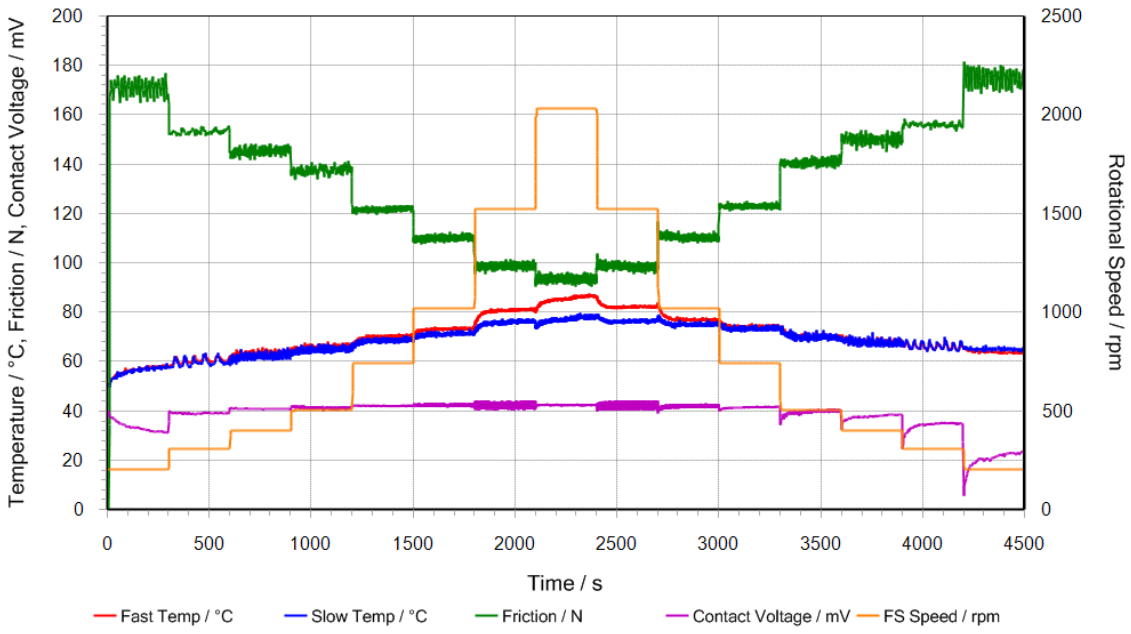

Figure 5-5 Speed varying experiment for maximum pressure of 1.4GPa at a SRR of 0.25 on disk set A

The results of this set of tests demonstrate the highly dependent nature of film thickness on lubricant viscosity and entrainment speed. The effect of viscosity on the contact can be seen in comparisons between experiments, where sudden changes in sliding speed result in transient bulk disk temperatures with speed held constant. At these times the levels of metallic contact can be seen to be greatly affected by seemingly mild fluctuations in temperature. At lower loads, the bulk disk temperature change between speed stages seldom exceeds a few degrees Celsius and the effect on metallic contact levels is less pronounced.

Under the moderate levels of sliding seen in this set of experiments, it is apparent that friction is most markedly affected by the step changes in entrainment speed. Increases and decreases in speed result in a step decrease or increase in friction, respectively, as the viscosity of the oil drawn through the contact varies. The temperature fluctuations experienced by the disks do not appear to have a major impact on the levels of friction recorded, and as a result the transducer signal appears nominally constant through each of the speed stages at the scale shown. At the beginning and end of each test, where the entrainment speed is lowest, increases in entrainment velocity can be seen to have a major impact on the friction value

recorded, as within the mixed lubrication region, increasing entrainment speed quickly reduces friction as the impact of roughness on the contact decreases.

Increased applied load causes greater heat generation at the contact, reduced inlet viscosity and decreased lambda ratios. Tests conducted at the highest load of 1.4GPa shown in Figure 5-5 demonstrate greater metallic contact occurring between the surfaces throughout. As the rig speed increases, it is also clear that heat is transferred more rapidly to the fast surface causing a divergence of the two thermocouple readings which is also apparent in results from scuffing tests by Patching et al. (1995). Throughout the experiments, it is clear a slight negative offset in the slow thermocouple signal occurs at the start of the highest speed stage – the cause of this was not isolated but is believed to be associated with electrical noise caused by the inverter driving the motor, due to the tendency for the offset to occur over the same high speed range in each of the experiments.

5.3.1.2 Disk Set B – Data Triggering Experiments

For disk set B which had different hardness values running in tests were carried out prior to conducting the speed variation tests which are reported in Section 5.3.1.3. In this investigation the disks were run together and their surfaces measured in accordance with the method described in Chapter 4. The plastic deformation that was recorded by stylus profilometry was seen to have occurred almost entirely in the softer surface with a degree of abrasive wear also present. The result of these experiments were two surfaces of significantly differing roughnesses.

Once the surfaces were considered to have stabilised, a number of experiments were conducted where the disks were loaded for brief intervals, in a similar manner to the running-in tests that had been carried out previously. The data acquired allowed the observation of the effects of rising bulk disk temperature on the repeatable contact voltage fluctuations which have been associated with intermittent metallic contact (Furey, 1969). Three different loads

were selected and the effect of heat generation on both the mean and instantaneous signal was examined.

Experiments were conducted at a fast shaft speed of 1500rpm using three maximum contact pressure values of 1.0GPa, 1.4GPa and 1.7GPa. Figure 5-6 shows the results for the 1.0 GPa load case. The upper figure (A) shows the variation of mean contact voltage, friction and disk thermocouple temperatures over the 25 second period for which the load was applied that commences at time t=0. These variables show a gradual increase in measured disk temperatures over the 30 s period with a steady reduction in contact voltage from 39 mV to 34 mV over the test and a constant, albeit noisy, value of measured friction. The lower figure (B) shows the measured contact voltage over 70 ° rotation of each of the triggered rotation cycles in a contour plot. The triggered cycles occur for every ninth rotation of the fast disk at the same point in the disk's rotation. The contour plot shows areas of near-zero contact voltage (orange and red plotted), suggesting metallic contact is occurring, that repeat at the same point in each rotation cycle over the length of the loading period with little change in mean contact voltage level. New areas of apparent contact become visible with the slight temperature rise, and an example of this is present at approximately 45 degrees and 6 seconds into the experiment. In general, the traces show low levels of metallic contact throughout, with the large bands of high voltage remaining relatively undisturbed. It is also important to note the intermediate voltages that occur sandwiching low regions. These could be related to the close approach of asperities where the film begins to conduct, or due to a capacitance effect with the lubricant charging and discharging. Even at this relatively low load there are still prominent bands of metallic contact occurring, which under extended operation could accelerate the initiation of fatigue failure. Also shown on the contact voltage contour plot are nominal values of the lambda ratio which show that over the length of the experiment, there is a slight decrease in value as bulk disk temperatures rise.

The calculated lambda value changes from Λ=2.7 to Λ=2 over the duration of the experiment as indicated in figure 5-6(b).

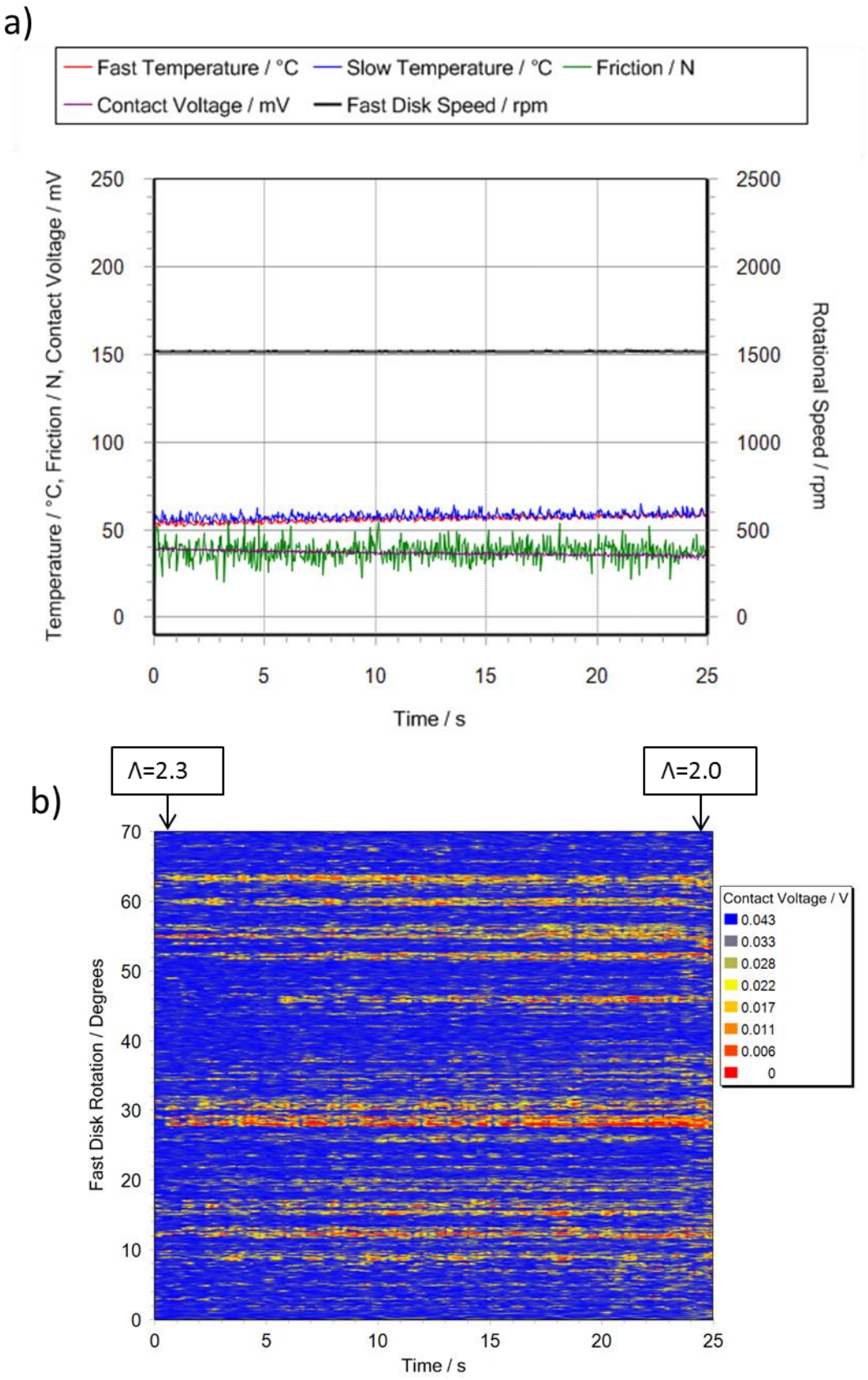

Figure 5-6 Experimental results from investigation of the effect of transient inlet temperatures on EHL contact run at 1.0GPa 1500rpm a) Test data b) Contour plot showing instantaneous voltage fluctuations

Figure 5-7 shows the corresponding results for the case where the load is 1.4 GPa. At this load there is a significant change in the measured temperatures with an increase of about 14 °C over the test with the measured contact voltage falling from 39 mV to 12.5 mV. The contour plot of triggered contact voltage traces shows a change of contact voltage conditions to lower values with increasing time at most rotation positions. There are some no contact regions that show greater persistence during the experiment. This can be observed in the bands of high voltage nominally aligned with 50 degrees of fast disk rotation that remains virtually unperturbed over the 25 seconds whilst regions either side can be seen to succumb to the effects of film thinning. This also agrees with approximate lambda values shown on Figure 5-7b which show a significant decrease from Λ=2.4 to Λ=1.6 over the 25 seconds. It is also clear that at high mean contact voltages generally shown in the figure at time zero there are isolated regions of persistent metallic contact, as can be seen aligned with the 30 ° position, where due to the combined topography of the surfaces, a narrow band of interaction can be seen to occur every 9th revolution due to the gear ratio between the test disks.

Figure 5.8 shows the results for the 1.7 GPa load case. At this load the measured disk temperatures rise by 24 °C over the 25s test and the mean contact voltage falls to near zero by time t = 15s. The initial instances of no contact, interpreted as 43mV, quickly give way to intermediate voltage levels and the low voltages associated with metallic contact as lambda ratios decrease with rising bulk disk temperatures. The lambda values fall from Λ=2.3 to Λ=1.25 over the duration of the test. The friction force measurement increases by over 20% during the test which is due to the rapidly thinning film. The triggered contact voltage contour plot paints a picture of rapid transition to persistent metallic contact, but it is important to remember that the actual regions over which asperity interaction occurs may be quite isolated and small in comparison to the whole contact, this is supported by a coefficient of friction in the region of 0.043 to 0.049.

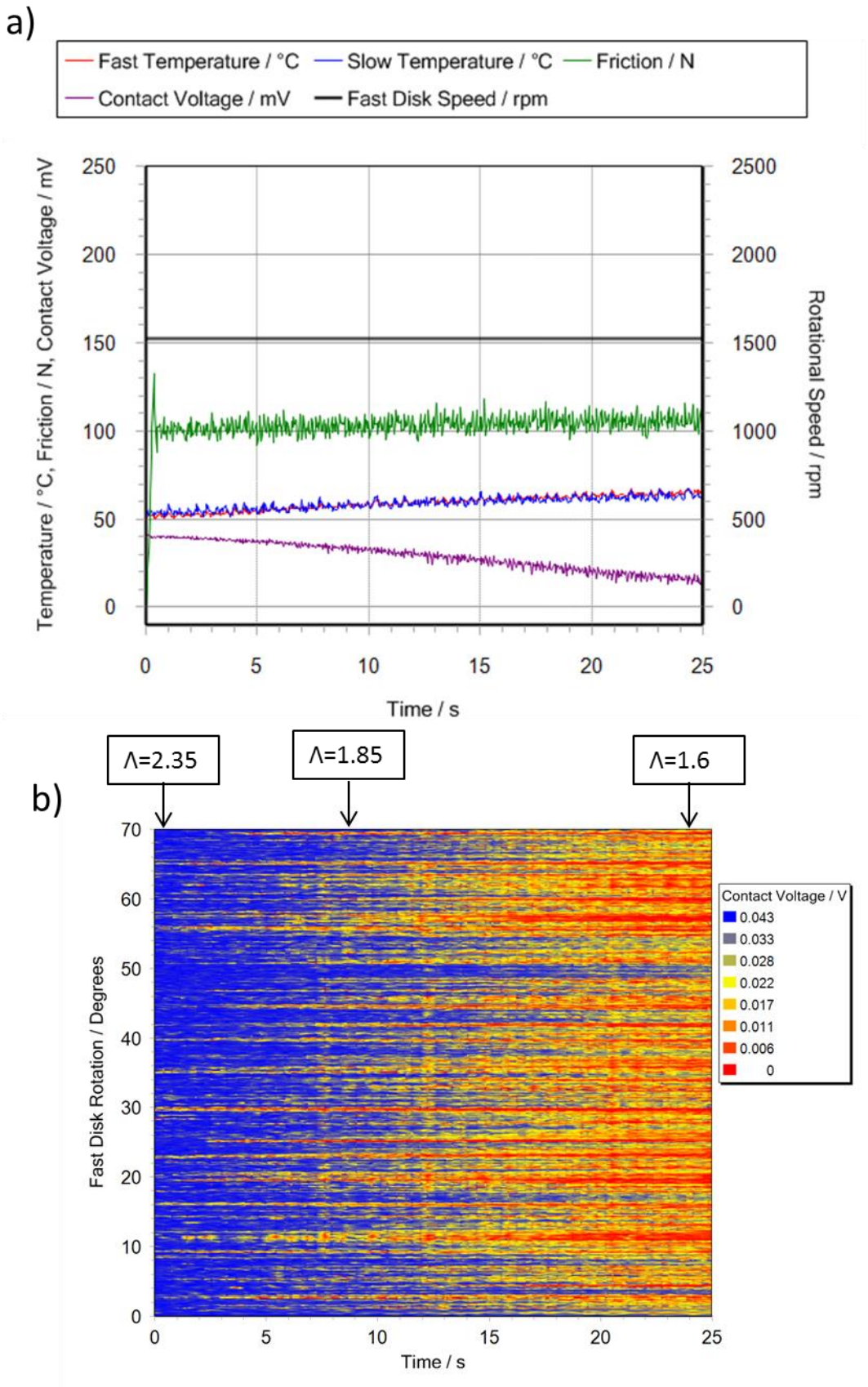

Figure 5-7 Experimental results from investigation of the effect of transient inlet temperatures on EHL contact run at 1.4GPa 1500rpm a) Test data b) Contour plot showing instantaneous voltage fluctuations

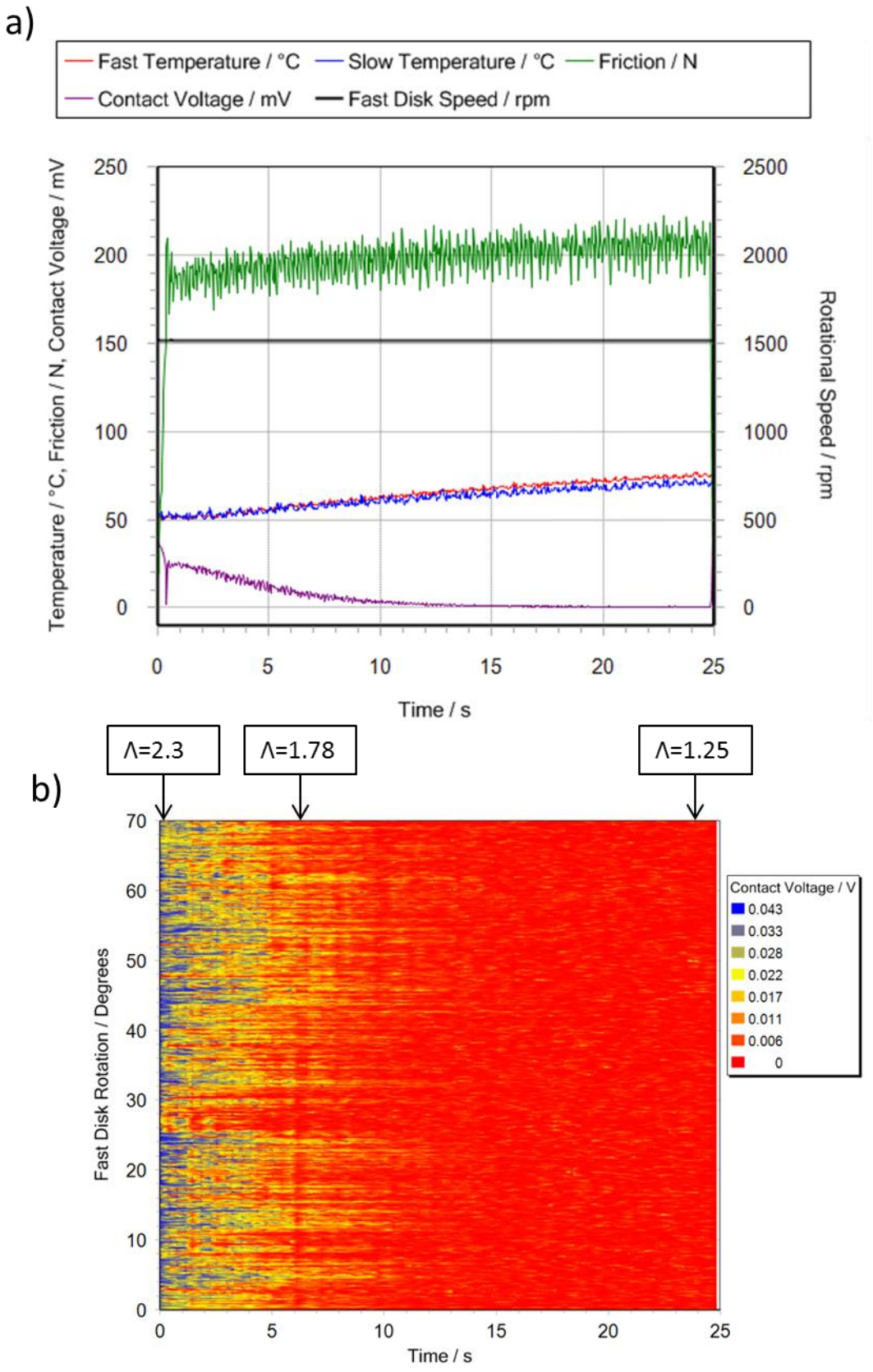

Figure 5-8 Experimental results from investigation of the effect of transient inlet temperatures on EHL contact run at 1.7GPa 1500rpm a) Test data b) Contour plot showing instantaneous voltage fluctuations

It can be seen by comparing Figure 5-7b and Figure 5-8b that although the increase in contact voltage corresponds with a reduction in lambda value for each figure, the calculated lambda values do not show good correlation with the mean contact voltage when compared across the figures. For example in Figure 5-7b where Λ = 1.6, the contact voltage has a value of approximately 15mV. In comparison to this, at higher load shown in Figure 5-8b where Λ = 1.78, the contact voltage is also 15mV. This is because the calculated lambda values are based on the measured temperatures of the thermocouples located 3mm beneath the running track. As the load is increased the radial temperature gradient within the disk will also increase, and so the difference between the surface temperature and the measured temperature will be greater at the higher load. This effect explains the apparent lack of correlation.

5.3.1.3 Disk Set B – Speed Varying Experiments

Speed varying experiments were conducted on these surfaces to examine behaviour of the contact voltage once the disks had run in. Upon commencing this set of experiments, the faster, softer surface had an Ra of approximately 0.09 µm whereas the slow surface had all but maintained the manufactured Ra of 0.35µm.

Due to the degree of abrasive wear that appeared to be occurring during the running in experiments documented in Chapter 4, it was decided to lower the maximum contact pressure to which the test disks were subjected to a maximum of 1.3GPa. Despite the measures taken to stabilise the surfaces prior to experiments it could inferred from the behaviour of the contact voltage signal throughout the initial speed varying experiments that a degree of modification was still occurring. This was unexpected as the running in conditions had subjected the contact to lower lambda ratios and therefore more aggressive normal asperity loading. The behaviour of the contact voltage signal suggests that deformation occurring in asperities is dependent on both the tangential loading due to friction force and asperity collisions. Consequently, the speed varying tests were conducted starting with the highest load case and the test was run repeatedly until repeatable results were obtained. This

procedure was followed with all the tests and results are illustrated here for disk set B as the effect was greatest with the hard against soft disk combination.

The contact voltage behaviour can be seen to vary greatly between the first speed varying experiments presented in Figure 5-9 and the second experiment presented in Figure 5-10. The figures present the same measured test information as Figures 5-1 to 5-5, described in detail in Section 5.3.1.1. The friction and temperature variation seen in these figures are very similar, but the contact voltage behaviour is very different. In Figure 5-9 a contact voltage of 40 mV is seen for the 1500 rpm and 2000 rpm speed stages, and all other speed stages show a sequence of lower contact voltages at progressively lower speeds with a value of 0 mV at both the 200 rpm stages. The characteristic changes in contact voltage during a speed stage is as presented for the examples with disk set A, with reducing values during the speed increasing phase and increasing values during the speed reducing phase. However, it is noticeable that during the speed increasing stages, the reduction in contact voltage to a plateau value seen for the 200 rpm stage in Figure 5.4, for example, is replaced by an initial reduction followed by subsequent voltage growth. A clear example of this is seen for the 500 rpm stage in Figure 5-9. This increase in contact voltage takes place in circumstances where the disk temperature measurements are clearly rising. The temperature change will cause reduced viscosity and lower film thickness, suggesting that the increase in contact voltage from a minimum of 22 mV at 980 s to a maximum value of 27 mV at 1200 s must be due to a reduction in metallic contact caused by plastic deformation of the surface asperities due to running in over the speed stage.

The contact voltage traces in the second test shown in Figure 5-10 shows the same characteristic behaviour as the disk set A tests as far as contact voltage is concerned and there is no clear evidence of plastic deformation occurring to the extent apparent in the first test. Several experiments were conducted at the maximum load of 1.3GPa and only slight discrepancies were witnessed in the behaviour of the contact voltage which was considered to

be a result of minor surface modification. To investigate this further, lambda values of the experiments and the contact voltage were plotted together and showed very close conformity. Further tests at the same conditions gave results that became increasingly repeatable, and the stable surface result is presented as Figure 5-14 as part of the set of tests with increasing load.

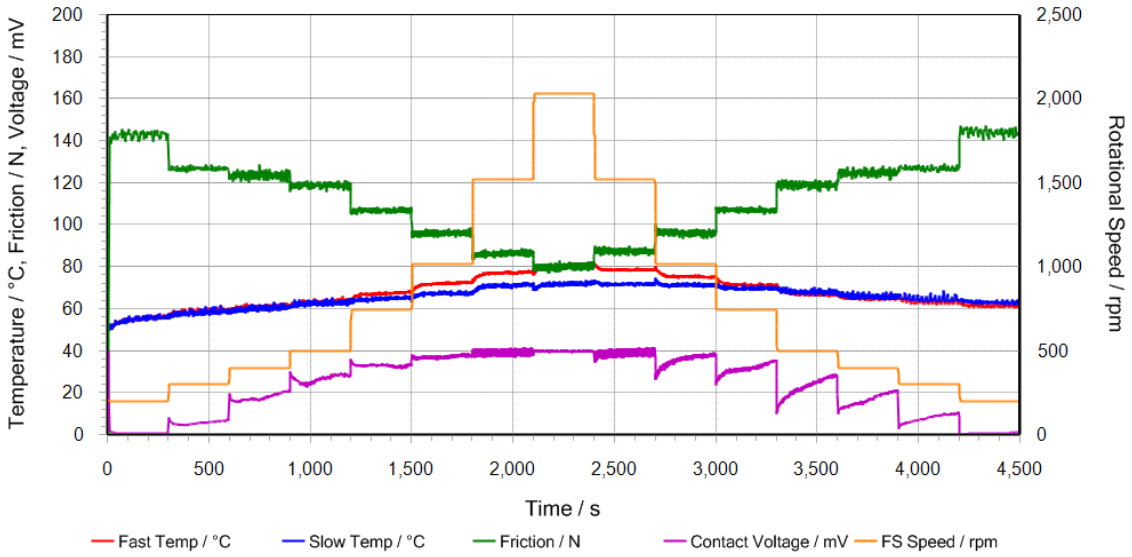

Figure 5-9 First speed varying test on disk set B at 1.3GPa showing running in behaviour of contact voltage

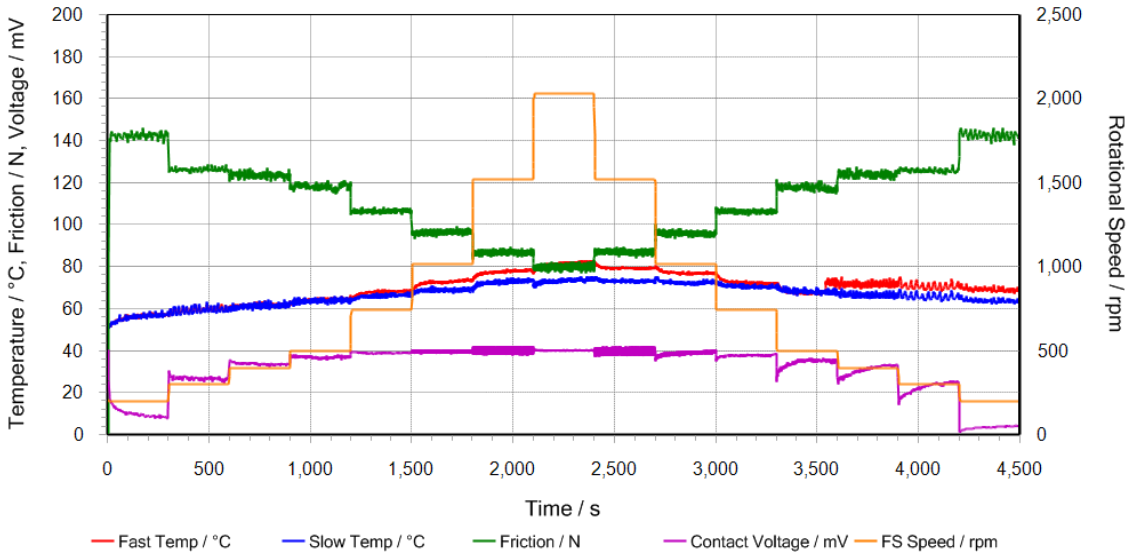

Figure 5-10 Second speed varying test on disk set B at 1.3GPa showing running in behaviour of contact voltage

Figures 5-11 to 5-14 present the stable surface speed varying results for disk set B at contact loads of 1.0, 1.1, 1.2 and 1.3 GPa. As with disk set A, the contact voltage results are close to 40 mV for all of the speed stages except for the first and last where there are indications of metallic contact and end of stage measurements of 30 mV. The measured friction values for each test are marginally higher than the corresponding test for disk set A. However, the peak measured temperatures are a little lower. The contact voltage measurements at the 1.2 and 1.3 GPa loads are different from those seen for disk set A, with disk set A showing lower contact voltage levels in the slowest speed stages. This can be interpreted as the result of the slow speed contacts for disk set B having a lower composite roughness and thus a higher lambda value for the same contact temperature.

The test data from the range of experiments conducted further demonstrates the impact of load on heat generation and the associated implications for film thickness levels. The experiments show high levels of film thickness throughout and the relative insensitivity of film thickness to applied load is shown in the final speed stage where frequency of metallic contact appears approximately consistent between all experiments despite the range of loads used.

Values for friction reflect those attained disk set A over the range of loads used, due to the majority of friction arising from shearing the viscous lubricant. As based on results from simulation work, even in regions where the contact voltage can be seen to drop, metallic junctions are seen to occur relatively sparsely and infrequently (Evans et al., 2013).

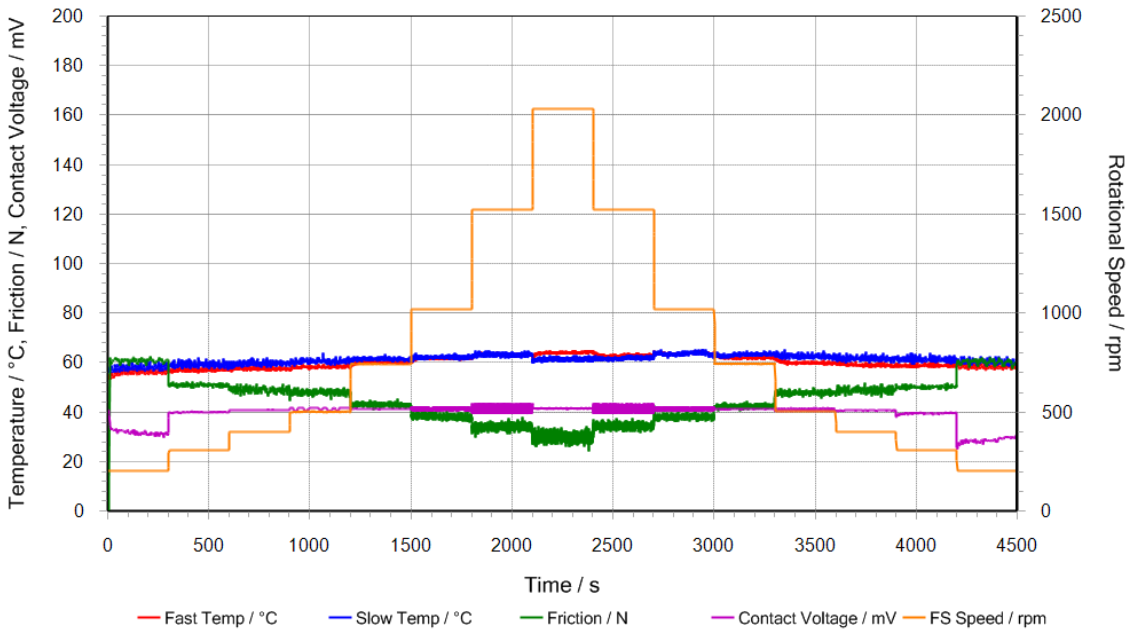

Figure 5-11 Speed varying experiment for maximum pressure of 1.0GPa at a SRR of 0.25 on disk set B

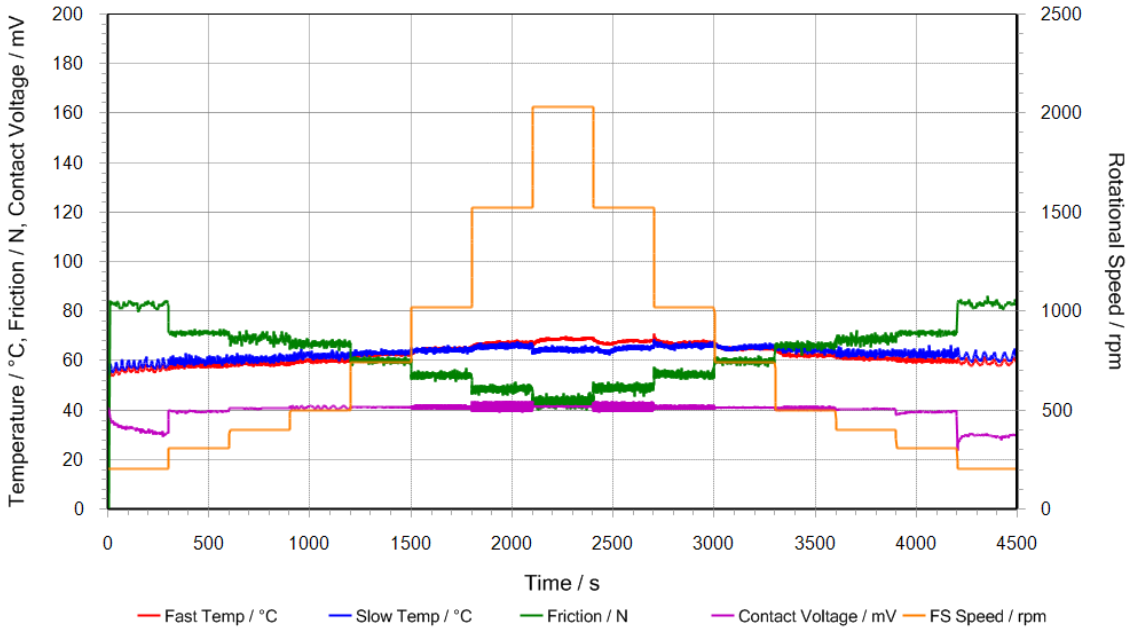

Figure 5-12 Speed varying experiment for maximum pressure of 1.1GPa at a SRR of 0.25 on disk set B

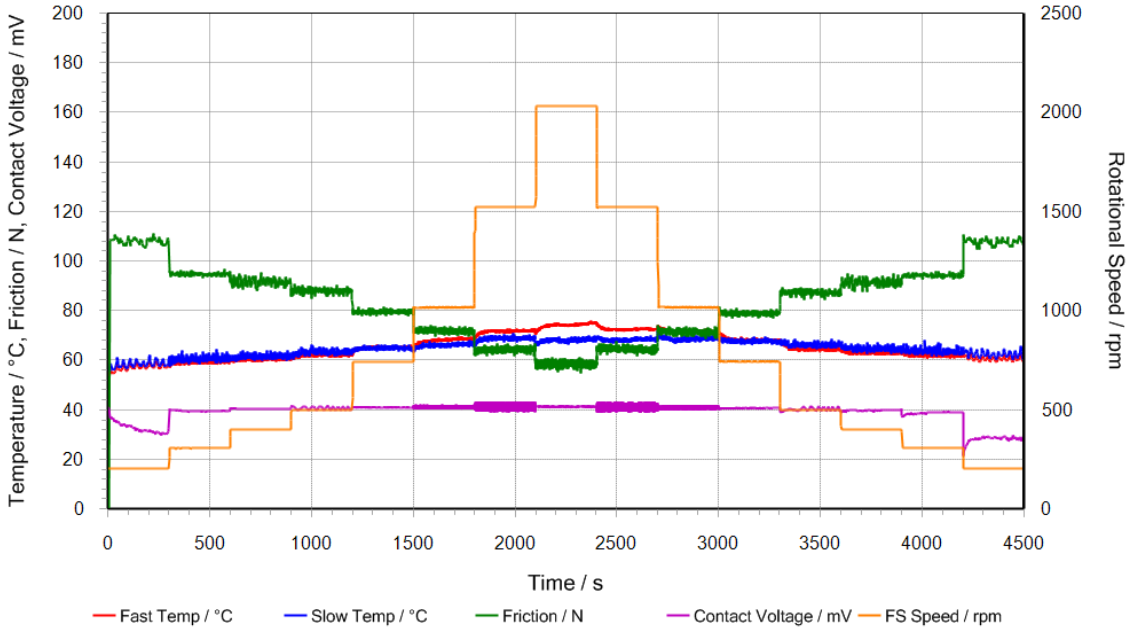

Figure 5-13 Speed varying experiment for maximum pressure of 1.2GPa at a SRR of 0.25 on disk set B

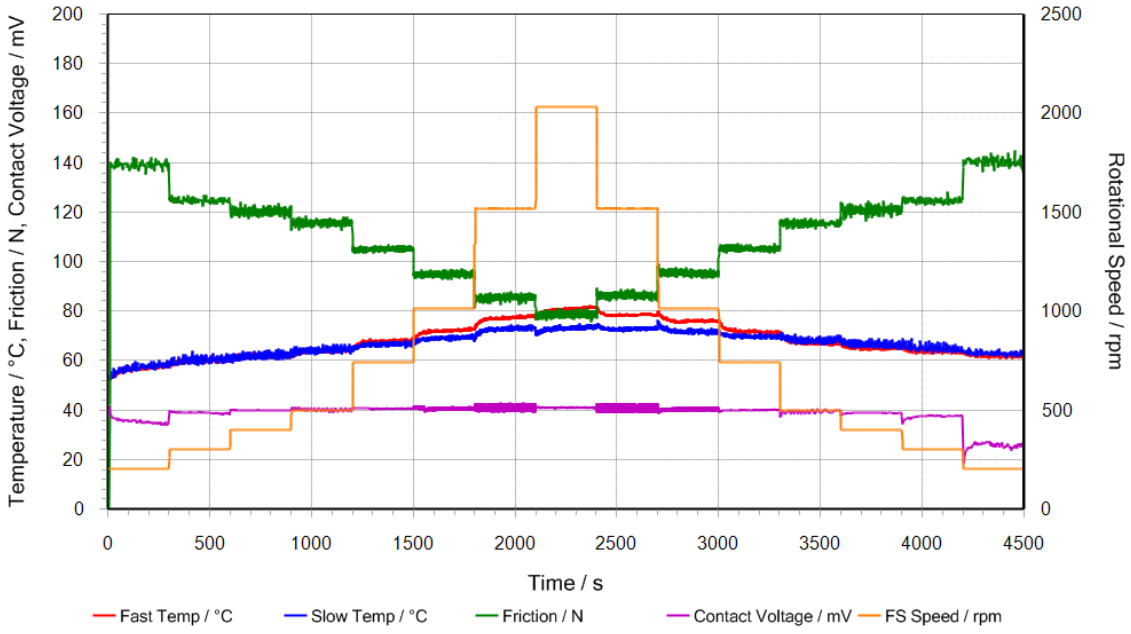

Figure 5-14 Speed varying experiment for maximum pressure of 1.3GPa at a SRR of 0.25 on disk set B

5.3.2 Disk Set C -Experiments Run at Slide Roll Ratio = 0.5

Following the experiments at a slide roll ratio of 0.25, a new pair of ground disks were used and the gearing between the shafts was substituted for a pinion with 30 teeth and a wheel

with 50 teeth, resulting in an increased slide roll ratio of 0.5. The gear ratio for the experiment was 3:5. The disks used were approximately similar in hardness (800HV) and in surface roughness to those used at the lower slide-roll ratio of 0.25, allowing some comparisons to be made. The surface velocities at each of the speed stages is shown in Table 5-4.

Table 5-4 Data for disk kinematics when geared to a slide-roll ratio of 0.5

Time / s	Fast Shaft Speed / rpm	Fast Surface Peripheral Velocity / ms^{-1}	Slow Surface Peripheral Velocity / ms^{-1}	Entrainment Speed / ms^{-1}	Sliding Speed / ms^{-1}
0	200	0.798	0.479	0.638	0.319
300	300	1.197	0.718	0.958	0.479
600	400	1.596	0.958	1.277	0.638
900	500	1.995	1.197	1.596	0.798
1200	750	2.992	1.795	2.394	1.197
1500	1000	3.990	2.394	3.192	1.596
1800	1500	5.985	3.591	4.788	2.394
2100	2000	7.980	4.788	6.384	3.192
2400	1500	5.985	3.591	4.788	2.394
2700	1000	3.990	2.394	3.192	1.596
3000	750	2.992	1.795	2.394	1.197
3300	500	1.995	1.197	1.596	0.798
3600	400	1.596	0.958	1.277	0.638
3900	300	1.197	0.718	0.958	0.479
4200	200	0.798	0.479	0.638	0.319

Although the disks had been run in as described in Chapter 4, previous experiments have shown that it was necessary to conduct a number of tests at the most extreme load case in order to stabilise the surface. For this reason the initial speed varying tests conducted were used to further run the disks in. The evidence of this gradual break-in process is demonstrated in the variation in both friction and contact voltage response between similar tests performed at 1.4GPa. These experiments are shown in Figure 5-15 and Figure 5-16 where examination of the recorded friction shows an overall downwards shift as the surfaces are progressively run-in reaching a stable value in later experiments. For the first test shown in Figure 5-15 the contact

voltage is much lower than seen in Figure 5-16, with the measured values of near zero at the lowest speed and hardly exceeding 20 mV at the higher speeds. Values approaching 40 mV are achieved at the highest speeds in the second test shown in Figure 5-16 which indicates that a relatively significant modification in surface roughness has occurred given that the temperatures in the corresponding speed stages are quite similar. This increase in contact voltage levels indicates that surface peaks are becoming more rounded and conformity with the counterface is increasing. The effect of the surface progressively becoming run-in is also evident in the recorded bulk disk temperatures, where rougher surfaces tend to yield higher temperatures in mixed EHL conditions.

It was found in these experiments that the friction signal was being influenced by a vibration effect occurring at a fast shaft speed of 400rpm as can be seen in Figure 5-15 and Figure 5-16. To reduce this the speed was lowered to 350rpm in the test sequence for the stable surface set of experiments. The repeatable run-in result for the 1.4 GPa case is shown in Figure 5-21.

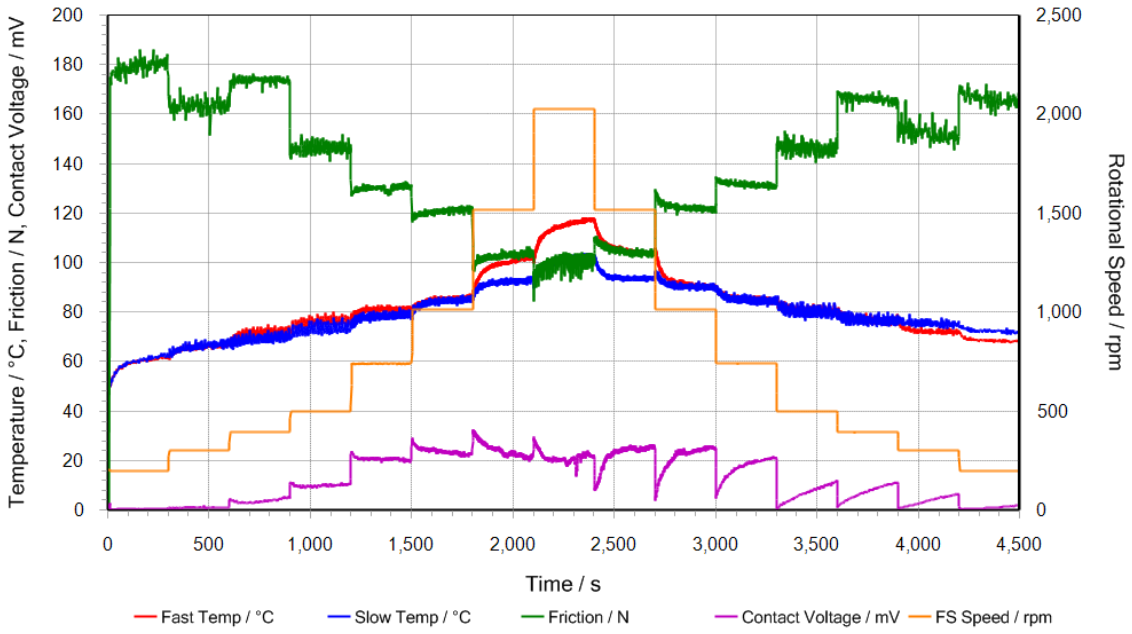

Figure 5-15 First speed varying test on disk set C run at a maximum Hertz pressure of 1.4GPa at a SRR of 0.5

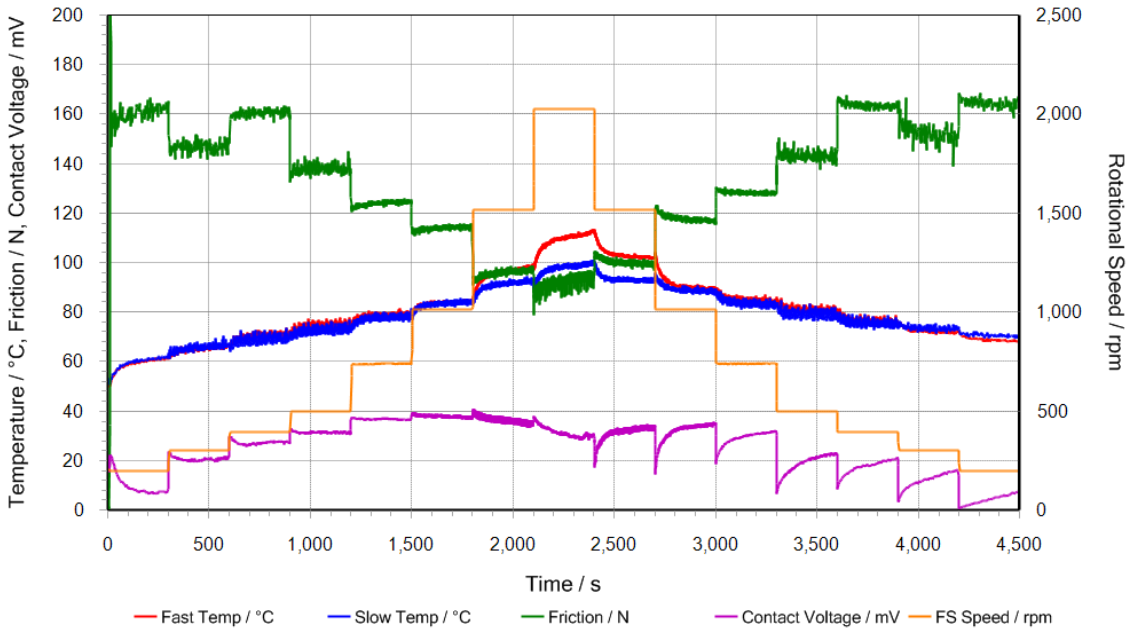

Figure 5-16 Second speed varying test on disk set C run at a maximum Hertz pressure of 1.4GPa at a SRR of 0.5

The set of stable surface experiments are presented in Figure 5-17 to Figure 5-21 for the range of loads considered. The measured friction force values are generally lower than for disk set A. In comparison with the corresponding disk set A tests the values at the maximum speed in each test are reduced by up to 10 % at the higher loads, and those at the lowest speed values are reduced by an average of 10%. The sliding speed is however doubled and so the tests performed at the higher slide roll ratio have much greater heat generation across all loads, in spite of the reduced friction force values. The maximum measured disk temperatures are on a par with the disk set A test measurements for the 1.0 and 1.1 GPa loads, but exceed the disk A test values by 7, 18 and 23 °C for the subsequent loads. The elevated temperature markedly effects the contact voltage response and at the highest speeds, the thermal response dominates the ability to effectively separate the surfaces. It can be seen in Figure 5-18 that at the highest load of 2320N (1.4GPa) between the 1500rpm and 2000rpm speed stage, an increase of entrainment speed from 4.79m/s to 6.78m/s has the effect of reducing the mean contact voltage signal. As the bulk disk temperature climbs due to the increased sliding, the temperature at the inlet rises and this has the effect of reducing oil entrainment, causing film collapse. At the end of the stage, the speed is reduced and the disks cool, which increases the oil viscosity resulting in a thicker oil film.

The thermal recovery effect that occurs over the slower speed stages in the speed reducing phase of the experiments can be seen most clearly at the higher loads. Unlike experiments performed at lower levels of sliding, the effect of temperature on friction is quite visible, where changing temperatures result in increasing or decreasing friction over a speed stage. This is clearly illustrated in Figure 5-18 where the film thickness can be seen to reduce under high speed conditions. Experiments conducted by Crook (1961) using smooth surfaces under full film lubrication have shown the sliding to have little direct effect on film thickness, however the film thickness is sensitive to the resulting increase in temperature at higher speeds.

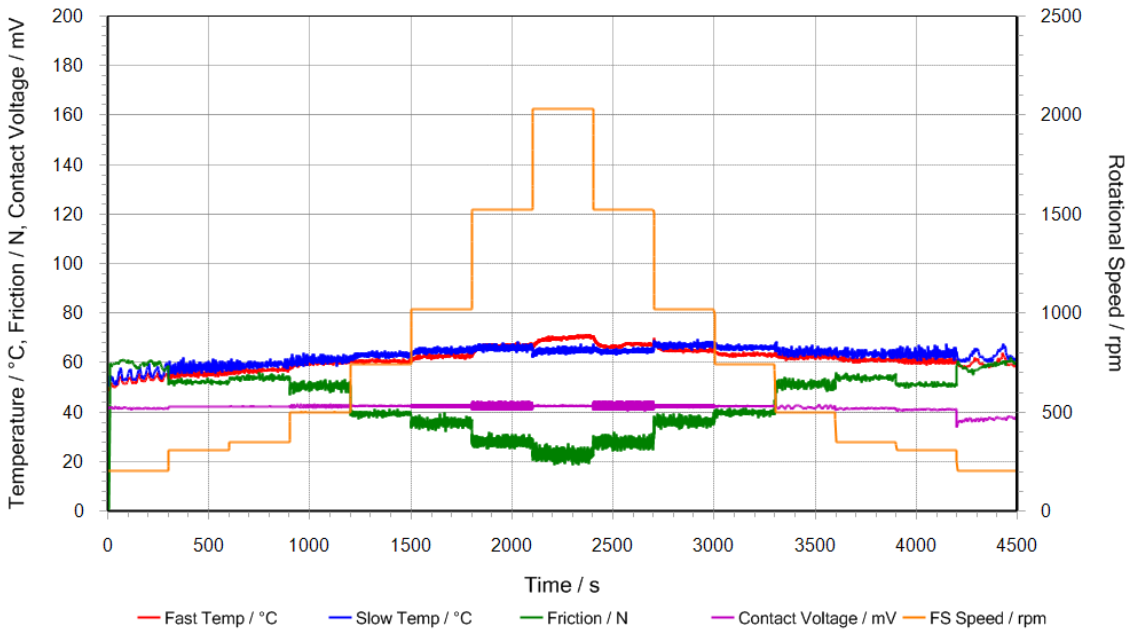

Figure 5-17 Speed varying experiment for maximum pressure of 1.0GPa at a SRR of 0.5 on disk set C

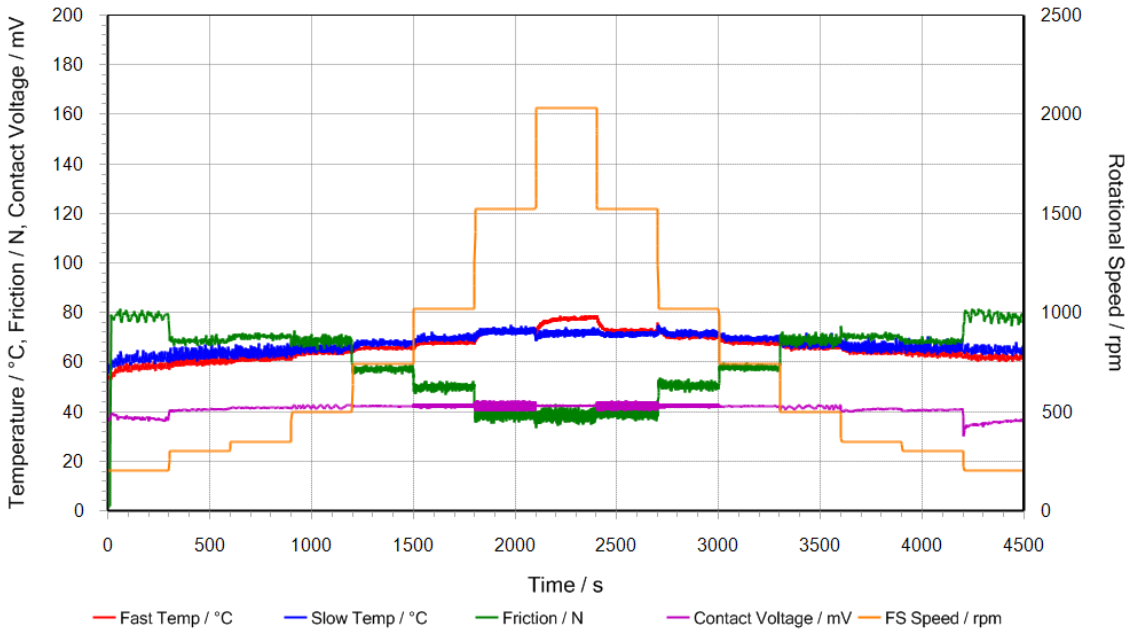

Figure 5-18 Speed varying experiment for maximum pressure of 1.1GPa at a SRR of 0.5 on disk set C

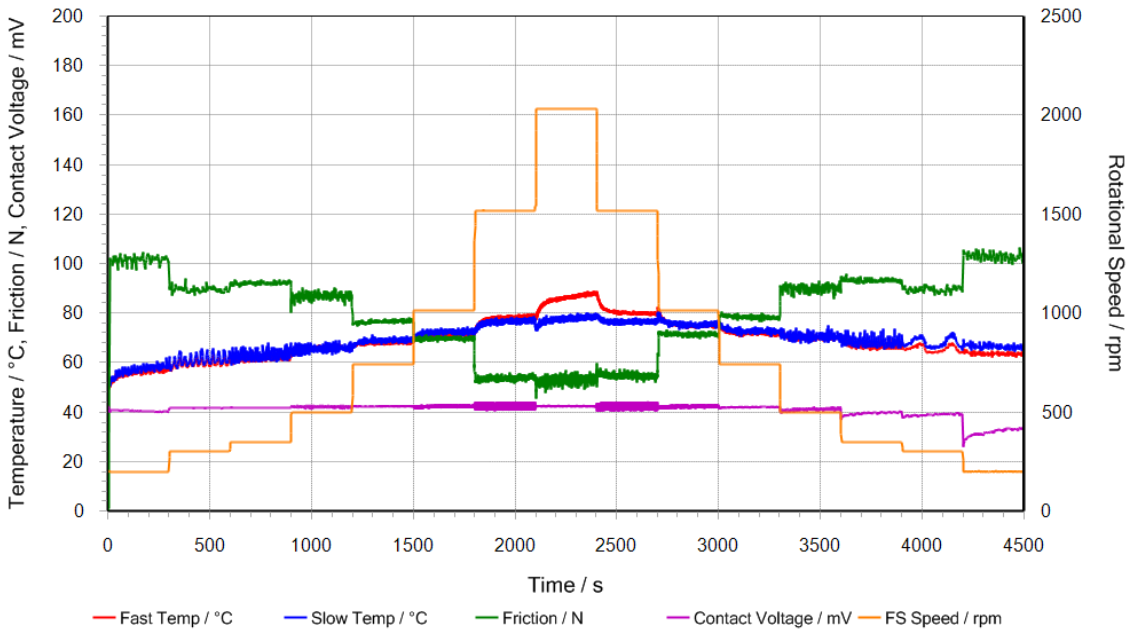

Figure 5-19 Speed varying experiment for maximum pressure of 1.2GPa at a SRR of 0.5 on disk set C

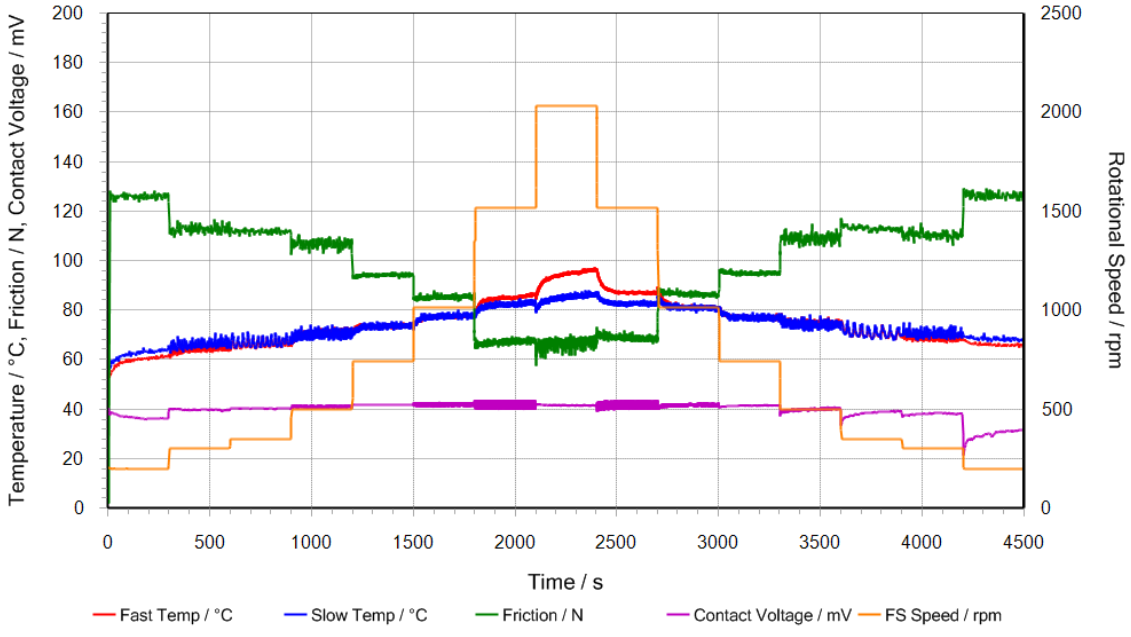

Figure 5-20 Speed varying experiment for maximum pressure of 1.3GPa at a SRR of 0.5 on disk set C

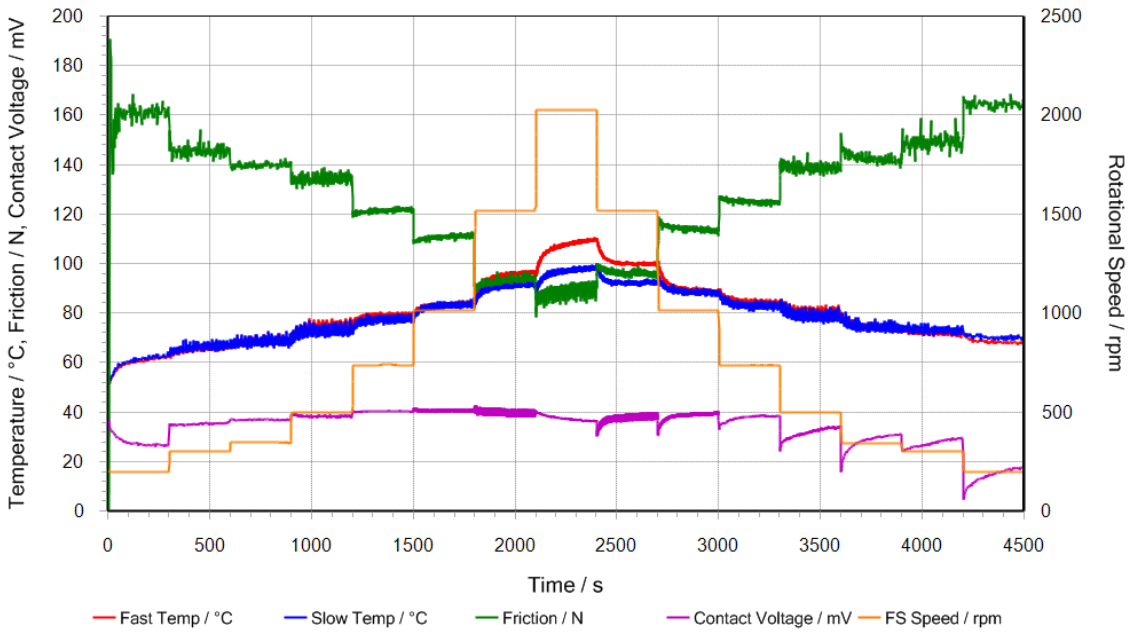

Figure 5-21 Speed varying experiment for maximum pressure of 1.4GPa at a SRR of 0.5 on disk set C

5.3.3 Lambda Ratio Plots

In order to make more meaningful comparisons between experiments conducted at different loads, the test data for the final 30 seconds of each speed stage was averaged, where conditions were at or approaching steady state. Using this data it was possible to approximate the EHL film thickness using the formula published by Chittenden et al. (1985). This was used in conjunction with measured surface roughness data from the test disks to calculate the lambda ratio for the steady state region of each speed stage. Comparisons could then been made between the disks based upon surface texture and slide roll ratio. Values for the RMS roughness are shown in Table 5-5.

Table 5-5 Rq values used in calculation of Lambda values

Disk Pair	Shaft Mounting	Rq / µm
A	Fast	0.35
	Slow	0.32
B	Fast	0.14
	Slow	0.43
C	Fast	0.31
	Slow	0.29

5.3.3.1 Comparison Between Relative Disk Hardness

Figure 5-22 shows the test data friction coefficient values plotted against calculated lambda values for all the experiments carried out at the slide roll ratio of 0.25. The loads vary between nominal contact pressures of 1.0GPa and 1.4GPa. The data points are reasonably close to the superimposed curve where increasing lambda ratio results in a rapid decrease in the friction coefficient, which is seen to level off as the contact becomes fully hydrodynamic at a lambda value of around 2. Close agreement is seen between all loads used in the experiments which follow a similar curve. The calculated friction coefficient can be seen to decrease from a value of approximately 0.075 to a value of a 0.034 over the range of lambda ratios experienced.

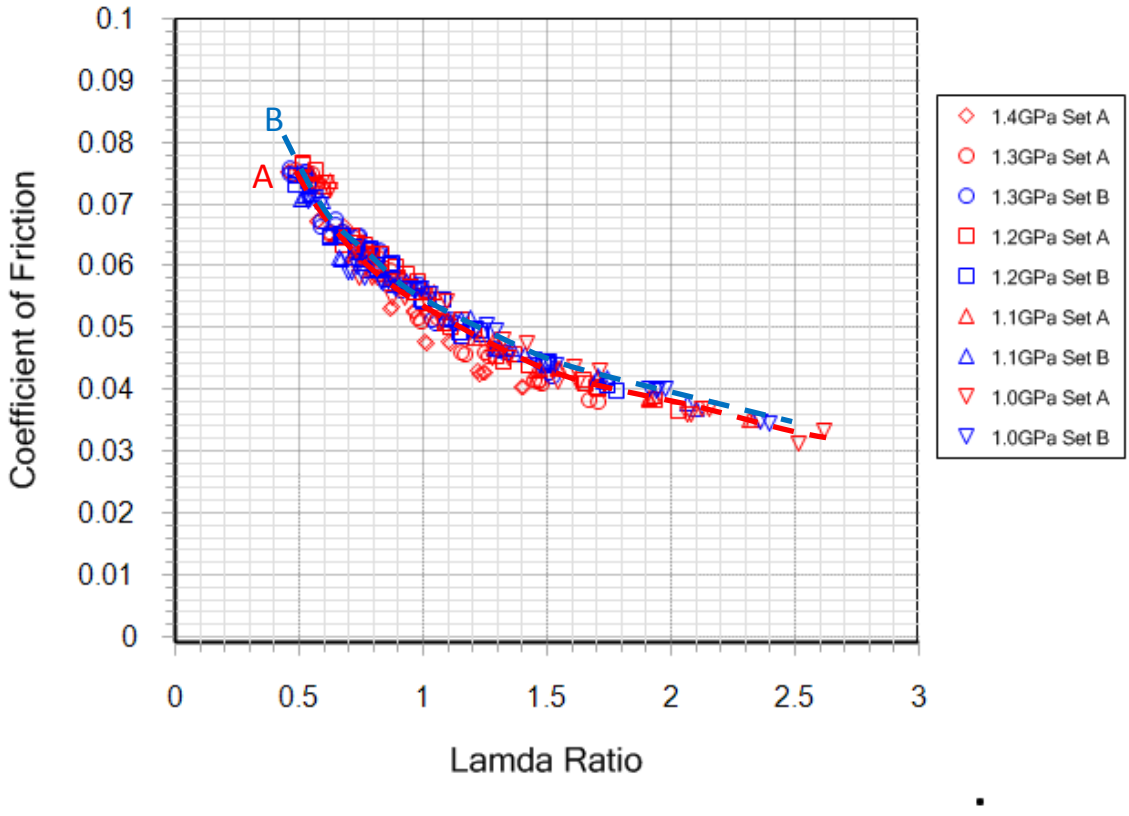

Figure 5-22 Relationship between lambda ratio and friction coefficient for ground surfaces of similar roughness and hardness and ground surfaces of differing roughness and hardness at SRR of 0.25

In Figure 5-23 the averaged value for contact voltage is plotted against lambda ratio. A clear trend is also seen across the range of contact pressures, where voltage is seen to be highly sensitive to changes in film thickness at lambda ratios below 0.7 in a region which is approximately linear. As the lambda ratio increases, metallic contact becomes less frequent

and as fewer asperities can interact causing the response to be less sensitive at higher lambda ratios. This plateauing effect demonstrates that the contact voltage technique gives an indication of metallic contact and is insensitive to film thickness over a certain threshold. Values of contact voltage can be seen to increase from a value of approximately 25mV at a lambda ratio of 0.5 to around 43mV at a lambda value of 1. Again all sets of data are close to a general trend but difference between disk set A and disk set B results are now apparent at the low lambda part of the curve where the same contact voltage generally corresponds to a higher lambda value for disk set A.

It can be seen in comparison between the two sets of disks that the Set B disk pair (when one surface is relatively smooth compared to the other) attains high voltage values more rapidly than the Set A disk pair (both surfaces of similar roughness).

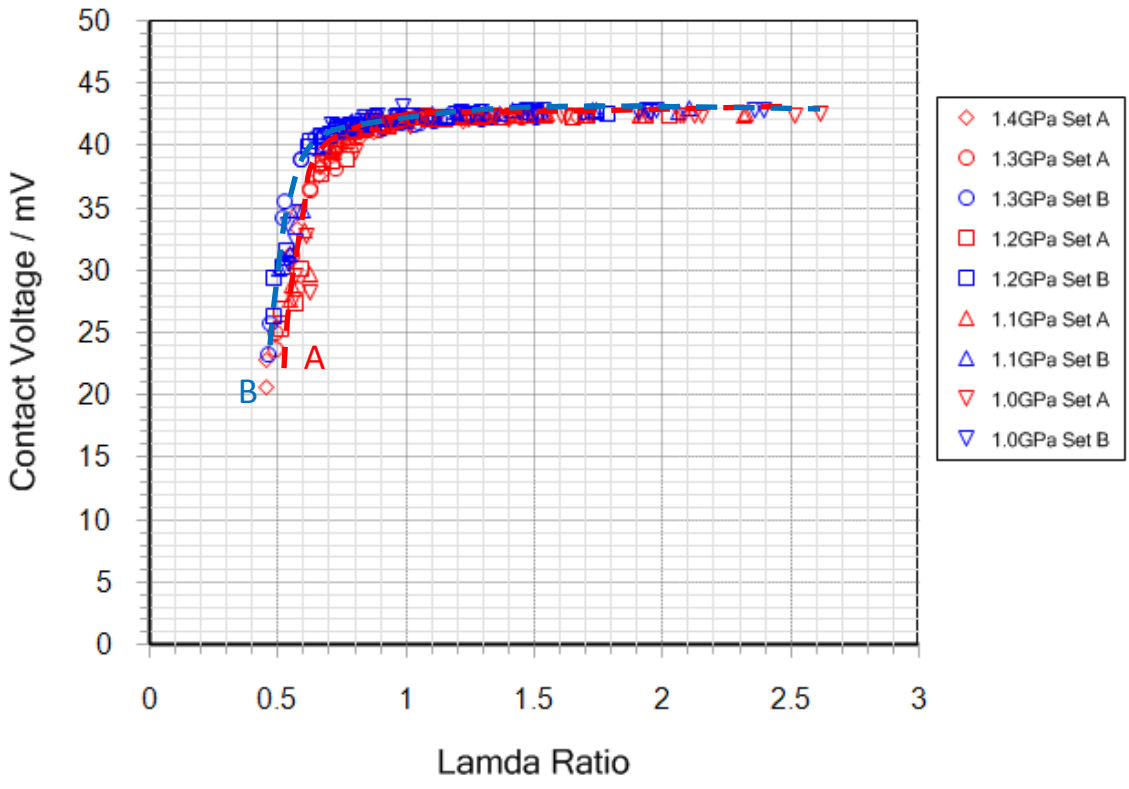

Figure 5-23 Relationship between lambda ratio and contact voltage for ground surfaces of similar roughness and hardness and ground surfaces of differing roughness and hardness at SRR of 0.25

5.3.3.2 Comparison Between Tests Run at Different Slide-Roll Ratios

In comparison with experiments conducted at lower slide/roll ratios, a narrower range of lambda values are attained with ξ=0.5 for each particular load due to the decreased oil viscosity. However, values for friction remain low despite this. The low friction is due to a combination of the shear heating at the contact reducing the viscosity of the lubricant and the shear thinning properties of the oil (Crook, 1963). Inspection of Figure 5-24, which shows the variation of coefficient of friction with lambda values, demonstrates this. The discrepancy between friction values at similar loads can be seen to increase with lambda ratio due to the effect of heat generation at higher sliding speeds.

The results for disk set B and C shown in Figure 5-24 do however show some similarities, with the highest loads in each dataset tending to yield lower values of friction than tests performed at lower loads. This can be attributed to the increased temperature lowering the viscosity and suggests that the reduced viscosity has more influence on the coefficient of friction than does the increased level of asperity contact, suggesting a larger hydrodynamic than metallic contribution to the measured friction.

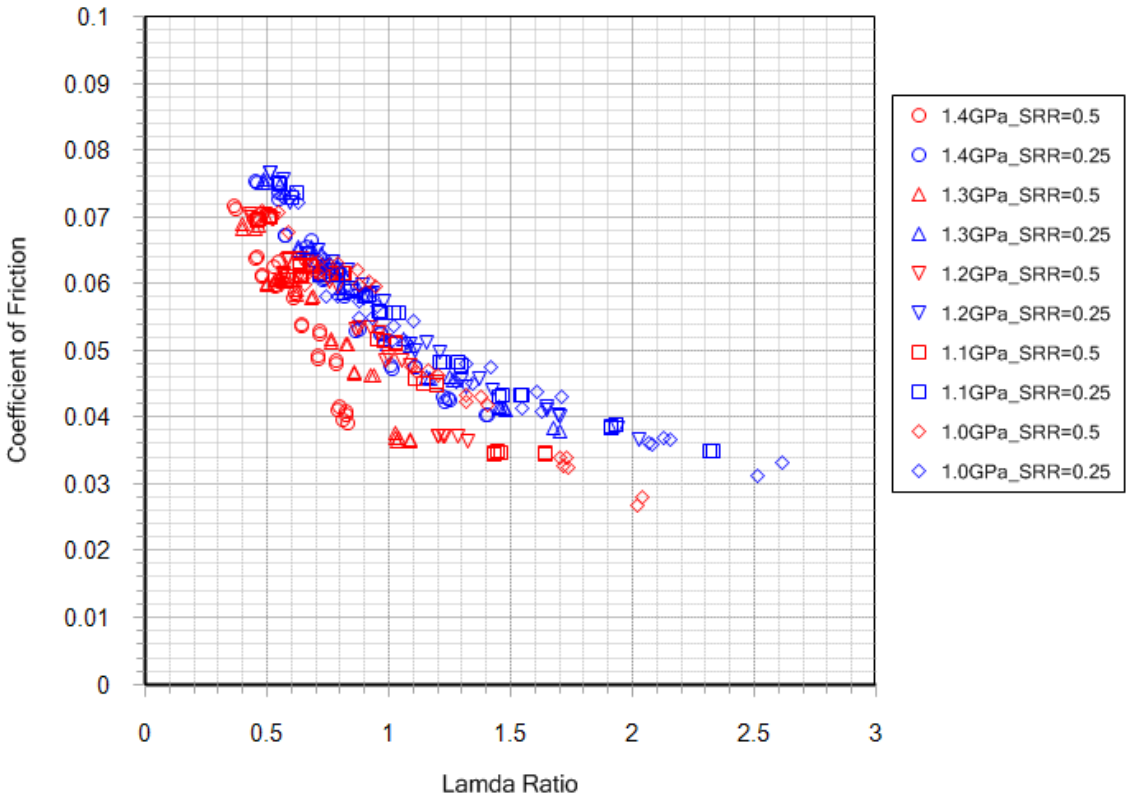

Figure 5-24 Relationship between lambda ratio and friction coefficient for ground surfaces of similar roughness and hardness at slide roll ratios of 0.25 and 0.5

A comparison of the behaviour of the contact voltage response to changing lambda ratio between the two slide roll ratios is shown in Figure 5-25 and shows a much stronger correlation between different slide/roll ratios. For both sets of data, high levels of contact voltage are attained relatively quickly at a lambda value of around 0.8, suggesting intermittent metallic contact. Higher loads across both slide to roll ratios show a tendency towards lower contact voltage values at similar lambda values, a reason for this could be due to an increased Hertzian contact zone, increasing the likelihood of asperity encounters.

Visible in the behaviour of the higher slide roll ratio however is the difference in the response of the contact voltage at the 'highest' lambda values attained in the 1.4 GPa experiment. The reduction in contact voltage value suggests that a reduction in film thickness occurs at the highest speed which is reflected in the experimental data. Another possible reason for the

inconsistent behaviour of these data points could be related to the transient temperatures occurring during this portion of the experiment which is visible in Figure 5-21 where bulk disk temperatures are still climbing towards the end of the speed stage.

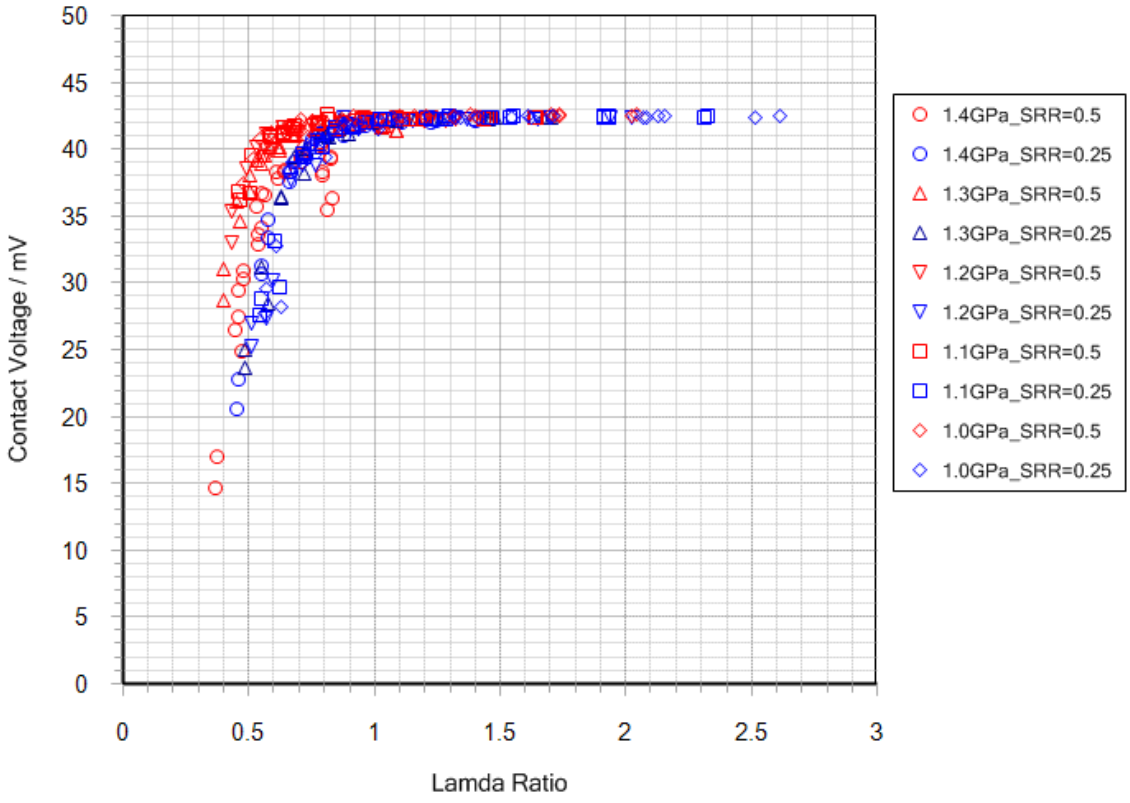

Figure 5-25 Relationship between lambda ratio and contact voltage for ground surfaces of similar roughness and hardness at slide roll ratios of 0.25 and 0.5

5.3.3.3 Lambda Ratio Plots of Running In Process

As mentioned previously, during the initial sets of speed varying experiments, it could be inferred that a degree of surface modification was taking place due to the behaviour of the mean contact voltage. To investigate this further the test data from repeated tests was averaged in a similar manner over the concluding 30 seconds of each speed stage. This data was used to calculate the smooth surface film thickness and a value for the lambda ratio was calculated using the *final surface roughness measurements* recorded after all tests.

Plotting the measured contact voltage against the value for the lambda ratio it can be seen that there is a definite reduction in the lambda value at which a particular contact voltage is reached as the surfaces modify and hence the hydrodynamic performance of the surfaces improve. The ascending and descending speed stages of each test run during this running in period are shown separately in Figure 5-26a for the 1.3GPa load case. It was important to differentiate between these regions as lower lambda ratios were generally experienced in the falling speed stages causing further modification. It has been found in previous work that where plastic deformation does occur, the surfaces will modify just enough to prevent further yielding. Any asperity loading in excess of this will cause further plastic deformation.

The graph demonstrates that as the surfaces undergo progressive running, there is a tendency for lower lambda ratios to yield higher contact voltages. There is also a greater difference between the ascending and descending speed curves for the initial speed varying experiments than there is for the latter, suggesting the trend observed is due to fast acting plastic deformation rather than a slower wear processes. Corresponding results for the running in process for the 1.4GPa load case are shown in Figure 5-26b. It is visible that higher lambda values are not obtained during these experiments, however the change in lambda ratio due to running in occurs over approximately the same range.

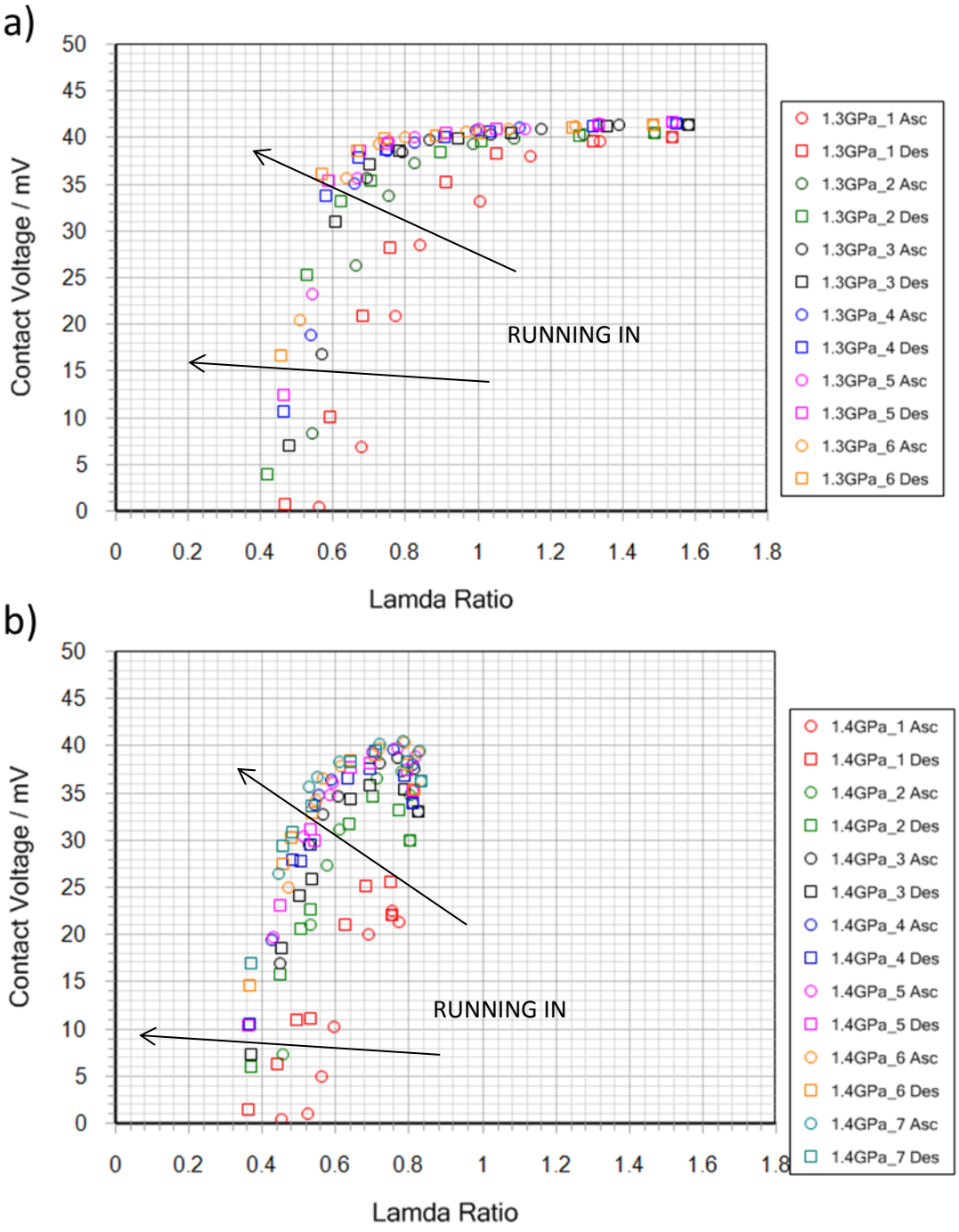

Figure 5-26 Relationship between lambda ratio and contact voltage in first speed varying experiments showing progressive surface modification conducted with (A) disk set B at a SRR of 0.25 (B) disk set C at a SRR of 0.5. Arrow have been used to indicate tendency of contact voltage levels to rise at similar lambda ratios as surfaces become run in.

5.4 Degradation of Test Surfaces

Once tests had been completed with a pair of disks, they were removed and cleaned in an ultrasonic bath prior to measurement. With the ability to effectively count the number of revolutions on the fast shaft, it was possible to accurately assess the number of revolutions each test specimen had experienced, the load cycles for the slow disk being dependent upon the gear ratio between the two test shafts.

The disks were measured using a 3D surface profilometer (Taylor Hobson Form Talysurf 2), with the data acquired used for simulation purposes. The high resolution of the equipment gives an accurate measurement of surface texture, and due to the crowned shape of the disks it was possible to measure across the running track to make comparisons with regions of the disk that experienced no loading and therefore remained as manufactured.

5.4.1 Disk Set A

The first pair of ground disks used had previously been run-in and a set of speed varying experiments conducted with them running through a total of 673,000 load cycles on the fast disk. After this they were removed from the rig and measured. A table detailing the range of loads and load cycles used is shown in disks Table 5-6.

Table 5-6 Accumulated load cycles for disk set A after initial loading sequence

Applied Load / N	Maximum Hertzian Pressure / GPa	Load Cycles on Fast Disk	Load Cycles on Slow Disk
4150	1.7	48,900	38,033
2320	1.4	170,310	132,463
1850	1.3	113,540	88,309
1460	1.2	113,540	88,309
1120	1.1	113,540	88,309
850	1.0	113,540	88,309
	Cumulative Total	673,370	523,732

Shown in Figure 5-27 and Figure 5-28 are the results of a surface scans for the fast and slow disk of disk set A. The scans are displayed as 'photo-simulations' as these best highlight the textures present. Within the figures, the running track can be clearly identified as a lighter band spanning the measurement in the entrainment direction. At the scale shown, the sweeping effect of the topography due to the nature of the grinding process can be seen very clearly. (Note that the angle is exaggerated by the scales chosen) A series of dark pits that follow the roughness features over the width of the running track are visible on the slower surface in Figure 5-27. Where these features are most prominent they have been identified with labelled arrows. Features A, B and C indicated on the figure all show the appearance of pits distributed across prominent asperity features. These pits do not extend beyond the running track. These features do not appear as visible in Figure 5-28. A prominent scoring mark is visible on the surface of the fast disk in and can be seen over the whole circumference.

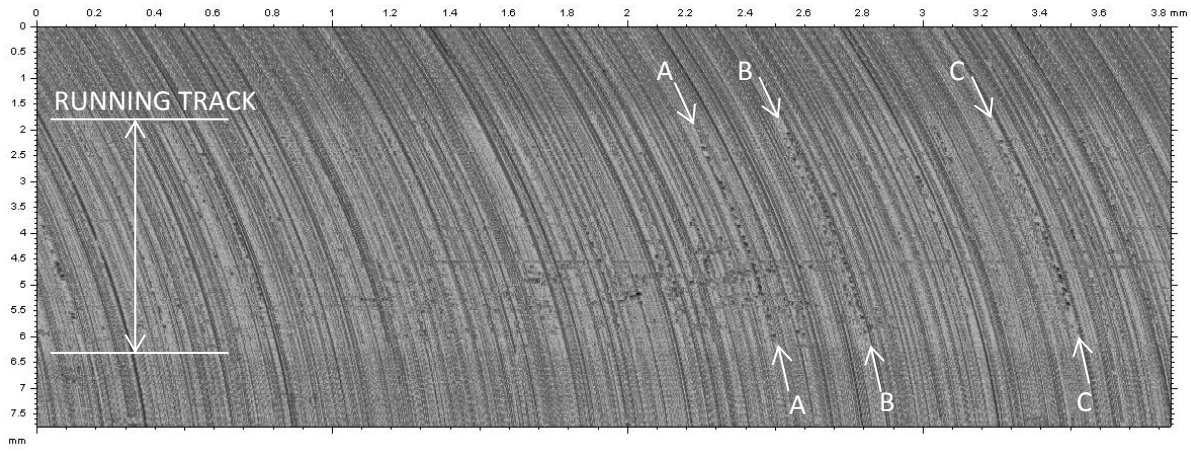

Figure 5-27 3D scan of slow surface disk set A following load cycles shown in Table 5-6.

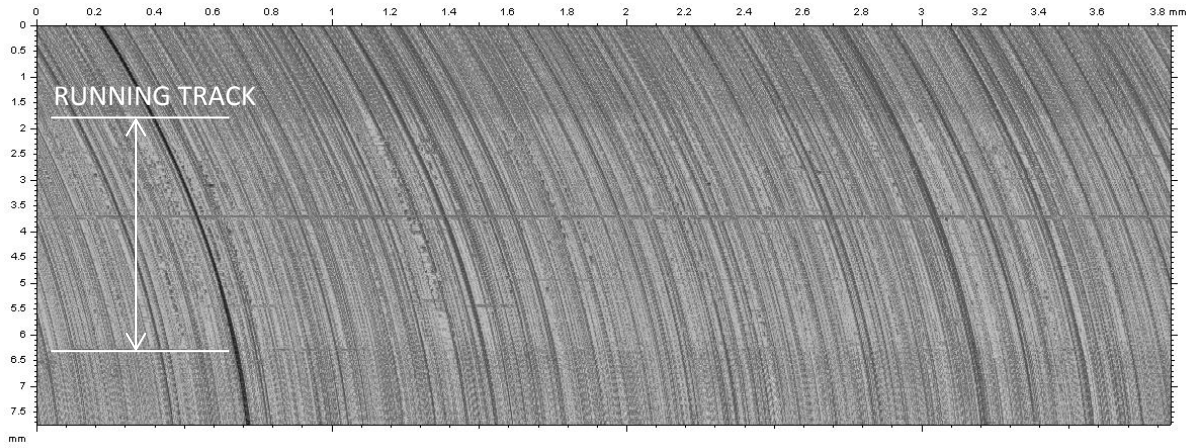

Figure 5-28 3D scan of fast surface from disk set A following load cycles shown in Table 5-6.

Table 5-7 shows the second set of load cycles applied to disk set A. Following this, the disks were removed and the running track was measured again.

Table 5-7 Accumulated load cycles for disk set A following second loading sequence

Applied Load / N	Maximum Hertzian Pressure / GPa	Load Cycles on Fast Disk	Load Cycles on Slow Disk
Initial Loading Sequence	-	673,370	523,732
4150	1.7	0	0
2320	1.4	283,850	220,772
1850	1.3	113,540	88,309
1460	1.2	113,540	88,309
1120	1.1	113,540	88,309
850	1.0	113,540	88,309
	Cumulative Total	1,411,380	1,097,740

Figure 5-29 and Figure 5-30 show the second set of scans for the fast and slow disk from disk set A. Figure 5-29 shows some pitted regions in the running track. These do not appear as

clearly as those features identified in Figure 5-27. Similarly, Figure 5-30 appears to show little change in comparison to the scan taken from Figure 5-28.

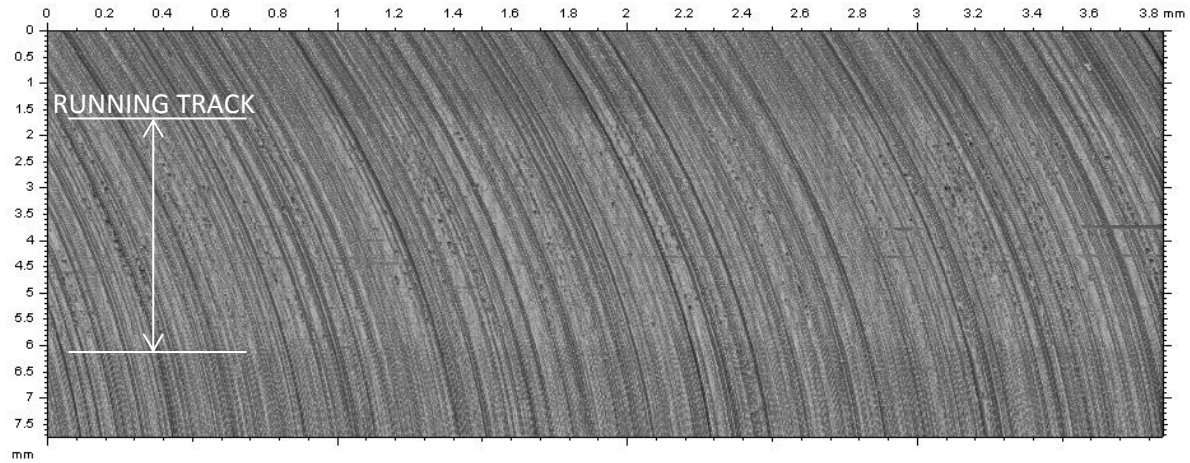

Figure 5-29 3D scan of fast disk from set A following load cycles shown in Table 5-7

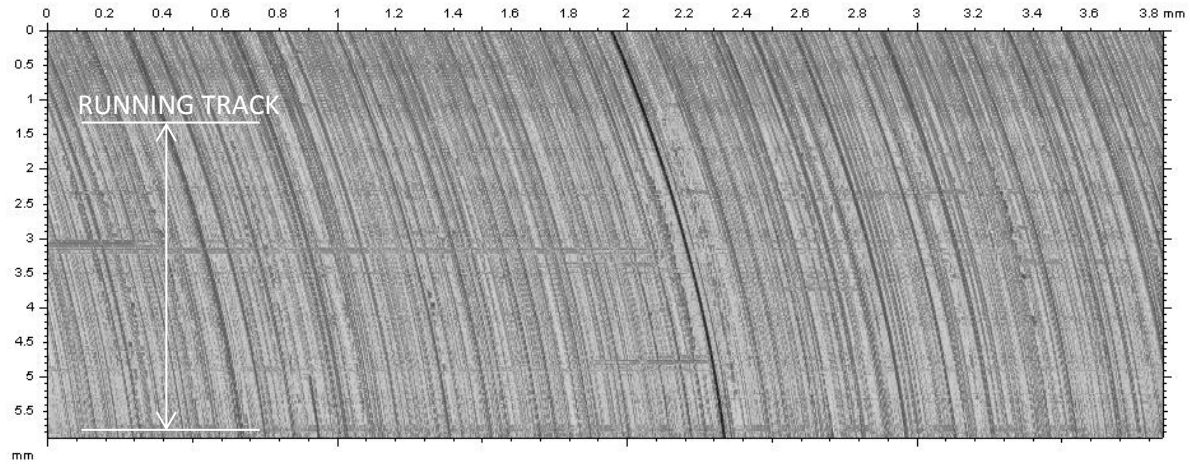

Figure 5-30 3D scan of slow disk from set A following load cycles shown in Table 5-7

5.4.2 Disk Set B

Table 5-8 shows the number of load cycles at different contact pressures applied to the disks in set B.

Table 5-8 Accumulated load cycles disk set B

Applied Load / N	Maximum Hertzian Pressure / GPa	Load Cycles on Fast Disk	Load Cycles on Slow Disk
4150	1.7	3,125	2,431
2320	1.4	5,833	3,500
1850	1.3	624,720	374,832
1460	1.2	113,540	68,124
1120	1.1	113,540	68,124
850	1.0	227,080	136,248
	Cumulative Total	1,087,838	653,259

Figure 5-31 shows a photograph of the disks from set B together after removal from the test rig. It is clear that the running track of the less hard disk, shown below, has developed a polished finish whereas the hard disk has retained its ground surface finish quite clearly. The dark and light banding transverse to the running track on the less hard disk are due to the reflective finish and are not as a result of differing topography. Unlike both disk sets A and C, neither of the disks in set B showed any indication of micropitting damage.

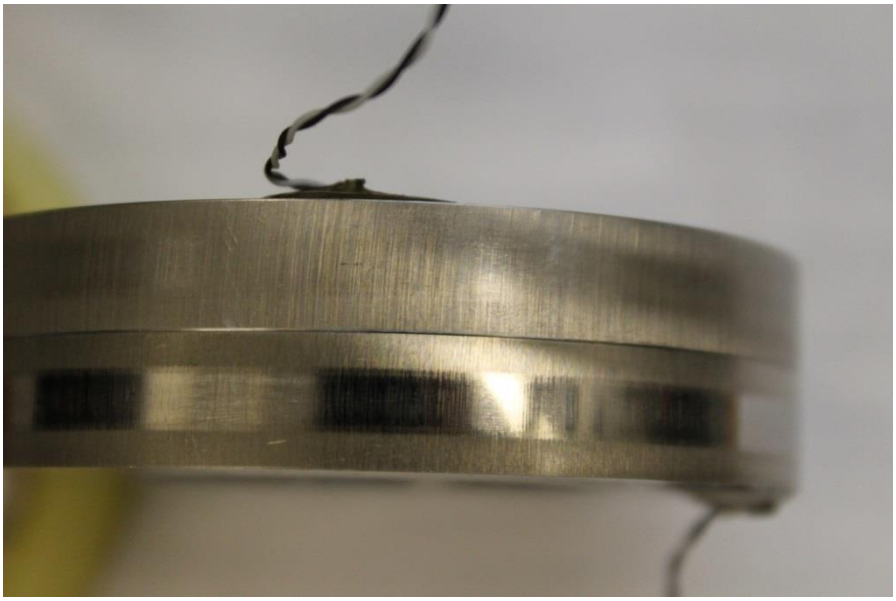

Figure 5-31 Close-up photograph of hard disk (upper) and soft disk (lower) beside one another following removal from their respective test shafts

Figure 5-32 shows the 3D profilometer scan for the fast disk from set B. Three distinct regions can be identified in the photo-simulation shown in Figure 5-32.

- Unrun areas; these are located at the top and bottom of the figure and have not experienced any modification due to the elliptical contact produced by the crowning of the surfaces.
- Outer track; these are located either side of the central running track and were produced by the initial loading stages at a maximum contact pressure of 1.7GPa.
- Central track; this region was produced by the decreased lambda ratio load stages. It is clear in Chapter 4 that the significant decrease in lambda ratio resulted in an increase in plastic deformation. This can be seen in the sharp drop in Ra value. The reduction in lambda value also generated more abrasive wear which can be seen by the aforementioned scoring marks in the circumferential direction.

The faster and softer surface demonstrate very clear wear marks in the circumferential direction. This is a result of the disparity in hardness, where aggressive features passing through the contact zone on the hard surface will plough or cut the surface of the softer body

if the strain cannot be accommodated elastically. It is also clear that reducing the lambda ratio has had a significant effect on the level of plastic deformation experienced by the asperity features.

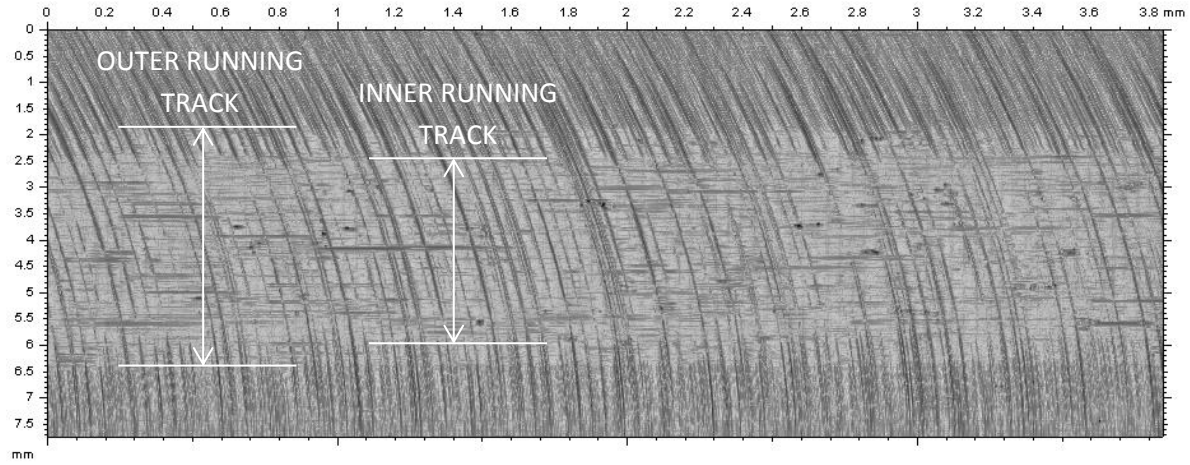

Figure 5-32 3D Scan of fast disk from set B showing distinct regions of plastic deformation following load cycles shown in Table 5-8

Figure 5-33a shows a scan of the topography of the fast disk from set B. A profile has also been extracted for section A-A and is displayed in Figure 5-33b. The profile illustrates the subtle slant developed by the asperities on the soft surface as a result of the traction force. This can be seen clearly in the range $0.4 \leq x \leq 0.45$ and also $0.5 \leq x \leq 0.6$ where features have developed sloped face towards the direction of the traction. Similar features occurring on the fast disk have been discussed in Chapter 4.

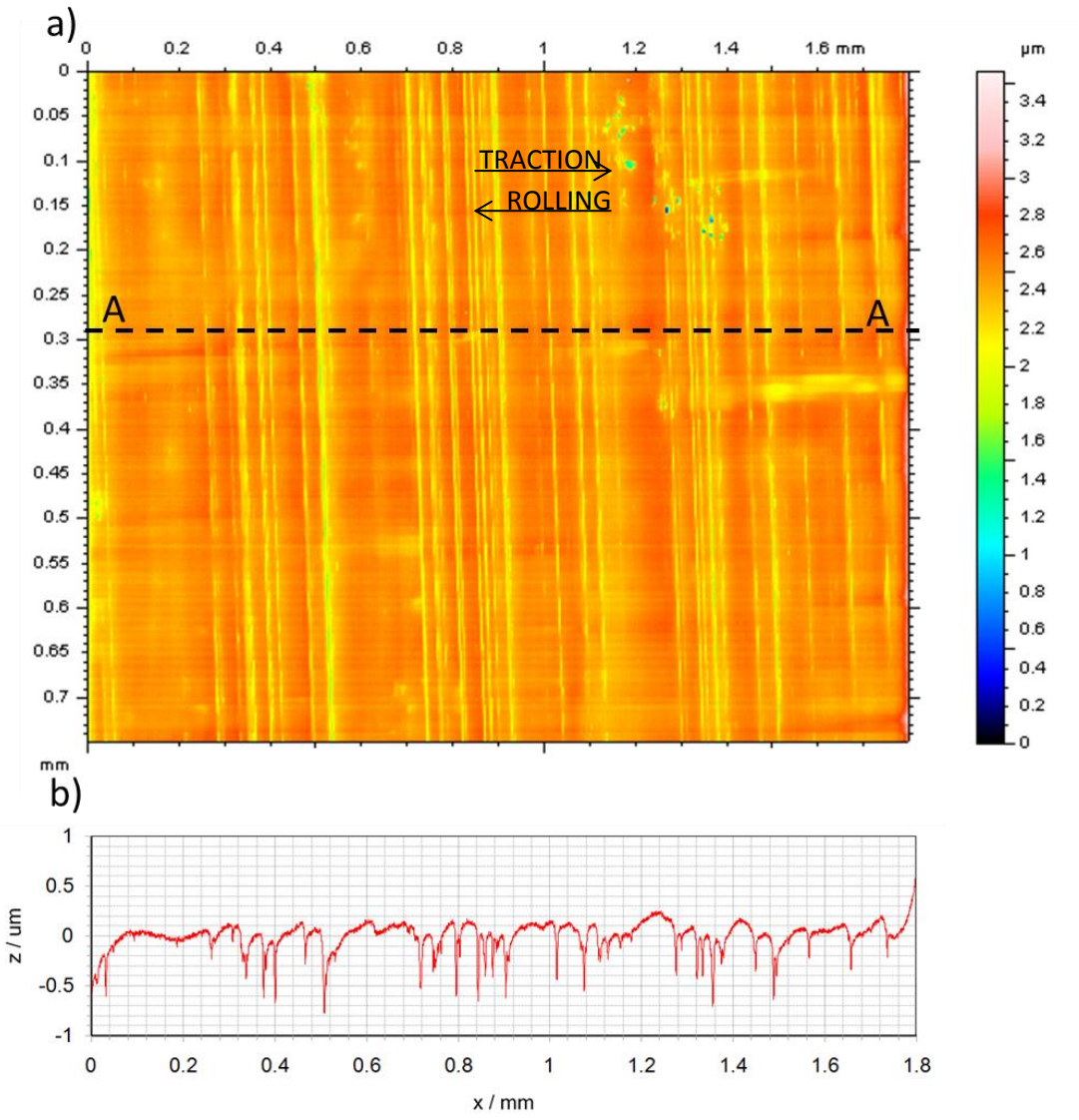

Figure 5-33 a) 3D scan of fast disk in set B shown as a pseudocolour image following load cycles in Table 5-8 b) profile trace taken along the line A-A

In comparison to the softer surface, it is very clear that the harder surface shown in Figure 5-34 has experienced very little modification. There is a faint running track and some sparse scoring marks visible on the surface. A likely cause for these are strain-hardened wear particles that have been drawn through the contact abrading the test surface.

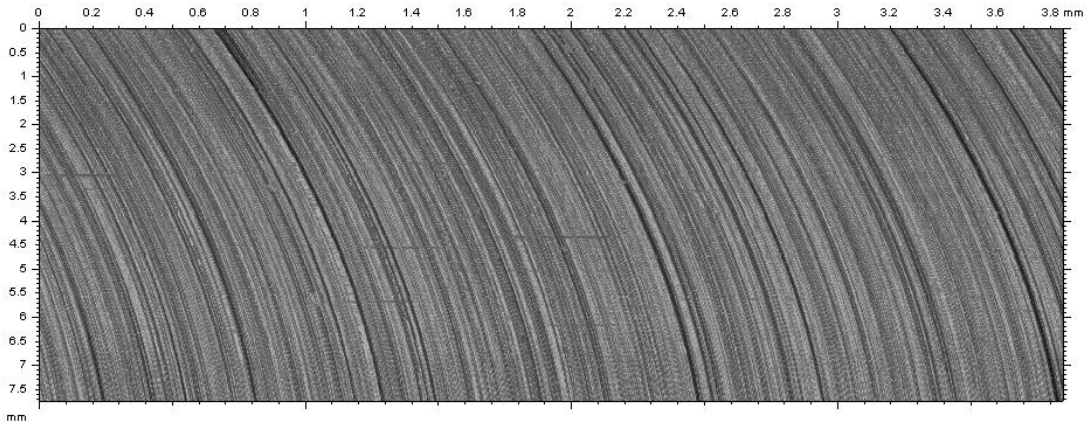

Figure 5-34 3D scan of slow disk from set B following load cycles shown in Table 5-8

5.4.3 Disk Set C

Upon observation of the running track following experiments, dark deposits are visible on either side of the contact which had not previously been seen at lower levels of sliding and are shown in Figure 5-35. These deposits were considered to be due to the higher temperatures attained in the contact and were most likely due to breakdown of oil products. The deposits were more prominent on the fast disk which attained higher temperatures across all experiments. The residue could be easily removed when wiped with disposable hand towels, after which the disk was again photographed as shown in Figure 5-36.

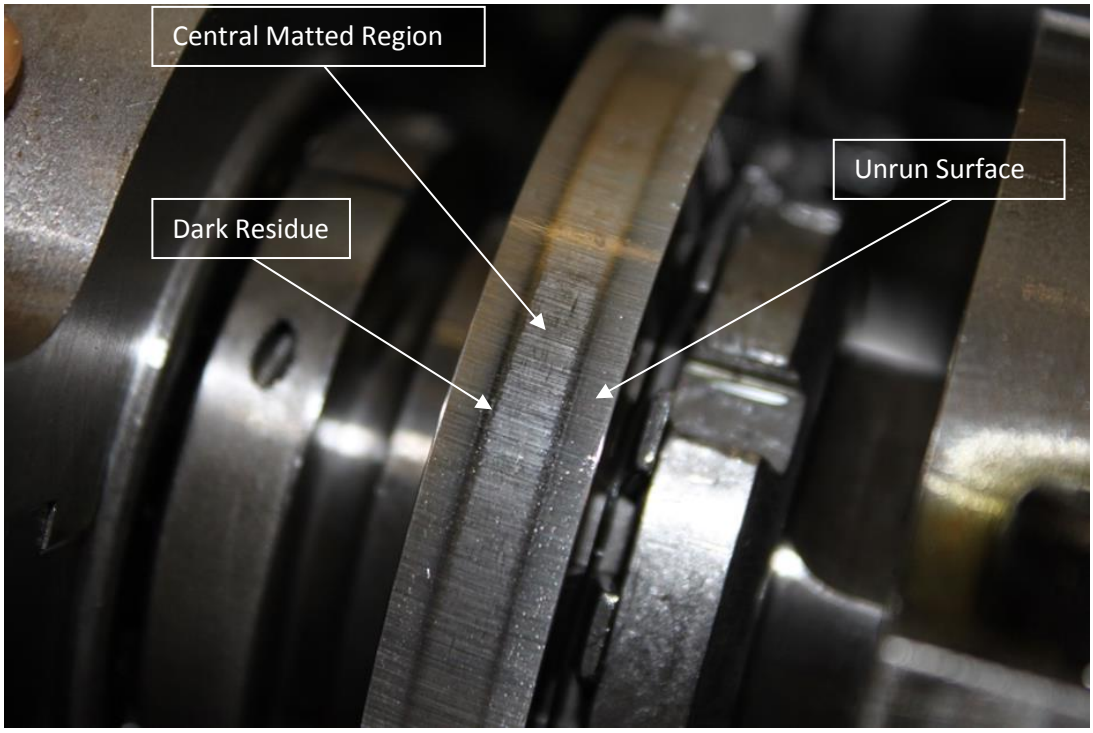

Figure 5-35 Photograph of test disk run at a SRR of 0.5 showing dark deposits at extreme edges of the running track

It could be seen following the removal of the residue that the extreme edges of running track still retained a more reflective appearance with a central region that appeared matted and dull in comparison.

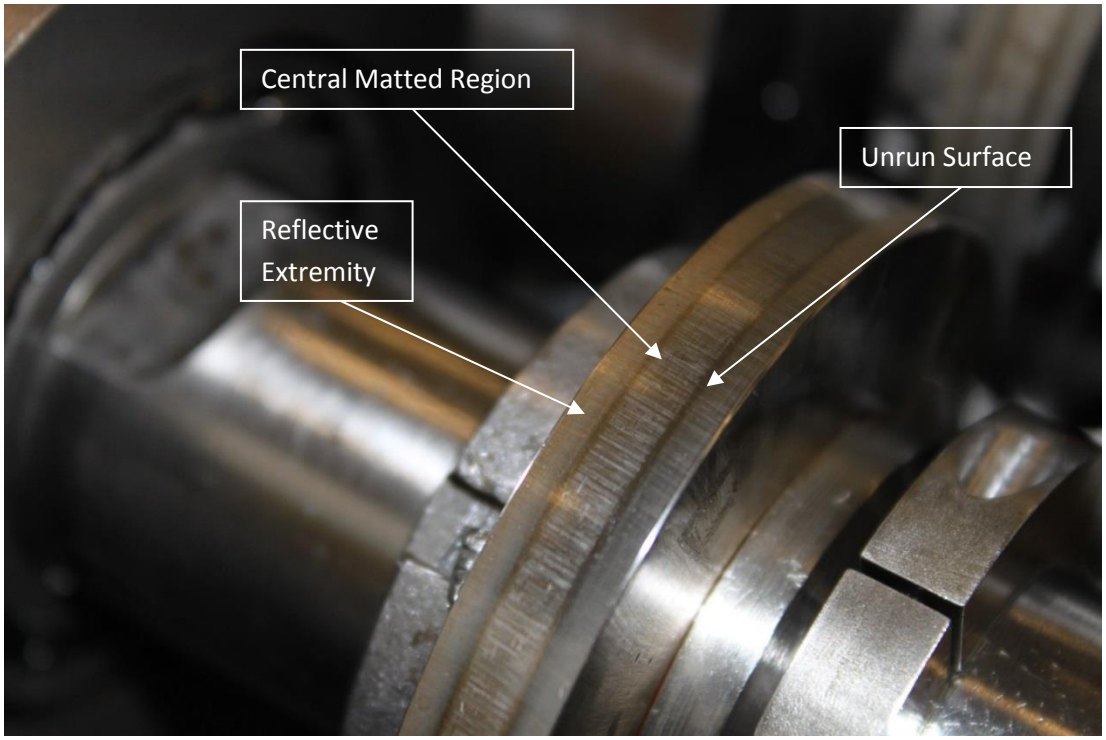

Figure 5-36 Photograph of test disk run at a SRR of 0.5 showing running track after removal of dark deposits

In total, the fast disk was run through 853,000 load cycles, far fewer than the number of cycles experienced by the disks run at a 0.25 slide roll ratio. The number of load cycles run at each load is shown below in Table 5-9.

Table 5-9 Accumulated load cycles for disk set C

Applied Load / N	Maximum Hertzian Pressure / GPa	Load Cycles on Fast Disk	Load Cycles on Slow Disk
4150	1.7	1,875	1,125
2320	1.4	397,390	238,434
1850	1.3	113,540	68,124
1460	1.2	113,540	68,124
1120	1.1	113,540	68,124
850	1.0	113,540	68,124
	Cumulative Total	853,425	512,055

Upon removing the disks from the rig and measuring the surfaces, it was clear that micropitting had taken hold and begun to alter the surface texture at the microscale on both test surfaces. The effect of this is also visible to the naked eye, when on observation of the central running track left by the speed varying tests under direct lighting shown in Figure 5-37. It is also clear from the scans shown in Figure 5-38 and Figure 5-39 that the reflective region shown is the result of plastic deformation in the absence of fatigue failure. Initial experiments run at high load for a low number of load cycles would have created a wider running track, but the low number of cycles in this region would have not been enough to initiate any kind of fatigue.

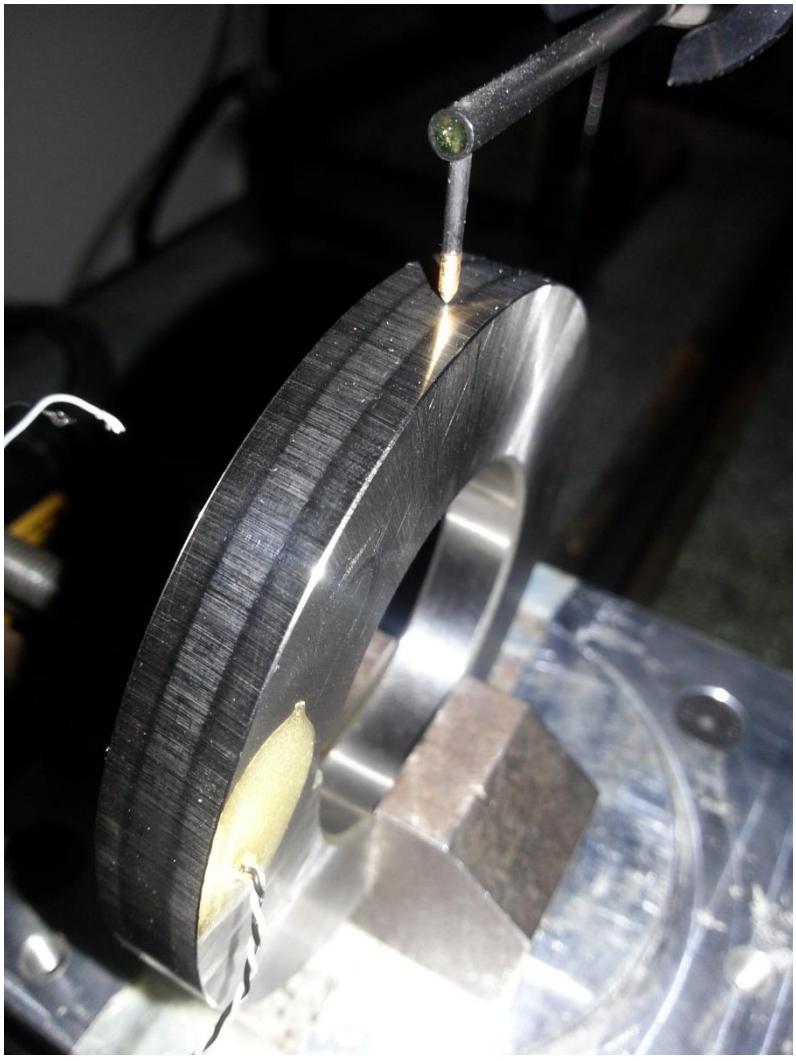

Figure 5-37 Photograph of test disk under direct lighting highlighting central frosted region

The photo simulations produced by the profilometer software show micropitting occurring with greater density across the running track for disk set C than for those in disk set A run in conditions of lower sliding. As with the disk set A measurements, the fatigue seems to be more pronounced on the slower of the two surfaces. An assessment of the linear profile traces in Chapter 4 also found that profiles taken from the slower surface had a lower cross correlation value with the original topography.

Micropitting appears to be distributed relatively evenly across the running tracks, despite the highest hertzian pressures occurring towards the centre. This being true, the most severe asperity loading in elliptical contacts has been found to occur at the extreme edges of the contact zone (Holmes et al., 2005a). As a result the even distribution may be due to the fact that the harshest loading experienced at the outer edges occurs less frequently as load is reduced and the contact area decreases whereas the central region sees the lower contact frequency with the damage accumulated over all the loads used.

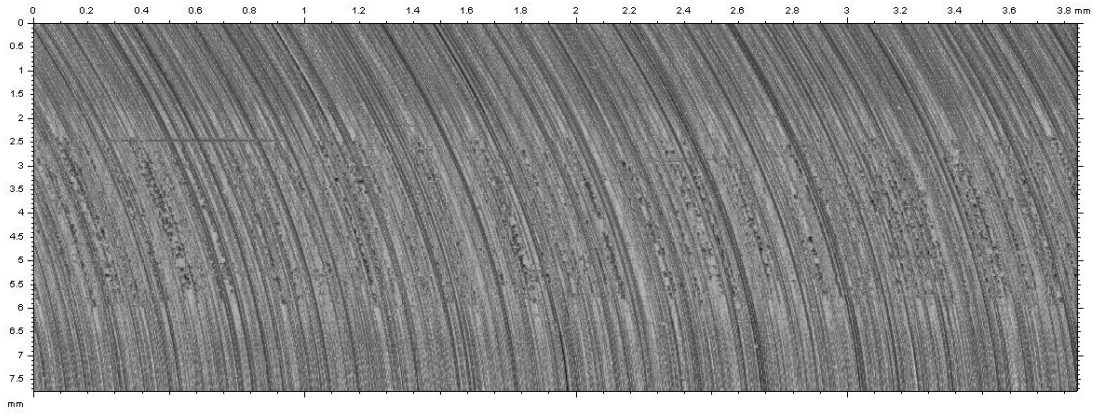

Figure 5-38 3D scan of slow surface from disk set C following load cycles shown in Table 5-9

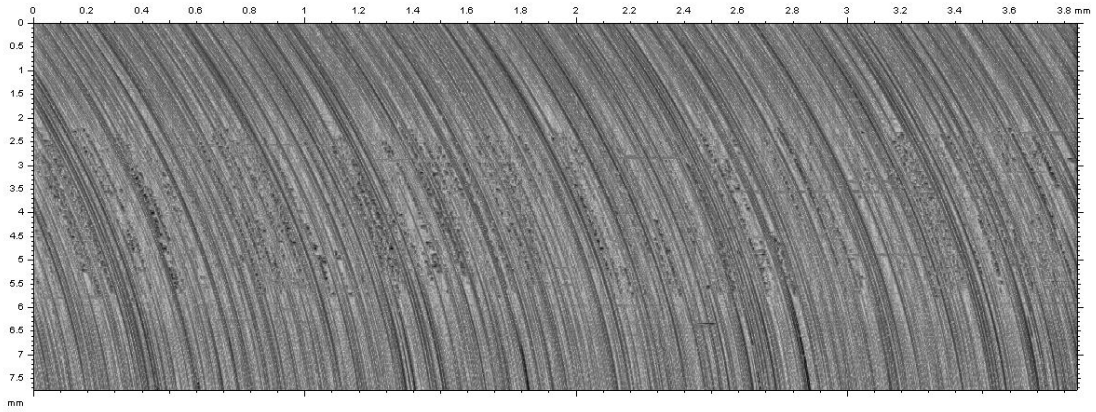

Figure 5-39 3D scan of fast surface from disk set C following load cycles shown in Table 5-9

Due to the grinding process the direction of the roughness is only approximately transverse and appears swept. The swept nature of the roughness lay is clearer in the 3D profilometer scans where the x-axis has been magnified for the purposes of presentation. Scans taken at higher resolution within the running track are shown in Figure 5-40 and Figure 5-41.

The faster surface is shown in Figure 5-40. Under greater detail, the heavy dependency of the fatigued region on roughness can be seen. Micropits appear distributed across prominent roughness ridges. Where micropitting has occurred, due to the nominally extruded nature of the finish, it appears to have occurred across the whole ridge. This has been highlighted with arrows. The ridge indicated with arrows appears to show micropits occurring very densely across the scan. It can be clearly seen that neighbouring asperity ridges do not show the same level of pitting.

There is no indication of pits occurring within valley features. Results shown in Chapter 4 demonstrate that interaction between surfaces occurs predominantly at the asperity tips, where modification occurs. In addition to the pit features, the scoring marks are aligned with the rolling/sliding direction and those at ordinate values y = 1.4mm and 0.9mm are probably due to debris travelling through the contact.

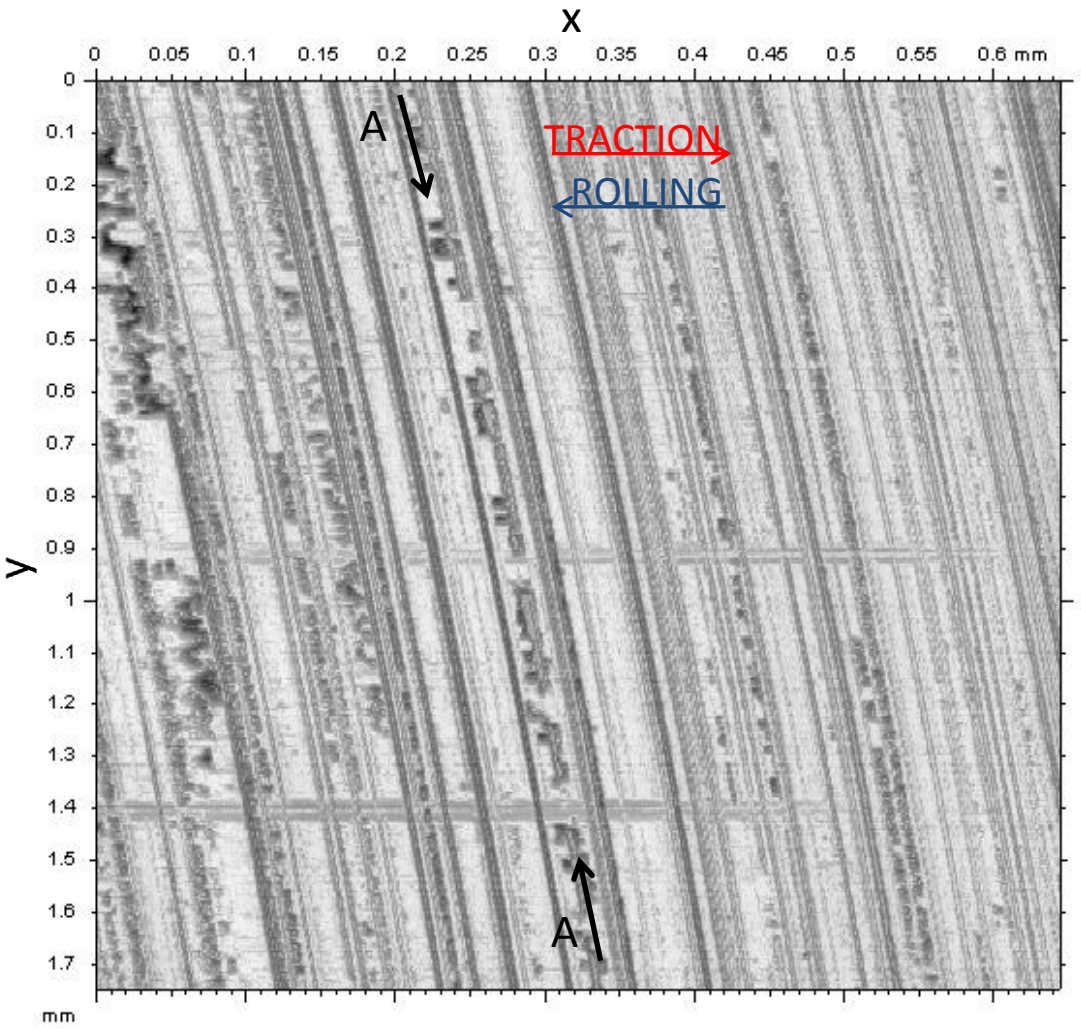

Figure 5-40 3D scan of micropitting damage on fast disk of set C

A higher resolution scan of the slow surface is shown in Figure 5-41. Pitted features can be clearly identified on the surface following the roughness lay. There are also some scoring marks present in the rolling/sliding direction. In comparison to Figure 5-40, the micropits appear to populate the surface more densely in both the x and y directions, with pits appearing closely packed on the prominent features. It can be seen that more of the major asperity ridges also appear to be experiencing a degree of fatigue. Although the scans presented are relatively short in the x direction, of the order of 2a, this tendency for the slower surface to accumulate more damage has also been confirmed qualitatively in Chapter 4 where results for cross correlation between original and fatigued profiles show less correlation on the slow surface.

As with Figure 5-40, where pitting occurs it occurs very densely on certain asperity ridges. There are also ridges that appear to experience no pitting. Ridge A, indicated in Figure 5-40 appears to show very closely packed pits occurring across the length of a roughness feature whereas feature B spans the same length and does not show any indication of pitting. Valley features in the scan again do not show any indication of pitting.

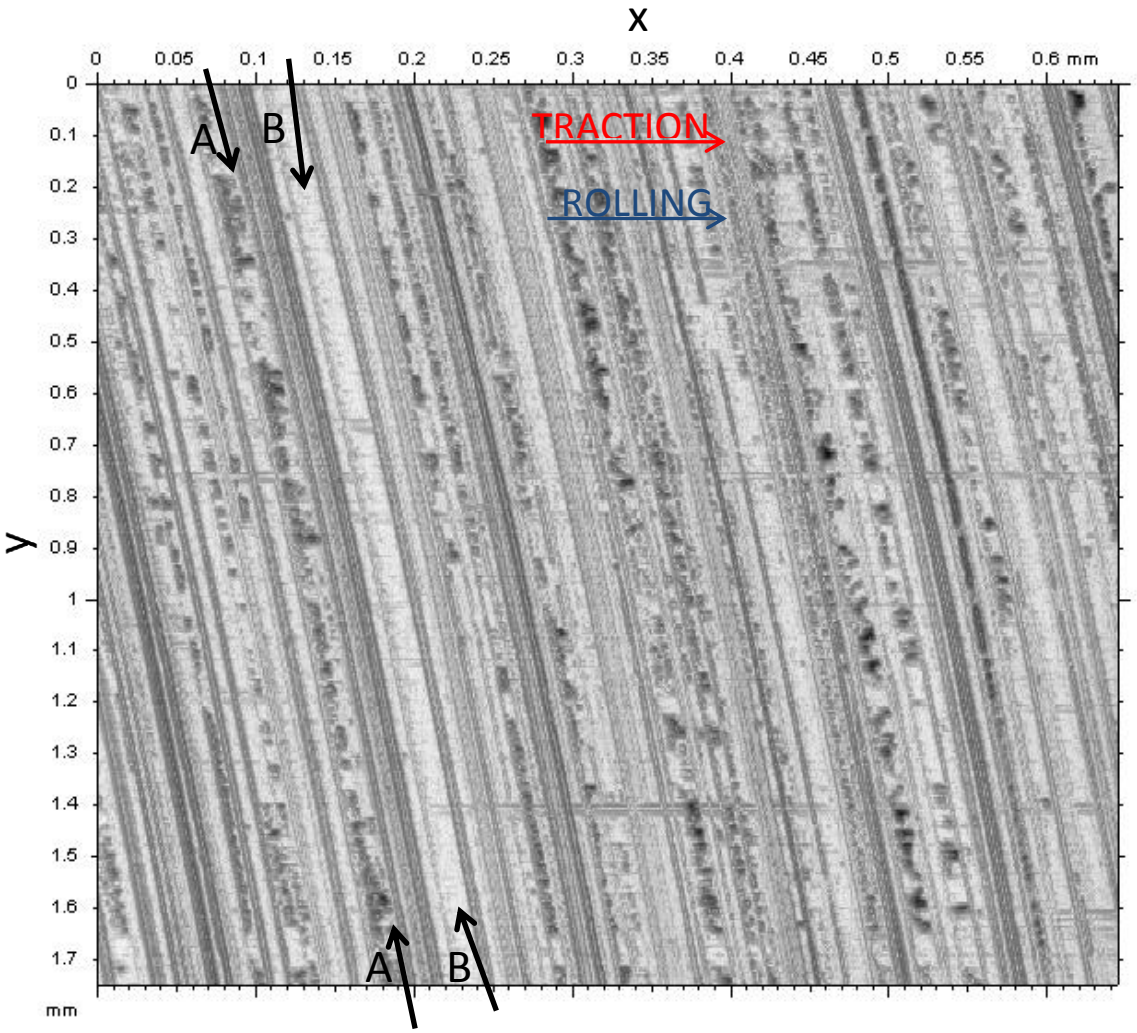

Figure 5-41 3D scan of micropitting damage on slow disk of set C

Figure 5-42 shows a scan taken at the extreme edge of the micropitted region on the slow surface. The shapes of some of the pit features can be seen more clearly. Again, pitting appears to be limited to the ridges on the surface topography, appearing densely on certain features and far less densely on others. It can be seen that the pitting region stops abruptly beyond the ordinate x = 1.15mm. Upon close inspection of the previous scans it can be seen in

some regions that some fatigue features appear to take on the shape of chevrons. This has been indicated and can be seen clearly at feature A and again on the same ridge at feature B. This has been associated with pitting failure in fatigued gears and has also been identified to occur in micropitted surfaces (Errichello, 2010) .

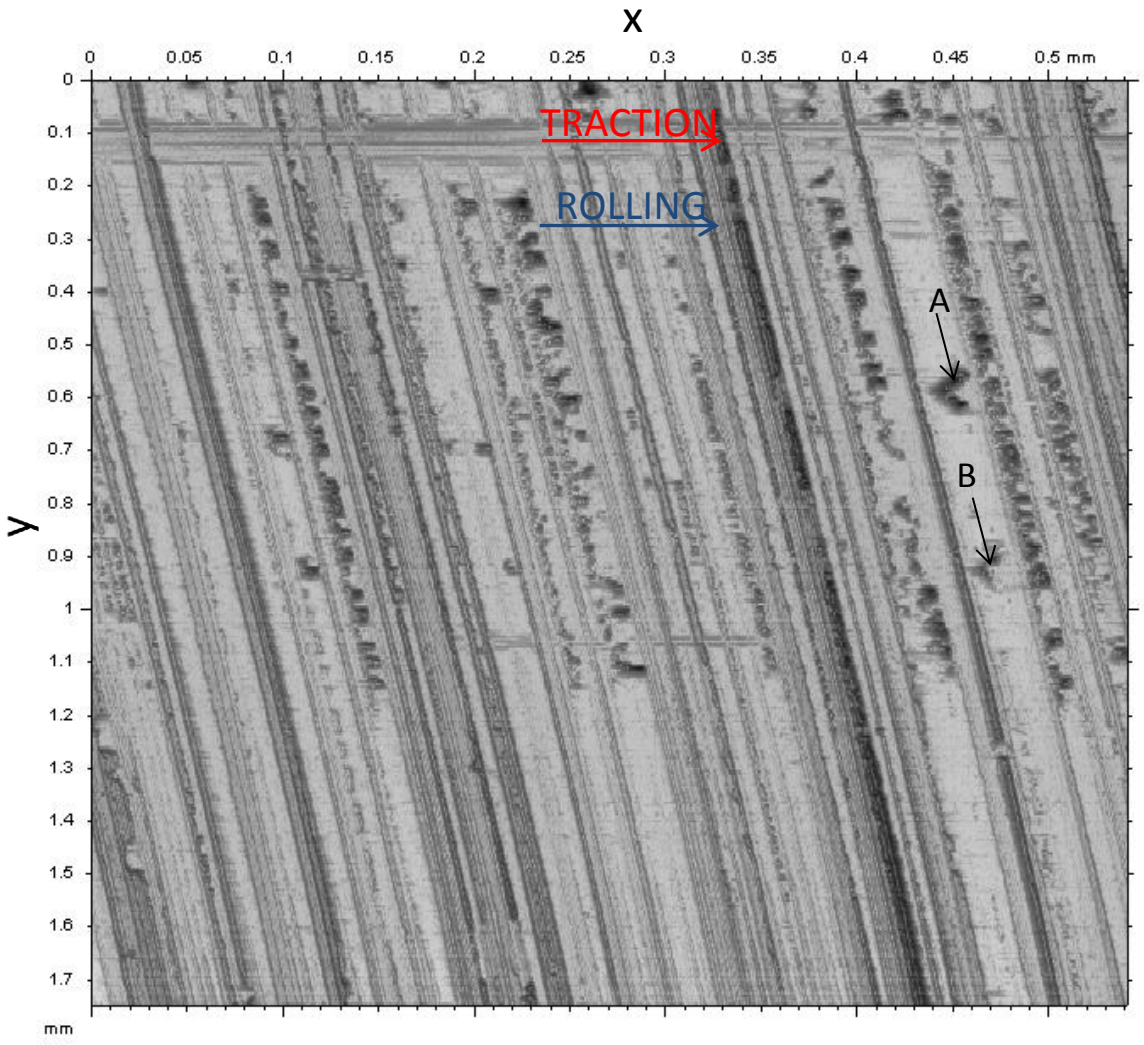

Figure 5-42 3D scan of micropitting damage on slow disk at extreme edge of contact zone of disk set C

5.5 Discussion

The experiments presented demonstrate the sensitivity of asperity contact frequency to the lambda ratio. This sensitivity is visible in both the calculated mean contact voltage values and instantaneous data in which contact events are displayed as contour plots. Contact frequency can be seen to vary greatly in lower speed regions, following a change in entrainment speed

where transient bulk disk temperatures result in changing film thickness. Comparison of the plots of friction coefficient against the lambda ratio with those of contact voltage against lambda ratio suggest that asperity contacts have little influence on the measured friction. This is probably due to the small fraction of the contact area over which direct interactions between the surfaces have been found to occur at any given time in numerical analyses (Evans et al., 2013).

Plots relating the coefficient of friction to the lambda ratio at higher levels of sliding demonstrate the influence of temperature rise within the contact on measured friction. Values of friction measured at higher levels of sliding are lower than those obtained at lower levels of sliding for comparable lambda ratios due to decreased viscosity within the contact.

Friction values obtained can be seen to be affected by film thickness where step changes in entrainment speed result in a corresponding change in the measured friction. Under higher levels of sliding, changes in friction are also observed in areas of steady entrainment speed due to the highly transient bulk disk temperatures which also lead to appreciable changes in lambda ratio.

Under these conditions of high sliding, it is shown that whilst low friction values may be achieved, the lambda ratios calculated indicate that the contact may still operate well within the mixed lubrication regime, where what is interpreted as direct metal-to-metal contact takes place. This may have implications for component lifespan. This has also been verified at high lambda ratios through observation of plots produced of contact voltage traces where even mean values approaching 43mV show repeated contact instances which, due to the experimental configuration, can be associated with the same groups of asperities interacting on the surfaces.

Where the level of sliding has been increased, the calculated lambda ratios occurring during a test have been found to cover a narrower range, remaining well within the mixed EHL regime. The reduction in load carrying capacity and surface separation of the oil film results in greater and more frequent asperity interaction. From consideration of the measured surface profiles, it is apparent that surfaces running at higher slide roll ratios degrade more rapidly. This is due to an increase in asperity interaction brought about by the change in contact kinematics and thin films, which also contribute to increasing asperity loading.

Where micropitting has been observed in the tests, it can be strongly associated with surface asperity features, where observed metallic contact is most likely to occur. The surface texture is shown to have a significant influence on the micropitting lifespan of a surface, where a smooth surface (the fast disk in Set B) that experienced a high number of load cycles did not show any indication of the failure mechanism, although the reason for this may also be associated with the abrasive wear processes seen to be occurring.

Experiments conducted by others have demonstrated the initiation of micropitting to be heavily dependent on applied load. The reason for this could be due to the phenomenon of martensite decay which has been seen to occur in micropitted gears (Oila et al., 2005). High levels of sliding have not been found to influence the initiation of micropitting, but to be associated with the rapid progression of failure (Oila and Bull, 2005).

On observation of micropitted surface scans presented in this work it is clear that pitting failure can be seen to occur heavily on certain asperity ridges whilst other ridges remain free of pits. This implies that contact has a tendency to occur cyclically between certain features whilst other asperity features do not experience the same level of interaction as they traverse the contact. This cyclic nature of contact between surfaces features also been implied with results from triggering experiments where the high level of repeatability between contact voltage traces suggests the same groups of asperities interact in the contact zone.

Future work would benefit from a more consistent approach as whilst fatigue failure had occurred on test specimens, comparisons were difficult to draw due to an inconsistent approach to experimentation in this research project. Tests in this work were run initially to observe the effect of lambda ratio on asperity contact and it was not foreseen that micropitting would appear so rapidly until this was observed at the latter stages of the testing programme.

In addition to this, an attempt at approximating the minimum film thickness through the use of the acquired contact voltage data and surface microgeometry as trialled by Tallian et al. (1964) could be of use.

5.6 Conclusions

Experiments using contact voltage as an indicator of film thickness have demonstrated the sensitivity of asperity contact frequency to the lambda ratio. This has can be seen in Figure 5-23 and Figure 5-25 where slight increases in lambda ratio, result in large increases in contact voltage – signifying a reduction in asperity interaction.

It has also been implied that the rate of metallic contact is associated with the micropitting lifespan of a surface, this is visible in the results of 3D profilometry where surfaces run at lower slide roll ratios did not experience the same level of micropitting.

At higher levels of sliding, contact is shown to occur more frequently. This is due to both the kinematics of the contact and impact of frictional heat dissipation on the lubricant inlet temperature. Contact between asperity features has also been shown to occur cyclically in contact voltage traces and the results of 3D profilometry has shown fatigue to accumulate on particular prominent asperity ridges. Where asperity contact does occur between surfaces, it is seen to have little influence on the measured friction value.

6 Simulation of Contacts

6.1 Introduction

In this chapter, the author describes the use of the coupled point solver used to simulate the rough surface mixed-EHL problem. The development and use of the coupled method to solve the EHL point contact is described in the thesis of Holmes (2002). The author has used a range of conditions recorded from experimental data as input conditions for analyses and modifications carried out as part of this work allow the use of real 3D rough surfaces as measured from test specimens.

Preliminary results using 3D rough surfaces in the point contact model demonstrate the occurrence of large pressure spikes both transverse and parallel to the oil entrainment direction. Thermal effects are also found to be significant in influencing the size of these pressure spikes.

Results for contact occurrence between asperities appeared to be an overestimate, this is likely due to the misalignment between the measured surfaces which simulate conditions that would result in further running in. However, results for contact appeared to follow the same trends as experimental data, demonstrating the applicability of the method for future modelling efforts.

6.2 Transient EHL Point Contact Model

The model solves the point contact EHL problem by simultaneously solving both the non-Newtonian Reynolds equation and the elastic deflection equation. Due to the use of real rough surfaces, the problem becomes transient and the solution must be divided into a series of time steps, each of which is a problem in itself. A description of the equations used will now be given.

6.2.1 Reynolds Equation

Introduced in Chapter 2, the Reynolds equation governs the pressure and film thickness within a thin fluid film.

$$\frac{\partial}{\partial x}\left(\sigma_x \frac{\partial p}{\partial x}\right) + \frac{\partial}{\partial y}\left(\sigma_y \frac{\partial p}{\partial y}\right) - \frac{\partial}{\partial x}(\rho \bar{U} h) - \frac{\partial}{\partial y}(\rho \bar{V} h) - \frac{\partial}{\partial t}(\rho h) = 0$$

6.2.2 Elastic Equation

The elastic equation was also introduced in Chapter 2, and now includes the additional term $\varphi(x, y)$which is the combined surface roughness of the two surfaces at the time in question.

$$h(x, y) = h_0 + \frac{x^2}{2R_x} + \frac{y^2}{2R_y} + \varphi(x, y) + \frac{2}{\pi E'} \iint_A \frac{p(s, v)}{\sqrt{(s - x)^2 + (v - y)^2}} ds dv$$

For use in the solution method it has been used in differential form and discretized as:

$$\frac{\partial^2 h(x_i, y_i)}{\partial x^2} + \frac{\partial^2 h(x_i, y_i)}{\partial y^2} = \frac{\partial^2 \varphi(x_i, y_i)}{\partial x^2} + \frac{\partial^2 \varphi(x_i, y_i)}{\partial y^2} + \frac{1}{R_x} + \frac{1}{R_y} + \frac{2}{\pi E'} \sum_{all\ k,l} f_{k-i,l-j}, p_{k,l} \quad \textbf{(6.1)}$$

The f_{ij} terms are the weighting functions for the influence of pressure on the deflection Laplacian; the evaluation of these are described by Evans and Hughes (2000). The weighting functions are highly localised and allow the coupled solution of the Reynolds and Differential Deflection equations.

The summation on the right hand side is split into three subareas and equation (6.2) is rearranged to the form:

$$\frac{\partial^2 h(x_i, y_i)}{\partial x^2} + \frac{\partial^2 h(x_i, y_i)}{\partial y^2} - \frac{2}{\pi E'} \sum_{near} f_{k-i,l-j} p_{k,l}$$

$$= \bar{E}_{i,j} + \frac{2}{\pi E'} \sum_{close} f_{k-i,l-j} p_{k,l} + \frac{2}{\pi E'} \sum_{far} f_{k-i,l-j} p_{k,l} \quad \textbf{(6.2)}$$

where $\bar{E}_{i,j}$ comprises the first four terms on the right hand side of equation (6.1) and is constant function of position during the timestep.

The area for the 'near' summation is the point (i,j) and the neighbouring points that are involved in the discretisation of the equation. The area for the 'close' summation is a rectangular band of points surrounding the neighbouring points, and the remaining area is that for the 'far' summation.

6.2.3 Solution Method

The solver begins by calculating the pressure distribution and film thickness for a smooth surface, steady state problem, this is performed using the input conditions and the formula by Chittenden et al. (1985) to establish an initial film thickness for the first trial pressure distribution.

Once the steady state problem has been solved, the roughness features are gradually fed into the contact. Each time step requires a converged solution of the pressure and film thickness with the modified surface geometry. The pressure and film thickness values for the previous time step are used as a starting point for the time step being solved.

The 'far contribution' to deflection is calculated periodically within the time step – this has been shown to have little influence on the overall solution and, as it requires significant computational power, it is beneficial to minimise the number of times it is recalculated.

The Reynolds and elastic equation are solved in a coupled formulation. In order to do this the Reynolds equation is discretised using linear quadrilateral finite elements with an implicit (Crank-Nicholson) time formulation and the elastic equation is discretized using finite

differences for the Laplacian with the pressure coefficients f_{ij}. The discretisation methods for both the transient Reynold's equation and elastic equation are fully described in the thesis of Holmes (2002) and associated papers. Both the Reynolds and elastic equations can be expressed in the generalised numerical form shown in equations (6.3) and (6.4).

$$\sum_{k=0}^{n_c} A_k p_k + \sum_{k=0}^{n_c} B_k h_k = R_{i,j} \tag{6.3}$$

$$\sum_{k=0}^{n_c} C_k p_k + \sum_{k=0}^{n_c} D_k h_k = \bar{E}_{i,j} \tag{6.4}$$

In equations (6.3) and (6.4) the notation adopted is that suffix 0 is the point of application of the differential equations, (i, j). Points with suffices 1 to n_c are the neighbouring points for the partitioned summation in equation (6.2) and include all the points involved in the discretisation of the differential equations. $R_{i,j}$ is the right hand side of the Reynolds equation which, in the Crank Nicholson formulation, is derived from the values of pressure and film thickness at the previous time step. $\bar{E}_{i,j}$ is the right hand side of equation (6.2)

Holmes (2002) found that when attempting a Gauss-Seidel point iteration method, where equation (6.3) is modified to attain an updated pressure and thus fed into equation (6.4) to attain a new film thickness the process was unstable. The equations are thus rearranged in the form of a pair of equations for the unknowns p_0 and h_0 at the point of application of the equations.

$$A_0 p_0 + B_0 h_0 = \hat{R}_{i,j} \left\{ = R_{i,j} - \sum_{k=1}^{n_c} A_k p_k + \sum_{k=1}^{n_c} B_k h_k \right\} \tag{6.5}$$

$$C_0 p_0 + D_0 h_0 = \widehat{\bar{E}_{\iota,J}} \left\{ = \bar{E}_{i,j} - \sum_{k=1}^{n_c} C_k p_k + \sum_{k=1}^{n_c} D_k h_k \right\} \tag{6.6}$$

For the unstable point iterative approach equation (6.5) is used to determine a new approximation to p_0 and equation (6.6) to give the new approximation to h_0 in the iterative sweep of the solution area.

It was found that a stable method resulted when equations (6.5) and (6.6) were regarded as a pair of equations and solved simultaneously to provide the new approximations to p_0 and h_0.

$$p_{i,j}^{new} = \frac{\hat{R}_{i,j} D_0 - \widehat{\bar{E}_{\iota,J}} B_0}{A_0 D_0 + B_0 C_0} \quad \textbf{(6.7)}$$

$$h_{i,j}^{new} = \frac{\widehat{\bar{E}_{\iota,J}} A_0 - \hat{R}_{i,j} C_0}{A_0 D_0 + B_0 C_0} \quad \textbf{(6.8)}$$

These equations are applied iteratively to solve the equations for the specified close and far summations and the pressure dependent boundary conditions for equation (6.1). The close summation contribution and the pressure dependent fluid properties are updated as soon as the linearized equations have been solved with the insensitive far summation and film thickness boundary conditions recalculated in an outer loop, as illustrated in Figure 6-1.

Mixed lubrication conditions are encountered when the solution to equations (6.5) and (6.6) result in negative film thickness. Holmes *et al.* have demonstrated that this corresponds to an inability of the EHL film to separate the surfaces at that particular point and time step. In these circumstances, at the points where h_0 values below zero are calculated, h_0 is set to zero and Reynolds equation does not apply. The elastic equation is then used as the equation that determines p_0.

$$p_0 = \frac{\widehat{\bar{E}_{i,j}}}{C_0}$$

when h_0 is set to zero.

This process allows the algorithm to determine the contact points dynamically within the solution method without any assumptions regarding which positions are in contact. A simple flow chart describing the solution method for the transient point solver is shown in Figure 6-1.

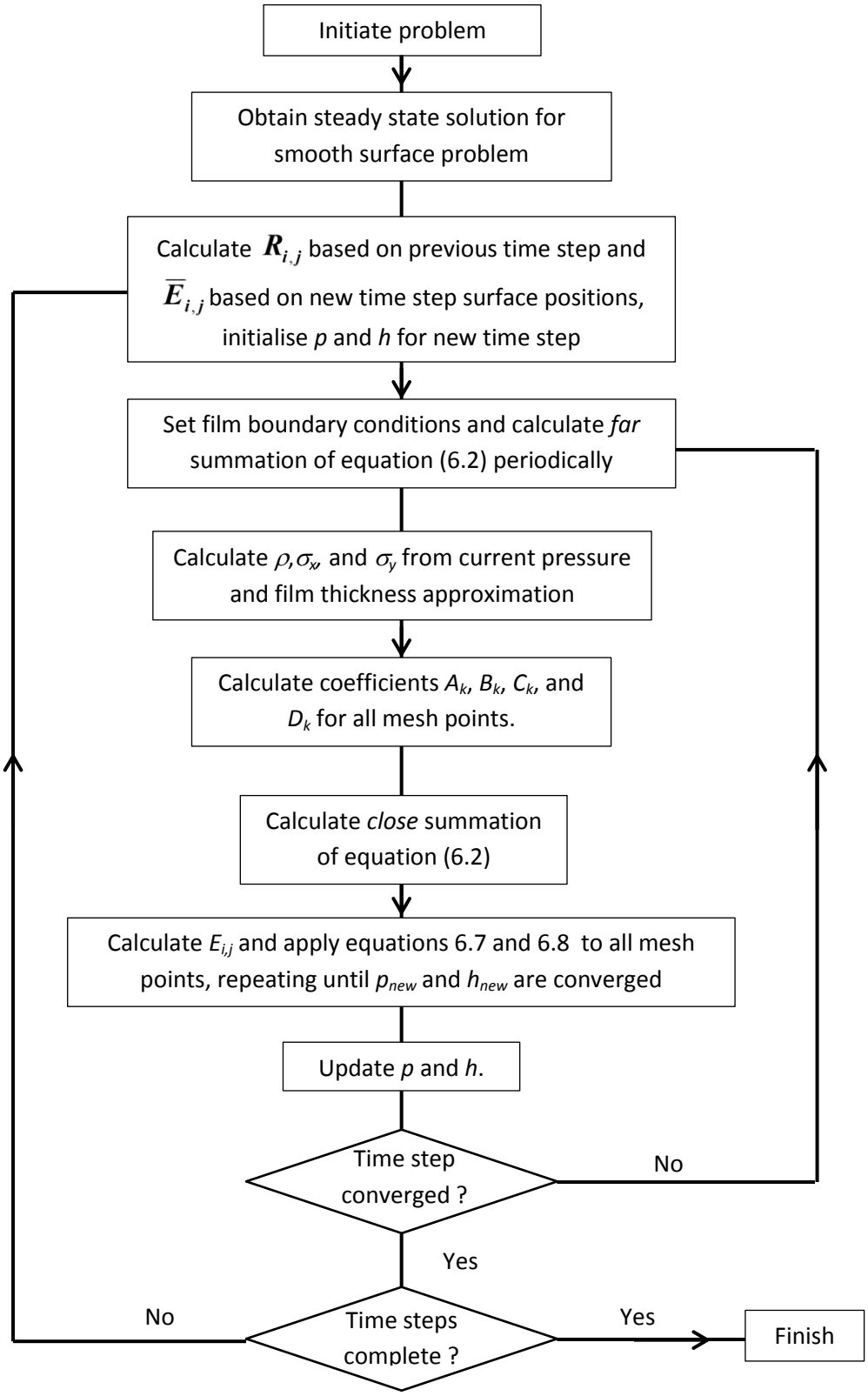

Figure 6-1 Flow chart describing basic function of the coupled EHL transient analysis

6.3 Modifications to point solver program for current work

6.3.1 Rough Surfaces

This section describes the modifications made to the solver to enable the use of measured 3D surface roughness. Previously, the software had used a measured roughness profile and extruded the features across the whole contact providing a roughness transverse to the direction of entrainment. An extruded roughness profile does not capture the sweeping nature of the roughness lay evident in figures 5.28 and 6.2, for example, nor any of the finer transverse direction features present on ground surfaces used in the experiments. Whilst the direction of entrainment is nominally transverse to the prominent asperity features, the grinding process does not produce an extruded roughness topography. To more accurately simulate contact, it was necessary to measure the real 3D roughness passing through the contact where the lay of the two surfaces generally results in asperity features crossing at a shallow angle as is also the case in helical gear surfaces as shown by Jamali (2014).

Roughness profiles were measured using the 3D Talysurf from each of the test disks from set A. Typical profilometer measurements for the positions of these surfaces are shown in Figure 6-3 and Figure 6-4. The figures displayed are values for surface height output for each point in the calculation area. The measurements contain examples of features that are not present in extruded rough surfaces. Note that the axis coordinates are scaled to the nominal Hertzian semi width in the rolling/sliding direction, x, and that the true aspect ratio of the area shown in these figures is 4:1.

6.3.1 Measuring the Surfaces

The surface roughness was measured over the width of the running track. A 3D surface roughness measurement is performed in the Taylor Hobson Form Talysurf by automatically measuring a series of linear profile traces and indexing the specimen in the y-direction after each profile trace so that, together, the profiles form a ‘roughness map.’

To take a surface measurement the disks were cleaned and mounted on the Talysurf stage as shown in Figure 6-2. The specimen was aligned using a straight edge to ensure the surface was correctly orientated to the stylus. A map measuring 4mm x 8mm was taken spanning the running track which was clearly visible.

This measurement could then be further edited using Talymap software, where portions of unwanted surface could be removed, allowing the plastically deformed running track to be more accurately centralised within the file. This was important as the surface is orientated from the 'centre' of the running track within the EHL software. Therefore a decentralised running track could result in misaligned surfaces in the analysis. Roughness map measurements were obtained with a spacing in the y-direction of 25µm which was nominally that of the EHL mesh spacing. This eliminated the requirement for interpolation transverse to the direction of entrainment. The form and waviness of the surface were then removed using a Gaussian filter with lower cut-off of 0.25mm, which would leave the surface roughness attenuated.

Figure 6-2 Test disk positioned on Talysurf stage

The topography of both surfaces has a swept appearance and is not perfectly transverse to the entrainment direction. They have been given a crossed orientation in the software to simulate their mode of contact when in the test rig. Figure 6-3 shows the fast disk surface and a prominent scoring mark nominally aligned with y=-0.4a is present on the running track. The slow surface shown in Figure 6-4 includes some artefacts introduced by processing the surface in the Talysurf software, where the digital removal of erroneous data points has distorted some of the roughness features. Examples of this can be seen at x=1.0a, y=-6.0a and also at x=-1.5a, y=-2.0a.

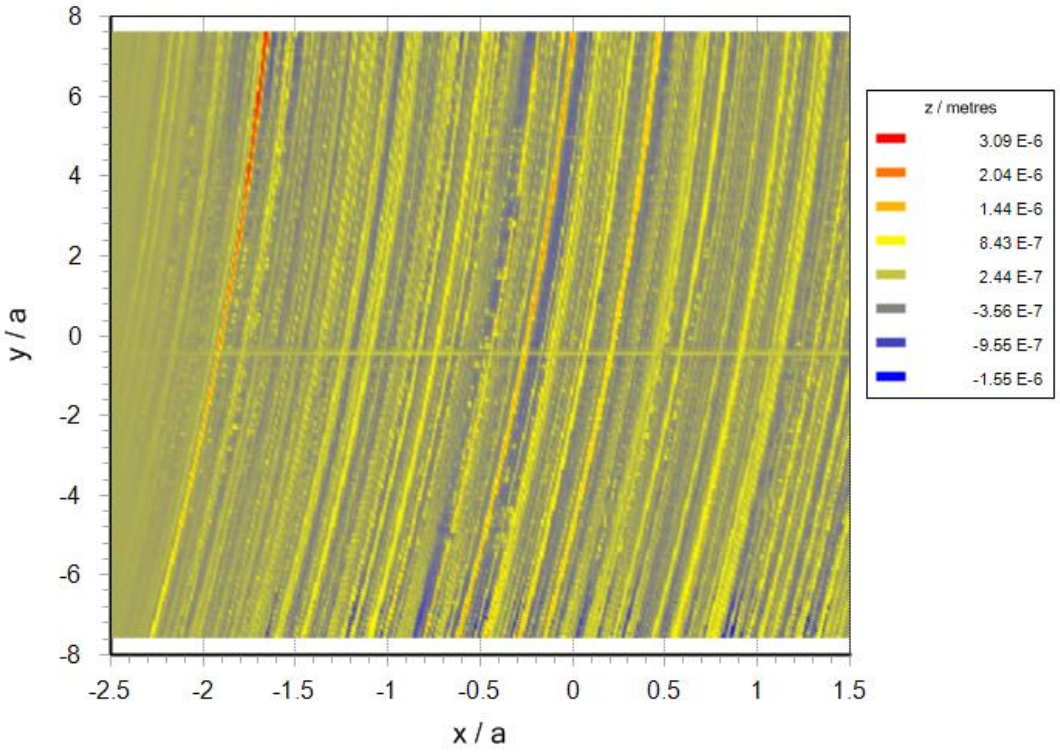

Figure 6-3 Measured roughness for surface 1, the faster surface

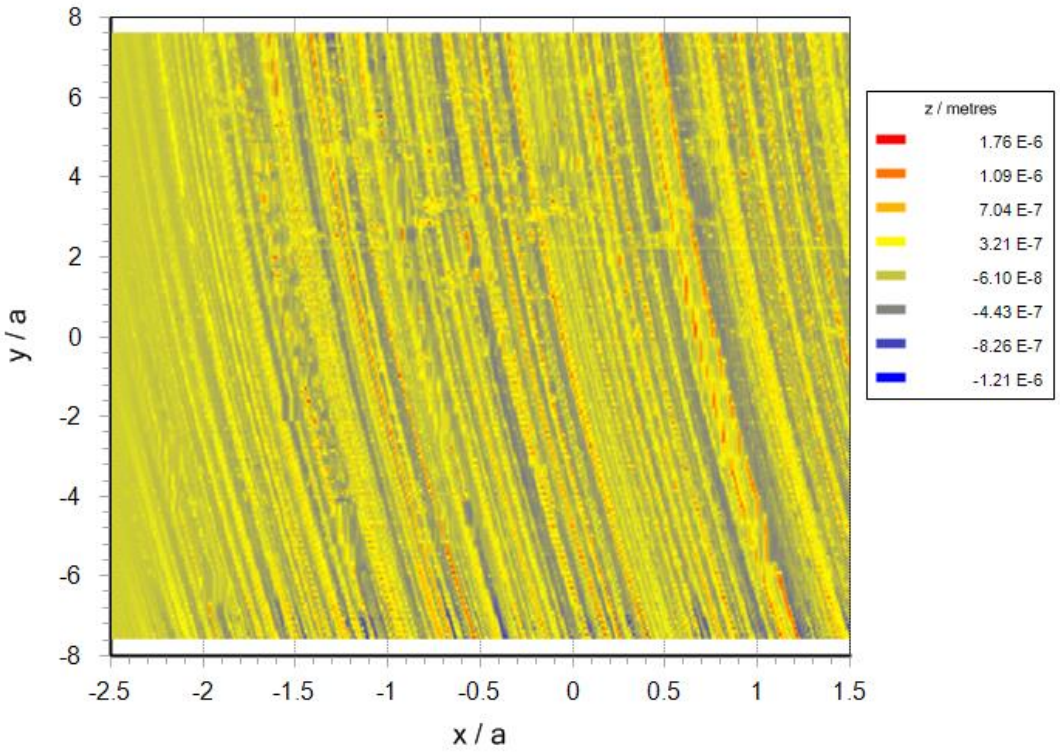

Figure 6-4 Measured roughness for surface 2, the slower surface

6.3.2 Software Modifications

To allow the use of 3D roughness files within the software, it was necessary to produce a new set of subroutines. A modification was chosen in order to preserve existing subroutines which would extrude the geometry in the transverse direction.

New versions of roughness handling subroutines were created which were capable of managing the new 3D geometry, and these are described in terms of their function in the next section.

6.3.2.1 INITIATE_ROUGHNESS_2D

INITIATE_ROUGHNESS_2D calls the relevant subroutines to read the roughness data from the text files as exported by the Taylor Hobson Talymap software and store them. The subroutine INITIATE_ROUGHNESS_2D also calls the subroutines responsible for the interpolation of the roughness data of the fast surface onto the EHL mesh and setting up the second derivatives for

the slower surface, which are used for the cubic spline interpolation required to give the surface height at the mesh points for each time step.

6.3.2.2 READRF_2D

READRF_2D reads the roughness files into 2D arrays which are stored in the program. The leading edge of the roughness map is also attenuated with a ramp factor to prevent the program failing when transitioning from a smooth surface solution due to sudden changes in pressure.

6.3.2.3 INTDER_2D

INTDER_2D reads through the initiated roughness data and calculates and stores the second derivatives for each linear profile trace in the x-direction.

6.3.2.4 RUFFINT_2D

RUFFINT_2D carries out the interpolation of the faster surface, using cubic splines. This is only performed once during INITIATE_ROUGHNESS_2D as the faster surface moves half a mesh spacing each time step. Therefore the simulation only requires two sets of data between which to alternate as the roughness progresses.

6.3.2.5 GEOMIN_2D

GEOMIN_2D is called at the end of each time step and interpolates the roughness for the slower surface. This occurs because the distance moved by the slower surface is dependent on the slide-roll ratio used and so a new interpolation is required for each time step as the EHL analysis mesh spacing is not necessarily an integer multiple of the distance moved in a time step (which would allow a number of sets of height data to be used in a repeated sequence, as is the case for the fast surface).

6.3.2.6 GEOMRO_2D

GEOMRO_2D is called at the end of each time step and sets up the roughness data for the faster surface by repositioning the profiles in the solution space.

6.3.2.7 GAUSS_SEIDEL

It was found that with the new geometry the program would fail on calculation of the non-Newtonian parameters. This was prevented by adopting a significant under-relaxation of the Gauss Seidel loop as it was found that high pressures were causing instability and time pressures did not allow a more satisfactory solution to be sought to the problem.

6.4 Results

This section discusses the preliminary results obtained using the EHL point solver where experimental results for bulk disk temperature, load and mean surface velocity were used as input conditions.

The results are presented in the form of cumulative distribution function plots which have been used to compare the variation in contact and thin films between different experimental conditions. Cumulative distribution plots for film thickness and pressure are calculated from tabulated data for each transient solution and show the averaged behaviour of the simulation.

Results for film thickness have also been presented in the form of contour plots which demonstrate the impact of moving roughness features, although with the plotting software available at the time of writing, differentiation between specific film thickness values has proved challenging.

The input conditions for the range of analyses are shown in Table 6-1. Material properities used are nominal values for steel.

Table 6-1 Input conditions for EHL analyses

R_{x1} / m	0.0381
R_{x2} / m	0.3048
R_{y1} / m	0.0381
R_{y2} / m	0.3048
E_1 / GPa	206.9
E_2 / GPa	206.9
ν_1	0.3
ν_2	0.3
τ_0 / MPa	12.5

6.4.1 Impact of Offset on Results

An important factor to consider was the impact of offset of the surface on the overall results from an analysis. This stemmed from the question of whether a given surface map was representative of a mean section of the test specimen. To investigate this – it was decided to offset the roughness by a significant amount, to ensure a different set of roughness features would interact. The conditions were maintained constant between simulations to isolate the effect of changing roughness features on the contact.

The data for the faster surface was offset by both 25µm and 500µm in the software. The offset of 500µm equated to over one Hertz dimension at the highest load used. The surface speed ratio is 7:9 so that a fast surface asperity interacts with $\frac{2}{9} \times 2a$ of the slow surface during passage through the contact on the centre line and with progressively shorter distance for asperities further away from the centre line. At the 1.0GPa load *a*=0.33µm. Therefore this interaction length is approximately 15µm. So the 25µm offset is mainly the same asperity interactions but at different positions within the Hertzian zone whereas the 500µm offset produces a completely different set of interactions.

A cumulative distribution function (CDF) plot shown in Figure 6-5 demonstrating the impact of offset on the total film thickness values is shown below. The CDF plots were calculated from the film thickness results spanning 1190 time steps of the 'fully rough' portion of the simulations when the attenuated leading edge of the roughness maps has completely left the Hertzian zone. Videos created for CDF plots of as a function of time step showed little fluctuation in $F(h)$ values and remained relatively stable over the simulation. The three curves shown on the graph represent the same pair of surfaces under the same experimental conditions, however different degrees of offset have been applied to the faster of the two surfaces. This results in a different set of asperity interactions during transit through the contact.

The ordinate axis, $F(h)$, describes the proportion of mesh point film thicknesses values that are less than or equal to the corresponding h-axis value. The values tabulated for the statistical analysis were all the mesh points included within the Hertzian contact. Observing the entire range of values, it is clear that little change is seen between differing levels of offset.

It is apparent that as the film thickness increases from zero, shown on the x-axis, that the function $F(h)$ also increases. In the range from 0.1 to 0.7, $F(h)$ can be seen to increase almost linearly. As film thickness values beyond 0.7µm are established, it is evident that the curves begin to taper off. This tapering continues as the curves meet an $F(h)$ value of 1, corresponding to a film thickness value of approximately 2.5µm.

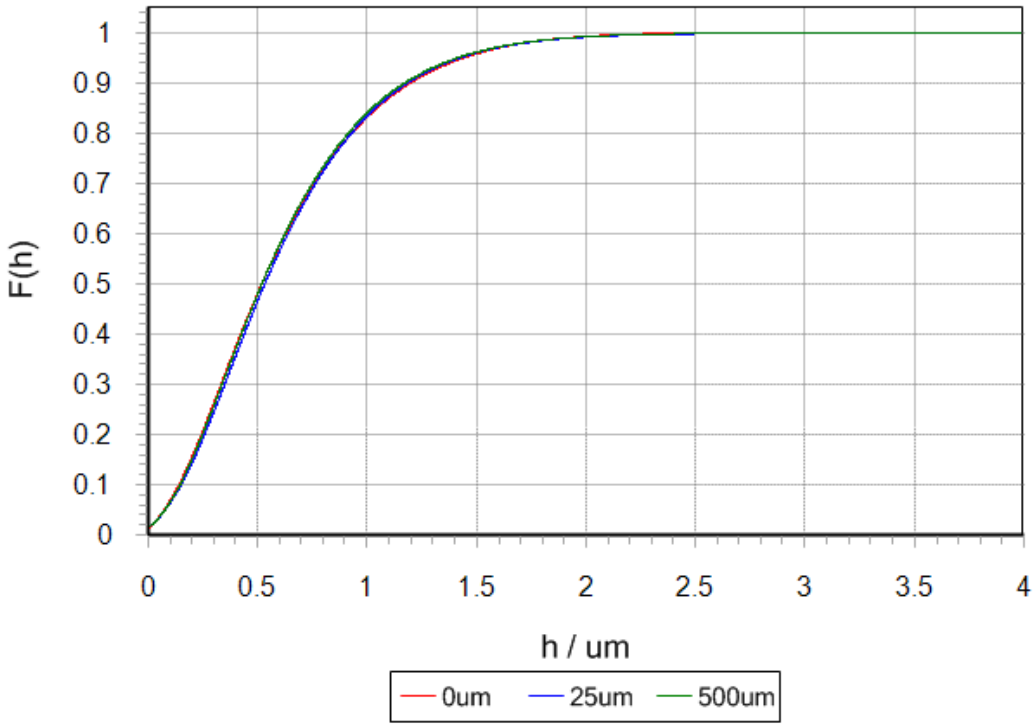

Figure 6-5 Cumulative distribution function for film thicknesses averaged over the simulation for a range of surface offsets

A more detailed look at the thin film region of the graph in Figure 6-6 reveals some discrepancies between levels of offset. To observe the variation of thin films very fine bin sizes of 1nm were specified.

Where the curves intercept the y-axis represents levels of film thickness calculated as being zero. This intercept is therefore an indicator of calculated asperity contact levels. It can be seen that the level of offset between simulations has very little effect on the position of the $F(h)$-intercept, which occurs at approximately $F(h)=0.015$. This indicates that offsetting the surface geometry has had little impact on the calculated level of metallic contact. This finding allows general trends to be extracted from simulations performed with the measured surfaces.

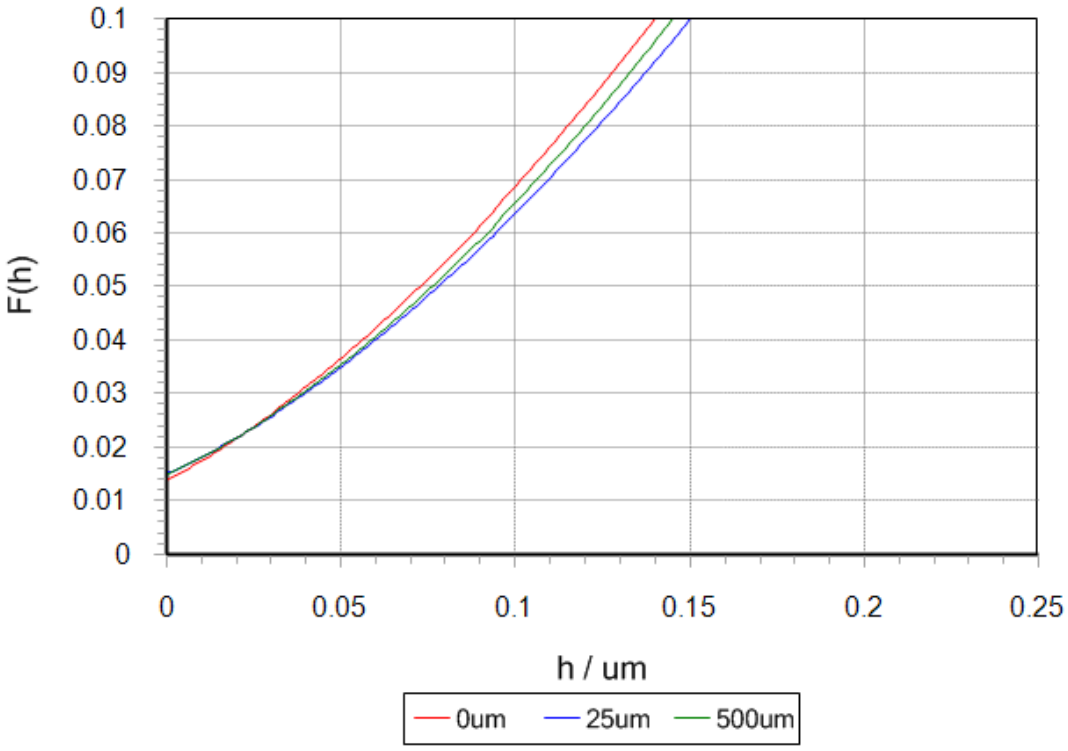

Figure 6-6 Cumulative distribution function plot for film thicknesses averaged over the simulation for a range of surface offsets showing thin film region

6.4.2 Cumulative Distribution Function Plots for Pressure and Film Thickness

A set of comparisons between simulations run at conditions recorded from experiments has been made. The conditions for these comparisons were taken from both the high and low load speed varying experiments. Conditions incorporating both the highest and lowest entrainment speeds were used for simulations, allowing the investigation of full film lubrication and regimes with significant asperity interaction. The isothermal analyses were carried out with lubricant properties corresponding to the mean measured bulk temperature of the two disks. The bulk disk temperatures used were those that were recorded during the steady state region of the speed increasing halves of the tests.

The test conditions used in the simulations are shown in Table 6-2. It can be clearly seen that the conditions taken from higher load experiments result in higher temperatures and reduced oil viscosity in comparison to the lower load conditions.

Table 6-2 Input conditions for simulations from experimental data

		200rpm	300rpm	500rpm	2000rpm
1.0GPa	T_{mean} °C	56.6	-	58.8	62.2
	LOAD /N	850	-	850	850
	$\bar{u}$ /ms^{-1}	0.7094	-	1.7709	7.1947
	η_0 /Pas	0.0339	-	0.0311	0.0272
	α_0 /Pa^{-1}	2.03E-08	-	2.01E-08	1.99E-08
1.4GPa	T_{mean} /°C	57.8	60.0	65.7	82.2
	LOAD /N	2320	2320	2320	2320
	$\bar{u}$ /ms^{-1}	0.7094	1.0723	1.7709	7.1947
	η_0 /Pas	0.0323	0.0297	0.0239	0.0134
	α_0 / Pa^{-1}	2.02E-08	2E-08	1.96E-08	1.85E-08

6.4.2.1 Thin Film Behaviour and Contact

Figure 6-7 shows the cumulative probability distributions for each of the lower load 1.0GPa conditions stated in Table 6-2. The curves demonstrate a similar shape, as can be expected for a cumulative probability distribution, with a nominally linear region that gradually tapers off as *F*(*h*) reaches the maximum value of 1 at the maximum film thickness occurring in the contact zone.

Modification of the entrainment speed clearly results in much significant offset between the CDF curves corresponding to the changes in the entrainment mechanism. A comparison between the 200rpm and 2000rpm simulations performed at 1.0GPa shows an offset of approximately 0.4μm, where the curves are nominally parallel at similar values of F(h). This large offset occurring between curves is indicative of a large change in mean film thickness, which is in broad agreement with calculations based on experimental data. Also, the intercept of the *F(h)* curve corresponding to 2000rpm indicates no metallic contact occurring when compared to the 200 and 500 rpm curves.

A comparison of the distribution in the lower film thickness region of plot in Figure 6-8 for the 1GPa load case shows the variation in thin film behaviour and contact occurrence between the simulations. A greater difference can be seen between the lower load curves. The 200rpm

curve intercepts the $F(h)$-axis at approximately $F(h)$=0.014. The blue curve representing the 500rpm conditions shows decreased contact with the curve intercepting the y-axis at a value of approximately $F(h)$=0.008. In contrast to this however, the higher speed 2000rpm curve appears to intercept the $F(h)$-axis at an $F(h)$ value of nominally zero. This nominally zero value attained for $F(h)$ at h=0µm is an indicator of very low levels of metal to metal contact can be expected with the thicker films that are present.

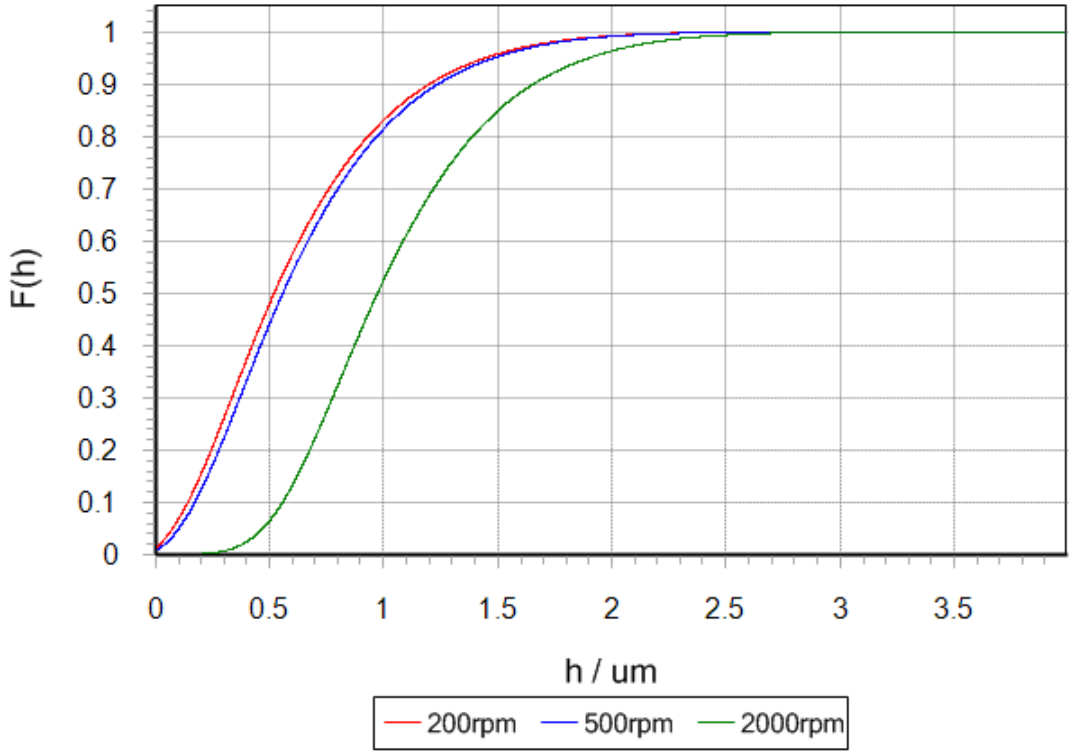

Figure 6-7 Cumulative distribution function plot for film thicknesses averaged over the simulation for a range conditions at a maximum Hertz pressure of 1.0GPa at three different shaft speeds.

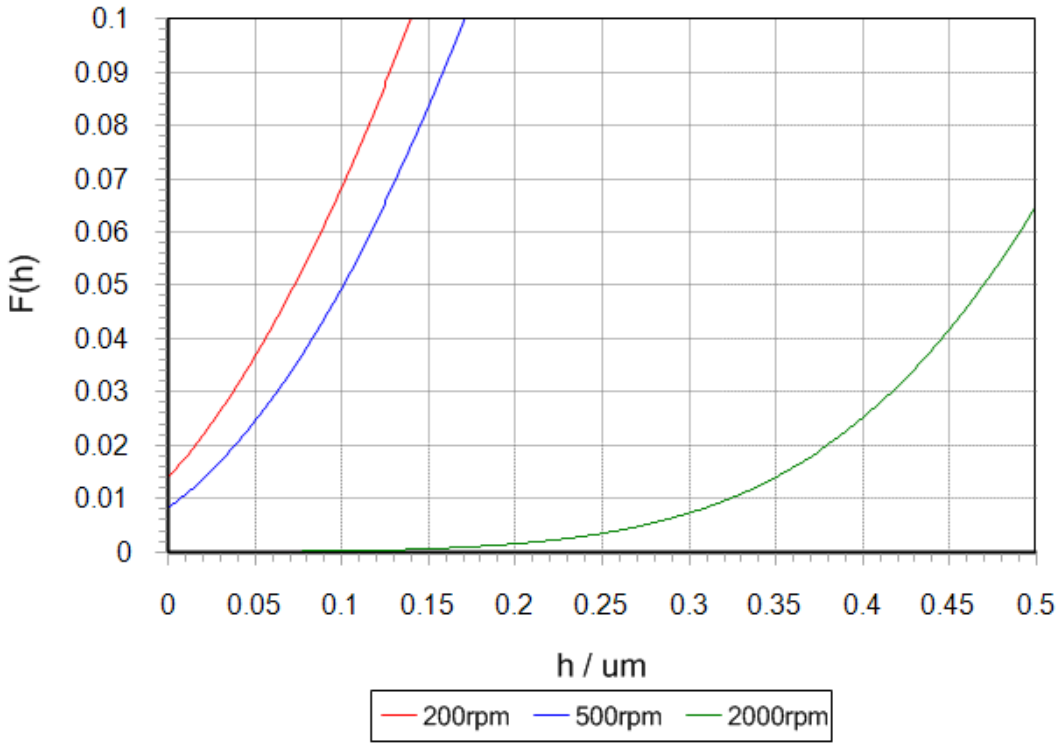

Figure 6-8 Cumulative distribution function plot for thin film region averaged over the simulation for a range of conditions at maximum Hertz pressure of 1.0GPa for three shaft speeds

In contrast to this, simulations run at a maximum contact pressure of 1.4GPa shown in Figure 6-9 give cumulative distribution function curves that lie only slightly offset from one another. The linear region of all curves appear approximately parallel to one another in the range $0.2 \leq F(h) \leq 0.8$. Beyond this region, they taper off as the curves attain their maximum value.

At the scale shown, lower speed values of 200rpm, 300rpm and 500rpm appear overlaid. A degree of offset between the curves is visible in the region $0.2 \leq F(h) \leq 0.8$. This is seen clearly between the 200rpm curve and the higher speed 2000rpm curve. This is shown as similar values of h/μm read off from the h-axis, equate to a lower proportion of the contact at higher entrainment speeds, as indicated by F(h).

Figure 6-10 shows the film thickness CDFs for the results obtained for the 1.4GPa load simulations in the thin film region. The curves are clearly offset from one another in the order of the entrainment speed. This offset is also evident at the $F(h)$ intercept where for the higher entrainment speed of 2000rpm, $F(h)=0.0058$. In comparison to this the lower speed simulation at the $F(h)$ intercept occurs at $F(h)=0.015$, resulting in a 2.6 times increase in the number of contacting mesh points over the speed range.

In contrast to the lower load simulations, the higher speed conditions do not yield the same large increase in the lower film thickness values as shown inFigure 6-10. Calculated metallic contact is seen to persist at higher loads despite the increased entrainment speed, which corresponds to experimental observations.

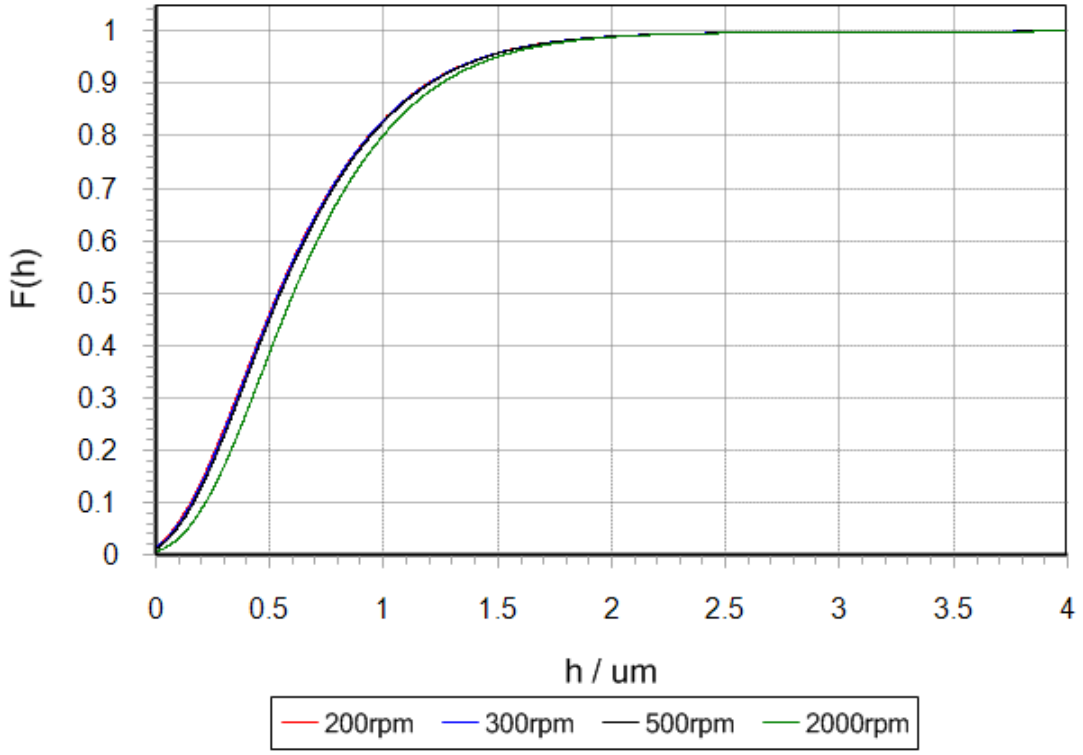

Figure 6-9 Cumulative distribution function plot for film thicknesses averaged over the simulation for a range of conditions at a maximum Hertz pressure of 1.4GPa at four different shaft speeds

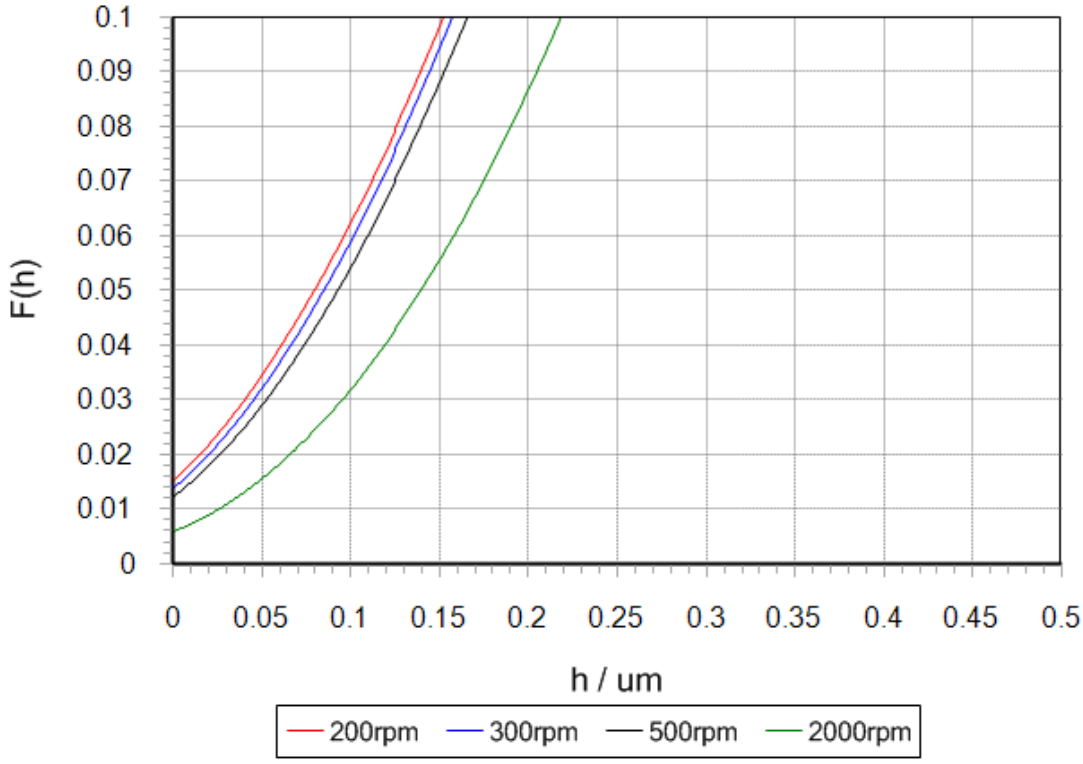

Figure 6-10 Cumulative distribution function plot for thin film region averaged over the simulation for a range of conditions at maximum Hertz pressure of 1.4GPa for four shaft speeds

6.4.2.2 Behaviour of pressure within the EHL contact under varying load and speed conditions

Plots investigating the distribution of pressure within the EHL contact have also been produced. These plots have been produced in the same manner to those presented in investigating film thickness. Cumulative distribution curves for the four previously investigated speeds at a maximum smooth surface contact pressure of 1.4GPa are shown. These curves are shown in Figure 6-11 where $F(p)$ indicates the proportion of the contact ellipse at or below a given contact pressure. The plots shown have all been produced for the surfaces in the same relative positions averaged over the same time steps. Therefore, the changes measured are due to the different input conditions of viscosity, speed and bulk disk temperature.

Upon inspection of Figure 6-11, it is clear that all four curves describing the 1.4GPa experiments lie very close to one another. All four curves show a distribution with a initial steep increase in $F(p)$ that gradually begins to taper off at p=1.4GPa, the maximum smooth surface pressure. It can also be seen that a relatively large proportion of mesh points, 20%, experience pressures above that of 1.4GPa, this is visible as $F(p)$ reads a value of approximately 0.8 when all three curves pass through a contact pressure of 1.4GPa.

Under the greater detail shown in Figure 6-12, it appears as though the four curves all lie very close to one another. In contrast to the film thickness distribution curves, the conditions relating to higher entrainment speeds do not result in a significant change in pressure distribution. Curves do not appear in order of entrainment speed, where curves describing film thickness distribution and contact were clearly offset by change in entrainment speed.

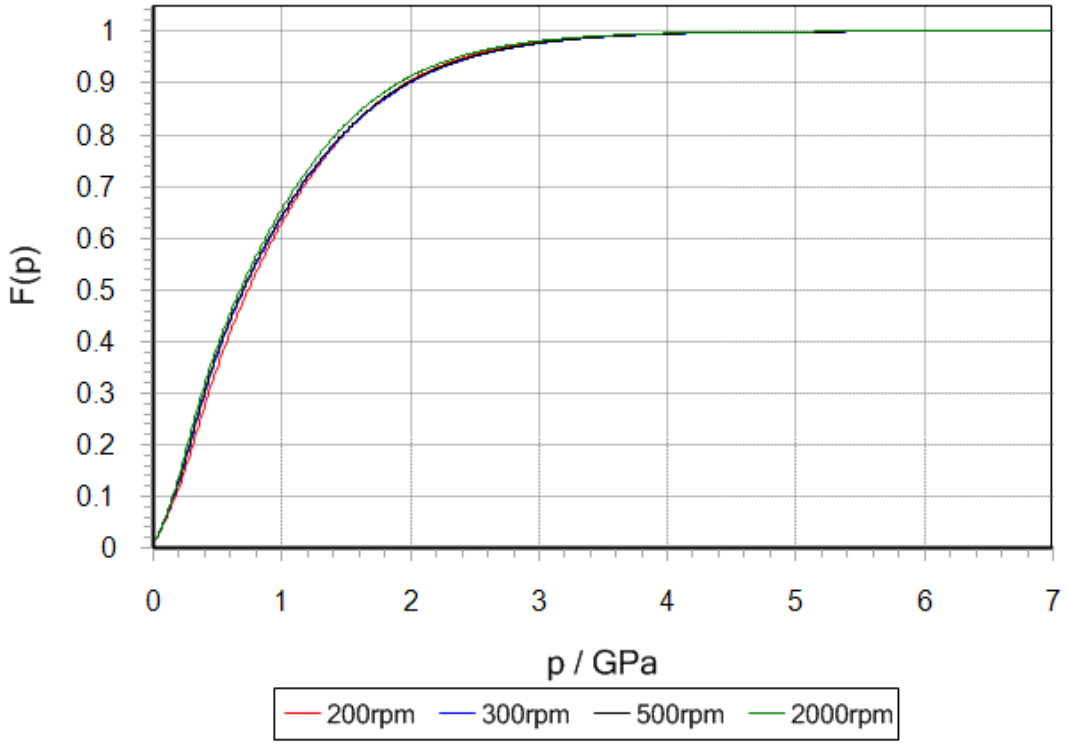

Figure 6-11 Cumulative distribution function plot for pressure averaged over the simulation for a range of conditions at maximum Hertz pressure of 1.4GPa for four shaft speeds

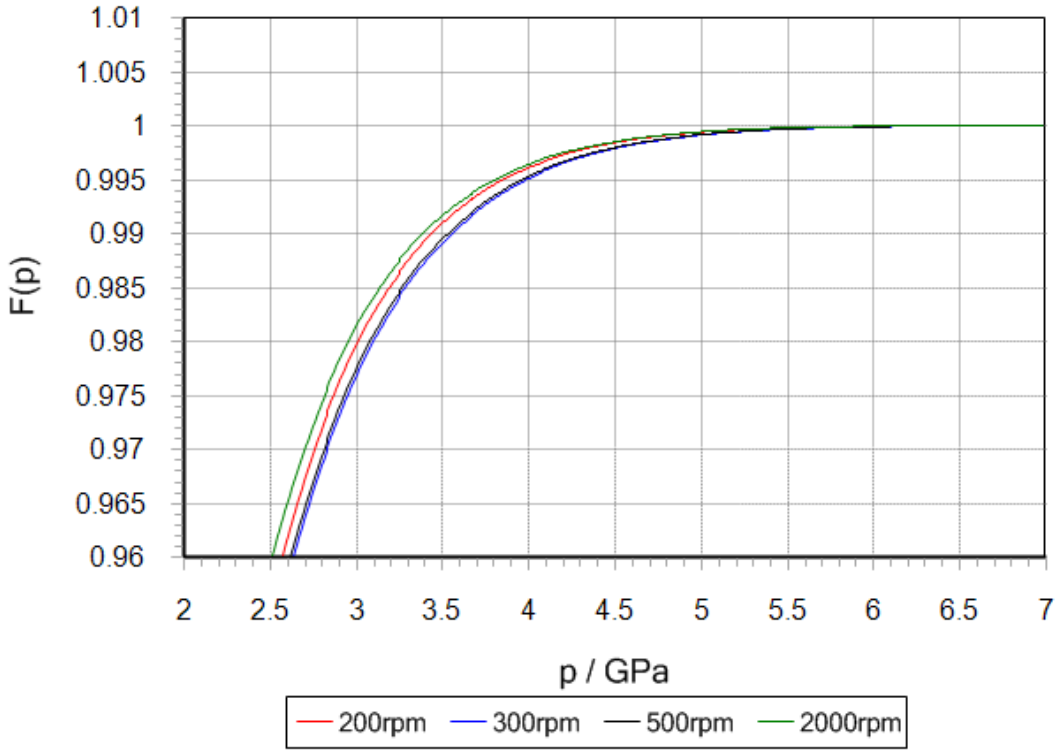

Figure 6-12 Cumulative distribution function plot for high pressure region averaged over the simulation for a range of conditions at maximum Hertz pressure of 1.4GPa for four shaft speeds

In contrast to this, simulations run at 1.0GPa, shown in Figure 6-13, demonstrate much greater change between conditions used. In a similar manner to the curves showing the 1.4GPa distributions, the 1.0GPa curves attain their maximum smooth surface contact pressure at an $F(p)$ of approximately 0.8. This demonstrates that for both 1.0GPa simulations 20% of the pressures within the contact exceed the maximum value of the smooth surface distribution.

Beyond the $F(p)$ value of approximately 0.8 the curves show significant divergence. The green curve representing the 2000rpm condition has a sharper kink in the distribution and attains an $F(p)$ value of 1 at a lower value pressure than the curves representing the lower speed experiments. This demonstrates lower peak pressures obtained under the conditions of high entrainment speed and overall thicker lubricant films.

Figure 6-14 shows the high pressure part of Figure 6-13 in greater detail where it can be seen that peak pressures tend to decrease as entrainment speed increases. Curves representing lower speed conditions lie beneath those of greater entrainment speed. This can be seen at the scale shown where the green line representing the 2000rpm condition appears to intercept the $F(p)=1$ gridline at approximately 3.4GPa. The 500rpm and 200rpm condition reach an $F(p)$ value of 1 at much higher pressures and are offset beneath the 2000rpm curve for the high pressure region of the graph.

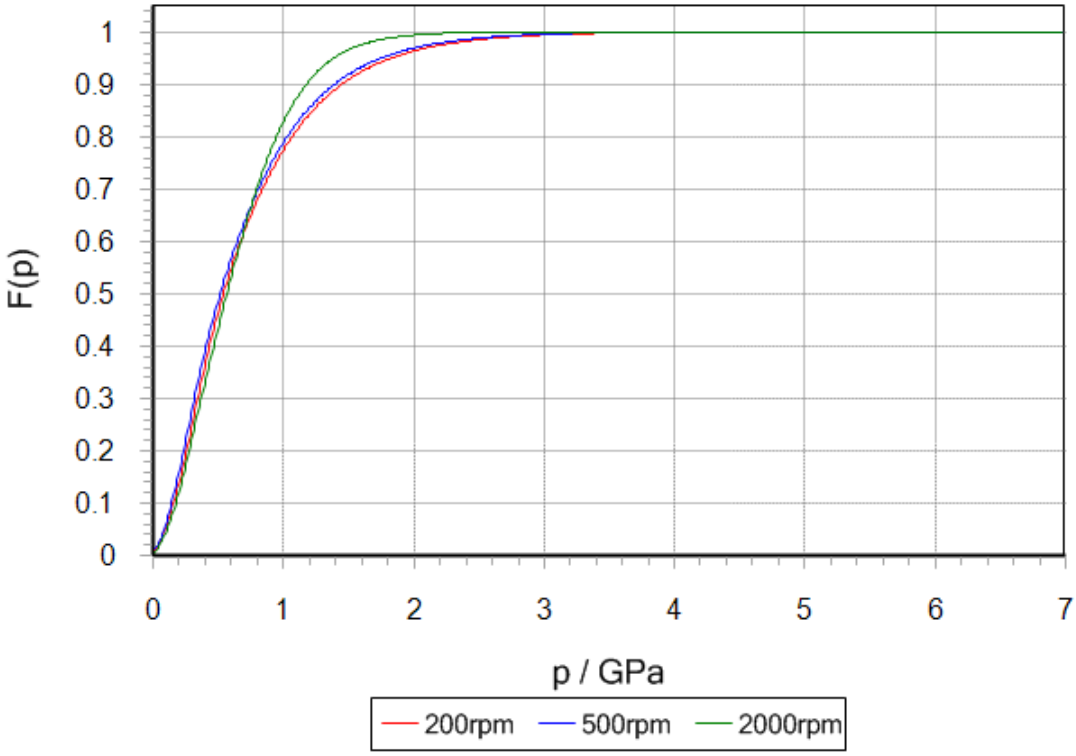

Figure 6-13 Cumulative distribution function plot for pressure averaged over the simulation for a range of conditions at maximum Hertz pressure of 1.0GPa for three shaft speeds

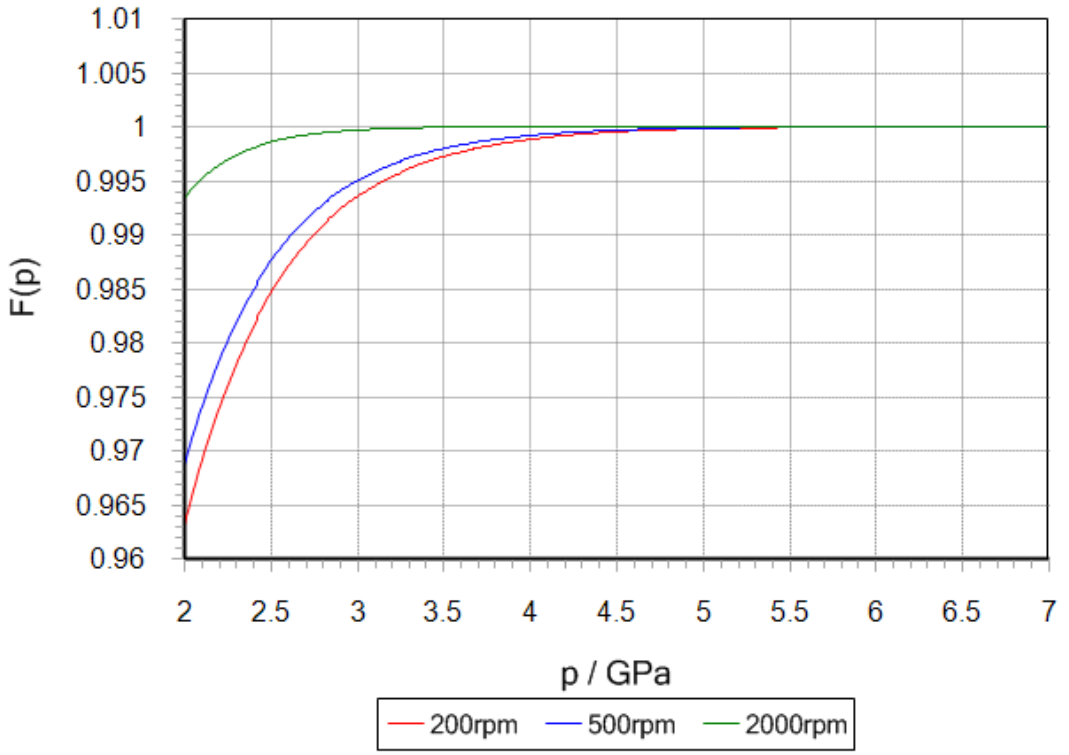

Figure 6-14 Cumulative distribution function plot for high pressure region averaged over the simulation for a range of conditions at maximum Hertz pressure of 1.0GPa for three shaft speeds

6.4.3 Surface Plots of Pressure Distribution

This section considers plots of the pressure distributions obtained for a maximum contact pressure of 1.0GPa and 1.4GPa. These show the variation in pressure across the contact. A smooth surface solution is shown along with two solutions from the same time step in the simulations where both surfaces are fully rough. The time steps from the fully rough simulations are taken from the results for conditions of 200rpm and also 2000rpm.

The initial steady state solution to the EHL problem is shown in Figure 6-15, for comparison. The pressure is distributed smoothly over contact with exception of the usual EHL pressure spike at the outlet. The peak pressure is positioned at the centre of the contact. Beyond the contact zone, the pressure rapidly declines to ambient levels. The steady state solution is also shown in Figure 6-16 at the scale used to display pressure distributions for time steps where the surfaces are both fully rough.

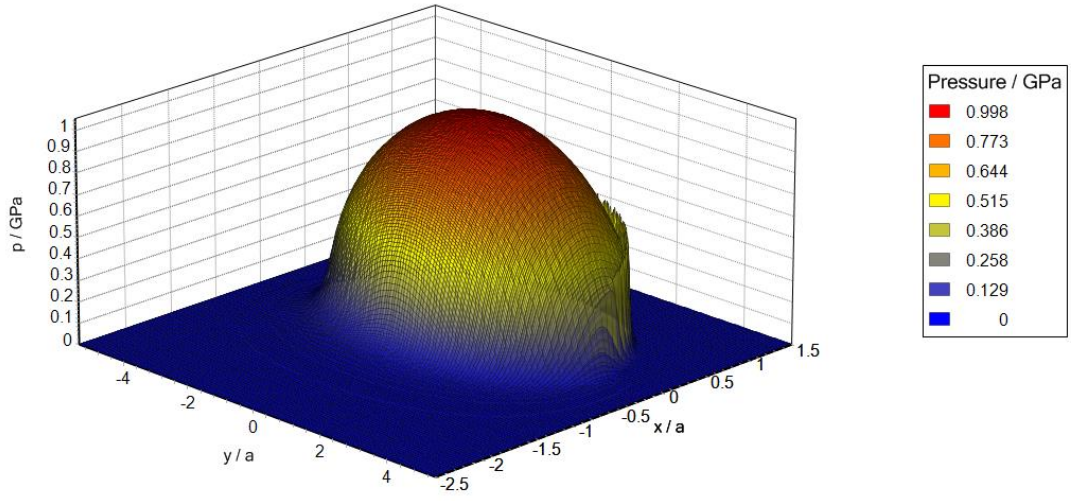

Figure 6-15 Steady state solution for a maximum Hertz pressure of 1.0GPa and 200rpm conditions

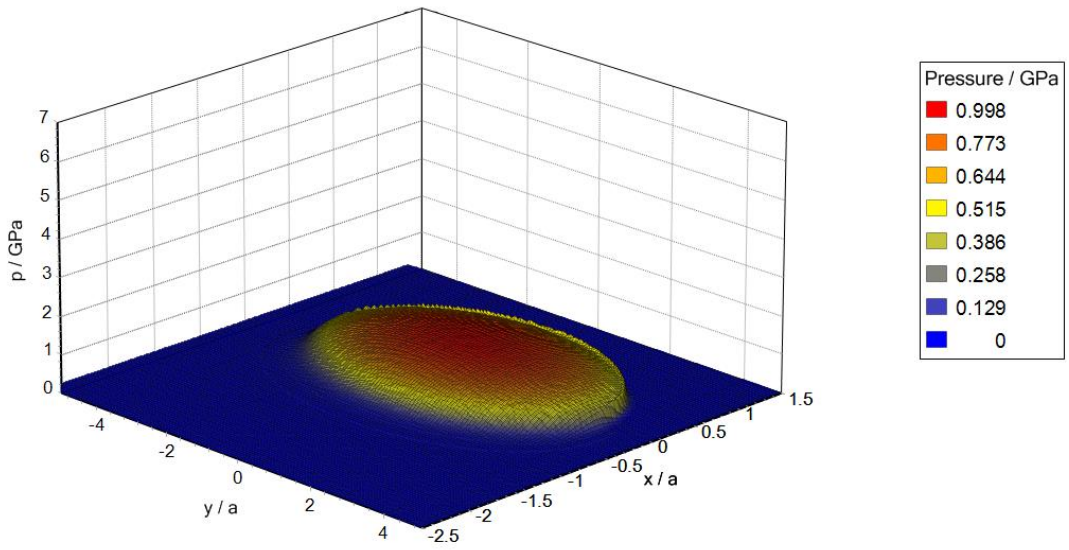

Figure 6-16 Steady state solution for a maximum Hertz pressure of 1.0GPa and 200rpm conditions

Transient EHL analyses were carried out for the run-in rough surfaces using a mesh spacing of 2µm in the entrainment direction and 25µm in the transverse direction. The roughness lay is close to transverse as can be seen in Chapter 5. Surface roughness features in terms of load bearing lands are typically between 10 and 30µm in width. The pressure distribution for the fully rough contact at a the 2000rpm conditions is shown in Figure 6-17. It can be seen that the introduction of roughness into the contact zone generates numerous pressure spikes far in excess of the maximum smooth surface value. These pressure spikes are distributed across the whole Hertzian contact zone and are not related to the smooth surface pressures at the same position. The higher pressures do tend to occur towards the centre of the ellipse though it can be seen that large pressure spikes still occur towards the edges. At the time step shown, there is a large pressure spike occurring at the centre of the inlet with a value of approximately 4.0GPa. Beyond the contact zone, the pressure declines rapidly to ambient values, although some lower pressure fluctuations can be seen due to the moving roughness features.

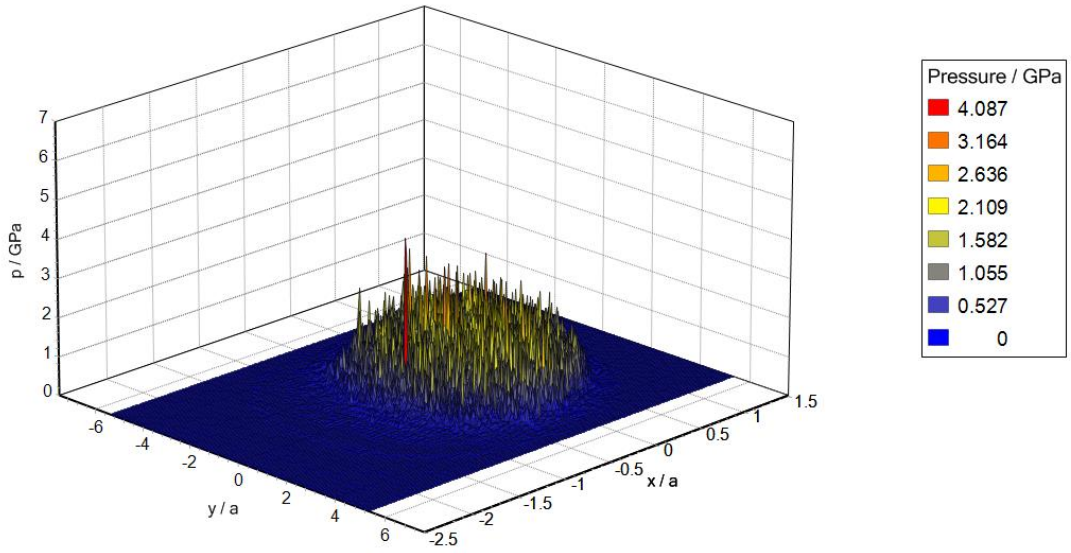

Figure 6-17 Fully rough solution for a maximum Hertz pressure of 1.0GPa at 2000rpm conditions

Displayed in Figure 6-18 is the solution for the same time step at conditions relating to the 200rpm test run. The same sections of the surfaces are in contact during both simulations at this time step. It can be clearly seen that the pressure spikes seen in Figure 6-17 have increased significantly. Large values of pressure can be seen to occur over the whole contact. Peak pressures can be seen to occur towards the centre of the ellipse with the pressure spike identified at the 2000rpm time step in the inlet increased in value.

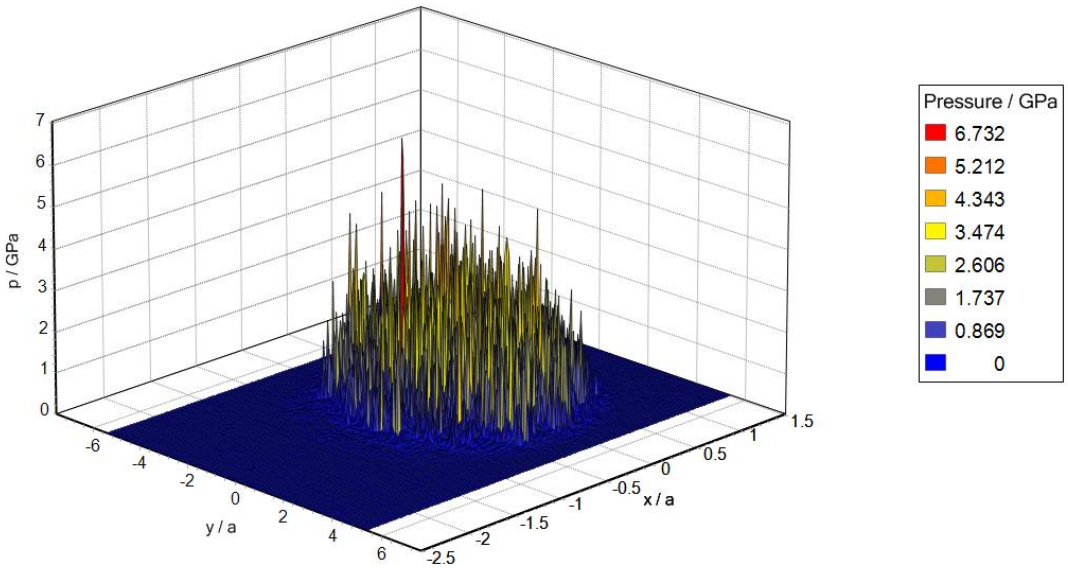

Figure 6-18 Fully rough solution for a maximum Hertz pressure of 1.0GPa at 200rpm conditions

Figure 6-19 shows the 3D pressure distribution plot for the 1.4GPa simulation at 200rpm. The distribution shows high pressure spikes over the whole contact. Comparison with the 1.0GPa simulation at 200rpm shows the intermediate pressure spikes have increased in value. High pressure spikes can also be seen to occur towards the transverse edges of the contact zone.

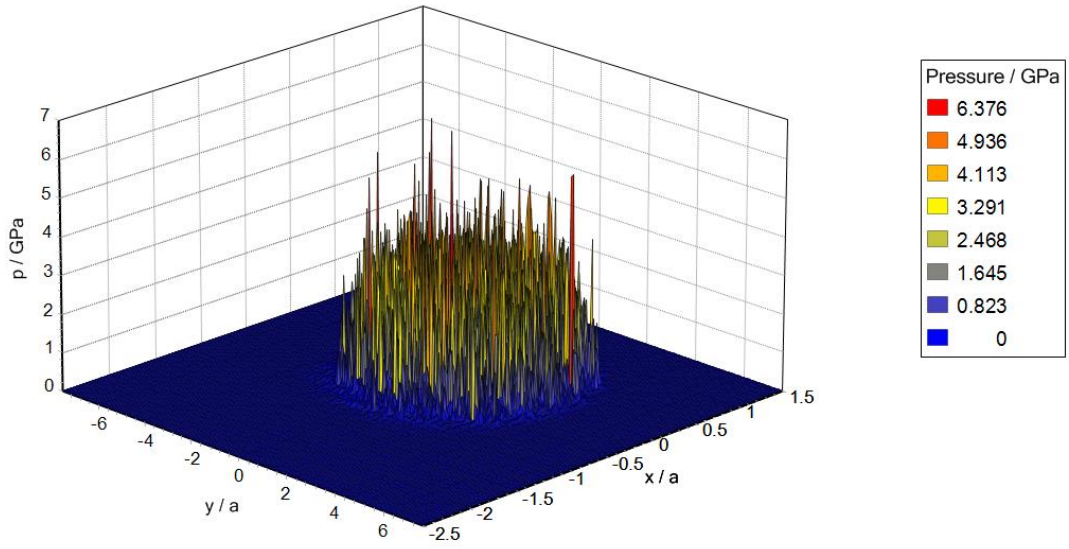

Figure 6-19 Fully rough solution for a maximum Hertz pressure of 1.4GPa at 200rpm conditions

The 1.4GPa simulation at 2000rpm shown in Figure 6-20 demonstrates a higher peak pressure than the lower speed 1.4GPa plot. However, it can be seen that the pressures towards the transverse edges have reduced with increased speed. In spite of the increase in speed, pressure spikes remain high throughout the contact. This result contrasts with the higher speed 1.0GPa where pressures across the contact were seen to reduce significantly.

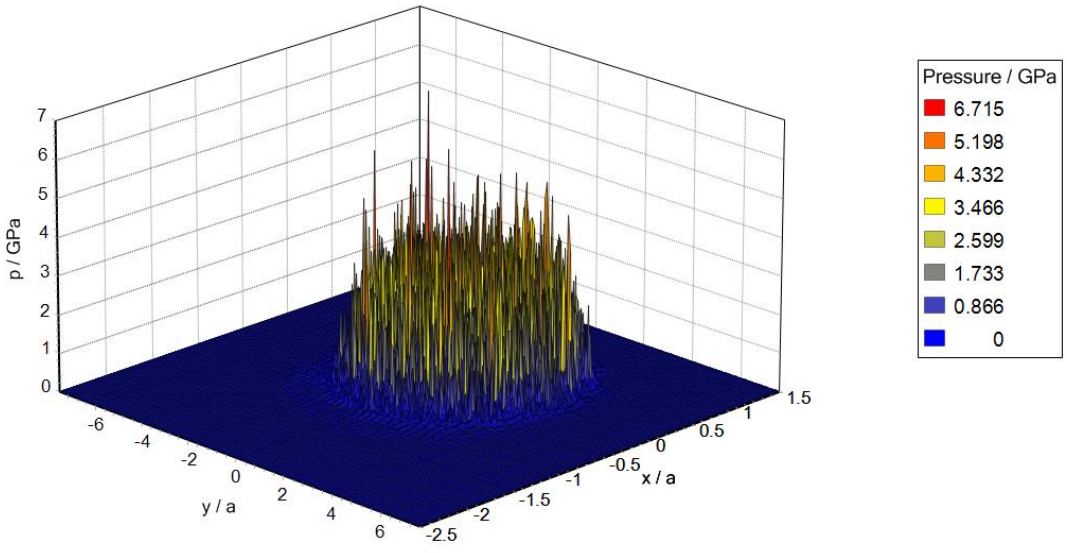

Figure 6-20 Fully rough solution for a maximum Hertz pressure of 1.4GPa at 2000rpm conditions

6.4.4 Film Thickness Contour Plots

Contour plots examining the film thickness for a range of simulations run for the same pair of surfaces are now presented. The surfaces used are at the same relative position for all the simulations meaning comparisons between corresponding time steps are therefore comparable in terms of relative surface geometry.

Simulations have been run with conditions obtained from averaged quasi-steady state regions of speed varying experiments run at a maximum contact pressure of 1.4GPa.

Contour plots show the variation in film thickness across the Hertzian contact zone. Regions shown in red equate to areas of very thin films. Areas of yellow and blue represent thicker

films. The elliptical shape of the contact is clearly visible in the contour plots. The contact ellipse is centred at x=y=0, where the units for x and y are normalised to the minor Hertzian contact dimension. Due to the geometry of the surfaces, the contact ellipse extends over $-1 \leq x/a \leq 1$ parallel to the axis of entrainment and over $-4 \leq y/a \leq 4$ transverse to the direction of entrainment. Beyond the contact ellipse, the film thickness can be seen to increase rapidly as the form of the surfaces diverge from one another.

To highlight instances of contact, a separate set of plots has been produced on which mesh points where film thickness is equal to zero have been indicated. Plots indicating contact are shown paired with the film thickness distribution corresponding to the same time step. These contact plots have ellipses representing the boundary of the Hertzian zone superimposed.

6.4.4.1 Smooth surface film thickness for a maximum Hertzian pressure of 1.0GPa at the 2000rpm condition

The smooth surface solution for film thickness is shown below in Figure 6-21. It is clear that throughout the majority of contact there is an even film thickness of nominally 1.0µm. The film thickness can be seen to increase rapidly outside of the contact zone. The outlet and side lobe constrictions are also clearly visible.

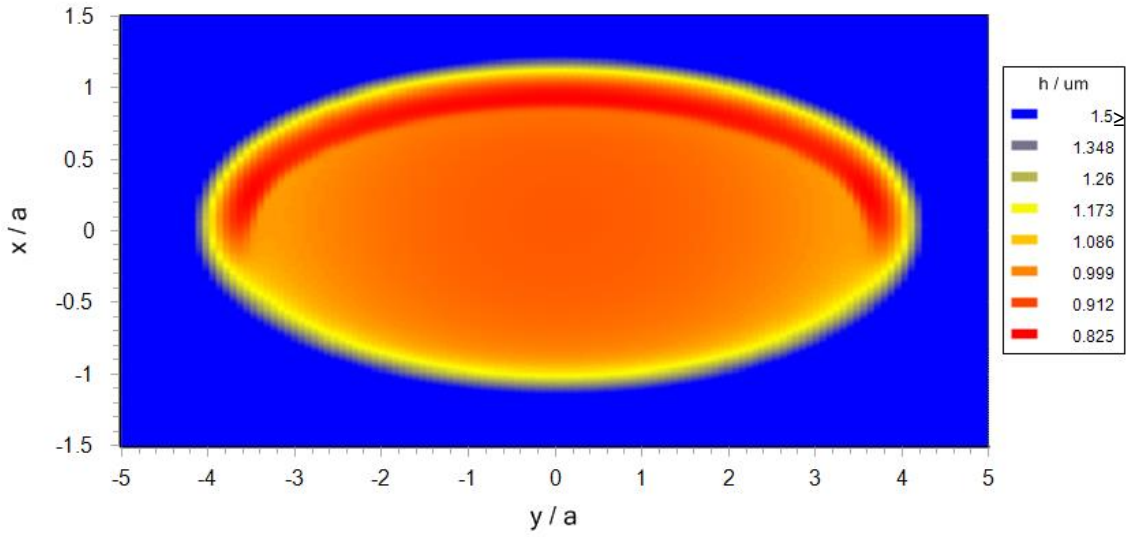

Figure 6-21 Smooth surface film thickness distribution for maximum Hertz pressure of 1.0GPa at 2000rpm conditions

6.4.4.2 Rough surface solution at p=1.4GPa, 2000rpm condition

Figure 6-22 shows the film thickness distribution for a time step where the contact is fully rough. It can be seen that within the contact zone, film thickness levels vary between values corresponding to very thin films and areas of significantly thicker films. A distinct band of blue can be seen diagonally across the contact, between positions x=0.15a y=-4.0a and x=0.48a y=4.0a, the extents of this have been indicated with the arrows A-A. This is in contrast to the majority of the contact in which film thickness values are below 1μm. Also visible is a yellow band spanning the Hertz zone in the longitudinal direction from x=-1.2a y=-0.4a to x=1.0a y=0.3a. These bands of relatively thick films correspond to deep valley features on one of the surfaces making a positive angle with the x axis, and those on the other surface making a negative angle.

The distribution in film thickness levels is seen to vary predominantly in the direction of entrainment. There are however some variations in the transverse direction. The contact as a whole appears to show a quite striking cross hatching on the film thickness distribution. It is also visible that regions of thin films can extend beyond the contact ellipse, this is most visible in the inlet region where zones of red are seen beyond in the inlet zone to the contact, x<-a.

Displayed below in Figure 6-22 is the contact plot for the corresponding time step. Regions coloured in black indicate mesh points where h=0μm. These regions of asperity interaction, shown within the contact ellipse, can be seen to be distributed over the area of the Hertzian zone. Contacts appear relatively isolated from one another covering a small proportion of the ellipse. Where adjacent contact can be seen to occur, they predominantly occur in the transverse direction, examples of this can be seen at x=0.7a, y=-1.0a and also clearly at x=-0.4a y=-1.0a. Adjacent contacts are however seen to occur in the entrainment direction at x=0.0a, y=-2.0a and again at x=0.0a, y=-2.3a. There are also examples where contact points occur along a line inclined at the same angle to the y axis as is seen for the deep valley features in the upper figure. These contact points are occurring where a prominent asperity ridge, such as

is illustrated in Figure 6-3 and Figure 6-4, is interacting with a sequence of crossing ridges on the counterface.

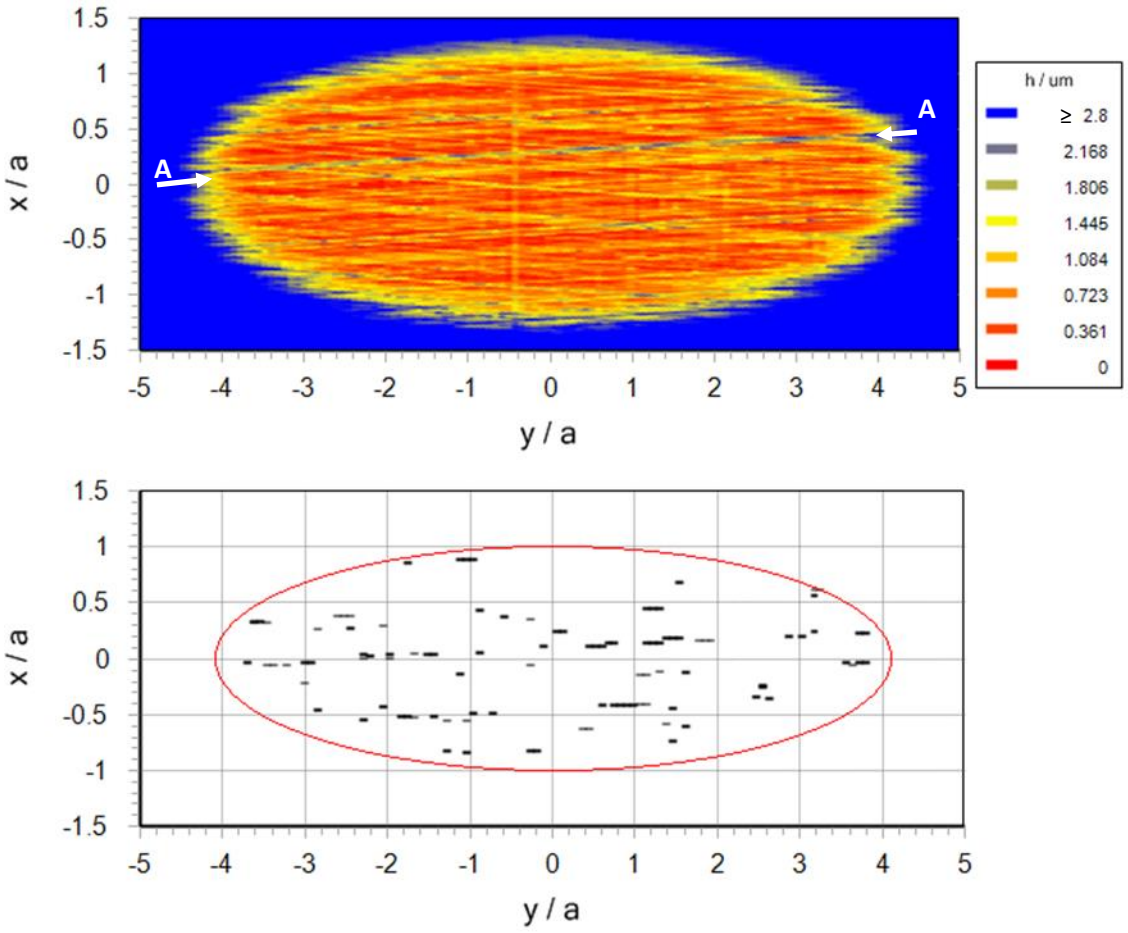

Figure 6-22 Film thickness distribution and contact plot for fully rough solution at a maximum Hertz pressure of 1.4GPa at 2000rpm conditions

6.4.4.3 Rough surface solution at p=1.4GPa, 500rpm condition

Values shown at the lower entrainment speed conditions of 500rpm in Figure 6-23 demonstrate similar variations between high and low values of film thickness across the contact. Isolated regions of thick films are separated by large areas of low film thickness.

Due to the same relative position of the surfaces, the same distinct blue region of high film thickness can be seen to span the contact from x=0.15a y=-4.0a to x=0.48a y=4.0a.

Isolated regions of thick films occur where two bands of moderate film thickness intersect, this can be seen at position x=-0.4a, y=1.0a. Along some of the regions of more moderate films, it can be seen that the film thickness fluctuates by approximately a micron; this fluctuation can be seen from x=0.4a, y=-4.0a to x=0.7a to y=3.5a. A clear band in this region is seen fluctuate from values of nominally h=0µm to over 2.8µm.

It is visible in Figure 6-23 where the entrainment speed is decreased that the surfaces see a greater level of asperity interaction as indicated by the contact plot. The same features can identified on comparison with Figure 6-22 where there is a higher level of entrainment. Examples of these are seen at x=0.35a, y=-3.5a and also at x=0.85a, y=-1.0a.

It can also be seen in Figure 6-23 that contact occurs at the very edge of the contact ellipse which can be seen at x=0.95a, y=1.3a.

Where new contacts have occurred due to the decrease in entrainment, these tend to appear as ‘separate contact points’ which occur disconnected from previous regions of contact, rather than as growth in existing contact points.

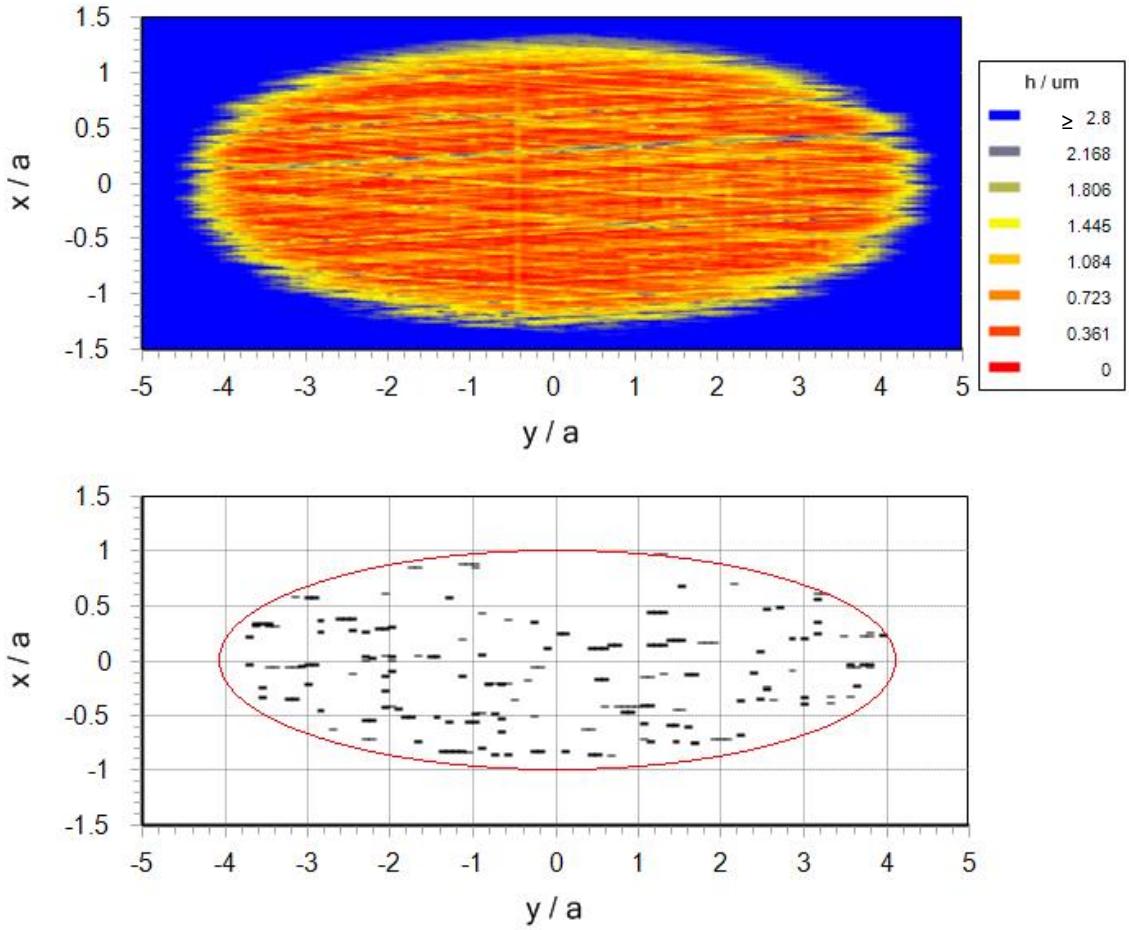

Figure 6-23 Film thickness distribution and contact plot for fully rough solution at a maximum Hertz pressure of 1.4GPa at 500rpm conditions

6.4.4.4 Rough surface solution at p=1.4GPa, 200rpm condition

Further decreasing the entraining velocity in Figure 6-24 does not appear to greatly affect the overall film thickness distribution. The same region of thin and thick films can be identified. Thin film regions appear to be more concentrated towards the edges of the Hertzian zone.

The contact plot however can be seen to demonstrate an increase in interacting asperities. Regions of interaction now appear to be more clearly skewed towards the transverse edges where similar results were obtained for transverse extruded surfaces by Holmes et al. (2005a). Contact also appears to be occurring outside of the Hertzian contact zone this can be seen at x=0.7a,y=3.4a. This occurrence was also recorded by Holmes et al. (2005a).

On comparison with the contact plot for the 500rpm simulation shown in Figure 6-23, it can be seen that some regions of contact appear to grow in both the transverse and longitudinal direction. This is visible, for example, at x=-0.2a, y=-0.7a.

It is also clear that for corresponding time steps, a decrease in entrainment velocity sees some mesh points move out of contact, which is counter-intuitive but could suggest the action of micro-EHL between some asperities. This can be seen at x=-0.35a, y=-0.5a on comparison with the higher speed simulation though these instances appear to be quite minimal in comparison to the net retention of interactions.

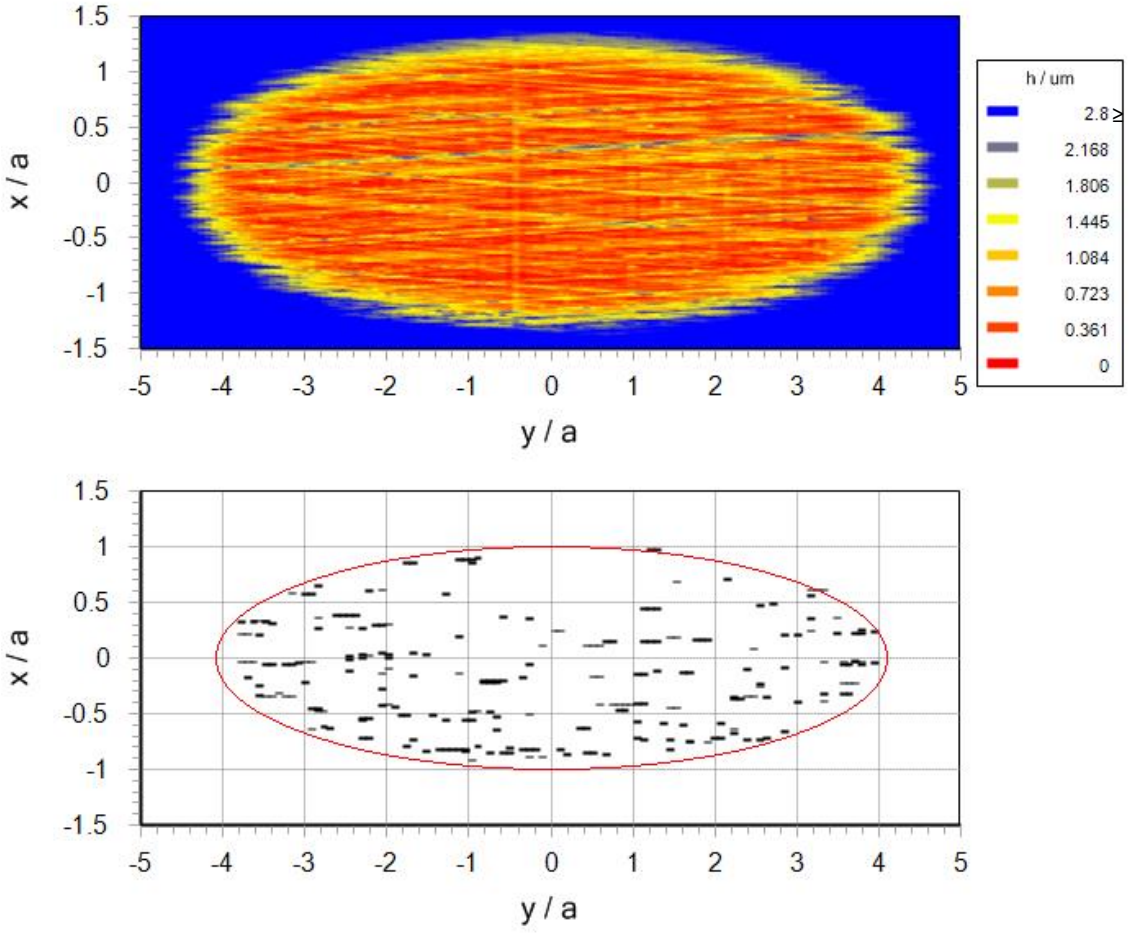

Figure 6-24 Film thickness distribution and contact plot for fully rough solution at a maximum Hertz pressure of 1.4GPa at 200rpm conditions

6.4.4.5 Rough surface solution at p=1.0GPa, 200rpm condition

The plot for the low speed 1.0GPa case is shown in Figure 6-25, low film thicknesses can be seen across the majority of the contact. Regions of thick films can be seen to span the contact at x=-0.7a, y=-4.0a, x=-0.25a, y=4.0a. The same longitudinal feature of x=-1.0a , y=-0.4a to x=1.0a, y=0.35a. It is also noticeable that in comparison to contour plots at 1.4GPa the film thickness grows more gradually outside of the contact region, due to the form of the surface curving away less rapidly.

The contact plot shows asperity interaction distributed over the contact region, with some occurring outside of the ellipse. It is visible that contact occurs more densely at the transverse edges of the contact. Contact also appears to be more likely to be composed of consecutive mesh points towards the edges. The outlet region, appears to show less contact occurring than the inlet. Interestingly, at lower loads, contact also appears to follow roughness features more closely, the arrows A-A have been used to indicate where a ridge is passing through the ellipse and experiencing contact along its length.

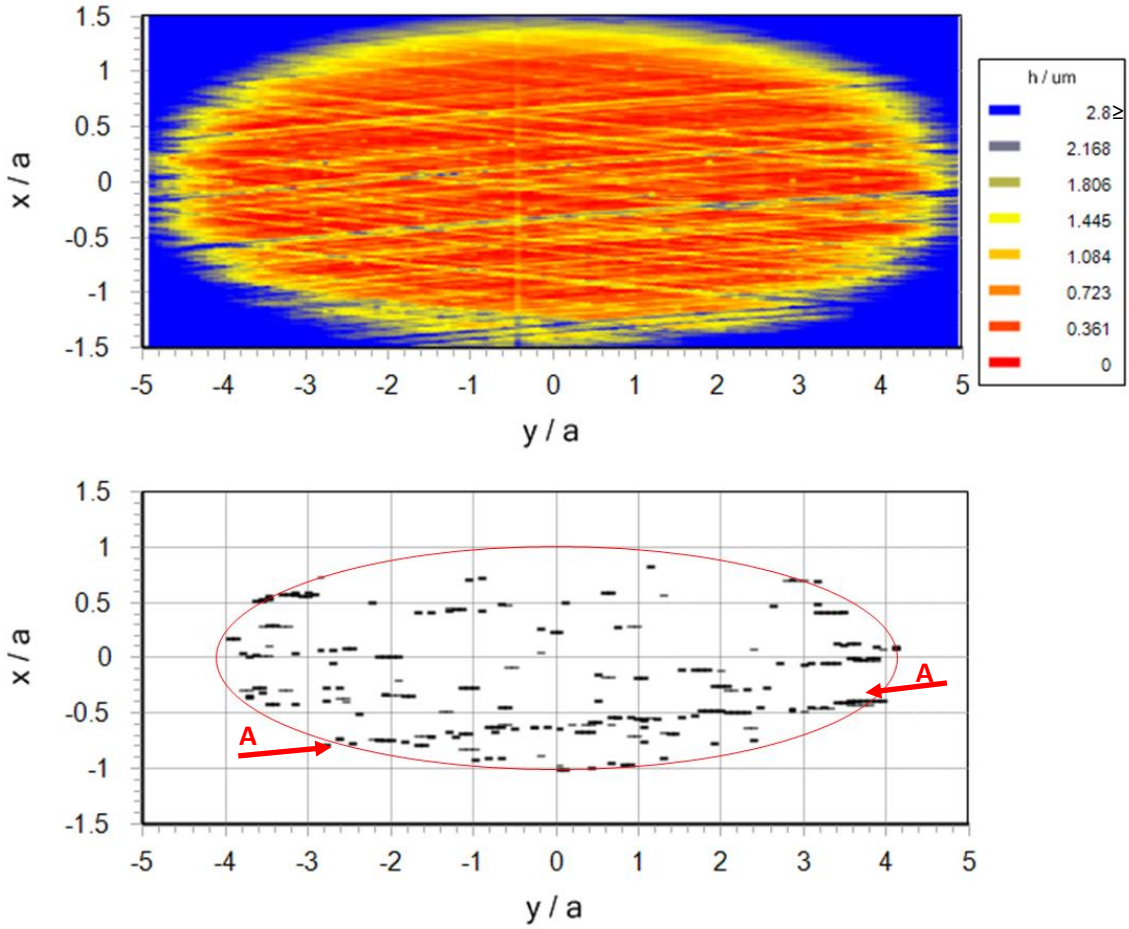

Figure 6-25 Film thickness distribution and contact plot for fully rough solution at a maximum Hertz pressure of 1.0GPa at 200rpm conditions

6.4.4.6 Rough surface solution at p=1.0GPa, 500rpm condition

The film thickness distribution for the 500rpm condition shown in Figure 6-26 demonstrates a similarly crosshatched film thickness distribution across the contact, however it can be seen on close inspection that the thinnest regions exist at the transverse edges of the ellipse. There are some instances of contact occurring outside of the Hertzian ellipse, though this can be seen to have decreased. The outlet of the contact can be seen to have experienced a reduction in overall levels of interaction.

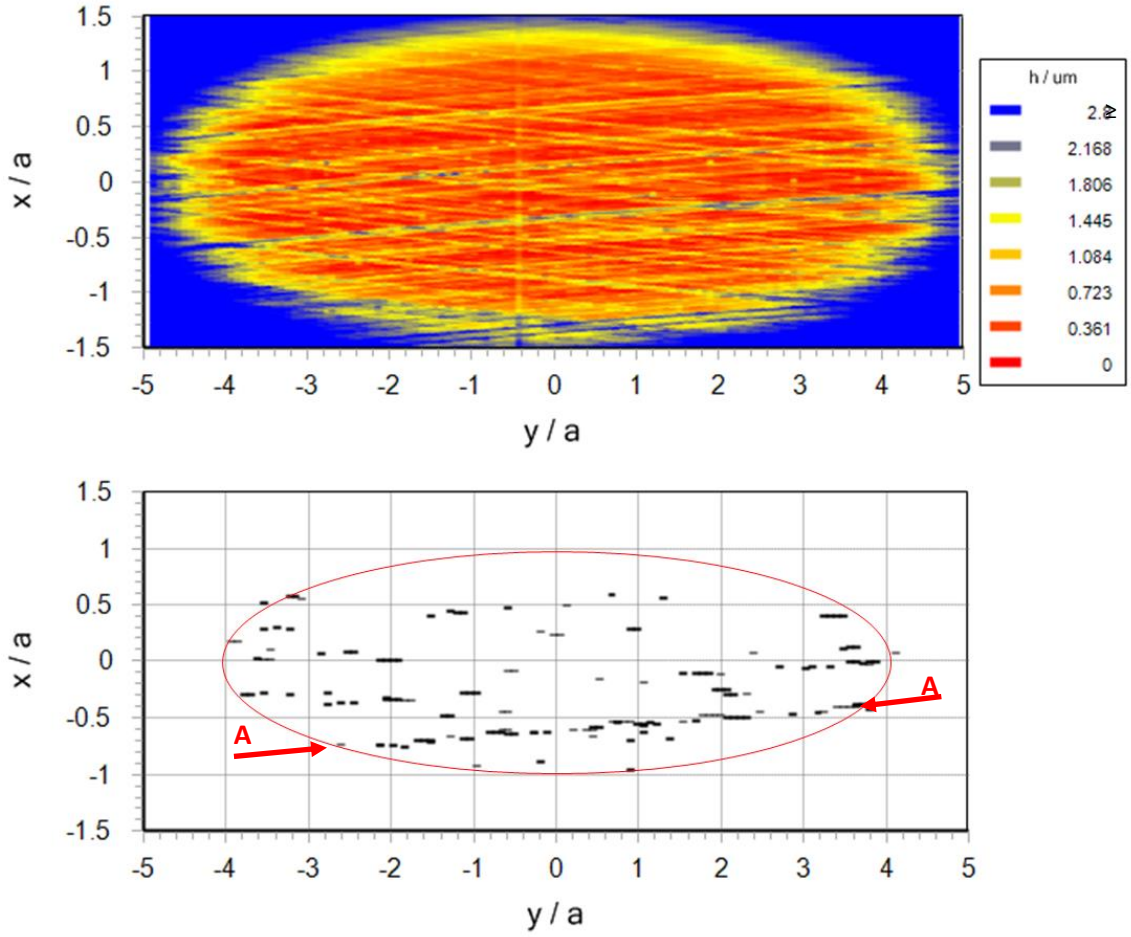

Figure 6-26 Film thickness distribution and contact plot for fully rough solution at a maximum Hertz pressure of 1.0GPa at 500rpm conditions

6.4.4.7 Rough surface solution at p=1.0GPa, 2000rpm condition

Figure 6-27 shows results for the highest speed of 2000rpm. The increase in entrainment velocity at the lower contact pressure of 1.0GPa shows a much more significant increase in film thickness in comparison to the 2000rpm condition at 1.4GPa illustrated in Figure 6-22. The contact can be seen to experience very thin films with a minimum value of 0.057µm. The feature x=-0.7a, y=-4.0a, x=-0.25a, y=4.0a can be more clearly identified. Thinner films are most concentrated at the transverse edges of the contact with small regions of thin films distributed within the ellipse. An example of an isolated region of low film thickness can be seen at x=-0.2a, y=-0.4a. The contact plot for the time step confirms that no contact occurred.

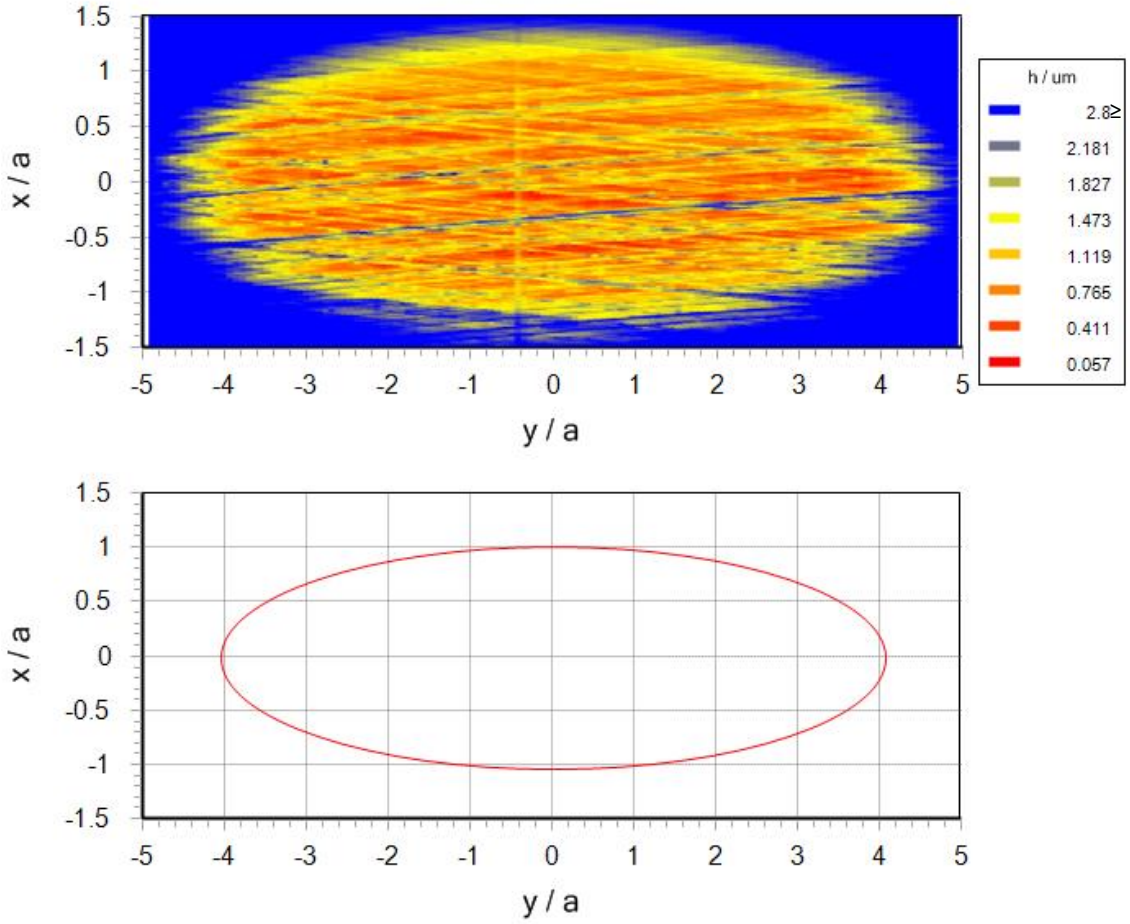

Figure 6-27 Film thickness distribution and contact plot for fully rough solution at a maximum Hertz pressure of 1.0GPa at 2000rpm conditions

6.4.5 Cumulative Contact Plots

Contact plots are produced with the total number of contacts at each mesh point and time step summed to produce an indication of contact frequency over the length of the simulation. The contact ellipse is clearly visible in these images. Certain locations within the ellipse are clearly shown to be more susceptible to asperity contact and some regions remain relatively free of contact.

Due to the nature of the plotting software used, the legend shows decimal values which does not accurately represent the discrete integer-value nature of the contact count. However, the maximum value shown in the legend is consistent with the highest number of contacts

experienced at a particular mesh point over the range of time steps considered, and the scale is indicative of the relative level of contact count for each mesh point.

It is clear on inspection of the plots that contact occurs distributed over the entire ellipse. Results are shown in descending order of speed as contact is seen to increase with a decrease in entrainment speed.

6.4.5.1 Rough surface solution at p=1.4GPa, 2000rpm condition

The cumulative contact plot for the highest entrainment speed shown in Figure 6-28 demonstrates the occurrence of contact distributed over the entire ellipse. Contact appears to occur most frequently at the transverse edges of the contact zone as indicated by the darker colouring. Contact also appears to occur more heavily at the EHL inlet rather than the outlet region, contrasting with the findings of Holmes et al. (2005a) for transverse finished contacts. This suggests that the cross hatched configuration of roughness is more difficult for the EHL film to separate before the higher pressure levels are established.

The cumulative contact plot shows a distinct band of low contact which spans the Hertzian ellipse longitudinally from x=-1.0a, y=-0.4a to x=1.0a, y=-0.35a. This band of low contact appears in a similar position to a prominent scoring mark present on the fast surface and can also be identified in the film thickness contour plots as a region of moderate film thickness.

Also visible in Figure 6-28 is a significant “sweeping” effect where there appear to be diagonal bands of varying contact frequency that span the ellipse from bottom right to top left of the figure.

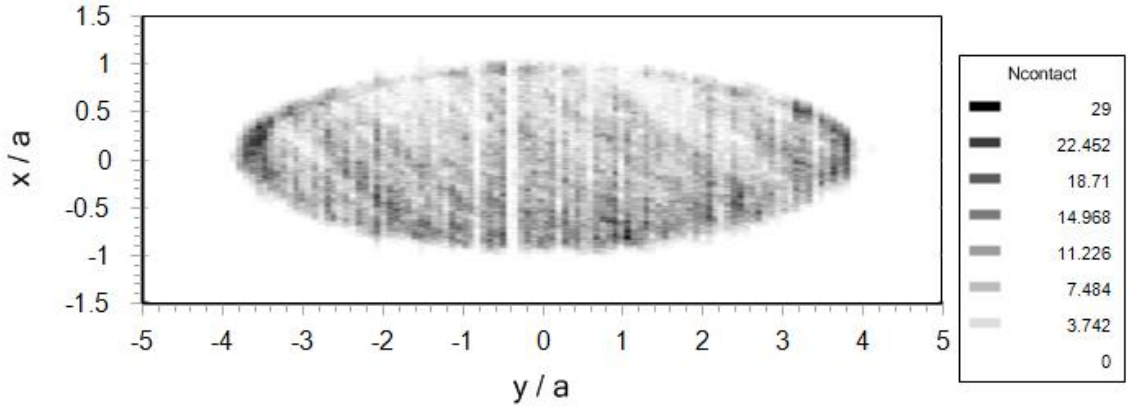

Figure 6-28 Cumulative contact plot for simulation run at a maximum Hertz pressure of 1.4GPa at 2000rpm conditions

6.4.5.2 Rough surface solution at p=1.4GPa, 500rpm condition

Lowering the entrainment speed as seen in Figure 6-29 results in increased contact frequency. Prominent longitudinal bands of low contact can be seen in the same position as was observed at higher speeds in Figure 6-28. Asperity contact appears to be more pronounced at the edges of the contact in comparison to the higher speed simulation. The diagonal bands are less prominent at lower entrainment speeds but can still be identified. Higher regions of contact can be seen to occur towards the inlet.

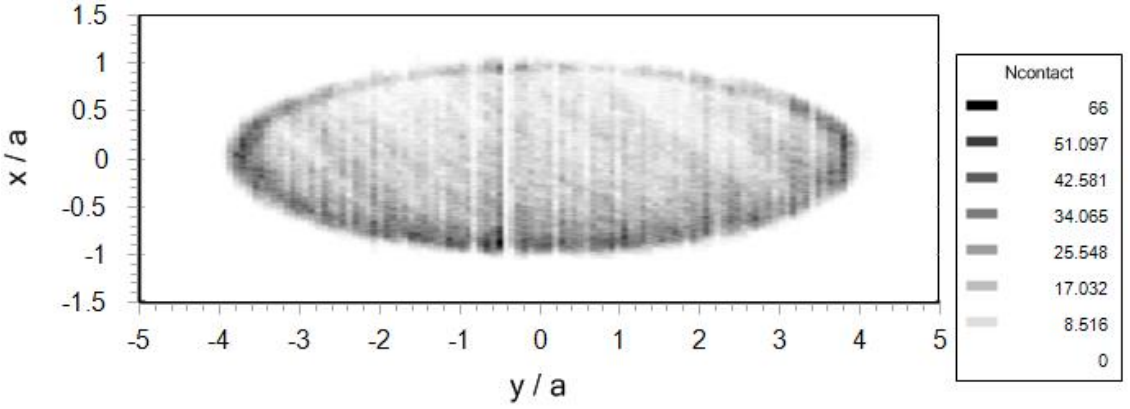

Figure 6-29 Cumulative contact plot for simulation run at a maximum Hertz pressure of 1.4GPa at 500rpm conditions

6.4.5.3 Rough surface solution at p=1.4GPa, 200rpm condition

The effect of further reducing the entrainment is an increase in contact frequency. The highest levels of contact can be seen to occur around the perimeter of the ellipse in Figure 6-30.

Despite this increase in contact frequency, longitudinal bands where little asperity interaction occurs are still visible. A particularly prominent region of contact can be seen towards the inlet of the ellipse at x=-1.0a, y=-0.6a. This region of high contact is shouldered by the two previously discussed bands of moderate contact.

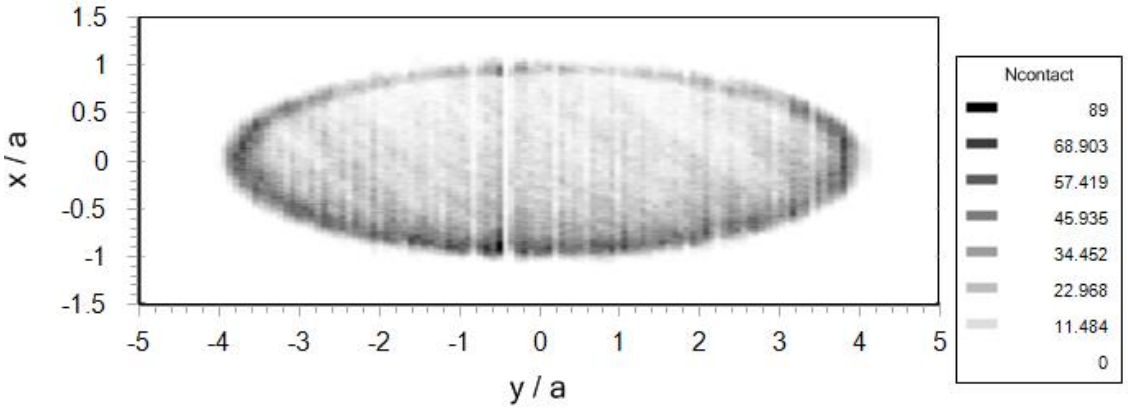

Figure 6-30 Cumulative contact plot for simulation run at a maximum Hertz pressure of 1.4GPa at 200rpm conditions

6.4.5.1 Rough surface solution at p=1.0GPa, 2000rpm condition

Lowering the load in Figure 6-31 at the entrainment speed equating to a fast shaft speed of 2000rpm, it can be seen that the high lambda ratio has greatly reduced the instances of contact. This is clearly shown where contact occurs as isolated at individual mesh points within the solution zone.

A band of contact can be seen in the longitudinal direction, aligned approximately with y=-2.0a, this is most probably due to the passage of a particularly aggressive surface feature. Due to the interpolation used within the plotting software, adjacent mesh points appear more prominent, which can be misleading. It is clear that the longitudinal band appears darker than mesh points at the edges of the contact despite each mesh point only experiencing contact in a single time step.

The remainder of the contact zone shows the majority of mesh points remaining free of contact. However, there are patches of contact occurring at the transverse edges of the ellipse

where contact was seen to occur most frequently during the 1.4GPa 2000rpm simulation in Figure 6-28. Similar results were also seen with transverse extruded roughness in the work of Holmes et al. (2005a).

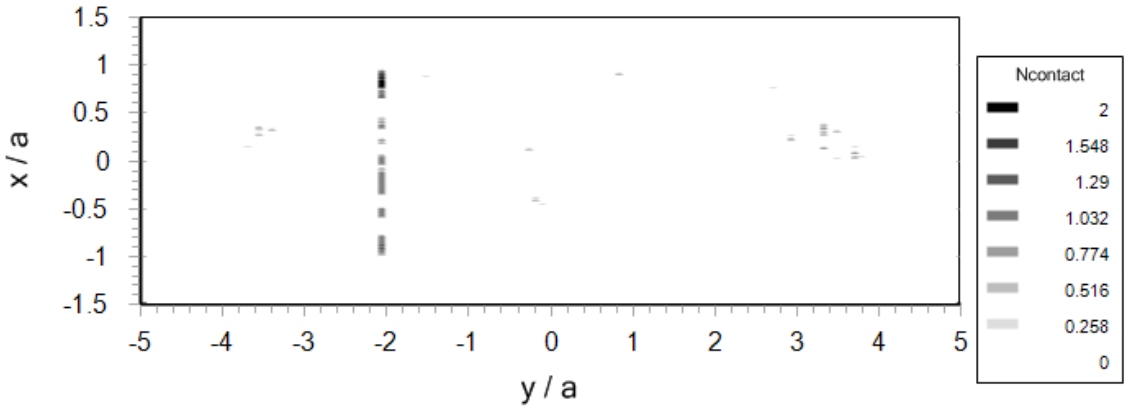

Figure 6-31 Cumulative contact plot for simulation run at a maximum Hertz pressure of 1.0GPa at 2000rpm conditions

6.4.5.2 Rough surface solution at p=1.0GPa, 500rpm condition

A decrease in entrainment speed shown in Figure 6-32 results in increased contact frequency over the simulation. Contact appears distributed over the entire ellipse, the shape of which can clearly be seen. Contact appears to be weighted more heavily towards the transverse edges of the Hertzian zone in comparison to lower speed conditions. The sweeping effect visible in simulations run at 1.4GPa across the contact can also be identified in this 1.0GPa simulation.

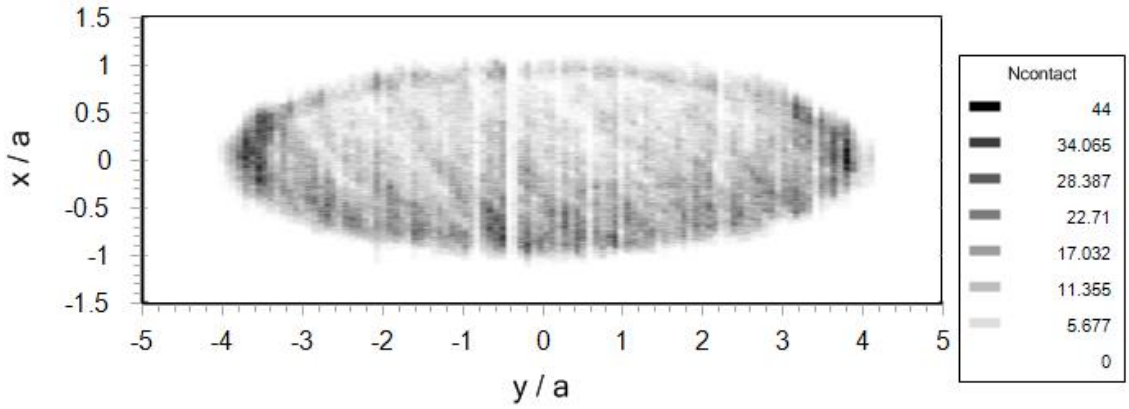

Figure 6-32 Cumulative contact plot for simulation run at a maximum Hertz pressure of 1.0GPa at 500rpm conditions

6.4.5.3 Rough surface solution p=1.0GPa, _200rpm condition

Reducing the entrainment speed further to 200rpm in Figure 6-33, the cumulative contact plot has a similar appearance to that of the 1.4GPa 200rpm condition shown in Figure 6-30, but the levels of contact are lower than those for the 200rpm condition at the higher contact pressure. The frequency of contact appears to be more heavily weighted to the inlet region at the lower speed, though the ring of contact occurring at the edge of the Hertzian zone appears less prominent in comparison to the higher load condition. Likewise with the lower load condition, a prominent region of high contact can be identified at x=-1.0a, y=-0.6a shouldered by two regions of low contact.

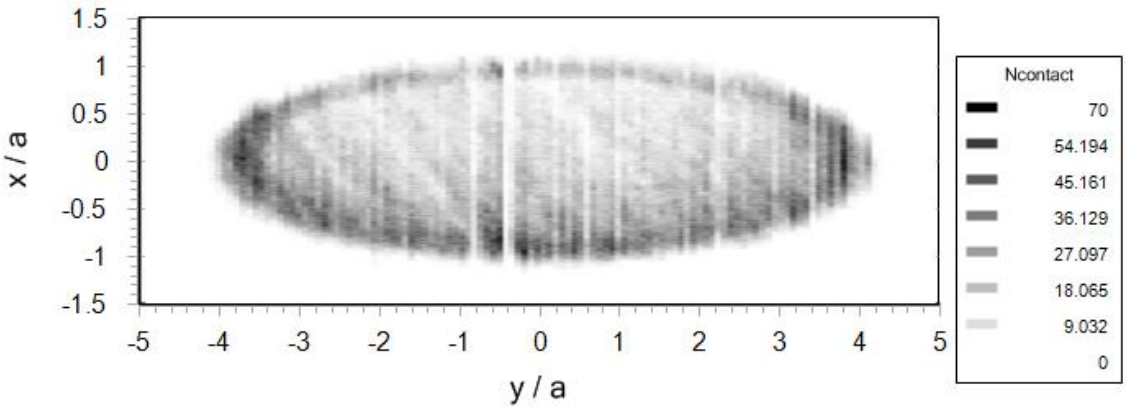

Figure 6-33 Cumulative contact plot for simulation run at a maximum Hertz pressure of 1.0GPa at 200rpm conditions

6.5 Discussion

Simulations investigating the film thickness distribution for conditions used in rig experiments show film thickness to be highly dependent on the thermal effects associated with high load conditions. Where simulations have been run at 1.4GPa, a great increase in film thickness was not experienced due to the decreased oil viscosity. The slight increase in film thickness did however reduce the instances of simulated contact. In lower load experiments where thermal effects were not as pronounced, entrainment speed can be seen have a greater impact on the

film thickness, this can be identified in the cumulative film thickness distributions where a large offset is generated with increasing entrainment.

Where higher load conditions are simulated the higher temperatures result in similar values of peak pressure being obtained despite increasing entrainment speed. In real applications, the thin films at the tips of asperity features may be enough to prevent excessive wear occurring but may not reduce large pressure spikes which may accelerate fatigue failure.

This can be seen more clearly in comparisons between 3D pressure distributions for both loads simulated at conditions of 200rpm and 2000rpm, where the thin films present in the 1.4GPa 2000rpm conditions result in very high pressure spikes. In contrast to this, the presence of a thick film which effectively separates the bearing surfaces reduces the peak pressures significantly.

When contrasted with the steady state smooth surface solution, it is apparent that the introduction of rough surfaces into the EHL contact generates pressure spikes far in excess of the maximum Hertz pressure. The pressure spikes can be seen to be distributed across the entirety of the contact. Despite the directional grinding, pressure can be seen to fluctuate heavily both transversely and in parallel to the roughness lay. The distribution of large pressure spikes across the entire contact is a plausible explanation for the uniform appearance of micropitting across the running tack on the test disks used in this work.

Plots of film thickness distributions for maximum contact pressures of 1.0GPa and 1.4GPa show thin films throughout the contact zone. In this work the slightly swept nature of the surface finish can be seen to produce a crosshatching effect within the film thickness distribution. Where prominent valley features on both sets of surfaces cross, regions of film thickness occur that can be far greater in thickness than the surrounding area, which can be a source of film leakage or cavitation. In addition to this the presence of imperfections could

influence the levels of contact seen, where the longitudinal scoring mark present on the faster surface used in the simulation resulted in increased contact on either side. The mechanism of this could be due to leakage into scoring marks and similar results with artificial sinusoidal roughness have been found in the work of Kweh et al. (1989).

Contact plots have also shown the real roughness features experience contacts along the length of some major asperity ridges. This could be associated with the manner in which fatigue damage has been seen in Chapter 4 to be distributed over the length of some prominent ridges whilst others are left undamaged. Surprisingly, the result of simulations has been for asperity contact to accumulate towards the inlet region of the Hertzian zone. This contrasts with previous work where contact was found to accumulate towards the outlet and could be associated with the crossed lay of the surfaces and the transverse extrusion of the previous work. The current work has shown contact to also accumulate at the edges of the contact, although the mechanism does not appear as pronounced as that reported with transverse extruded roughness. This could be due to the crossed lay of the surfaces reducing the side leakage effect thought to occur with transverse ground surfaces (Patching et al., 1995). Where surfaces were run at higher speed contact appeared to be more heavily weighted to the transverse edges of the contact as opposed to the inlet.

As has been previously discussed, the instances of contact observed in the simulations are judged to be overestimates due to the effect of misaligning the surfaces. The impact of misaligning the surfaces in a real sense has been seen in experimentation previously by Tudor (1948). The impact has been to increase contact levels of and further run the surfaces in. That being said, though contact may be an overestimate, changes in surface topography that occur from running in due to misalignment are small and plastic deformation that does occur on the tips of these features result in formation of thin films which have been shown to transmit high pressures here.

6.6 Conclusions

An existing numerical model for solving the isothermal EHL point contact problem has been modified and adapted to allow the use of 3D roughness measured from real surfaces. It has been demonstrated that the use of 3D roughness in the point contact problem results in contact along the prominent ridges, reflecting the results for fatigue shown in 3D profilometry. The introduction of this roughness has been shown to generate pressure spikes far in excess of the maximum Hertzian contact pressure.

At moderate to high loads, contact occurs distributed through the EHL zone with a contact occurring most frequently at the transverse edges and inlet this result is in agreement with simulations run with transverse roughness by Holmes et al. (2005a). Similar results have also been obtained experimentally by Patching et al. (1995) where scuffing was seen to initiate at the edge of the elliptical point contact on steel test disks.

7 Discussion

7.1 Summary

Experiments investigating the mixed lubrication regime have demonstrated that metallic contact occurs cyclically between groups of asperities when operating under realistic conditions and the level of contact is heavily influenced by the lambda ratio. This has been exhibited most strikingly in contact voltage contour plots shown in Chapter 5. Results have shown that even under high speed high lambda ratio conditions, surfaces experience a degree of interaction which over extended operation could accelerate fatigue. The cyclic nature of contact has also been conveyed in 3D surface measurements where following a extended operation, fatigue can be clearly identified to be occurring on the most prominent roughness features.

The impact of the prominence of roughness features on their propensity to accumulate damage can also be seen in Chapter 4 where linear surface profiles show new valley features appearing in place of former asperities as material is removed through fatigue. Similar results have also been reflected in fatigue simulations where over a range of lambda ratios asperity tips were observed to accumulate damage more rapidly than other regions of the surface (Sharif et al., 2012). The proportion of sliding taking place at the contact has also been found to impact the rate at which fatigue occurs, where disks operating at higher levels of sliding have been found to experience fatigue more rapidly than those run at lower slide to roll ratios. Similar results were also found by Oila and Bull (2005) and this can also be identified on the flanks of micropitted gear teeth where micropitting is seen to increase with distance from the pitch point.

Comparisons of the values calculated for cross correlation of fatigued profiles with as manufactured geometry implied that more change took place on topography of the slower surface from disk set C. It is believed that this is related to the pressure cycling that individual

asperities undergo as they traverse the contact – asperities on the slower surface experience a greater number of interactions and therefore pressure cycles per traverse of the contact than features on the faster surface (Sharif et al., 2012).

Transient temperatures have been shown to impact levels of interaction between the surfaces through variations in lubricant viscosity. This is reflected once again in contact voltage contour plots where increasing bulk disk temperature over the length of the experiment causes an overall decrease in contact voltage as new groups of asperities are brought into contact.

Where the surface modification has been monitored the most prominent roughness features also experience the largest initial plastic deformation as they come into contact with opposing groups of asperities. Previous workers have shown that the residual stresses identified by Bryant et al. (2012) as well as phase transformations seen by Oila et al. (2005) introduced by the running in process may be contributing factors in micropitting failure providing locations susceptible both to crack initiation and crack growth. In addition to this, modification of asperities can occur as a result of thin film conditions where individual asperity features are loaded more heavily.

Numerical models investigating the isothermal point contact with measured 3D roughness have demonstrated that where interaction occurs between groups of asperities, high pressures far in excess of the maximum Hertzian pressure are generated at these isolated regions. These high pressures may be a contributing factor in the propagation of micropitting. Results for instances of contact showed interactions distributed across prominent roughness features which has also been reflected in 3D scans taken from the micropitted surfaces. However, as has been commented on previously throughout this work – the simulation of “stable” (no plastic deformation) topography requires precise alignment between surfaces in order to accurately reflect experimental conditions. This is related to the accommodation that takes place between interacting asperities as they run in where realignment from a previously stable

pair of surfaces results in further modification (Tudor, 1948). It is therefore stated by the author that whilst general trends can be extracted from the simulation of EHL contacts results describing pressure spikes and instances of contact may be an overestimate.

7.2 Future Work

With these considerations in mind, it would be interesting to make comparisons with future experiments that could be run with one disk highly superfinished as the decreased scale of the geometry on one surface would reduce the impact of misalignment in simulations. In addition to this 2D roughness profiles carefully measured from interacting regions on each disk could be used in line contact models and simulated at varying degrees of offset. The author predicts that as surfaces approach the alignment corresponding to their positioning in experiments a decrease in both high pressures and frequency of contact will become apparent.

The initiation of micropitting failure has been previously associated with the load applied during the running in process, where experiments performed by Oila and Bull found that micropitting initiation was mostly controlled by the contact pressure (Oila and Bull, 2005). It would therefore be interesting to run experiments on disks which have isolated regions which been heavily loaded in stationary dry contact. Doing this would allow researchers to investigate whether micropitting occurs more heavily at these isolated locations and further examine the impacts of residual stresses on micropitting initiation.

Future work should also continue to investigate the modification in surface topography that occurs as a result of both running in and also micropitting. As this thesis has established that micropitting fatigue can be generated in relatively few load cycles, it would be interesting to examine the evolution of profile measurements taken in situ from a range of axial offsets. Numerical models and the results of scuffing experiments have shown contact to occur more frequently towards the edge of the contact ellipse; this may have an impact on the rate at which fatigue damage progress at different locations within an elliptical contact. In addition to

this continuing to monitor fatigue experiments with profilometry will provide useful data in order to compare and contrast with current models.

7.3 Conclusions

Results from experiments using electrical contact resistance have shown that contact occurs cyclically between groups of asperity features. At higher lambda ratios, contact occurs less frequently.

Profilometry has been used to monitor the surface topography of ground test disks during operation. The initial stage of operation for freshly manufactured surfaces is a termed running-in where features on the bearing surfaces accommodate to one another through plastic deformation as high pressures are transmitted through the EHL film and direct contact. The results of profilometry has strongly associated the location of micropitting with prominent asperity features, this has been observed where prominent asperity features have become been removed over extended running, leaving valley features. This removal of asperities gives the surface a pitted appearance at the roughness scale.

Results from simulations have shown that pressures encountered between interacting asperities are far in excess of the maximum Hertzian contact pressure. It is believed that these high pressure, applied cyclically to prominent asperity features results in the fatigue and removal of material, which is termed micropitting.

References

ABBOTT, E. J. & FIRESTONE, F. A. 1933. Specifying Surface Quality - A Method Based on Accurate Measurement and Comparison. ***Journal of Mechanical Engineering,*** **55, 569-572.**

AHLROOS, T., RONKAINEN, H., HELLE, A., PARIKKA, R., VIRTA, J. & VARJUS, S. 2009. Twin disc micropitting tests. ***Tribology International,*** **42, 1460-1466.**

ALANOU, M. P. 2006. ***Study of Parameters Influencing Surface Distress of Gears.*** **Ph.D, Cardiff University.**

ANDERSSON, S. 1977. Initial wear of gears. ***Tribology International,*** **10, 206-210.**

ARCHARD, J. F. & KIRK, M. T. 1961. Lubrication at Point Contacts. ***Proceedings of the Royal Society of London. Series A. Mathematical and Physical Sciences,*** **261, 532-550.**

BARBER, G. C., LEE, J. C. & LUDEMA, K. C. 1987. Materials and Surface Finish Effects in the Breaking-in Process of Engines. ***Journal of Engineering for Gas Turbines and Power,*** **109, 380-387.**

BIDWELL, S. 1883. On the Electrical Resistance of Carbon Contacts. ***Proceedings of the Royal Society of London,*** **35, 1-18.**

BINDER, L. 1912. Contact Resistance. ***E.u.M.,*** **30.**

BISHOP, I. F. & SNIDLE, R. W. 1982. Some experimental aspects of running-in and scuffing failure of steel discs operating under elastohydrodynamic conditions. ***In:*** **DOWSON, D., TAYLOR, C. M., GODET, M. & BERTHE, D. (eds.)** ***The Running-in Process in Tribology.*** **Butterworth-Heinemann.**

BISHOP, I. F. & SNIDLE, R. W. 1983. Running-In of Ground Surfaces Under Elastohydrodynamic Conditions. ***Society of Automotive Engineers*****, 53-64.**

BISHOP, I. F. & SNIDLE, R. W. 1984. ***An investigation of alternative methods of quantifying running-in of surfaces,*** **Warrendale, PA, Society of Automotive Engineers.**

BLAU, P. J. 2005. On the nature of running-in. ***Tribology International,*** **38, 1007-1012.**

BOWDEN, F. P. & TABOR, D. 1939. The Area of Contact between Stationary and between Moving Surfaces. ***Proceedings of the Royal Society of London. Series A. Mathematical and Physical Sciences,*** **169, 391-413.**

BRYANT, M. J., EVANS, H. P. & SNIDLE, R. W. 2012. Plastic deformation in rough surface line contacts—a finite element study. ***Tribology International,*** **46, 269-278.**

BULL, S. J., EVANS, J. T., SHAW, B. A. & HOFMANN, D. A. 1999. The effect of the white layer on micro-pitting and surface contact fatigue failure of nitrided gears. ***Proceedings of the Institution of Mechanical Engineers, Part J: Journal of Engineering Tribology,*** **213, 305-313.**

BURGHARDT, G., WÄCHTER, F., JACOBS, G. & HENTSCHKE, C. 2015. Influence of run-in procedures and thermal surface treatment on the anti-wear performance of additive-free lubricant oils in rolling bearings. ***Wear,*** **328–329, 309-317.**

CAMERON, A. 1954. Surface Failure in Gears. ***J Inst Pet,*** **40, 191-202.**

CAMERON, A. & GOHAR, R. 1966. Theoretical and Experimental Studies of the Oil Film in Lubricated Point Contact. ***Proceedings of the Royal Society of London. Series A. Mathematical and Physical Sciences,*** **291, 520-536.**

CHITTENDEN, R. J., DOWSON, D., DUNN, J. F. & TAYLOR, C. M. 1985. A Theoretical Analysis of the Isothermal Elastohydrodynamic lubrication of concentrated contacts. 1. Direction of Lubricant Entrainment Coincident with the Major Axis of the Hertzian Contact Ellipse. ***Proceedings of the Royal Society of London Series a-Mathematical Physical and Engineering Sciences,*** **397, 245-269.**

CLARK, F. M. 1935. Dielectric strength of mineral oils. ***Electrical Engineering,*** **54, 50-55.**

COURTNEY-PRATT, J. S. & TUDOR, G. K. 1946. An Analysis of the Lubrication between the Piston Rings and Cylinder Wall of a Running Engine. ***Proceedings of the Institution of Mechanical Engineers,*** **155, 293-299.**

CROOK, A. W. 1957. Simulated Gear-Tooth Contacts: Some Experiments upon Their Lubrication and Subsurface Deformations. ***Proceedings of the Institution of Mechanical Engineers,*** **171, 187-214.**

CROOK, A. W. 1961. The Lubrication of Rollers II. Film Thickness with Relation to Viscosity and Speed. ***Philosophical Transactions of the Royal Society of London. Series A, Mathematical and Physical Sciences,*** **254, 223-236.**

CROOK, A. W. 1963. The Lubrication of Rollers IV. Measurements of Friction and Effective Viscosity. ***Philosophical Transactions of the Royal Society of London. Series A, Mathematical and Physical Sciences,*** **255, 281-312.**

DAVIES, C. N. 2005. ***Effects of Non-Newtonian Rheology on the Line Contact Elastohydrodynamic Lubrication Problem.*** **Ph.D, Cardiff University.**

DOWSON, D. H., G.R. 1959. A Numerical Solution to the Elasto-Hydrodynamic Problem. ***Journal of Mechanical Engineering Science,*** **1, 6-15.**

DOWSON, D. H., G.R. 1961. New Roller Bearing Lubrication Formula. ***Engineering,*** **192, 158-159.**

DOWSON, D. H., G.R. 1966. ***Elastohydrodynamic Lubrication,*** **Oxford, Pergamon**

DOWSON, D. T., S. 1979. A Central Film Thickness Formula for Elastohydrodynamic Line Contacts. ***Procedings of the Fifth Leeds-Lyon Symposium on Tribology.*** **Bury St. Edmunds, UK: Mechanical Engineering Publications.**

EL-SISI, S. I. & SHAWKI, G. S. A. 1960. Measurement of Oil-Film Thickness Between Disks by Electrical Conductivity. ***Journal of Fluids Engineering,*** **82, 12-16.**

ELCOATE, C. D., EVANS, H. P., HUGHES, T. G. & SNIDLE, R. W. 2001. Transient elastohydrodynamic analysis of rough surfaces using a novel coupled differential deflection method. ***Proceedings of the Institution of Mechanical Engineers, Part J: Journal of Engineering Tribology,*** **215, 319-337.**

ERRICHELLO, R. L. 2010. Point Surface Origin, PSO, Macropitting Caused by Geometric Stress Concentration GSC. Alexandria, Virginia: American Gear Manufacturers Association.

ERRICHELLO, R. L. 2012. Morphology of Micropitting. ***Gear Technology.*** **Randall Publications.**

EVANS, H. P. & HUGHES, T. G. 2000. Evaluation of deflection in semi-infinite bodies by a differential method. ***Proceedings of the Institution of Mechanical Engineers, Part C: Journal of Mechanical Engineering Science,*** **214, 563-584.**

EVANS, H. P., SNIDLE, R. W., SHARIF, K. J., SHAW, B. A. & ZHANG, J. 2013. Analysis of Micro-Elastohydrodynamic Lubrication and Prediction of Surface Fatigue Damage in Micropitting Tests on Helical Gears. ***Journal of Tribology-Transactions of the Asme,*** **135.**

FUREY, M. J. 1969. Friction, Wear and Lubrication. ***Industrial and Engineering Chemistry,*** **61, 12-&.**

FURUSTIG, J., ALMQVIST, A., BATES, C. A., ENNEMARK, P. & LARSSON, R. 2015. A two scale mixed lubrication wearing-in model, applied to hydraulic motors. ***Tribology International,*** **90, 248-256.**

GOGLIA, P. R., CUSANO, C. & CONRY, T. F. 1984. The Effects of Surface Irregularities on the Elastohydrodynamic Lubrication of Sliding Line Contacts. Part II—Wavy Surfaces. ***Journal of Tribology,*** **106, 113-119.**

GREENWOOD, J. A. & TRIPP, J. H. 1967. The Elastic Contact of Rough Spheres. ***Journal of Applied Mechanics,*** **34, 153-159.**

GREENWOOD, J. A. & WILLIAMSON, J. B. P. 1966. Contact of Nominally Flat Surfaces. ***Proceedings of the Royal Society of London. Series A. Mathematical and Physical Sciences,*** **295, 300-319.**

GUANGTENG, G., OLVER, A. & SPIKES, H. 1999. Contact Resistance Measurements in Mixed Lubrication. ***In:*** **Q. WANG, J. N., F. SADEGHI (ed.)** ***The Advancing Frontier of Engineering Tribology.*** **STLE/ASME.**

GUANGTENG, G. & SPIKES, H. A. 1997. An Experimental Study of Film Thickness in the Mixed Lubrication Regime. ***Tribology Series.*** **Elsevier.**

HALLING, J. 1975. ***Principles of Tribology*****, Macmillan.**

HERTZ, H. 1882. Über die Berührüng fester elastischer Körper. ***Journal für die reine und angewandte Mathematik,*** **92, 156-171.**

HOLM, R. 1967. ***Electric Contacts - Theory and Application,*** **Berlin Heidelberg, Springer.**

HOLMES, M. J. A. 2002. ***Transient Analysis of the Point Contact Elastohydrodynamic Problem Using Coupled Methods.*** **PhD, Cardiff University.**

HOLMES, M. J. A., EVANS, H. P. & SNIDLE, R. W. 2005a. Analysis of mixed lubrication effects in simulated gear tooth contacts. ***Journal of Tribology-Transactions of the Asme,*** **127, 61-69.**

HOLMES, M. J. A., QIAO, H., EVANS, H. P. & SNIDLE, R. W. 2005b. Surface contact and damage in micro-EHL. ***In:*** **D. DOWSON, M. P. G. D. & LUBRECHT, A. A. (eds.)** ***Tribology and Interface Engineering Series.*** **Elsevier.**

HU, Y.-Z. & ZHU, D. 1999. A Full Numerical Solution to the Mixed Lubrication in Point Contacts. ***Journal of Tribology,*** **122, 1-9.**

HUTCHINGS, I. M. 1992. ***Tribology: Friction and Wear of Engineering Materials*****, Butterworth Heinemann.**

JAMALI, H. U., SHARIF, K. J., EVANS, H. P. & SNIDLE, R. W. 2014. The Transient Effects of Profile Modification on Elastohydrodynamic Oil Films in Helical Gears. ***Tribology Transactions,*** **58, 119-130.**

JOHNSON, K. L. & TEVAARWERK, J. L. 1977. Shear Behaviour of Elastohydrodynamic Oil Films. ***Proceedings of the Royal Society of London. A. Mathematical and Physical Sciences,*** **356, 215-236.**

KANETA, M. & CAMERON, A. 1980. Effects of Asperities in Elastohydrodynamic Lubrication. ***Journal of Tribology,*** **102, 374-378.**

KWEH, C. C., EVANS, H. P. & SNIDLE, R. W. 1989. Micro-Elastohydrodynamic Lubrication of an Elliptical Contact With Transverse and Three-Dimensional Sinusoidal Roughness. ***Journal of Tribology,*** **111, 577-584.**

KWEH, C. C., PATCHING, M. J., EVANS, H. P. & SNIDLE, R. W. 1992. Simulation of Elastohydrodynamic Contacts Between Rough Surfaces. ***Journal of Tribology,*** **114, 412-419.**

LAINÉ, E., OLVER, A. V. & BEVERIDGE, T. A. 2008. Effect of lubricants on micropitting and wear. ***Tribology International,*** **41, 1049-1055.**

LANE, T. B. & HUGHES, J. R. 1952. A study of the oil-film formation in gears by electrical resistance measurements. ***British Journal of Applied Physics,*** **3, 315.**

LI, S. 2015. A Computational Study on the Influence of Surface Roughness Lay Directionality on Micropitting of Lubricated Point Contacts. ***Journal of Tribology,*** **137, 021401-021401.**

LI, S. & KAHRAMAN, A. 2013a. Micro-pitting fatigue lives of lubricated point contacts: Experiments and model validation. ***International Journal of Fatigue,*** **48, 9-18.**

LI, S. & KAHRAMAN, A. 2013b. A physics-based model to predict micro-pitting lives of lubricated point contacts. ***International Journal of Fatigue,*** **47, 205-215.**

LORD, J. & LARSSON, R. 2008. Film-forming capability in rough surface EHL investigated using contact resistance. ***Tribology International,*** **41, 831-838.**

MACCONOCHIE, I. O. & CAMERON, A. 1960. The Measurement of Oil-Film Thickness in Gear Teeth. ***Journal of Fluids Engineering,*** **82, 29-34.**

MARTIN, H. M. 1916. Lubrication of Gear Teeth. ***Engineering (London),*** **102, 119-121.**

MERRITT, H. E. 1935. Worm Gear Performance. ***Proceedings of the Institution of Mechanical Engineers,*** **129, 127-194.**

MEYER, A. 1898. Ofvers Vetenskakad Forh. ***Stockh,*** **55, 199.**

O'CONNOR, B. 2005. The Influence of Additive Chemistry on Micropitting. ***Gear Technology.*** **Randall Publications.**

OILA, A. & BULL, S. J. 2005. Assessment of the factors influencing micropitting in rolling/sliding contacts. ***Wear,*** **258, 1510-1524.**

OILA, A., SHAW, B. A., AYLOTT, C. J. & BULL, S. J. 2005. Martensite decay in micropitted gears. ***Proceedings of the Institution of Mechanical Engineers, Part J: Journal of Engineering Tribology,*** **219, 77-83.**

ØSTVIK, R. & CHRISTENSEN, H. 1968. Changes in Surface Topography with Running-In. ***Proceedings of the Institution of Mechanical Engineers, Conference Proceedings,*** **183, 57-65.**

PALACIOS, J. M. 1983. Elastohydrodynamic films in mixed lubrication: An experimental investigation. ***Wear,*** **89, 303-312.**

PATCHING, M. J. 1994. The effect of surface roughness on the micro-elastohydrodynamic lubrication and scuffing performance of aerospace gear tooth contacts.

PATCHING, M. J., KWEH, C. C., EVANS, H. P. & SNIDLE, R. W. 1995. Conditions for Scuffing Failure of Ground and Superfinished Steel Disks at High Sliding Speeds Using a Gas Turbine Engine Oil. ***Journal of Tribology,*** **117, 482-489.**

PEPPLER, W. 1936. Untersuchungen uber die Druckubertragung bei Belasteten und Geshimierten Umlaufenden Achsparllelen Zylindern. ***Maschinenelemente-Tagung Aachen,*** **42.**

PETRUSEVICH, A. I. 1951. Fundemental Conclusions from the Contact-Hydrodynamic Theory of Lubrication. ***Izv. Akad. Nauk SSR. Otd. Tekh. Nauk,,*** **2, 209-233.**

PULLEN, J. & WILLIAMSON, J. B. P. 1972. On the Plastic Contact of Rough Surfaces. ***Proceedings of the Royal Society of London. A. Mathematical and Physical Sciences,*** **327, 159-173.**

ROELANDS, C. J. A. 1966. ***Correlation aspects of the viscosity-temperature-pressure relationship of lubricating oils.*** **PhD PhD, Technical University Delft.**

ROWE, G. W., KALISZER, H., TRMAL, G. & COTTER, A. 1975. Running-in of plain bearings. ***Wear,*** **34, 1-14.**

SHARIF, K. J., EVANS, H. P. & SNIDLE, R. W. 2012. Modelling of elastohydrodynamic lubrication and fatigue of rough surfaces: The effect of lambda ratio. ***Proceedings of the Institution of Mechanical Engineers, Part J: Journal of Engineering Tribology,*** **226, 1039-1050.**

SHARIF, K. J., KONG, S., EVANS, H. P. & SNIDLE, R. W. 2001. Contact and elastohydrodynamic analysis of worm gears Part 1: Theoretical formulation. ***Proceedings of the Institution of Mechanical Engineers, Part C: Journal of Mechanical Engineering Science,*** **215, 817-830.**

TABOR, D. 1951. ***The Hardness of Metals,*** **Oxford, UK, Clarendon Press.**

TALLIAN, T. E. 1972. The theory of partial elastohydrodynamic contacts. ***Wear,*** **21, 49-101.**

TALLIAN, T. E., CHIU, Y. P., HUTTENLOCHER, D. F., KAMENSHINE, J. A., SIBLEY, L. B. & SINDLINGER, N. E. 1964. Lubricant Films in Rolling Contact of Rough Surfaces. ***A S L E Transactions,*** **7, 109-126.**

TAO, J., HUGHES, T. G., EVANS, H. P., SNIDLE, R. W., HOPKINSON, N. A., TALKS, M. & STARBUCK, J. M. 2003. Elastohydrodynamic Lubrication Analysis of Gear Tooth Surfaces From Micropitting Tests. ***Journal of Tribology,*** **125, 267-274.**

TIMOSHENKO, S. P. & GOODIER, J. N. 1951. ***Theory of Elasticity*****, McGraw Hill.**

TUDOR, G. K. 1948. An Electrical Method of Investigating the Lubrication in a Journal Bearing. ***Journal of C.S.I.R.,*** **21, 202-209.**

VENNER, C. H. 1991. ***Multilevel Solution of EHL Line and Point Contact Problems.*** **Ph.D Ph.D, University of Twente.**

VLADESCU, S.-C., OLVER, A. V., PEGG, I. G. & REDDYHOFF, T. 2015. The effects of surface texture in reciprocating contacts – An experimental study. ***Tribology International,*** **82, Part A, 28-42.**

VOSKAMP, A. P. 1985. Material Response to Rolling Contact Loading. ***Journal of Tribology,*** **107, 359-364.**

WEBSTER, M. N. & CARDIS, A. B. 1999. Gear oil micropitting evaluation. American Gear Manufacturers Association (AGMA).

WEDEVEN, L. D. 1970. ***Optical Measurements in Elastohydrodynamic Rolling Contact Bearings.*** **PhD PhD, University of London.**

WHITEHOUSE, D. J. & ARCHARD, J. F. 1970. The Properties of Random Surfaces of Significance in their Contact. ***Proceedings of the Royal Society of London. A. Mathematical and Physical Sciences,*** **316, 97-121.**

WILLIAMS, P. A., FINNIS, M. P. & KELLY, D. A. 1988. History Dependence in 2-Disc Scuffing Tests. ***Proceedings of the Institution of Mechanical Engineers Part C-Journal of Mechanical Engineering Science,*** **202, 211-218.**

WILLIAMSON, J. B. P. & HUNT, R. T. 1968. Relocation profilometry. ***Journal of Physics E: Scientific Instruments,*** **1, 749.**

WILLIAMSON, J. B. P. & HUNT, R. T. 1972. Asperity Persistence and the Real Area of Contact Between Rough Surfaces. ***Proceedings of the Royal Society of London. A. Mathematical and Physical Sciences,*** **327, 147-157.**

WINTER, H. O., P. 1990. Influence of Lubrication on Pitting and Micropitting Resistance of Gears. ***Gear Technology.*** **Randall Publications.**

XU, G. & SADEGHI, F. 1996. Thermal EHL Analysis of Circular Contacts With Measured Surface Roughness. ***Journal of Tribology,*** **118, 473-482.**

ZHU, D. & AI, X. 1997. Point Contact EHL Based on Optically Measured Three-Dimensional Rough Surfaces. ***Journal of Tribology,*** **119, 375-384.**

ZHU, D., WANG, J. & JANE WANG, Q. 2015. On the Stribeck Curves for Lubricated Counterformal Contacts of Rough Surfaces. ***Journal of Tribology,*** **137, 021501-021501.**

ZHU, D. & WANG, Q. 2013. Effect of Roughness Orientation on the Elastohydrodynamic Lubrication Film Thickness. ***Journal of Tribology,*** **135, 031501-031501.**

ZHURAVLEV, V. A. 1940. On the question of theoretical justification of the Amontons-Coulomb law for friction of unlubricated surfaces. ***Journal of Technical Physics,*** **10, 1447-1452.**